Device fabrication using Bi nanoclusters

A thesis submitted in partial fulfilment of the
requirements for the Degree of

Doctor of Philosophy in Physics
in the
University of Canterbury

by

Ahmad Ayesh

Department of Physics and Astronomy
University of Canterbury
2007

Abstract

Nanoclusters have special importance in nanotechnology because of their low dimensionality, which provides electronic, chemical, and magnetic properties that differ from those of the equivalent bulk materials. Suitably controllable self-assembly methods are required in order to incorporate nanoclusters into useful devices.

The self-assembly method used in this study employs V-grooves as a template element for nanocluster device fabrication. The V-grooves are fabricated by optical lithography on SiO_2/Si wafers and KOH wet etching. Bi clusters deposited on a V-groove form a self-assembled conducting wire. The clusters are produced using an inert gas aggregation source inside an ultra high vacuum compatible system.

In order to characterise the assembly process, Bi clusters with different average sizes and velocities are deposited on V-grooves with different widths. The cluster bouncing was found to be the main process in forming the cluster wires. The bouncing angles were smaller than the incident angle, and they are dependent on the cluster size and velocity. For a certain bouncing angle, the wire width reflects the V-groove width because of the fixed bouncing angle.

Nanocluster devices were fabricated by depositing the clusters on V-grooves with pre-formed Au/NiCr electrical contacts. The amount of the deposited material required to form an electrically conducting wire was found to be a function of the V-groove width and the wire length. The two point *I(V)* measurements in the voltage range between -1 and +1V showed linear characteristics for low resistance wires (kΩ), and non-linear characteristics for the high resistance ones (MΩ). The silicon substrate was used as a back gate. Applying a voltage to the gate was found to modify the electrical conduction of the cluster wire. The temperature dependence of the resistance of the nanocluster wires was studied in the temperature range of 4.2-473K, and all of the measured wires showed a negative temperature coefficient of resistance. These measurements allowed a detailed study of the conduction mechanisms through the cluster wires. The study showed that Bi clusters can be used for device fabrication.

To size select the clusters prior to using them for the device fabrication, a high transmission mass filter is required. This transmission can be obtained using the von Issendorff and Palmer mass filter if it is operated using the optimum operation conditions. The mass filter consists of two pairs of parallel plates with horizontal openings in Plates 1 and 2, and it operates on the time of flight principle. During this project, the operation conditions of this mass filter were studied using both experiment and simulation. The study showed that the beam deflection angle is a critical factor in optimising the mass filter transmission efficiency. This angle is dependent on the accelerating voltage, ion mass, and the horizontal velocity of the ions. The optimum operation conditions for the mass filter were found and used to study the mass distribution of Pd ions produced by a magnetron sputtering source with variable cluster aggregation length.

1. Introduction

Preface

The prefix nano in the word nanotechnology means a factor of 10^{-9} (billionth). Nanotechnology is a field of technology that involves the design, characterization, and production of devices and systems by controlling shape and size at the nanometre scale.[1]

Decreasing material dimensions to the nanometre scale has received a great deal of attention as it can be used to modify material properties. In some systems, the new properties can be manipulated to fabricate materials with enhanced characteristics over their bulk. The strong catalysis of gold nanoparticles,[2] although the bulk is inert, provides an example of the enhanced properties.

The dependence of the nanomaterial properties on its dimensions can allow one to engineer these properties in order to use them in potential applications. These applications range from producing stronger and lighter materials, to manufacturing medicines with improved delivery and control where they can infiltrate cancer cells while leaving normal cells alone,[3] and nanodevices such as nanoswitches[4] and nano field effect transistors[5] which are the basic elements of the computer. Some of these applications are already in the commercial market such as the magnetic tape devices where the nanostructuring increases the storage capacity.[6]

An example of the transformations which occur as the material dimensions drop to nanosize and can be engineered by controlling material dimensions is the semimetal to semiconductor transformation. Bismuth (Bi) nanowires provide an example of this transformation.[7-10] Theoretical studies[8] supported with experimental results[11, 12] showed an increase in the band gap of Bi nanowires when reducing the nanowire diameter below a particular value (65nm).

Reducing material dimensions into the nanometre regime causes electrons to become confined inside the material. The confinement leads to the appearance of singularities in the density of states which develop at special energies, as shown schematically in Figure 1.1. This is different from the continuous density of states of the bulk material where electrons are unconfined. The singularities in the density of states of cluster exhibit large values and their positions are size dependent.[13] These singularities determine many unique electronic properties of the clusters.

Nanomaterials can be produced using two approaches: the bottom-up and the top-down. In the bottom-up approach the individual atoms and molecules are collected, consolidated, and fashioned into the nanomaterial. The inert gas aggregation and the sputtering methods for making clusters are examples of this approach. The top-down approach starts with a bulk material and reduces its dimensions gradually. The lithography technique is an example of this approach and it produces nanostructures with dimensions as low as 10nm.

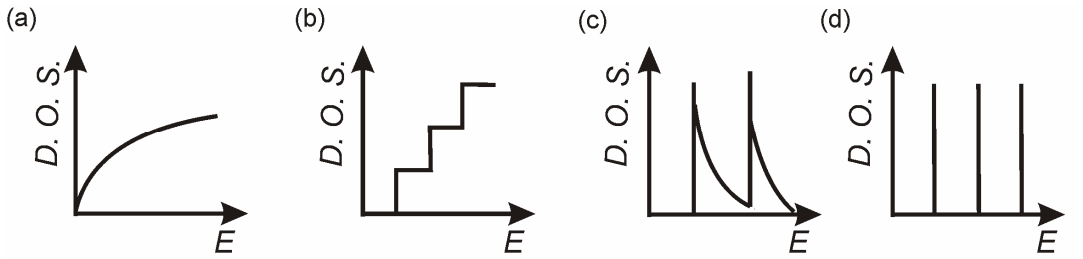

Figure 1.1 Electronic densities of states for (a) bulk conductor (b) quantum well (c) quantum wire (d) quantum dot.

Atomic clusters (described in detail in the next section) are an example of a nanomaterial. In order to make use of the size dependent properties of these clusters for device applications, clusters need to be assembled between electrical electrodes and used as building blocks for the device.

The problem of assembling atomic clusters into useful devices can be solved if a combination of the bottom-up and top-down approaches is used. The top-down approach can be used to produce a particular template with pre-formed electrical contacts. V-grooves in SiO_2/Si substrates with pre-formed electrical contacts provide a suitable template to produce nanocluster wire devices.[14] Clusters slide and/or bounce off the V-groove walls to form a self-assembled cluster wire in the apex of the V-groove.

Bi nanoclusters were used in this project to fabricate cluster wires. These clusters were produced using an inert gas aggregation source. The template assembly method was used to form nanocluster wires in an ultra high vacuum compatible system. The template used in this study was V-grooves in SiO_2 passivated Si wafers. Nanocluster wires fabricated using non-contacted V-grooves were used for morphological studies. Bi nanocluster devices were fabricated using contacted V-grooves, and their morphology and electrical properties were studied.

Bi clusters are attractive clusters to study the effects of quantum confinement on the transport properties of the carriers because of their small electron effective mass[15] and the large Fermi wavelength (Fermi wavelength of Bi is ~40nm[16] - see appendix A - which is similar or greater than the cluster size in our experiments). Bi nanowires are also promising for thermoelectric applications.[8, 17]

This chapter comprises of four sections. Section 1.1 provides an overview of important properties of atomic clusters with a focus on the properties of Bi clusters. The recent studies performed on both single crystal and nanocluster Bi wires are reviewed in Section 1.2. The next section illustrates an overview of the template assembly method used in this work, electrical conduction mechanisms through a material, non-linear *I(V)* characteristics, and the operation principle of the metal oxide semiconductor field effect transistor (MOSFET). The aspects discussed in Section 1.3 are of use in Chapters 4 and 5. The last section provides the thesis outline.

1.1. Atomic clusters

Atomic clusters are aggregates of atoms a few nanometres in diameter and their properties, which are different from the properties of bulk materials, vary with their size and shape.[13, 18] The atoms forming these clusters may be joined together by ionic, Van-de-Waals, covalent, or other forces.

Clusters have existed in nature and have been used for centuries. Roman glassmakers have used metallic clusters to colour glass as early as the fourth century A.D. The Lycurgus cup (which resides in the British museum in London) is an example of this use of the clusters. The cup is made of soda lime glass and contains gold and silver clusters and its colour changes from green to deep red when a light is placed inside it. Gold and silver clusters were also used to colour the glass in church windows. It was not until 1908 that G. Mie provided an explanation for the colours of the glass and related it to the metal cluster type and size.[19]

Atomic clusters can be prepared using the inert gas aggregation method,[14, 20, 21] sputtering techniques, and direct laser ablation.[18] Clusters are made from a vapour of elementary atoms which aggregate because of the supersaturation of the hot vapour in the presence of a cool inert gas. Clusters can also be prepared by chemical methods or by knocking them directly out of their bulk materials.[13]

Atomic clusters can be produced in different sizes. However, clusters were found to be more stable when they contained particular numbers of atoms. These numbers of atoms are called 'magic numbers'. One set of these numbers is 8, 20, 40, 58.. .[22] In order to explain these magic numbers, the cluster was interpreted in terms of the Jellium model.[13, 18] This model considers that a cluster core consists of atoms excluding their valence electrons. The core can be replaced by a uniform positive background. Thus, the valence electrons of the atoms are confined in a spherical potential well and their energies are quantized. These energies are organized in discrete levels, i.e. electronic shells. The magic numbers correspond to the numbers of valence electrons that completely fill one or more shells in a cluster and make it especially stable.[23] Spherical metal clusters with magic numbers show the greatest stability compared to clusters with other shapes. However, if the electronic shells are partially filled the cluster can become flattened or elongated to reduce the total energy of the cluster.[18, 23, 24]

A different set of magic numbers was found in 1991 when allowing atoms to coalesce at low temperatures.[25] This set corresponds to the numbers of atoms packing into perfect polyhedra. A specific sequence of magic numbers arises as the polyhedra become larger and larger through the addition of layers of atoms that are one atom thick, i.e. atomic shells. The atomic shells can be imagined as the layered skin of an onion. The polyhedral shape formed through the addition of a new atomic shell is more stable than that of a partially filled atomic shell since it minimizes the energy required to hold atoms in place by minimizing the number of edges.

Many of the differences between the properties of clusters and bulk materials can be explained as a result of the large percentage of surface atoms compared to the total

number of atoms. The fraction of the surface atoms (F_s) is negligible for bulk materials while it is important for clusters. For example, a cluster of 13 atoms has ~92% of its atoms on the surface (12 atoms), and a cluster of $1x10^5$ atoms has ~9% of its atoms on the surface (F_s is given as $4N^{-1/3}$ for pseudo-spherical clusters,[23] where N is the number of atoms in the cluster). The surface atoms have fewer nearest neighbours and accordingly are less strongly bound, which has a large impact on all of the energy related properties.

The upper limit of the size of a nanomaterial can be defined as the size at which a particular property is indistinguishable from that of the bulk. Each property of a material has a characteristic or critical dimension associated with it. For example, when the dimensions of a solid become comparable or less than the Fermi wavelength, the electrons become confined, thus, the solid cannot be treated in a similar way to the bulk.

Among the various size dependent properties of the clusters, the ability to engineer the band gap of some materials has a special importance in device applications. Band gap engineering by controlling the cluster size was used to fabricate semiconducting mercury clusters with different band gaps (although bulk mercury is metal).[26] It was also used to control the band gap of silicon clusters.[27]

The size dependent properties of Bi clusters are of special interest in this project. These clusters were used to fabricate nanocluster devices. The properties of these clusters are discussed in the following subsection.

1.1.1. Bi clusters

Bismuth provides a suitable system to study low dimensional physical phenomena because of the large carrier mobility, the long mean free path of the carriers, the light effective masses of the carriers, and the large anisotropy of the three ellipsoidal constant energy surfaces of electrons.[7, 28, 29] Bi nanomaterials also have applications in thermoelectric[8, 17] and superconductivity,[30] and they are promising for device applications.[31]

Bi clusters are similar to their bulk in terms of the crystal structure where both have a rhombohedral structure. This crystal structure was reported for Bi clusters with diameters of 5–8.4nm,[32] 5-20nm,[33]and 6–10nm.[34]

Since Bi exhibits a fast oxidation rate,[35] an oxide shell can be found around the cluster surface.[36] Bi-oxide was found to form either an amorphous[33] or a crystalline[36] shell around the cluster. The most likely form of this oxide is β-Bi_2O_3.[35]

A decrease in the melting temperature with decreasing Bi cluster size is also expected as this effect was reported for other metallic clusters.[37] Molecular dynamics simulations predict a melting temperature of 300K for Bi clusters when their size drops to 6nm.[36]

Schulze et al.[38] studied the conductance of Bi cluster films. Clusters of the size ~20nm were deposited from an inert gas aggregation source between electrical contacts

defined by electron beam lithography. Random telegraph noise and some irreproducible steps were observed in the resistance-time measurements. The former was explained in terms of tunnelling of the carriers from a conducting path to a nearby defect or island. The perturbation of the current flow in the original path by charged defects or islands will lead to reproducible conduction levels for each charge state of the island. The latter was assigned to changes in the morphology of the films driven by the electrical current such as cluster coalescence caused by the resistive heating, or electro-migration of atoms between clusters.

In a cluster film, the percolation threshold is a measure of the lowest value of the cluster coverage that causes formation of a continuous network of clusters, allowing current to flow between the contacts. Schmelzer et al.[21] found that the percolation threshold of a percolating Bi cluster film can be reduced by reducing the separation between the contacts. Reducing the contacts' separation from 40 to 5 lattice sites reduced the percolation threshold from ~0.6 to ~0.25. This result was found experimentally using Bi clusters assembled between electron beam lithography defined contacts and by simulation.[21]

1.2. Nanowires

The singularities in the density of state function of a nanowire (Figure 1.2(c)) is one reason behind many new properties of nanowires. These properties are dependent on the wire diameter. Controlling the nanowire diameter provides an opportunity to engineer many properties and to control the band gap of the nanowire. Hence, nanowires have potential applications in many areas such as field effect transistors,[39] gas sensors,[40] nanoresonators,[41] nanolasers,[42] and magnetic field sensors.[43] This project focuses on Bi nanowires. These nanowires have a special importance because of their thermoelectric applications[17] and possible device applications.[10, 31]

This section contains three subsections. The semimetal-semiconductor transformation of the single crystal Bi nanowires is discussed first, followed by the recent experimental development of the Bi cluster wire fabrication. The last subsection presents the recent development in Bi nanodevice fabrication.

1.2.1. Single crystal Bi nanowires

Although bulk Bi is a semimetal with an equal number of carriers and a band gap overlap at the L and T points of 38meV, it can be transformed into a semiconductor by alloying Bi with a small concentration of antimony (Sb).[7] However, by reducing the Bi nanowire diameter,[8, 44, 45] the band gap at the L-point increases and the band gap between the L and T points decreases leading to a semimetal to semiconductor transition (Figure 1.2.[8] shows the trend towards this transition as a function of wire diameter).

Arrays of Bi nanowires with diameters below 110nm were prepared using the pressure injection method by Zhang et al.[8] and more recently by Tian et al.[31] and Li et al..[45] Zhang and Li studied the temperature dependence of the wires' resistance, carrier concentration, and carrier mobility in the temperature range of 4.2-300K.

Nanowires with diameters of 65nm or below showed a negative TCR, and carrier concentration and mobility of about one and two orders of magnitude lower than those of the bulk at 4.2K, respectively. This is shown in Figure 1.3. They explained the negative TCR in terms of the increase in the carrier concentration which outweighs any decrease in the carrier mobility as the temperature increases from 4.2 to 300K. The carrier mobility at temperatures below 77K of wires with diameters below 65nm is affected mainly by the carrier scattering at the wire boundaries, where the phonon scattering could be neglected. They also found that, for a particular temperature, increasing the wire diameter increases the carrier mobility which supports the idea that the boundary scattering is stronger for wires with smaller diameters. Zhang found using the Lax model[46] that the band gap at the L-point increases from 15meV for bulk Bi to 44 and 60meV for wires with diameters of 90 and 65nm respectively. The band overlap between the T-point in the valence band and the L-point in the conduction band also drops from 38meV for bulk Bi to 22 and 14meV for the 90 and 65nm wires (Figure 1.2).

The semimetal-semiconductor transformation of Bi nanowire arrays prepared using the pressure injection method was also confirmed experimentally and theoretically by Black et al.,[11] who studied the infrared absorption of ~40nm nanowires. They found that the direct band gap at the L-point increases to 123meV for the nanowire compared with 36meV for the bulk.

Although Bi nanowires exhibit negative TCR, the temperature dependence of resistance reported in the literature varied for nanowires with different diameters and preparation methods. For example, Huber et al.[47] reported a *ln(1/T)* dependence of the resistance in a temperature range of 0.3-300K of Bi nanowire arrays prepared using the pressure injection method in porous vycor glass with a diameter of 6nm. This dependence could not be observed for nanowires with a diameter of 65nm prepared using the same method.

The reduction of the nanowire diameter also changes the magneto resistance (MR) dependence on temperature. Liu et al.[48, 49] and Graf et al.[49] studied the MR of arrays of Bi nanowires with diameters of 200nm and 6nm. The MR was found to be dependent on the strength and the orientation of the magnetic field. Liu reported a large positive MR which varied from ~300% at 4.2K to ~70% at 300K when using a transverse magnetic field of 50kOe.

1.2.2. Bi cluster wires

Cluster wires are more complex than the single crystal wires. A cluster wire can be considered as a quasi one-dimensional wire if the current conduction occurs through a single conduction path. In this sense, the electrons experience a confinement where they are free to move only in one direction. However, cluster wires are not as simple as that in reality. For example, if the conduction between the clusters occurs through a small cluster, it will act as a bottleneck against the current flow which increases the confinement of the electrons. Moreover, Bi-oxide layers may exist around clusters, because of their fast oxidation rate, forming tunnelling barriers in the cluster network. On top of that, electrons experience extra scattering due to the cluster boundaries through the wire.

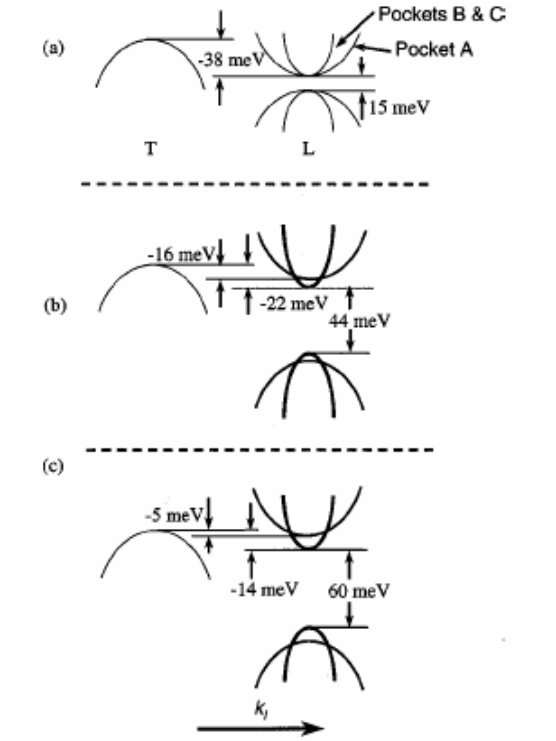

Figure 1.2 The energy band diagram at the L and T points of (a) bulk Bi, (b) nanowire with a diameter of 90nm, and (c) nanowire with a diameter of 65nm, after Reference [8].

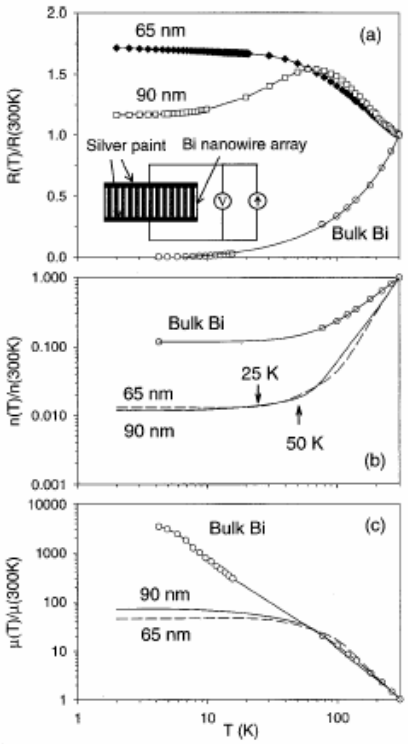

Figure 1.3 The dependence on temperature of the normalized resistance (a), carrier concentration (b), and carrier mobility (c) of Bi nanowires with diameters of 65 and 90nm compared with the bulk values, after Reference [8].

In the following, recent developments in Bi cluster wire experiments are reviewed. The review focuses on the work performed by the Cluster Group at the University of Canterbury since it is the main group working on these wires.

Bi cluster wires were prepared using three methods. The first method used V-grooves in SiO_2 passivated Si wafers as a template.[14, 20, 50, 51] The second method used electron beam lithography defined slots in a PMMA resist on top of SiO_2/Si or Si_xN_y/Si wafers.[51, 52] The last method was performed by cluster deposition through stencils.[51] In all three methods, Bi clusters were deposited on samples with pre-formed electrical contacts, and electrical measurements were taken for the samples in-situ under vacuum to reduce cluster oxidation.[20, 38]

V-grooves in SiO_2/Si wafers are a suitable template to self-assemble Bi clusters to form cluster wires. V-grooves were fabricated using the standard optical lithography and wet etching.[14, 20, 50, 51] Bi clusters with a size ranging between 20 and 100nm were produced using an inert gas aggregation source inside either a high vacuum or an ultra high vacuum compatible system.[14] Wires were formed by depositing clusters on the V-grooves where clusters bounce and/or slide to the apex of the V-groove forming the wires.[14] The studies found that the wire width reflects the V-groove width.[50] The current-voltage ($I(V)$) characteristics of the cluster wires in a voltage range between −100 and 100mV were linear.[14, 50]

Cluster wires with minimum widths as low as 10nm were produced by depositing Bi clusters on slots in PMMA.[51, 52] Bi clusters were found to exhibit low probability of sticking to the PMMA compared with the SiO_2/Si or Si_xN_y/Si substrates. This caused the formation of a continuous wire inside the slot before forming continuous network of clusters on the PMMA.

Bi cluster wires were also formed by depositing clusters through a stencil (an aperture slot formed in a Si_xN_y membrane) on Si_xN_y/Si substrates with two planar Au/Ti contacts.[51] The stencil was coated with a PMMA layer prior to the cluster deposition. The wetting and reflection characteristics of the incident clusters were exploited and provided a distinct benefit over standard nanostencilled atomic deposition processes.

1.2.3. Bi nanodevices

Three types of Bi-based nanodevices have been reported in the literature. These devices were fabricated using Bi clusters,[28] single crystal Bi nanowires,[9, 10] and polycrystalline Bi nanowires.[17] The recent developments in each of these devices is reviewed below.

Kubatkin et al.[28, 53] produced single electron transistors using Bi clusters aligned between two contacts (fabricated using an electron beam lithograph) with a separation of 10nm. Bi clusters with a diameter of ~3nm were (prepared using a quench-condensed technique) deposited on the substrate while its temperature was between 4.2 and 10K. The cluster network was discontinuous, and the carrier transport occurred through the device by tunnelling. The source-drain current (I_{SD}) was modified by applying a voltage to an alumina gate of each sample at temperatures below (or equal) 11K, as shown in Figure 1.4. The effect of changing the temperature

on the conductance was also studied. The conductivity was enhanced five times when the temperature decreased from 11K to 4.2K. However, to the best of our knowledge, Kubatkin's group is the only group reporting Bi cluster devices.

The semimetal-semiconductor transition of the single crystal Bi nanowire which occurs when the wire diameter is below 65nm[8] was the basic idea used by Tian et al.[10, 31] and Li et al.[9] to fabricate devices using single crystal Bi nanowires. Tian and Li fabricated metal-semiconductor junctions by fabricating wires consisting of two segments with different diameters. One segment had a diameter below 65nm and exhibited semiconducting properties, while the other was semimetallic with a diameter above 65nm. Tian[10] prepared Y-branched Bi wires using the pulsed electrodeposition within a porous anodic alumina oxide as a template, as shown in Figure 1.5. The diameters of the wire were 80nm for the stem and 50nm for the branch. The *I(V)* measurements for the nanowire arrays showed non-linear characteristics which were explained in terms of the semimetal-semiconductor transition (Figure 1.5). However, instead of fabricating Y-branched wires, Li[9] (and Tian in a different study[31]) fabricated straight wires with two diameters each. The diameters were 35-40nm and 70-100nm for each segment, and they obtained similar *I(V)* characteristics (to Tian's[10]).

Boukai et al.[17] fabricated polycrystalline Bi nanowires with diameters of ~40nm by the atomic deposition of Bi on substrates with pre-formed contacts. The measurements were performed at 20K, and the conductance of the wires was modified by controlling the gate voltage. They also observed linear *I(V)* characteristics in the range between –1 and 1.5V. The wires were found to exhibit semimetallic conduction despite the small wire diameter.

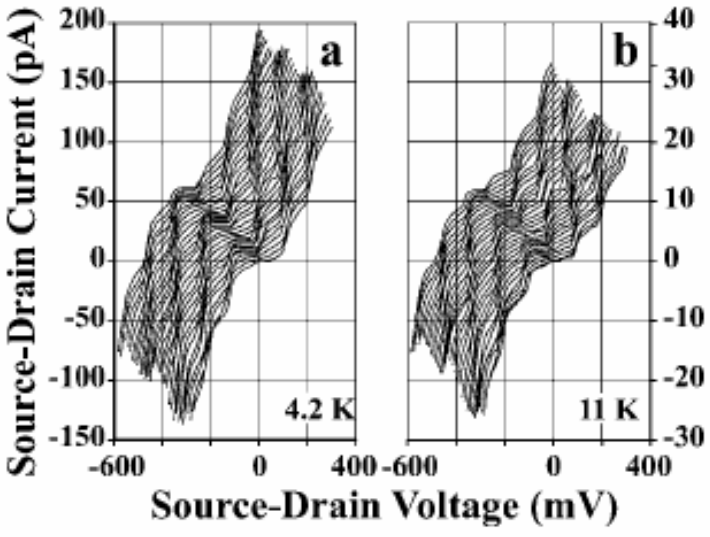

Figure 1.4 The dependence of the I(V) characteristics on the gate voltages at 4.2K (a) 11K (b), after Reference [28].

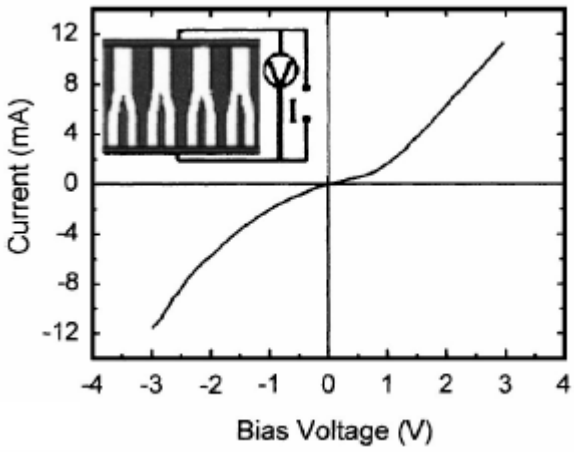

Figure 1.5 I(V) characteristics of parallel Y-branched Bi nanowires embedded in an anodic alumina template, after Reference [10].

1.3. Issues concerning device fabrication using Bi cluster wires

This section focuses on issues related to device fabrication using Bi clusters in the current project. These issues are referred to extensively in the discussion of device fabrication and performance in Chapters 4 and 5. The template assembly method used to form cluster wires is illustrated first. The next subsection provides reasons behind the non-linear *I(V)* characteristics. The last subsection demonstrates the typical MOSFET operation principle.

1.3.1. Template assembly

The assembly of nanoclusters or nanowires to fabricate a functional device is a serious challenge. Various templates can be used to solve the assembly problem. However, these templates should be compatible with the current semiconductor industry.

Anodic aluminium oxide was used as a template to fabricate Bi nanowire devices in some studies.[8-10, 31] Although these studies enhanced our understanding of the carrier transport in the nanowires and provided a method for Bi wire device fabrication, this method is not convenient to be used in industrial applications for various reasons. For example, the device was fabricated using an array of wires rather than a single wire. Positioning a single wire between electrodes is not an easy work. Where a single wire has been positioned successfully, the wire will oxidize before any electrical contacts are made to the wire. This means that a Bi-oxide layer (a barrier) will be formed between the wire and the contacts.

The template used in this study is a V-groove in a SiO_2 passivated Si wafer. The V-groove provides a large cluster collection area ensuring the formation of an electrically conducting wire inside the V-groove earlier than the formation of a continuous network of clusters on the plateaus next to the V-groove. The deposited

clusters bounce and/or slide on the V-groove walls to the apex owing to their initial kinetic energy gained from the inert gas aggregation source. This provides self-assembled cluster wires.

The compatibility of the V-groove fabrication with the current processes used in the semiconductor industry is another advantage which supports using it as a template. Electrical contacts were fabricated on the V-groove using the standard optical lithography and lift-off method prior to the cluster deposition. Clusters were deposited on the template under low vacuum. This allows electrical measurements on the sample while it is under vacuum to reduce the growth of Bi-oxide layers between the contacts and the wire. Using the V-groove as a template has another advantage. The triangular shape of the V-groove walls exposes a larger area of the wire to the gate electric field (the Si wafer is used as a back gate) compared with wires deposited on a planar substrates.

1.3.2. Non-linear *I(V)* characteristics

The *I(V)* characteristics of a junction provide information concerning the electrical conduction mechanisms and the contact type in the junction. A linear *I(V)* curve indicates Ohmic conduction and the lack of any tunnelling barriers in the junction at low temperatures. However, the non-linearity in the *I(V)* may result from tunnelling barriers existing in the junction. Schottky barrier and Bi-oxide layers between a Bi cluster wire and the contacts are examples of these barriers.

A Schottky contact is a metal-semiconductor contact where a rectifying behaviour is observed. When a metal and a semiconductor with different work functions are brought into contact, the Fermi levels in the two materials must equalise (at thermal equilibrium) and the vacuum level must be continuous. Hence, a Schottky barrier should be introduced at the metal-semiconductor interface. The barrier height ($q\Phi_B$) is the difference between the metal work function ($q\Phi_m$) and the electron affinity of the semiconductor ($q\chi$), i.e.

$$q\Phi_B = q(\Phi_m - \chi) \tag{1.1}$$

The non-linear *I(V)* characteristics can also be due to the existence of barriers within a device. Kaiser et al.[54] introduced a generic expression which describes the conductance of one (and quasi-one) dimensional wires where the conduction occurs by tunnelling and produces non-linear *I(V)* characteristics. This expression is

$$G = \frac{I}{V} = \frac{G_o(T)\exp(V/V_o)}{1 + h[\exp(V/V_o) - 1]} \tag{1.2}$$

where $G_o(T)$ is the zero voltage conductance, V_o is the voltage scale factor which is dependent on the energy barrier, and h is the ratio between $G_o(T)$ and the saturation conductance. Equation 1.2 was applied to the conductance of a wide range of quasi one dimensional systems, where the conduction occurs through tunnelling barriers, and it showed a good fit to the non-linear *I(V)* characteristics.[54, 55]

Ozturk et al.[56] studied the conductance of networks of gold nanorods using a special case of Equation 1.2, where they used h=0 and $V_o=N_b k_B T/e$ (N_b is the number of the nanorods in the network). Their equation was in good agreement with their experimental data.

Reichel[57] used both Equation 1.2 and Ozturk's special case of the equation to fit the conductance of the Bi cluster wires produced at the Cluster Laboratory in the University of Canterbury. Equation 1.2 showed a better fit to the conductance of the cluster wires than Ozturk's special case.

Sheng et al.[58, 59] studied a special case of the conductivity of a system of disordered metallic islands separated by non-conducting regions. This system is similar to a system of metallic clusters separated by barriers. The resistivity is[58, 59]

$$\rho(T) = \rho_t e^{\frac{T_t}{T+T_s}} \tag{1.3}$$

where ρ_t is the zero temperature resistivity, T_t is the lowest temperature where the voltage fluctuations can overcome the barrier, and T_t/T_s finds the tunnelling in the low temperature limit. The above dependence of the resistivity applies for a system where Coulomb blockade (caused by the electrostatic charging energy of the transferred electrons) is not an important effect, and the resistivity should be affected greatly by the voltage fluctuations across the non-conducting barrier.

1.3.3. MOSFET

The typical MOSFET works in two modes: enhancement and depletion.[60] In the enhancement mode, the source-drain current (I_{SD}) is normally very low (off mode). Applying a voltage to the gate accumulates charge and forms a conducting channel which increases I_{SD}. If an n-channel is formed by applying a positive voltage to the gate, this would be an n-channel MOSFET; whereas, if a p-channel is formed by applying a negative voltage to the gate, it would be a p-channel MOSFET. The n-channel MOSFET is made of a p-type substrate, while the p-channel MOSFET is made of an n-type one.

I_{SD} is normally large in the depletion mode of the MOSFET (normally on). Applying a negative voltage to the gate of an n-channel MOSFET in the depletion mode depletes the electrons and decreases I_{SD}, and applying positive voltage to the gate accumulates more electrons which increases I_{SD}. Applying a positive voltage to the gate of a p-channel MOSFET in the depletion mode depletes the holes and decreases I_{SD}, while applying a negative voltage to the gate accumulates more holes and increases I_{SD}.

In an n-channel MOSFET, the drain is connected to a positive voltage and the source is connected to the ground. The ammeter is connected between the source and the ground in such a way that the positive of the ammeter is connected to the source, and the negative is connected to the ground as shown in Figure 1.6(a). If a p-channel MOSFET is considered, the side which is connected to the positive of the power

supply will be the source, while the side which is connected to the ammeter will be the drain as shown in Figure 1.6(b).

The 'conventional' direction of the current through the ammeter in the following discussion is from the source to the ground for the n-channel MOSFET, while it is from the drain to the ground for the p-channel MOSFET. The ammeter reading is a positive value if a current in the conventional direction passes through it.

Depending on the direction of the conventional current, we can find four cases for the ammeter readings:[60]

1. n-channel MOSFET in the enhancement mode: When applying a positive voltage to the gate, electrons will be accumulated in the channel. The electron current produced by the power supply connected to the drain will flow through the ammeter from the ground to the source. As a result, the current will pass through the ammeter in the conventional direction. Applying a negative voltage to the gate will not produce any change in I_{SD} as the negative gate voltage will deplete the existing electrons in the channel and the MOSFET will stay in the off mode.
2. n-channel MOSFET in the depletion mode: When applying a negative voltage to the gate, electrons will be depleted in the channel. However, applying a positive voltage to the gate will accumulate more electrons in the channel. The current produced by the power supply connected to the drain will always flow through the ammeter from the source to the ground (conventional direction). However, applying a positive voltage to the gate will increase I_{SD}, whereas, applying a negative voltage will decrease I_{SD}.
3. p-channel MOSFET in the enhancement mode: When applying a negative voltage to the gate, holes will be accumulated in the channel. Hence, the current produced by the power supply connected to the source will flow in the direction of the conventional current. Applying a positive voltage to the gate will deplete the already existing holes in the channel producing no difference in I_{SD}.
4. p-channel MOSFET in the depletion mode: When applying a positive voltage to the gate, holes will be depleted in the channel. Applying a negative voltage to the gate will create more holes in the channel. The current produced by the power supply connected to the source will always flow in the conventional direction. However, I_{SD} will increase when applying a negative voltage to the gate, and it will decrease when applying a positive voltage.

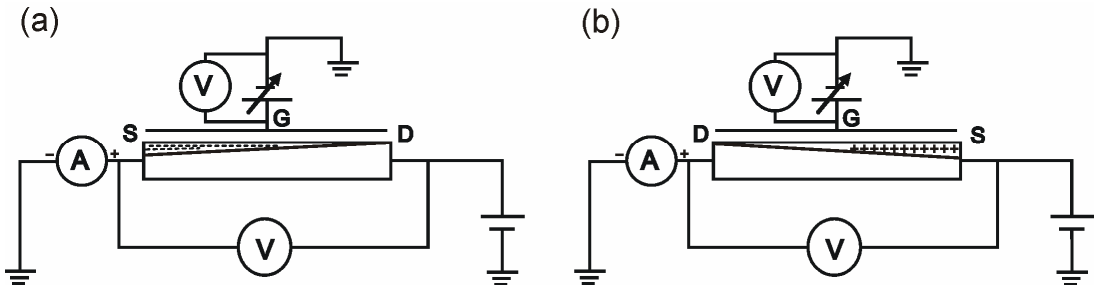

Figure 1.6 The circuits for (a) n-type MOSFET and (b) p-type MOSFET.

1.4. Thesis outline

This section reviews the outline of the remaining chapters in the thesis.

Chapter 2 illustrates the experimental procedures used in this thesis. The cluster deposition apparatus including the inert gas aggregation source, the deposition chamber, and the cryostat arm are described first. The second section illustrates the sample preparation using the optical lithography and etching methods. It also describes the mask design. The last section discusses the methods used to characterize the morphology and the electrical properties of the cluster wires.

Chapter 3 presents an experimental and simulational study of the operation conditions of the von Issendorff and Palmer mass filter. The operation principle is described first. Next, the experimental technique and the simulation procedure used to study the mass filter are described. This also includes a description of the sputtering source which was used to produce the palladium (Pd) clusters used in the study. The remainder of the chapter discusses the experimental and simulational results of the operation conditions. It also studies, as an example, the mass distribution of Pd clusters produced using the sputtering source. The chapter concludes by providing a procedure for the optimum operation of the mass filter.

Chapter 4 discusses the morphology of Bi cluster wires produced using non-contacted V-grooves as a template. The effects of the different source conditions on the cluster size distribution are discussed first. The dependence on the amount of the deposited material and the substrate temperature of the cluster coverage and morphology on the plateaus next to the V-grooves is then discussed. The next section illustrates cluster wire formation mechanisms inside V-grooves. The dependence of the cluster wire width on the source inlet Argon (Ar) flow rate and the amount of the deposited material and the dependence on different source conditions and substrate temperatures of the cluster bouncing angle are discussed before providing a summary of the chapter.

Chapter 5 discusses the electrical properties of Bi cluster wires fabricated using contacted V-grooves. The morphologies of the contacted wires and the clusters on the plateaus and impact on the electrical conduction process are discussed first. Next, the *I(V)* characteristics and the electrical conductance of the cluster wires are discussed. The gate effect of the cluster wires is then explored. This includes introducing two models to describe the gate effect. The next section discusses the noise in the electrical measurements. Hall effect of Bi cluster percolating samples is then investigated. Next, the dependence of the wire's resistance on temperature is also discussed. In an attempt to determine the dominant conduction mechanism of the cluster wires, the data was fitted to equations which represent different conduction mechanisms. The effect on the conduction of annealing the wire and depositing clusters on hot substrates is explored in the next section. This is followed by an investigation of the dependence on the wire length of the amount of deposited material required to form an electrically conducting wire.

Chapter 6 concludes the previous chapters. It also contains an outlook for future work concerning the device fabrication using nanoclusters.

References

1 Ministry of research, science, and technology, *Roadmaps for science: nanoscience & nanotechnology*, New Zealand, (2007).
2 M. Haruta, Catal. Today **36**, 153 (1997).
3 B. K. Johnson, W. Saad, and R. Prud'homme, Polymeric drug delivery II – polymeric matrices and drug particle engineering, ACS symposium series **924**, 278 (2006).
4 K. Terabe, T.Hasegawa, T. Nakayama, and M. Aono, Nature **433**, 47 (2005).
5 S. J. Tans, A. R. M. Verschueren, and C. Dekker, Nature **393**, 49 (1998).
6 R. Hicken, Phil. Trans. R. Soc. Lond. A **361** 2827 (2003).
7 M. S. Dresselhaus, Y. M. Lin, O. Rabin, A. Jorio, A. G. S. Filho, M. A. Pimenta, R. Saito, G. G. Samsonidze, and G. Dresselhaus, Mater. Sci. Eng. C **23**, 129 (2003).
8 Z. Zhang, X. Sun, M. S. Dresselhaus, J. Y. Ying, and J. Heremans, Phys. Rev. B **61**, 4850 (2000).
9 L. Li, Y. Zhang, G. H. Li, W. H. Song, and L. D. Zhang, Appl. Phys. A **5**, 3056 (2004).
10 Y. Tian, G. Meng, S. K. Biswas, P. M. Ajayan, S. Sun, and L. Zhang, Appl. Phys. Lett. **85**, 967 (2004).
11 M. R. Black, Y. M. Lin, S. B. Cronin, O. Rabin, and M. S. Dresselhaus, Phys. Rev. B **65**, 195417 (2002).
12 A. Nikolaeva, D. Gitsu, T. Huber, and L. Konopko, Physica B **346**, 282 (2004).
13 H. Haberland, *Clusters of atoms and molecules* (Springer-Verlag, Heidelberg, 1994).
14 J. G. Partridge, S. Scott, A. D. F. Dunbar, M. Schulze, S. A. Brown, A. Wurl, and R. J. Blaikie, IEEE Trans. Nanotech. **61** (2004).
15 R. T. Isaacson and G. A. Williams, Phys. Rev. **185**, 682–688 (1969).
16 G. E. Smith, G. A. Baraff, and J. M. Rowell, Phys Rev **135**, A1118 (1964).
17 A. Boukai, K. Xu, and J. R. Heath, Adv. Mater. **18**, 864 (2006).
18 W. A. de Heer, Rev. Mod. Phys. **65**, 611 (1993).
19 G. Mie, Annalen der Physik **25**, 377 (1908).
20 J. G. Partridge, S. A. Brown, C. Siegert, A. D. F. Dunbar, R. Nielson, M. Kaufmann, and R. J. Blaikie, Microelectron. Eng. **73**, 583 (2004).
21 J. Schmelzer, S. A. Brown, A. Wurl, and M. Hyslop, Phys. Rev. Lett. **88**, 226802 (2002).
22 W. D. Knight, K. Clemenger, W. d. Heer, W. A. Saunders, M. Y. Chou, and M. L. Cohen, Phys. Rev. Lett. **52**, 2141 (1984).
23 M. Brack, Sci. Am. **277**, 50 (1997).
24 A. Wurl, *PhD thesis, Electron diffraction studies of unsupported bismuth clusters* (Physics and Astronomy Department, University of Canterbury, Christchurch, 2003).
25 H. Göhlich, T. Lange, T. Bergmann, and T. P. Martin, Mod. Phys. Lett. B **5**, 101 (1991).
26 R. Busani, M. Folkers, and O. Cheshnovsky, Phys. Rev. Lett. **81**, 3836 (1998).
27 T. v. Buuren, L. N. Dinh, L. L. Chase, W. J. Siekhaus, and L. J. Terminello, Phys. Rev. Lett. **80**, 3803 (1998).

28 S. K. Kubatkin, A. V. Danilov, H. Olin, and T. Claeson, Phys. Rev. Lett. **84**, 5836 (2000).
29 J. P. Michenaud and J. P. Issi, J. Phys. C: Solid State Phys. **5**, 3061 (1972).
30 B. Weitzel and H. Micklitz, Phys. Rev. Lett. **66**, 385 (1991).
31 Y. T. Tian, G. M. Meng, G. Z. Wang, F. Phillipp, S. H. Sun, and L. D. Zhang, Nanotechnology **17**, 1041 (2006).
32 Y. Oshima, K. Takayanagi, and H. Hirayama, Zeitschriftb Fur Physik D **40**, 534 (1997).
33 G. Fuchs, M. Trielleux, F. S. Aires, B. Cabaud, A. Hoareau, and P. Melinon, Phil Mag. A **61**, 45 (1990).
34 A. Yokozeki and G. D. Stein, J. Appl. Phys. **49**, 2224 (1978).
35 H. A. Harwig, Zeitschrift fur anorganische und allgemeine chemie **444**, 151 (1978).
36 K. J. Stevens, K. S.Cheong, D. M. Knowles, N. J. Laycock, A. Ayesh, J. Partridge, S. A. Brown, and S. C. Hendy, Curr. Appl. Phys. **6**, 453 (2006).
37 S. Lai, J. Guo, V. Petrova, G. Ramanath, and L. Allen, Phys. Rev. Lett. **77**, 99 (1996).
38 M. Schulze, S. Gourley, S. A. Brown, A. Dunbar, J. Partridge, and R. J. Blaikie, Eur. Phys. J. D **24**, 291 (2003).
39 X. Duan, Y. Huang, Y. Cui, J. Wang, and C. M. Lieber, Nature **409**, 66 (2001).
40 W. Comini, G. Faglia, G. Sberveglieri, Z. Pan, and Z. L. Wang, Appl. Phys. Lett. **81**, 1869 (2002).
41 B. A. Buchine, W. L. Hughes, F. L. Degertekin, and Z. L. Wang, Nano Lett. **6**, 1155 (2006).
42 M. H. Huang, S. Mao, H. Feick, H. Yan, Y. Wu, H. Kind, E. Weber, R. Russo, and P. Yang, Science **292**, 1897 (2001).
43 Y. Lia, F. Qiana, J. Xianga, and C. M. Liebera, Mater. Today **9**, 18 (2006).
44 I. M. Bejenari, V. G. Kantser, M. Myronov, O. A. Mironov, and D. R. Leadley, Semicond. Sci. Technol. **19**, 106 (2004).
45 L. Li, Y. Yang, X. Fang, M. Kong, G. Li, and L. Zhang, Solid State Commun. **141**, 492 (2007).
46 B. Lax and J. G. Mavroides, *Advances in solid-state physics* (Academic press, New York, 1960).
47 T. E. Huber and M. J. Graf, Phys. Rev. B **60**, 16880 (1999).
48 K. Liu, C. L. Chien, and P. C. Searson, Phys. Rev. B **58**, 14681 (1998).
49 M. J. Graf and T. E. Huber, Physica E **18**, 260 (2003).
50 A. Ayesh, J. G. Partridge, R. Reichel, A. D. F. Dunbar, and S. A. Brown, Proceedings of the 2004 conference on optoelectronic and microelectronic materials and devices, IEEE press 324 (2005).
51 J. G. Partridge, R. Reichel, A. Ayesh, D. M. A. Mackenzie, and S. A. Brown, Phys. Stat. Sol. (a) **203**, 1217 (2006).
52 R. Reichel, et al., Appl. Phys. Lett. **89**, 213105 (2006).
53 S. E. Kubatkin, A. V. Danilov, H. Olin, and T. Claeson, Physica B **280**, 401 (2000).
54 A. B. Kaiser and Y. W. Park, Synth. Met. **152**, 181 (2005).
55 S. K. Goh, A. B. Kaiser, S. W. Lee, D. S. Lee, H. Y. Yu, and Y. W. Park, Curr. Appl. Phys. **6**, 919 (2006).
56 B. Ozturk, C. Blackledge, and B. Flanders, Appl. Phys. Lett. **88**, 073108 (2006).

57 R. Reichel, *PhD thesis, Nano scale cluster devices* (Physics and Astronomy Department, University of Canterbury, Christchurch, 2007).
58 P. Sheng, Phys. Rev. B **21**, 2180 (1980).
59 P. Sheng, Phil. Mag. **65**, 357 (1992).
60 S. M. Sze, *Semiconductor devices physics and technology* (John Wiley and sons, New York, 1985).

2. Experimental techniques

This chapter consists of three main sections. The cluster deposition system is described in the first section. This includes a description of the cluster sources used in the experiments. The contacted and non-contacted V-groove fabrication is discussed in the second section. The rest of the chapter discusses the cluster wire characterization. This focuses on the wire width measurement procedure using Field Emission Scanning Electron Microscope (FE-SEM) images, the FE-SEM image processing method used to characterize the deposited clusters, the cluster height measurement procedure using the Atomic Force Microscope (AFM) images, and the electrical measurements performed on the sample.

2.1. The ultra high vacuum compatible cluster apparatus

An Ultra High Vacuum (UHV) compatible system was used for sample preparation.[1, 2] The system consists of four main parts: the source, the space between the source and the main chamber, the main chamber (the mass-selection chamber), and the deposition chamber (Figure 2.1). The source is described in more detail in the next section. Four stages of pumping were used in the UHV system as shown in Figure 2.2. The source chamber jacket was pumped down using a two-stage rotary pump (Edwards E2M18) (first stage of pumping). The space between the source and the main chamber was pumped down using a Pfeiffer roots pump (WKP 1000A) and its backing pump (second stage of pumping). A pressure of $1x10^{-6}$ mTorr was achieved in the main chamber using a Pfeiffer (TC600) turbo pump (third stage of pumping). A Balzer (TPH270) turbo pump was used to pump down the deposition chamber (fourth stage of pumping). A pressure of $1x10^{-7}$ mTorr was usually achieved in the deposition chamber prior the sample deposition.

2.1.1. The inert gas aggregation source

In the Inert Gas Aggregation source (IGA), a metal is heated in a crucible using a heating filament around the crucible. The metal is evaporated inside the source chamber and introduced into the flow of an inert gas which cools down the vapour, leading to supersaturation. This leads to the growth of clusters by homogeneous nucleation[3] where the cluster grows mainly by atom adsorption from the vapour phase. The clusters are then pushed by the inert gas flow through the first and the second pumping stages through a series of nozzles.

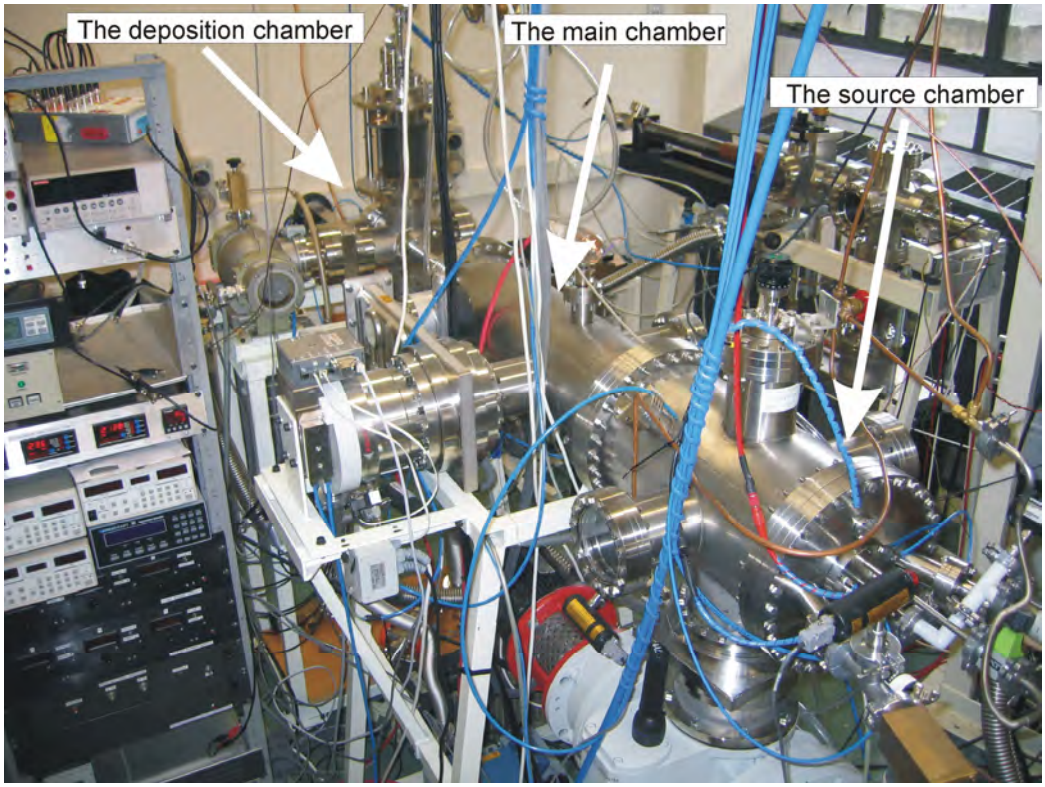

Figure 2.1 The ultra high vacuum compatible cluster system.

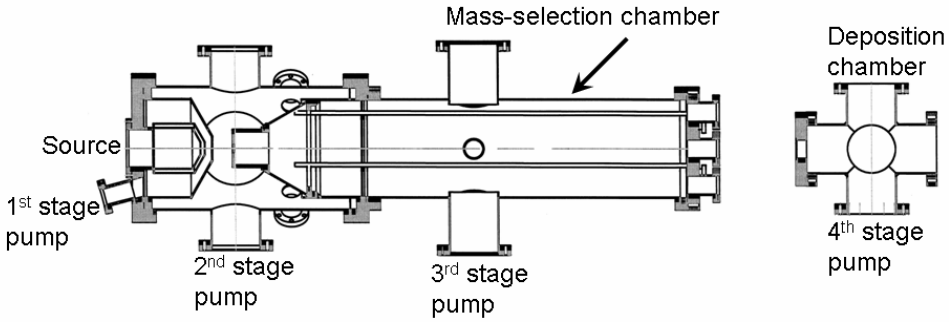

Figure 2.2 Side view of the UHV compatible deposition chamber showing the four stages of pumping. After Reichel[2, 4]

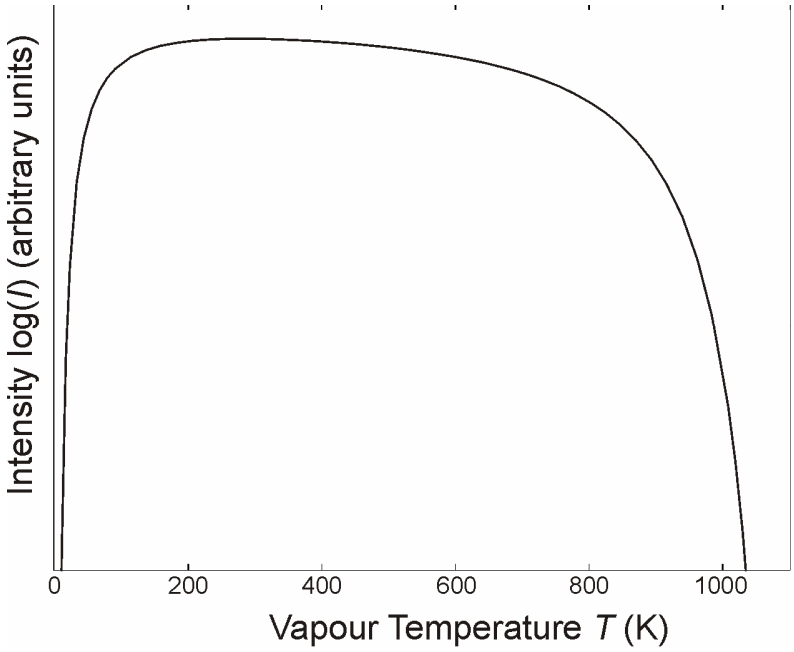

Figure 2.3 The nucleation rate as a function of the vapour temperature for Bi.[5]

Homogeneous nucleation theory presents the dependence of the nucleation rate (I) on the cooled vapour temperature (T) as:[3]

$$I = s\frac{n^2}{\rho}\sqrt{\frac{2\gamma m}{\pi}}e^{\frac{-\Delta F^*}{k_B T}} = s\frac{P}{\rho k_B T}\sqrt{\frac{2\gamma m}{\pi}}n^* \qquad (2.1)$$

where s is the condensation coefficient, n is the number of monomers per unit volume, ρ is the cluster density, m is the cluster mass, γ is the surface tension, ΔF^* is the maximum free energy due to the creation of new surface when the cluster formed from the vapour, k_B is the Boltzmann constant, P is the pressure of the supersaturated vapour, n^* is the number of the critically-sized droplets. Figure 2.3 shows the dependence of the nucleation rate on the vapour temperature for Bi.[5] It should be noted that I has a complex dependence on T since n^* depends also on temperature as $\sim e^{-1/k_B T}$. The figure shows that Bi can be produced with a high nucleation rate in a wide vapour temperature range with a maximum around 290K. The temperature of the walls of the IGA source and the inert gas used to assist the aggregation was also around 290K which produced a high nucleation rate (the source walls were cooled down using water at room temperature except one experiment where liquid nitrogen was used to cool down the source walls - liquid nitrogen cooling decreases the temperature of the inert gas and therefore increases the supersaturation, leading to a greater nucleation rate).

The cluster source design

The design of the IGA source is shown schematically in Figure 2.4.[4, 5] The walls of the source were cooled down using water flowing through a path around the wall. Water was also used to cool down the back plate. The crucible and the heat shields sit

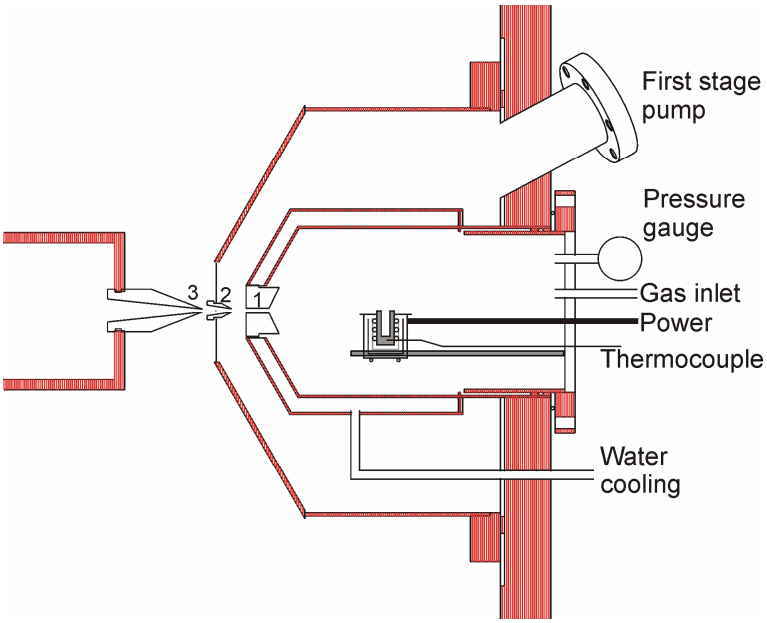

Figure 2.4 The IGA source. The nozzles are labelled 1, 2, and 3. After Reichel [2, 4].

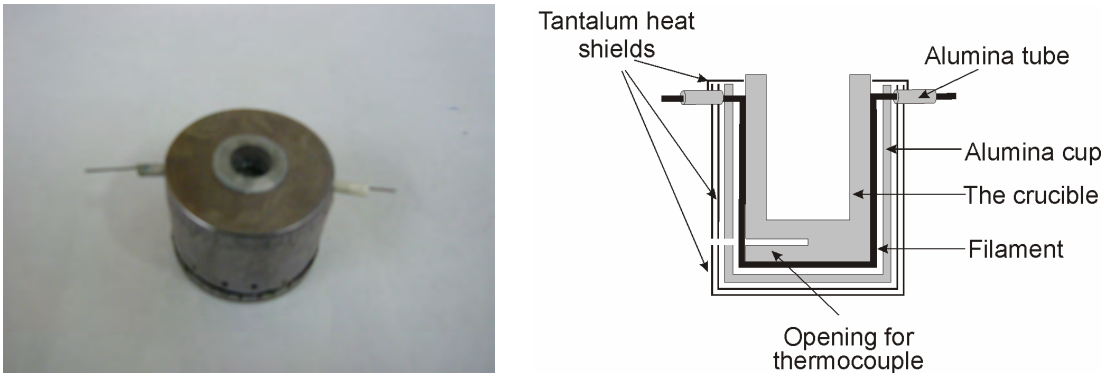

Figure 2.5 The crucible arrangement (left) and a schematic diagram of the arrangement (right).

on two support rods fixed to the back plate. The heater and the thermocouple feedthroughs, the inert gas outlet, and the pressure gauge are fixed to the back plate.

The crucible and the heat shields and their schematic design are shown in Figure 2.5. A tungsten filament was used to heat the crucible which was made of boron nitride. The crucible and the heater were placed in an alumina cup for electrical insulation. The alumina cup was surrounded by two tantalum heat shields. A tantalum lid was used to cover the alumina and the heat shields as shown in Figure 2.5. Small alumina tubes were used to electrically insulate the filament on both sides of the heat shield and the thermocouple so that no short circuit could occur between the filament and the tantalum shield (and so the system).

The source was filled with Bi pellets of 99.999% purity purchased from Kamis Inc. The crucible was heated to a temperature ranging between 700 and 900˚C. The crucible temperature was measured using a K-type thermocouple fixed in the bottom

of the crucible which provided a feedback to the Omega (CN1601) temperature controller. The temperature controller achieves stability of ±1°C.

Three nozzles were used in the IGA source as shown in Figures 2.4 and 2.6. The nozzle dimensions and geometry are important in determining the source pressure and the characteristics of the inert gas flow. This is critical in determining the cluster properties such as the cluster size and velocity. Table 2.1 shows the dimensions and the geometry of the nozzles. The first nozzle was found to have the largest effect on the source pressure. Therefore it was the nozzle which had the largest effect on the cluster properties. The same nozzles were used in all experiments. This set of nozzles was found to produce clusters with consistent sizes when repeating the experiment.

Argon (Ar) and Helium (He) inert gases were used to assist the aggregation in the source. To control the inert gas flow, two flow controllers (type MKS-1179A) were used to control the flow of the gases individually or the ratio between the two of them. Changing the inert gas type was found to change the source pressure (P_s). Table 2.2 presents typical values of the source inlet inert gases' flow rates and P_s at room temperature.

The cluster velocity is mainly defined by the pressure difference between the source chamber and the space between the source and the main chambers (P_b). The pressure difference occurs since the source chamber has no direct pumping while the source jacket and the space between the source and the main chamber were pumped down as

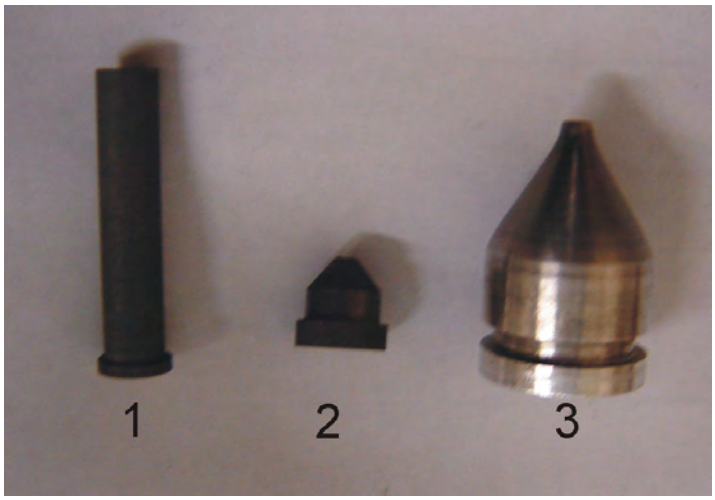

Figure 2.6 The nozzles used in the source. The numbers corresponds to the numbers in Figure 2.4.

Table 2.1 The nozzles' geometries and dimensions. The nozzles numbers are as indicated in Figures 2.4 and 2.6.

Nozzle	Geometry	Length (mm)	Diameter (mm)
1	Cylindrical	40	1.2
2	Conical (skimmer)	12	2
3	Conical (skimmer)	33.5	3

Table 2.2 Typical values of the source inlet Ar and He flow rates and P_s at room temperature.

Ar flow rate (sccm)	He flow rate (sccm)	P_s (Torr)
45	0	13.7
100	0	23.2
180	0	35.9
144	36	34.8
108	72	33.2
72	108	31.4

explained above (the first and the second stages of pumping). The pumping also removes most of the inert gas coming out of the source chamber. P_s is always much higher than P_b (>10Torr and <0.1Torr for P_s and P_b respectively). Hence, P_s determines the cluster velocity.

The source temperature is the other factor which affects the source pressure and the cluster velocity. The source temperature, nozzle set, and the type of the inert gas (Ar) where similar in most of the experiments. Hence, the cluster velocity is determined mainly by the source inlet Ar flow rate. This limited the minimum Ar flow rate that could be used in the experiments since the clusters are required to have a minimum cluster velocity to reach the deposition chamber.

The size of the beam spot deposited on the sample was ~10mm. This size was defined by using a copper aperture to limit the cluster deposition within the sample (the cluster source produces a beam spot with a diameter of few centimetres). A small variation in the amount of the clusters within the beam spot was observed. This variation was found to be minimal within the small dimensions of the cluster wire (few micrometers) compared with that of the beam spot.

2.1.2. The deposition chamber and the cryostat

To deposit clusters on the samples, the samples were fixed on a cryostat finger. The cryostat was fixed on top of a linear translator inside the deposition chamber, as shown in Figure 2.7.[2, 4] The linear translator allowed the height of the sample to be controlled in the vertical direction. A film thickness quart crystal monitor (FTM) controlled by a Sycon Instruments (STM-100/FM) controller was fixed in-line with the cluster beam behind the cryostat cooled finger to check the cluster deposition rate before (and after) cluster deposition.

Once the cluster deposition rate was measured, the sample was moved down (Figure 2.7) to be inline with the cluster beam. The clusters were deposited on the samples through a square window (4x4 mm^2) in the sample holder (Figure 2.8). The deposition chamber in Figure 2.2 was isolated from the main chamber using a gate valve after the cluster deposition to keep the sample always under high vacuum during the electrical measurements.

A Janis research cryostat, model ST-400 was used to cool down the samples in the temperature range of 4.2–300K or 77–300K using liquid helium or nitrogen respectively. Liquid nitrogen was poured directly into the cryostat, while liquid

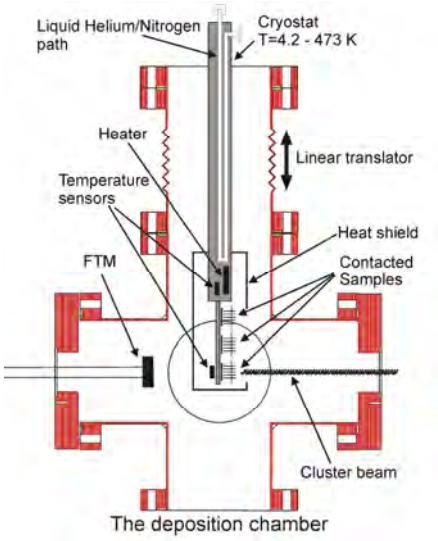

Figure 2.7 The deposition chamber, the cryostat, and the linear translator. After Reichel [2, 4].

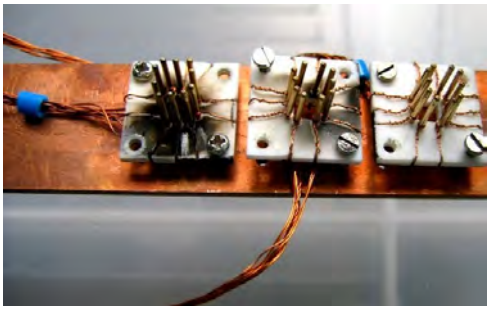

Figure 2.8 The sample holders.

helium was transferred from the dewar into the cryostat using a transfer tube. A pressure difference causes the flow of the helium from the dewar to the cryostat. A flow valve controls the amount of liquid helium flowing through the transfer tube and allows tuning the cooling rate of the cryostat.

The temperature was controlled using a Cryogenic Control Systems Inc. (model 32) temperature controller, which controls the power sent to a heater fixed inside the cryostat arm and receives a feedback temperature from two temperature sensors (Lakeshore, DT-670B-SD diode). The first sensor is fixed inside the cryostat arm next to the coolant path and the heater, while the second sensor is fixed next to the sample on the cooled finger to provide the real sample temperature, as shown in Figure 2.7.

2.2. Sample preparation

Passivated V-grooves on Si wafers were used as templates for the Bi cluster deposition in this study. Contacted and non-contacted V-grooves were fabricated and used to study the electrical properties and the morphology of the cluster wires. In the

following, the optical lithography used for the sample fabrication is described along with the current leakage tests performed on the sample to assure that it can be used for the gate measurements.

2.2.1. Optical lithography and mask design

The optical lithography system includes an exposure tool, a mask, a UV sensitive photoresist, and all of the required processing tools such as developing and the etching. The exposure was performed using the Karl Suss (MA6) UV mask aligner available in the Electrical Engineering Department at the University of Canterbury.

An optical lithography mask is a tool which can be used to replicate a pattern in a UV sensitive positive photoresist (AZ1518). The exposed pattern was then developed using the photoresist developer (AZ300). Figure 2.9 shows the pattern used to produce the 2μm non-contacted V-grooves. This pattern created long parallel V-grooves along the wafer. The hashed areas are the transparent areas on the mask, while the black areas are the areas of the mask covered with Cr (non-transparent areas). Any photoresist under the transparent areas is exposed to UV light and can be developed. The V-grooves were aligned so that they are perpendicular to the (111) plane of the substrate. Masks with similar patterns but with different line width were used to produce parallel non-contacted V-grooves with different widths.

Figure 2.10(a) shows the patterns used to fabricate the V-grooves for the contacted samples. Figure 2.10(b) shows the pattern used to etch the SiO_2 layer under the areas marked A and B, so that Contacts A and B in Figure 2.10 would be connected to the Si substrate. This pattern was aligned by fitting the A and B rectangles on top of the A and B rectangles in Figure 2.10(a).

The pattern in Figure 2.11 was then used to fabricate the contacts. The contact pattern was aligned on top of the V-grooves pattern by using the alignment marks i.e. the square in the up-left corner in the figure on top of another square on the upper left corner of the V-groove pattern. The V-groove and contact fabrication processes are described in detail in the next section.

The V-grooves and the contact patterns were designed in such a way that each sample provides two contacted V-grooves. Each V-groove is contacted by two pairs of contacts. The first V-groove is connected to Contacts 1 and 2 on one side, and Contacts 3 and 4 on the other side as shown in Figure 2.11. Similarly, the second V-groove is connected to Contacts 5 and 6 on one side, and Contacts 7 and 8 on the other side. The areas marked A and B in Figure 2.11 are the gate contacts. Each pair of contacts on the sample (for example: 1 and 2) are connected together so it can be checked whether the spring loaded probes are in good contact. The contacts A and B are also connected together through the Si substrate (the gate). A resistance measurement between contacts A and B was used to confirm that both contacts were connected to the Si substrate.

The separations between the contacts which define the wire lengths for each pair of V-grooves were either: 0.8 and 0.8µm, 0.8 and 1.6µm, or 0.8 and 3.2µm (inset of Figure 2.11(a)). The width of the V-groove pattern was 0.8 µm (inset of Figure 2.10(a)).

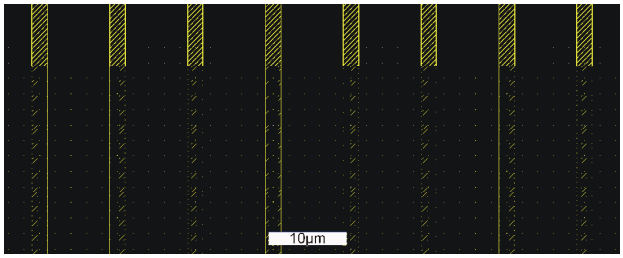

Figure 2.9 The pattern used to produce the 2µm non-contacted V-grooves.

(a)

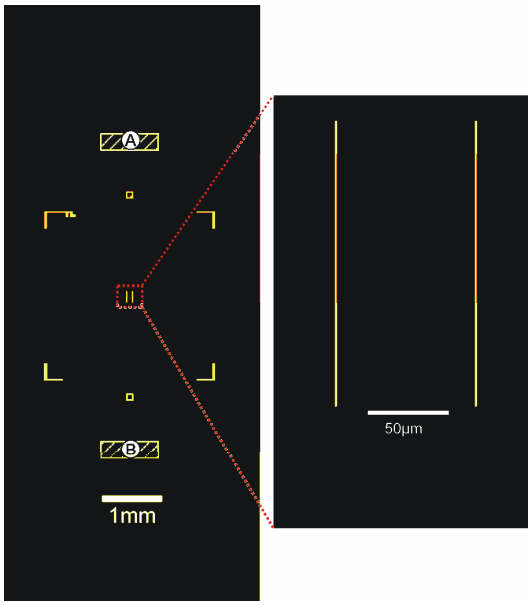

(b)

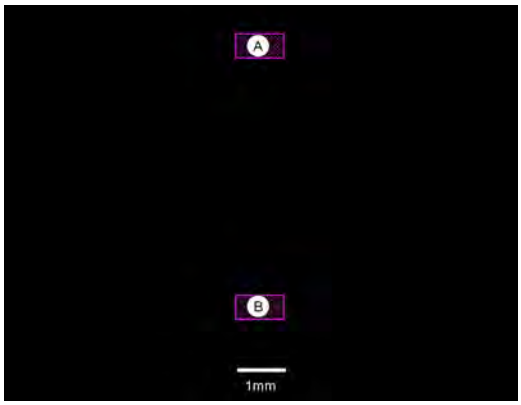

Figure 2.10 The patterns used to produce the V-grooves (a), and to etch two openings (A and B) for the gate contacts (b). The inset is an enlargement of the V-grooves.

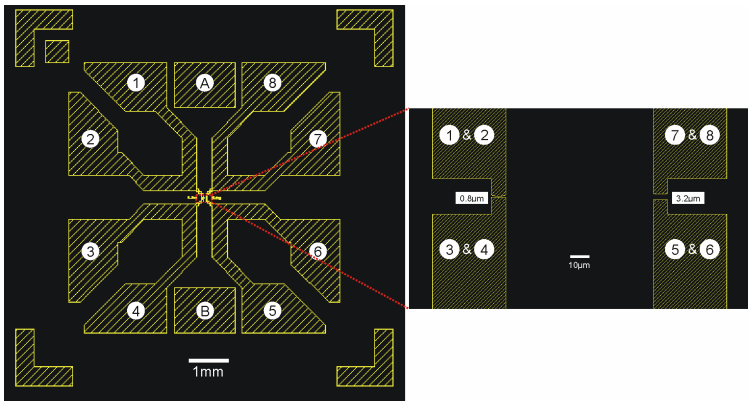

Figure 2.11 The patterns used to produce the the sample contacts. The inset is an enlargement of the contact pattern.

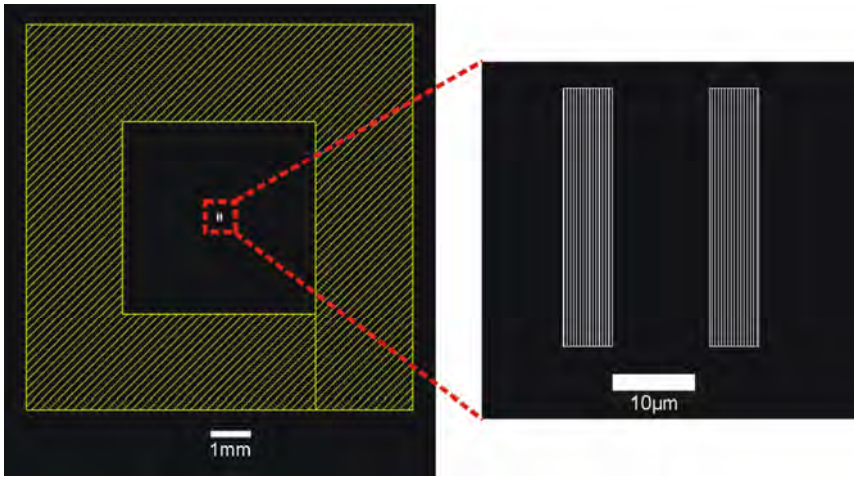

Figure 2.12 The pattern used to create a photoresist passivation layer on the sample surface but the V-grooves and the contact pads.

The pattern in Figure 2.12 was used to provide a passivation photoresist layer which covers the entire sample surface except the contact pads and two windows around the V-grooves in the centre of the pattern (the inset in the figure). The windows' pattern was aligned so that the V-grooves were in the centre of the windows. An optical microscope image with high magnification is provided below (Figure 2.19) to show the windows pattern. The photoresist passivation layer ensures that the deposited clusters will not establish electrical conduction between the Au electrodes but through the cluster wire (inside the V-groove). The area of the cluster beam spot deposited on the sample is limited by the area of the window in the sample holder which the deposited clusters pass through (~4x4mm). Since the beam spot area is smaller than the photoresist layer area (~5x5mm), an overlap between the deposited beam spot and the gate electrodes is unlikely to occur.

2.2.2. Sample fabrication

Samples were fabricated using commercial SiO_2/Si wafers. The SiO_2 thickness is ~100nm, and the Si crystal orientation is (001). In the following, the main steps used for the V-groove fabrication are described.

1. AZ1518 positive photoresist was spun on the wafer at a speed of 4000rpm, exposed using the mask in shown Figure 2.9 (for the contacted V-grooves, the mask in Figure 2.10(a) was used) and then developed. This process is shown schematically in Figures 2.13(a) and 2.13(b).
2. The SiO_2 layer under the opening in the photoresist (Figure 2.13(b)) was etched using a buffered HF acid solution (HF etching rate for SiO_2 ~120nm in 80sec) as shown in Figure 2.13(c). The buffered solution is made of NH_4F with a concentration of 40% and HF with a concentration of 49% with a mixing ratio of 7:1 respectively.
3. The Si layer was then etched using a KOH/DI H_2O solution (the solution is made of KOH pellets mixed with H_2O with a weight ratio of 40%) at 60^{o}C with 5% IPA (iso propol alcohol). The KOH solution etches the Si (111) plane at a lower rate than the other planes, creating the V-groove (Figure 2.13(d)). The angle of the V-groove, shown in Figure 2.13(d), is 70^o.
4. The SiO_2 was etched using 1:10 HF:H_2O solution (HF concentration is 49%) , the wafer was then cleaned (Piranha cleaning), and a new 120nm SiO_2 passivation layer thermally grown on the wafer at 1050^{o}C in the presence of oxygen flow (15L/sec) as shown in Figure 2.13(e). The SiO_2 was grown using a Thermco Burte furnace tube available in the Electronic and Electrical Engineering Department at the University of Canterbury. Figure 2.14 shows a FE-SEM image of the final V-groove. The two white lines (added to the image) are the V-groove edges, while the dark line in the middle is the apex of the V-groove.

Once the V-grooves were created they were used to fabricate the contacted samples. Gold (Au) or Silver (Ag) was used for the contacts, and Nickel/Chrome (NiCr) was used as a sticking layer between the SiO_2 and the Au (or Ag). The contacts were fabricated using the bi-layer method,[6] discussed below, which creates an undercut in the first photoresist layer. The undercut forms contacts with smooth slope at the contacts edges, which guarantees good contact between the cluster wire and the Au/NiCr contacts. However, if the contacts were fabricated without the bi-layer method, the contact edges would form a protrusion. This would make a bad contact between the cluster and the contact edge since the Bi cluster height is ~20nm and the Au/NiCr contact height is ~ 37nm. This is illustrated schematically in Figure 2.15.

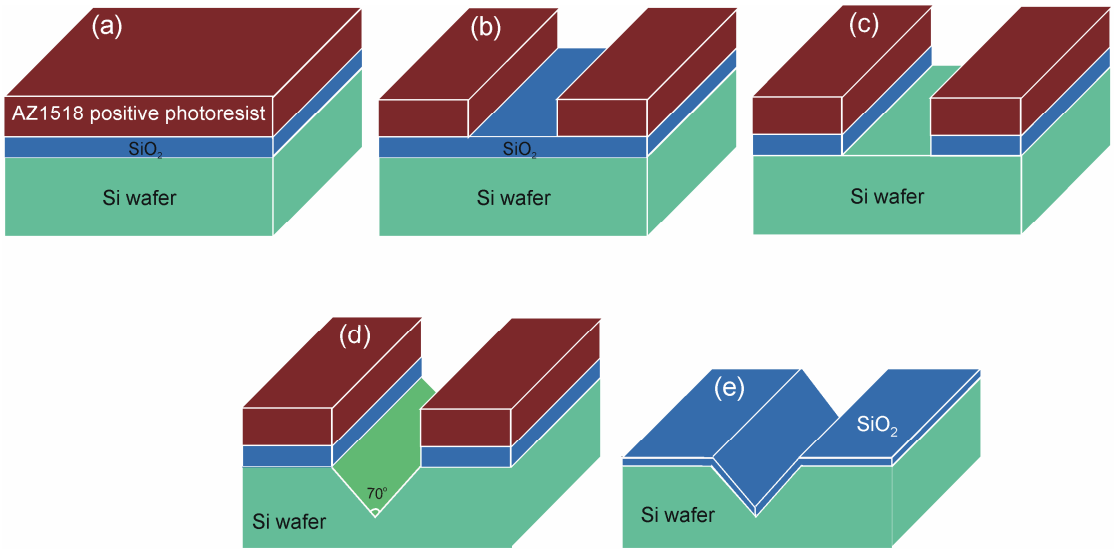

Figure 2.13 Schematic diagram shows the V-groove fabrications. The dimensions in the figure are not scaled. The photoresist was spun on the wafer (a), exposed and developed (b), SiO_2 etching (c), KOH etching (d), and growing a new SiO_2 layer (e).

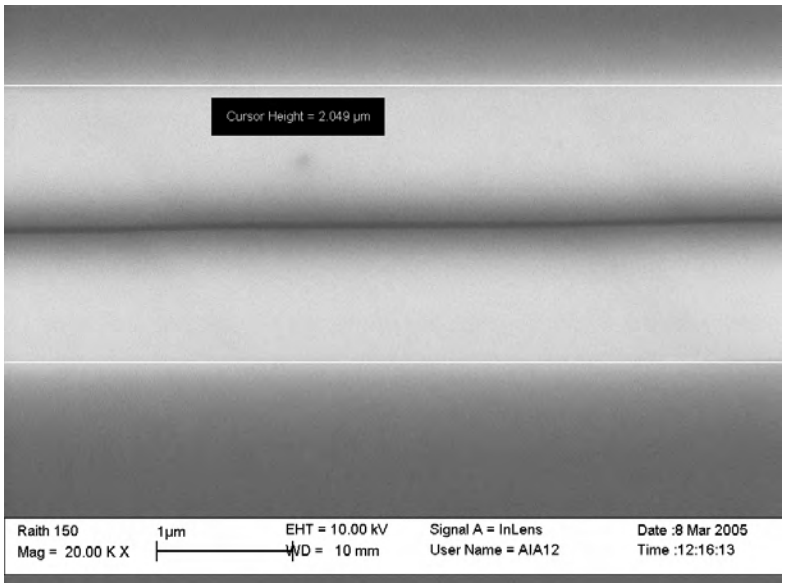

Figure 2.14 FE-SEM image of a ~2µm wide V-groove.

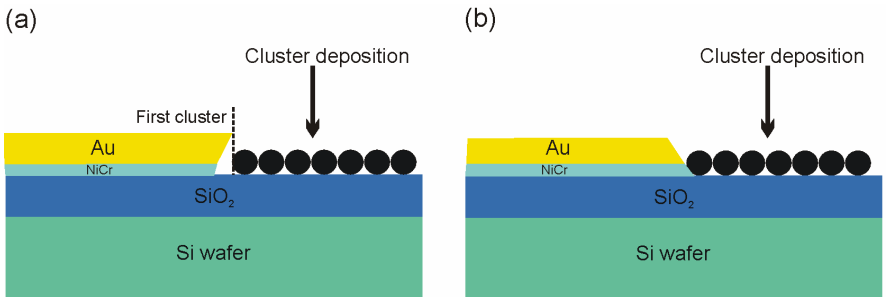

Figure 2.15 Au/NiCr contacts fabricated using (a) the normal lift-off method, and (b) the bi-layer method. The dimensions in the figure are not scaled.

The following processing steps were performed on the V-grooves sample to etch the openings in the SiO_2 layer required to make gate contacts, and to deposit the contacts on the SiO_2 surface.

1. The mask in Figure 2.10(b) was used to create a pattern in the AZ1518 positive photoresist spun on the V-groove samples. The sample was placed in HF buffered 7:1 solution for 1/3 of the time required to etch the SiO_2 layer. The photoresist was then removed. The masking and the SiO_2 etching processes above were repeated two more times (Figure 2.16). The reason for etching the SiO_2 in three steps is to avoid creation of pinholes to the gate in places other than the gate contacts due to impurity particles in the photoresist.
2. The bi-layer process is shown schematically in Figure 2.17. A photoresist layer was spun on the wafer and overexposed without using any mask. A 60nm Aluminium (Al) layer was thermally deposited on the photoresist. A new photoresist layer was spun on the Al layer, exposed using the contact mask in Figure 2.11, and then developed (Figure 2.17(b)). The Al layer was then etched using Al-Etch (Figure 2.17(c)). The Al etch consists of 80% concentrated H_3PO_4, 5% CH_3COOH, 5% concentrated HNO_3, and 10% DI water.[6] Finally, the first layer of the photoresist was overdeveloped to create the undercut as shown in Figure 2.17(d).
3. To fabricate the contacts, 7nm of NiCr and 30 nm of Au were deposited (Figure 2.17(e)). The sample was placed in Acetone at 60˚C to lift off the photoresist (Figure 2.17(f)). The sample was then inspected under the FE-SEM to confirm the smooth slope of the contacts edges, as shown in the inset of Figure 2.18, where the gray area in the image is the Au contact.
4. The sample was then diced ($10.5 \times 10.5 mm^2$).
5. To create a photoresist passivation layer, photoresist was spun, exposed using the window mask shown in Figure 2.12, and then developed.

Figure 2.19(a) shows optical microscope images of the final sample. The photoresist passivation layer is within the dashed square. Figure 2.19(b) shows an enlargement of the contacts numbered as in Figure 2.11. Figure 2.19(c) shows an enlargement of the V-grooves, the Au contacts, and the photoresist window layer around the V-grooves.

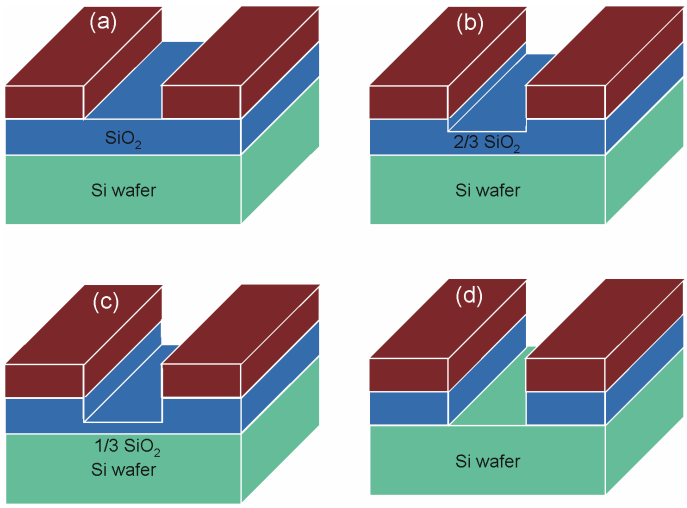

Figure 2.16 The process used to open the gate in the SiO_2. The dimensions in the figure are not scaled.

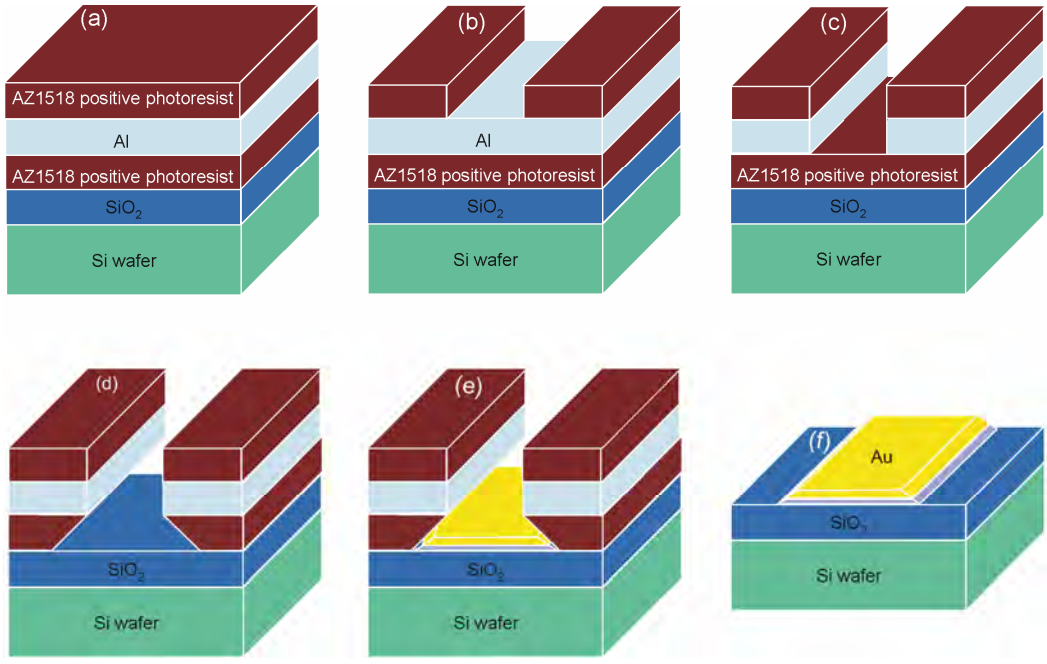

Figure 2.17 The bi-layer method used to produce Au/NiCr contacts with smooth slope of the contacts edges. The dimensions in the figure are not scaled.

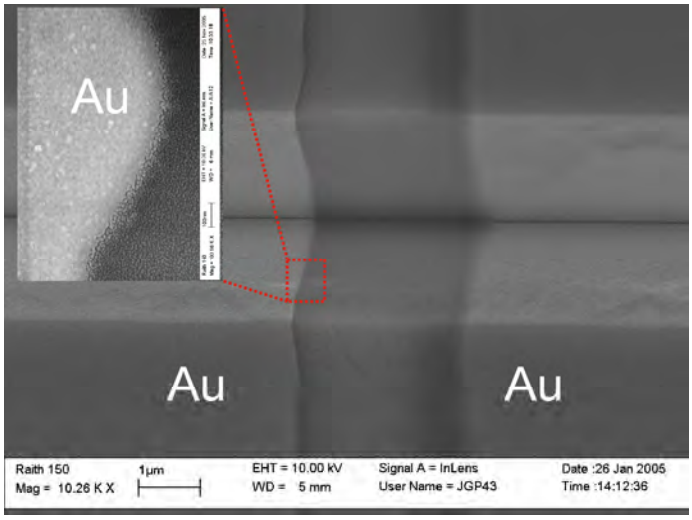

Figure 2.18 FE-SEM of Au/NiCr contacts on V-groove fabricated using the bi-layer method.

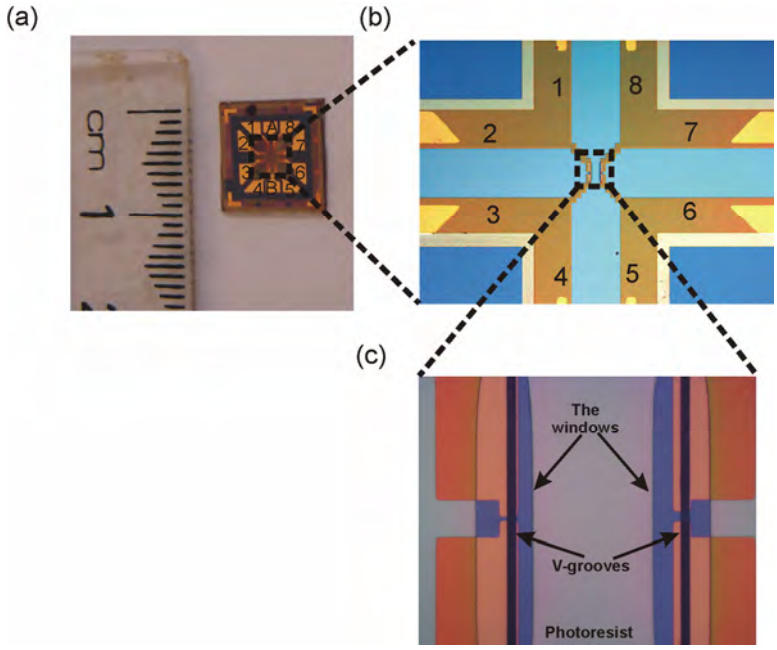

Figure 2.19 (a) The fabricated sample, and enlargement of the contacts and the V-grooves in (b) and (c) respectively.

2.2.3. Current leakage testing

The SiO_2 grown on the Si substrate (Figure 2.13(e)) provides an insulating layer between the Si substrate, and the contacts pads and the Bi clusters deposited on the samples. To measure the SiO_2 layer thickness, a V-groove sample was cleaved and its cross section was imaged using the FE-SEM, as shown in Figure 2.20. The SiO_2 layer in the figure is the gray layer between the two white lines. The oxide thickness was found to be ~120nm.

All of the samples were tested for leakage from the contacts to the Si substrate (gate) before depositing clusters on them. The leak test was done by performing *I(V)* measurements between each pair of contacts, and between the contacts and the gate (A and B). Only samples with current less than 1nA when applying 10V (R>10GΩ at 10V) between each pair of contacts, and the contacts and the gate were used in the experiments. Figure 2.21 shows an example of a typical current leakage test performed on one sample between the different contacts.

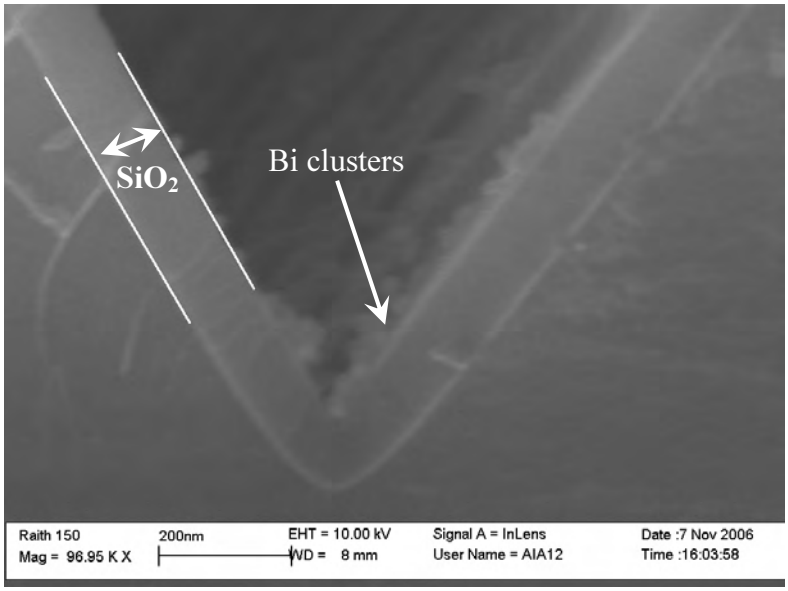

Figure 2.20 FE-SEM image of V-groove sample shows the SiO_2 layer (between the two white lines).

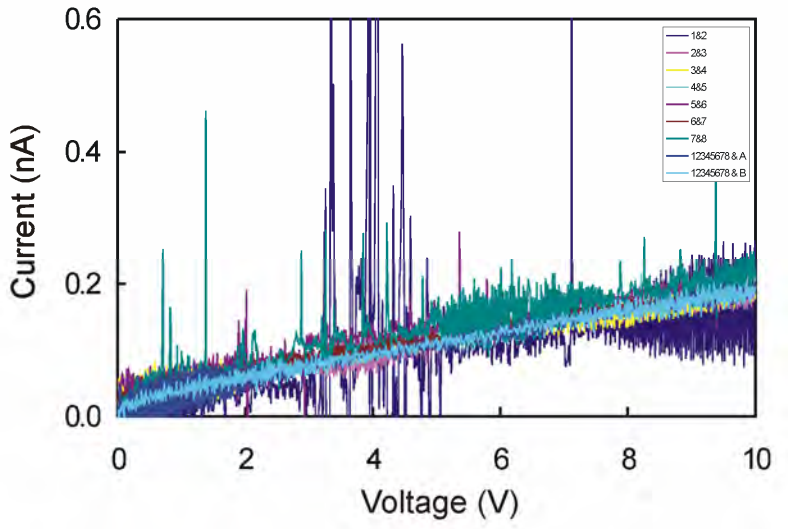

Figure 2.21 Current leakage test: I(V) curves between the different pairs of contacts, and the contacts and the gate for one sample.

2.3. Cluster wire characterization

This section describes the image processing method and the electrical measurements used to characterize the samples. The first subsection describes the use of the FE-SEM images to measure the wire width, the bouncing angle, the cluster coverage, the island area, and the cluster size distribution. The use of the AFM to measure the cluster height is outlined in the second subsection. In the last subsection the electrical measurements are described.

2.3.1. Field emission scanning electron microscope

A Raith 150 FE-SEM was used to image the samples in order to study the morphology of the non-contacted wires. It was also used for the contacted samples to study the contact area between the wire and the contacts, the effect on the morphology of annealing the wire, and the bottleneck connections within the wire. In this section, the procedures used to measure the wire width using the FE-SEM images are described. These measurements were used to study the dependence of the wire width on different variables, and to estimate the cluster bouncing angle. This section also includes a description of the procedures used to process the FE-SEM images and to estimate the cluster coverage and the cluster (or aggregate of cluster) size.

Wire width measurement

Two methods were applied to measure the wire width. The first method was used to determine the average wire width for samples with high cluster coverage. The second method was used to determine the average wire width for samples with low cluster coverage where wire consist of unconnected clusters, thus, a different method was required. The later method was used to find the cluster bouncing angle, as explained below. FE-SEM images of a fixed magnification of 20000x were used in all of the wire width measurements. The wire width was measured from the FE-SEM images using the distance measurement tool in CorelDraw.[1]

High coverage non-contacted samples

The average wire width for the non-contacted samples was found as follows. Each cluster spot (diameter of ~10mm) was imaged at five different points with an equal separation of 2mm to obtain a representative measurement of the wire width, as shown in Figure 2.22(a). An estimate of the wire width was done by making three measurements on each FE-SEM image with a fixed separation between each pair of measurements of the five wires (1.5μm), as shown in Figure 2.22(b). Only clusters which were connected to the cluster wire were considered when finding the wire width.

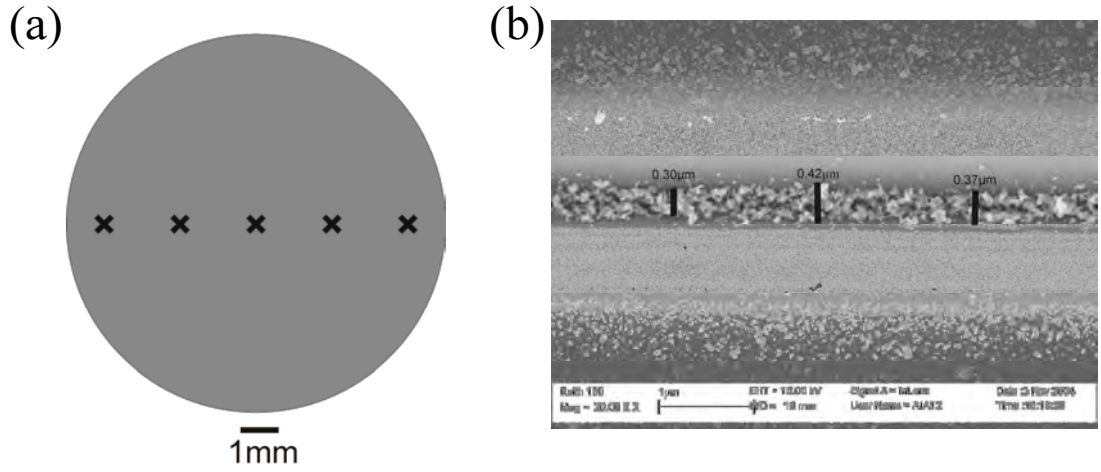

Figure 2.22 (a) The cluster beam spot. The crosses indicate the points where the FE-SEM images were taken. (b) An example of the average wire width measurement.

Low coverage samples

Samples with low cluster coverages (nominal deposited thickness of 2nm measured using the FTM) were used to find the wire width (W) (in this low coverage case this can be considered to be the "cluster scatter width"). W was then used to calculate the cluster bouncing angle (φ) (it will be shown in Section 4.4 that the cluster wire is formed due to the cluster bouncing). To find W, FE-SEM images for three different wires in the centre of each beam spot were used for each sample. Fifteen measurements of the wire width were taken for each FE-SEM image. The distance between each pair of points where the wire width was measured was constant at 0.4μm, as shown in Figure 2.23(a). All of the clusters found on the V-groove walls were included in the wire width measurement. W was found by averaging 45 measurements of the wire width for each sample (15 measurements per wire x 3 images). The wire width distribution for this example is shown in Figure 2.23(b). The uncertainty in measuring the maximum wire width (ΔW) and in all of the following measurements is one standard deviation. A similar value of the wire width was obtained when the wire width was estimated using two parallel lines placed at the wire sides where the cluster coverage drops sharply, i.e. the wire width was the separation between the two lines.

The cluster bouncing angle

The wire width found from the FE-SEM images was used to calculate φ, as shown in Figure 2.24. The calculations were made using the clusters which bounce off points close to the V-groove edges. These clusters will land on the farthest points from the V-groove apex (Figure 2.24), thus, they determine the wire width. However, clusters which bounce off the V-groove walls at points other than the V-groove edges will land at points closer to the V-groove apex. Those clusters will not affect W nor φ calculation.

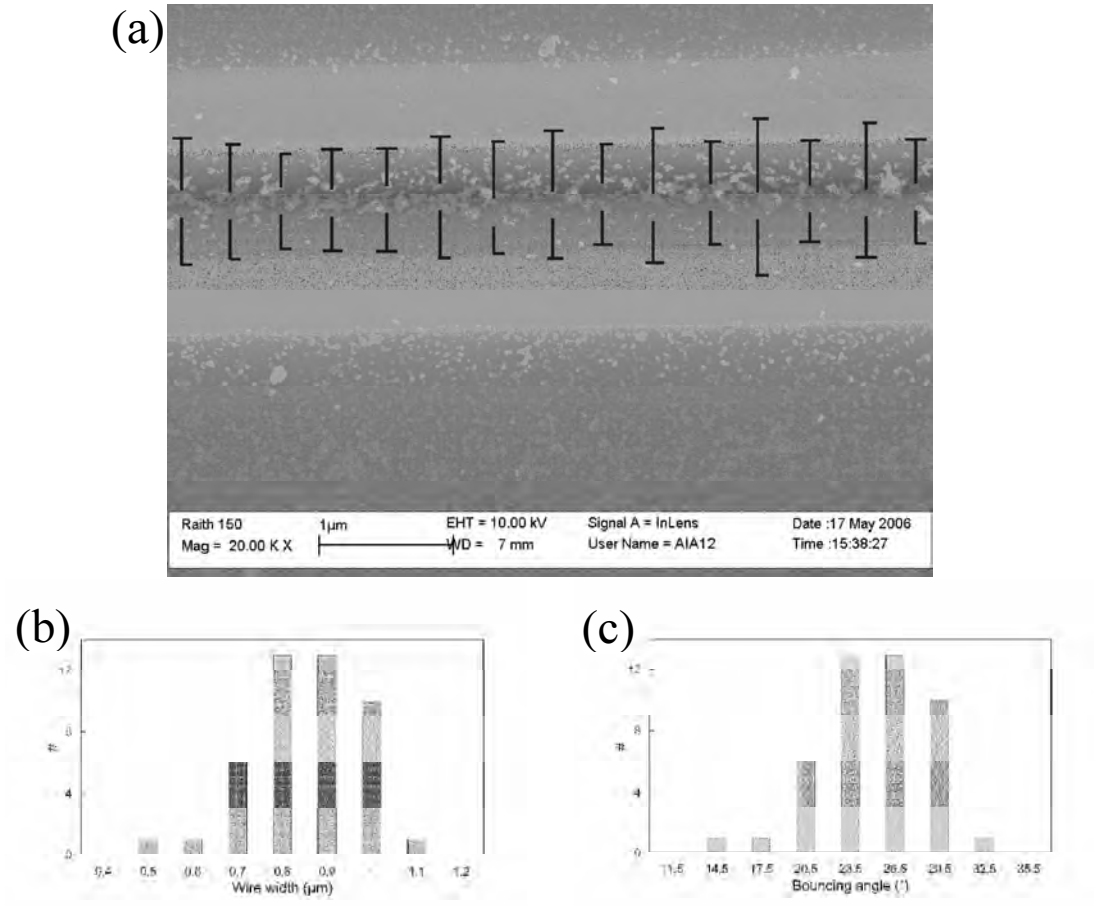

Figure 2.23 (a) Measuring the wire width using CorelDraw. The wire width and bouncing angle distribution, (b) and (c) respectively, found using three FE-SEM images of the sample in (a).

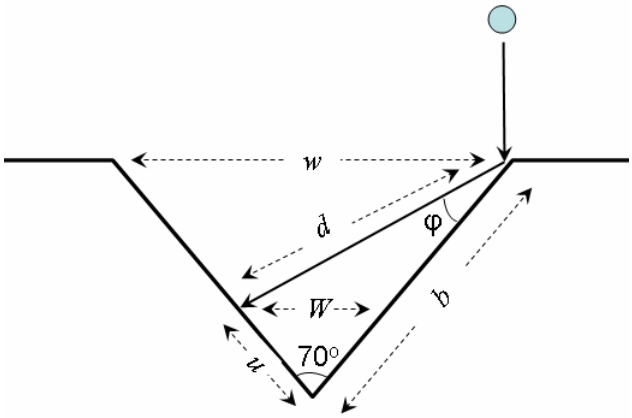

Figure 2.24 The maximum bouncing angle calculation.

Using trigonometry, φ can be given as

$$\frac{\sin\varphi}{u} = \frac{\sin 70}{d} \tag{2.2}$$

where u, b, and d are given as

$$\begin{aligned} d &= \sqrt{u^2 + b^2 - 2ub\cos 70} \\ u &= \frac{W/2}{\sin 35} \\ b &= \frac{w/2}{\sin 35} \end{aligned} \tag{2.3}$$

where w is the V-groove width measured from the FE-SEM image. Since φ is a function of W only, the error in φ ($\Delta\varphi$) was approximated using W and ΔW as follows:

$$\begin{aligned} \varphi &= f(W) \\ \Delta\varphi &\cong f(W + \Delta W) - f(W) \end{aligned} \tag{2.4}$$

Figure 2.23(c) shows the angle distribution for the given example. W, ΔW, φ, and $\Delta\varphi$ were found to be 0.85μm, ±0.13μm, 25º, and 4º respectively for this example.

Processing the FE-SEM images of the clusters

This section discusses the processing of FE-SEM images of the clusters on the plateaus between the V-grooves. This includes discussion of the cluster coverage, island area, and the cluster size in two subsections.

FE-SEM images of magnification of 40000x of the plateaus next to the V-grooves were used to find the cluster coverage, while images with magnification of 80000x were used to find the cluster size and the island area. The choice of these magnifications based on a balance between the image magnification and the area the image shows, i.e. high magnification images were used to find the cluster size, while images which cover as large area as possible with reasonable magnifications were used to find the cluster coverage. Low coverage samples (nominal deposited thickness of 2nm measured using the FTM) were used to find the cluster size distribution to assure that most of the clusters in the samples are single clusters (rather than aggregates of clusters). The cluster coverage was found using two methods: a program written in Matlab[7] and ImageJ software, whereas ImageJ only was used to find the cluster size. Manual measurements of the cluster sizes on the raw SEM images were performed to check the results produced by ImageJ. The same image processing steps were used in both the Matlab program and ImageJ. The two methods gave similar results as shown below.

In the FE-SEM image, the cluster colour is white or grey, and the background is dark, as shown in Figure 2.25(a). The first step in the image processing was to enhance the image contrast between the cluster and the background. This was performed using Microsoft Office Picture Manager when the Matlab program was used, or the contrast

option in ImageJ. The second step was to decrease the noise in the image using a mean filter with size 3x3 pixels for the Matlab program and 2x2 pixels for ImageJ. The image was then subdivided into smaller sections and the peak of the greyscale histogram for each section was determined.

The third step was to adjust the threshold level of the greyscale between 0 (black pixel) and 255 (white pixel) so that the image is converted from greyscale to black and white. When thresholding an image using the Matlab program, the white pixels in the image represent the cluster and the black pixels represent the background. However, ImageJ inverts the colours, so that the cluster is the black pixels and the background is the white pixels, as shown in Figure 2.25.

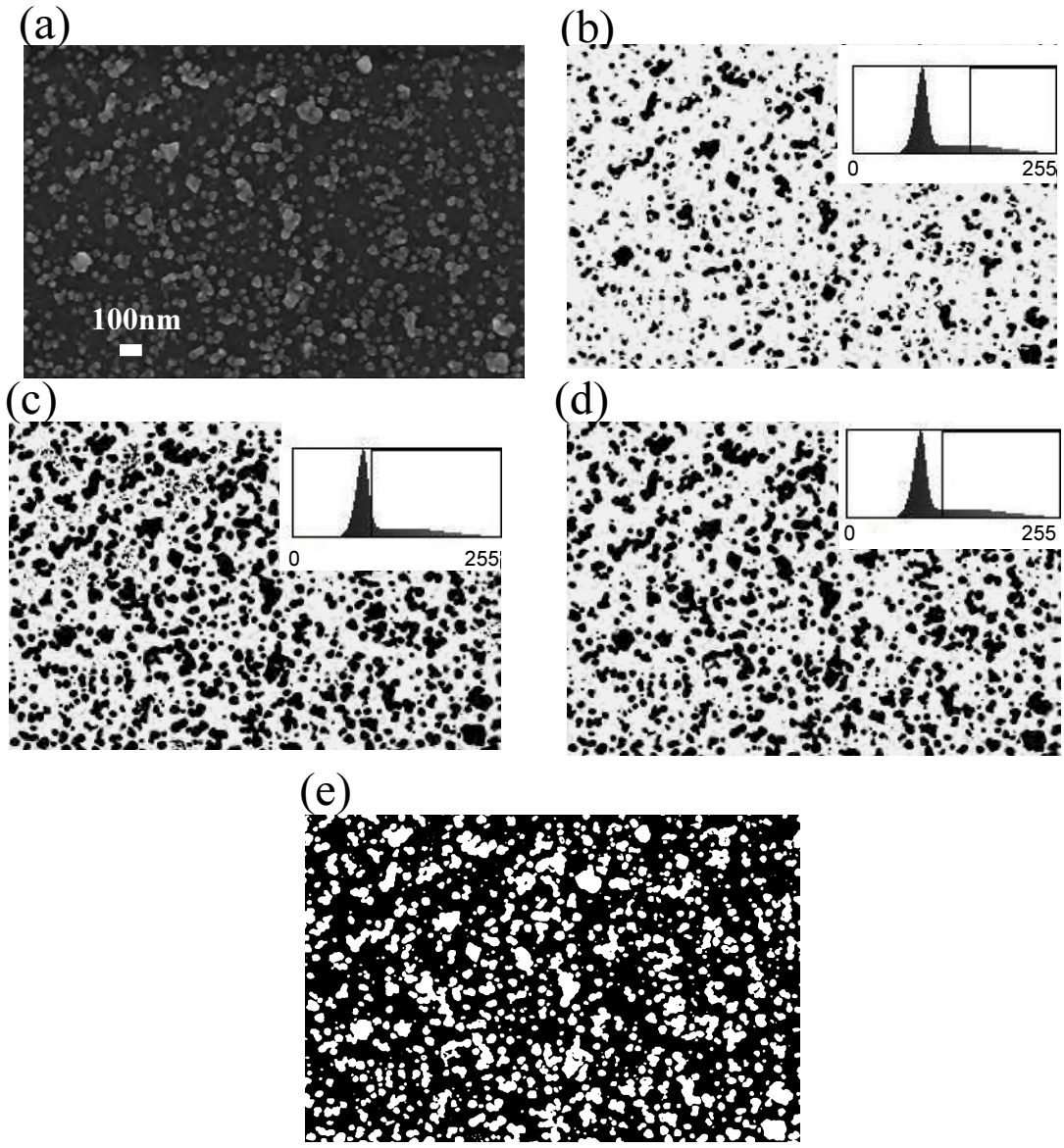

Figure 2.25 (a) The raw FE-SEM image. (b, c, and d) The processed images using ImageJ software for different threshold levels. The insets (in b, c, and d) are the greyscale histograms. (e) The processed image using the Matlab program. The image was produced using a threshold level equivalent to the one used in (d).

Both programs fit the greyscale histogram (insets in Figure 2.25 (b), (c) and (d)) to a Gaussian function. The lack of contrast in the grey areas can be adjusted by selecting a suitable threshold level in the histogram. The raw image was then compared with the processed images with different threshold levels to select the best threshold level (Figures 2.25(b), 2.25(c), and 2.25(d)). The threshold level was not fixed for all of the SEM images, and it was changed from one image to another to give the best match between the raw and the processed image.

The choice of threshold level is crucial in this processing. The selected threshold levels in Figures 2.25(b), 2.25(c), and 2.25(d) are shown as vertical lines in the inset. The choice of a high threshold level will eliminate the grey colour areas which cause the cluster size to be underestimated (Figure 2.25(b)).The choice of a low threshold level will include more background noise in the processed image and increase cluster/island size (Figure 2.25(c)). Through our analysis we found that the better the image contrast, the more accurate the threshold level can be selected. Both the Matlab and the ImageJ programs produced very similar processed images as can be seen Figures 2.25(d) and 2.25(e). ImageJ is used in the rest of this study unless we mention the use of the Matlab program.

Cluster coverage, island area, and the cluster size

The previous three steps are essential steps in the image processing regardless of whether the image will be used to find the cluster coverage or the cluster/island area. The cluster coverage was found by finding the ratio between the number of cluster pixels and background pixels in the processed image. In the example given in Figure 2.25, the surface cluster coverage was found to be 30% using both programs. A correction due to the cluster stacking, which is not considered in this example, is discussed in Chapter 4. However, the corrected cluster coverage is ~36% for this example.

To find the cluster/island area and the cluster size, the earlier three processing steps were performed for high magnification FE-SEM images with low cluster coverage. The cluster (or island) area was found by finding the number of cluster pixels in each island. If two or more clusters are connected with each other, they will appear as a single island in the processed image. All of the islands were fitted to ellipses. In the cluster size distribution study, we discarded all of the clusters/islands with a ratio between the two ellipse axes (a and b) less than 0.7, as they may be two or more connected clusters. A single cluster diameter was calculated using the cluster area (area=πab). The calculated diameters were used to produce a histogram for the cluster size distribution as shown in Figure 2.26. The mean cluster size was calculated, and the uncertainty is given as one standard deviation in all of the following analyses.

The island area was measured regardless of the number of the clusters in the island. However, for the cluster size measurements, the maximum possible cluster diameter was found manually from the raw images where it is easier to decide whether the island of interest is a single cluster or an aggregate of clusters. The maximum diameter was found to be ~52nm for Bi clusters produced using a water cooled IGA source, and using a source inlet Ar flow rate of 45 (Figure 2.26). Hence, for cluster size measurement purposes, clusters with diameters larger than the maximum cluster diameter were excluded.

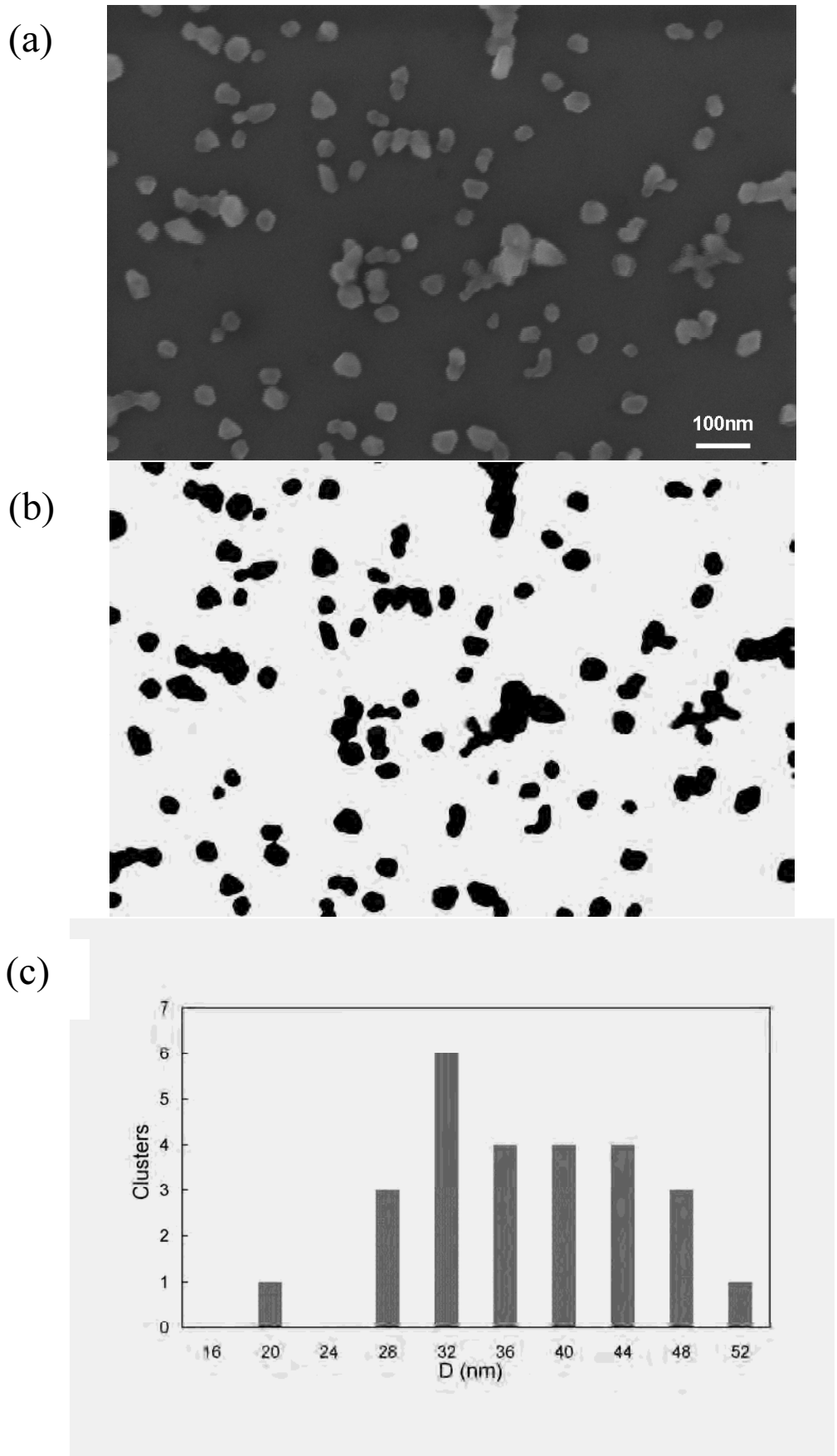

Figure 2.26 (a) The raw FE-SEM image, (b) the image after processing using ImageJ, and (c) the cluster size distribution.

Although the threshold level was adjusted to be as accurate as possible, there was a contribution to the results from the background noise. Hence, we excluded clusters/islands with areas less than a minimum cluster size. The minimum size was found from the raw FE-SEM images (since it is easier to distinguish between the cluster and the noise) by the direct measurement of the cluster diameters. This minimum size was found ~20nm for the example given in Figure 2.26. Good agreement has been found between the above method and the manual calculations for the average cluster size in Section 4.1 (Figure 4.2).

The same procedure was also used to find the cluster size distribution from the TEM images when performing the von Issendorff and Palmer mass filter study (discussed in Chapter 3). This study was performed using ionized Palladium clusters. Good agreement was found between the cluster size distribution found using the above method and the cluster size distribution found using the von Issendorff and Palmer mass filter.

2.3.2. Atomic force microscope

A Digital Instruments Dimension 3100 AFM was used to measure the height of the deposited clusters. The AFM operates on the principle of measuring the attractive and repulsive force between a cantilever tip and the scanned surface, and it provides high resolution 3D images for the scanned object. A full description of the AFM operation principle can be found in the Digital Instruments AFM manual.[8] In all of the following measurements, a silicon tip type NSC11/AIBS was used. The tip radius of curvature is <10nm.

Sample height measurement

In this section, the method used to find the cluster height is described. The cluster height was used to investigate the effect of increasing the substrate temperature the cluster morphology.

Samples with nominal deposited thicknesses of 2nm were used to find the cluster height. Low coverage samples were used because it is easier to find and distinguish single clusters. The scan size in all of the used measurements was 1 or 2μm, while the scan rate was 512Hz. The scanning size and rate determine the number scanning lines per the selected scan size i.e 512 lines/1μm when using a scan size and rate of 1μm and 512Hz respectively. Each scanning line provides a cluster height profile.

The AFM software (Nanoscope III) was used to find the average cluster height as follows. The height profile of each scan line was found using the "section analysis" option in the software. A certain horizontal scanning line can be selected by moving the "mouse cursor" in the vertical direction (Figure 2.27(a)). A single cluster was selected for each measurement, and the scanning line was moved until the cluster height was maximized. The cluster height can be found using two indicators provided by the software (Figure 2.27(b)). One of the indicators was set on the flat area (the substrate), and the other indicator was set on the maximum height of the cluster. The software provides a direct measure of the cluster height (Figure 2.27(c)). The average cluster height was found for each source inlet Ar flow rate and substrate temperature

(a)

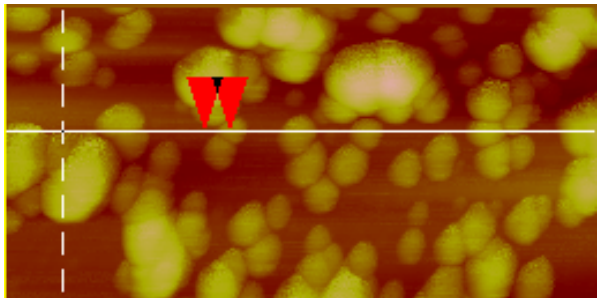

(b)

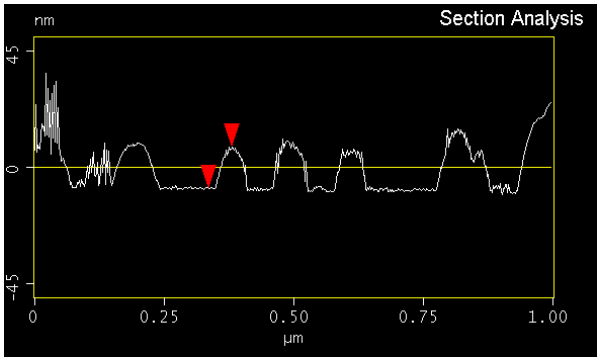

(c)

Surface distance	54.180 nm
Horiz distance(L)	44.922 nm
Vert distance	15.797 nm
Angle	19.374 °
Surface distance	
Horiz distance	
Vert distance	
Angle	
Surface distance	
Horiz distance	
Vert distance	
Angle	
Spectral period	DC
Spectral freq	0 Hz
Spectral RMS amp	0 nm

Figure 2.27 Example of using the AFM image (a) to find the cluster height profile (b) and the cluster height (c).

by averaging the height of fifteen different single clusters of the same size. The error in the average cluster height measurements was estimated to be one standard deviation.

2.3.3. Electrical measurements

Both contacted and non-contacted V-grooved samples were mounted on the cryostat cold finger in the deposition chamber. Spring-loaded probes were used to establish contact to the planar pads on the contacted sample (Figure 2.8). A Keithley Instruments System Electrometer (6514) and Multimeter (2000) were used for the current and voltage measurements respectively. The voltage was supplied to the sample by a custom-made voltage generator. The generator provides sawtooth waves with adjustable frequency and maximum voltage between 5mV and 10V. The ammeter and voltmeter were controlled by computer using a Labview program. The program provides a sampling rate between 5-10 reading/s, and it also provides the real measurement time for each data point.

The electrical conductivity was measured throughout the cluster deposition on the contacted V-groove. A fixed voltage of 100mV was applied to the sample and the current was measured. A sharp rise in the conductivity, as shown in Figure 2.28, indicates the formation of an electrical conducting continuous wire. The cluster deposition was stopped within 5-seconds of measuring an onset current (manifesting itself as a rise in current flow from ~10pA to ~1µA).

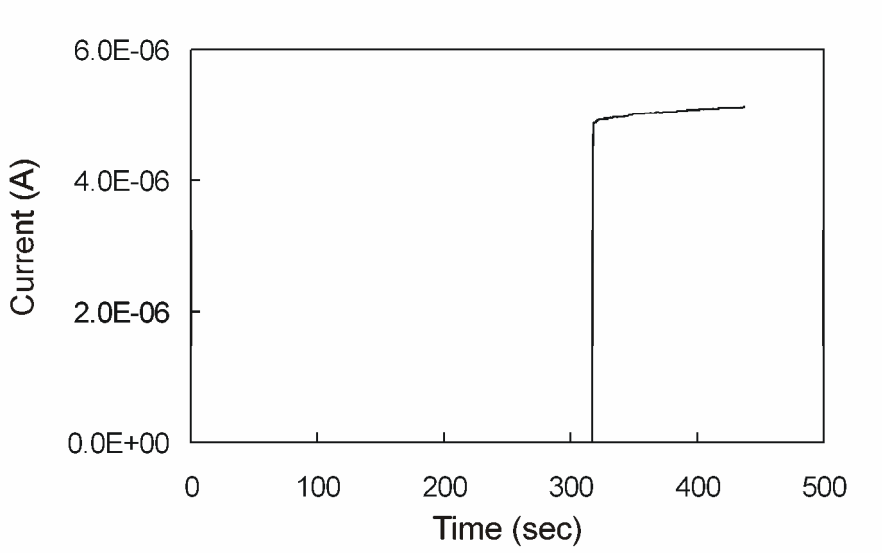

Figure 2.28 The onset of conduction occurs once a continuous cluster wire is formed.

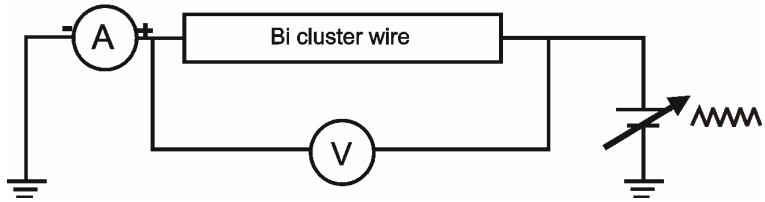

Figure 2.29 The I(V) measurement circuit.

Three main types of measurements were performed on the wire after the onset of conduction while the sample was still under vacuum: current-voltage *I(V)*, gate effect, and resistance-temperature (*R(T)*) measurements. The electrical measurements were performed at different temperatures in the temperature range of 4.2–300K.

The *I(V)* measurements were performed by sweeping the voltage and measuring the current. The circuit used in the measurements is shown in Figure 2.29. The voltage range used in the *I(V)* measurements was selected depending on the sample resistance in such a way as to limit the amount of heat generated in the wire by the electrical power. A large electrical power causes discontinuity in the wire due to the changes in the morphology of the wire caused by the resistive heating. For the cluster wires fabricated in this study, it was found that no discontinuity in the wire occurs as long as the electrical power is $\leq 10^{-7}$W.

The circuit used for the gate measurements is shown in Figure 1.6(a). The gate effect was measured either by applying a fixed voltage between the SD and sweeping the gate voltage (typically between -5 and 5V), or by applying several fixed voltages to the gate (between -5 and 5V) and sweeping the voltage between the SD for each gate voltage. The SD voltage was selected in a similar way as described for the *I(V)* measurements.

The resistance-temperature (*R(T)*) measurements were performed by applying a fixed voltage of 100mV across the sample and measuring the current and the temperature simultaneously. All of the *R(T)* measurements were taken while heating up the sample since the sample temperature can not be easily controlled when cooling down the cryostat. The sample temperature was increased with a rate of 1˚/min through the measurements. However, in some *R(T)* measurements the heater was found to cause some noise in the measurements. To avoid the noise, the heater was turned off, the liquid Helium flow was stopped, and the cryostat was left to heat up naturally. Each run performed without using the heater took around 20 hours.

References

1 A. Ayesh, J. G. Partridge, R. Reichel, A. D. F. Dunbar, and S. A. Brown, Proceedings of the 2004 conference on optoelectronic and microelectronic materials and devices, IEEE press 324 (2005).

2 R. Reichel, J. G. Partridge, A. D. F. Dunbar, S. A. Brown, O. Caughley, and A. Ayesh, Journal of Nanoparticle Research **8**, 405 (2006).

3 F. F. Abraham, *Homogeneous nucleation theory* (Academic press, 1974).

4 R. Reichel, *PhD thesis, Nano scale cluster devices* (Physics and Astronomy Department, University of Canterbury, Christchurch, 2007).

5 A. Wurl, *PhD thesis, Electron diffraction studies of unsupported bismuth clusters* (Physics and Astronomy Department, University of Canterbury, Christchurch, 2003).

6 W. M. Moreau, *Semiconductor lithography principles, practices, and materials* (Plenum press, New York, 1988).

7 M. Hyslop, *PhD thesis, Electron diffraction studies of unsupported clusters* (Physics and Astronomy Department, University of Canterbury, Christchurch, 2002).

8 Group-Scientific, *Digital instruments scanning probe microscopy training notebook* (Digital instruments, Australia, 2001).

3. Study of the operation conditions of the mass filter

Tuning the cluster properties by selecting the cluster size has received a great deal of attention recently because of its fundamental importance in physics and chemistry and the related applications in catalysis and nanotechnology.[1,2] To access the size dependent properties in technological applications it is desirable to mass-select the clusters before deposition.

This chapter discusses an experimental and simulational study of the operation conditions of the von Issendorff and Palmer mass filter. This mass filter provides a high cluster transmission if it is operated using the optimum operation conditions. The experimental study was performed using ionized Pd clusters produced using a sputtering source, whereas the simulational study was carried out using Simion software. The optimum operation conditions were then used to operate the mass filter in order to study the Pd mass distribution and the effect of the source aggregation length on the mass distribution.

The chapter illustrates the mass filter study in six sections. The first section provides an introduction to the mass filter. The second section discusses the mass filter operation principle. The third section describes the sputtering source and the experimental setup. The simulational and experimental results are presented in the fourth and fifth sections. The last section concludes the chapter and provides a procedure for the optimum operation of the mass filter.

3.1. Introduction

This section presents the operation principles of some of the well known mass filter designs, and then it illustrates the advantage of the current mass filter over them. It also demonstrates the focus of this study.

The Wien mass filter, the quadrupole mass filter, and the Time-of-flight mass spectrometer (TOF) are established designs which mass select ionised clusters.[3] The Wien filter consists of two parallel plates with crossed homogeneous electric and magnetic fields, perpendicular to the ionized cluster beam. The net force on the cluster becomes zero if the electric field equals the product of the magnetic field and the ratio of the cluster speed to the speed of light, which means that the cluster will exit out of the filter, i.e. it is mass selected. The quadrupole mass filter operation principle is based on using a two dimensional quadrupole field to trajectories clusters. Clusters with charge to mass ratio corresponding to the applied AC and DC voltages will exit out of the mass filter. The standard TOF consists of a field-free drift space and an ion detector. A consecutive homogenous electric field accelerates the ions that pass through the field-free drift space. The time of flight of the ions depends on their masses.

All of the above designs have inherent limitations which limit their suitability for many cluster deposition experiments. The resolution of the Wien filter is dependent on the initial cluster velocity, and it typically works only in the mass range of 1-5000amu.[3] In the quadrupole mass filter, the trajectories of singly charged ions are stable only within a very narrow mass range.[4] The TOF works for a wide range of cluster masses, but its duty cycle is very low which leads to a transmission of only 10^{-5}-10^{-4} at best. The resolution of the TOF is also dependent on the ions' initial energies, and, most importantly, the standard TOF cannot be used to mass select ions for deposition experiments. TOFs are important in allowing an understanding of cluster properties since they provide high resolution but an alternative is required for high flux deposition of clusters, especially for those larger than 1-2nm in diameter.

The mass filter used in this study was built according to the design of von Issendorff and Palmer.[5] This filter works for a wide range of cluster masses, and its resolution does not depend on either the ion mass or initial ion velocity.[5] The main advantage of this mass filter is the high transmission which makes it suitable for device applications.[6, 7] The operation of this mass filter is explained below.

Given the many attractive properties of the design, it is surprising that the von Issendorff and Palmer mass filter has not been widely adopted by the cluster deposition community. To our knowledge, only one mass filter has been built according to this design and the only paper available describing the operation and performance of this filter is the original one.[5] While the design concept is relatively simple, the operation of the filter requires a detailed understanding, and the successful implementation at the Cluster Laboratory in the University of Canterbury required a set of complimentary simulations. The comparison of experiment and simulation in the present work is expected to encourage more widespread adoption of this mass filter.

This study focuses on the effect on the mass filter performance of factors such as the ion's initial velocity, the ion mass, and the acceleration voltage applied to the mass filter plates. Both simulation and experiment were used to study these factors. As a result of this study, a procedure is described for obtaining the best possible performance.

3.2. Operation principle of the mass filter

This section describes the mass filter operation principle as discussed by von Issendorff and Palmer.[5] The mass filter consists of four parallel plates with horizontal openings in Plates 2 and 3 covered by mesh as shown schematically in Figure 3.1(a). A short high voltage pulse applied to Plate 1 (Figure 3.1(b)) causes the ions in the space between Plates 1 and 2 to accelerate upwards. The ions pass though the field free region between the openings in Plates 2 and 3, and when the ions enter the region between Plates 3 and 4 another identical high voltage pulse is applied to Plate 4. The mass-selected ions then lose their perpendicular velocity, and are therefore redirected horizontally through the exit aperture. The size of the exit aperture defines the mass filter resolution. The time of flight from the acceleration region to the deceleration

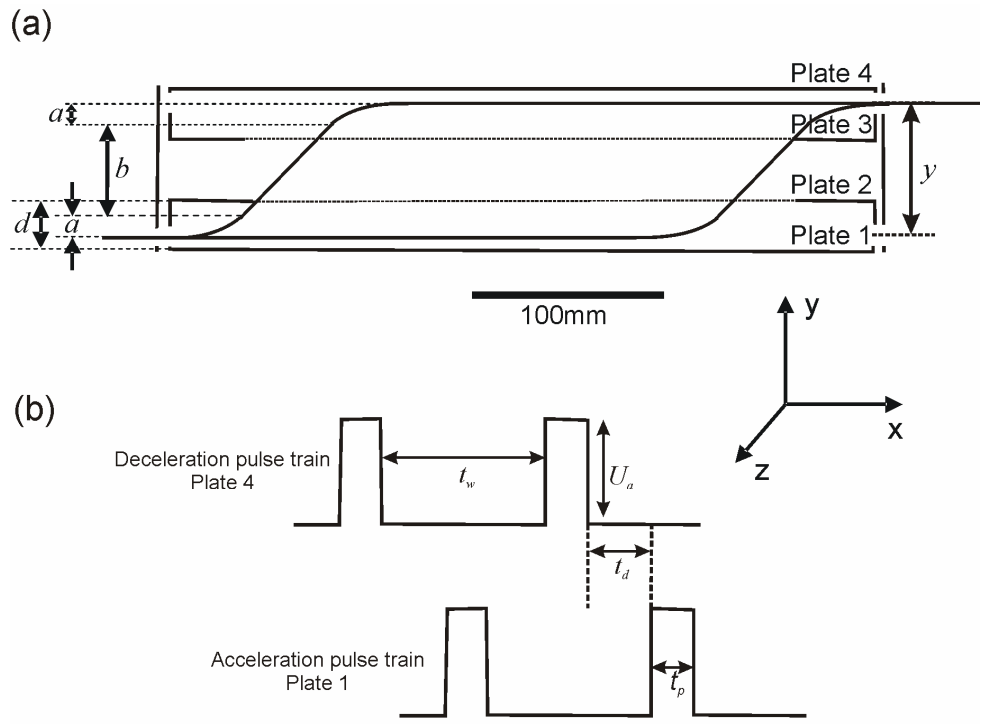

Figure 3.1 (a) Schematic diagram of the side view of von Issendorff and Palmer mass filter. (b) The timing of the identical high voltage pulses' trains.

region (lateral distance b in Figure 3.1(a)) depends on the ion mass. One can control the mass of the clusters which come out of the mass filter by controlling the pulse widths (t_p), and the delay between the end of the acceleration pulse and the start of the deceleration pulse (t_d). The pulse and delay times are given by the desired lateral distance (a) the ions cover during the acceleration (and deceleration), and the lateral distance (b) the ions cover in the field free region respectively.[5] i.e.

$$t_p = \frac{2a}{\sqrt{2eU_p / m}} \tag{3.1}$$

$$t_d = \frac{b}{\sqrt{2eU_p / m}} \tag{3.2}$$

where eU_p is the energy the ions gain from the high voltage pulse: its value is $eU_p=(a/d)eU_a$, where U_a is the high voltage pulse height, and d is the separation between Plates 1 and 2; m is the ion mass; $b=y-2a$ where y is the vertical distance between the centres of the entrance and exit slits.

The optimal mass filter resolution (*MFR*) is given by[5]

$$MFR = \frac{y}{\Delta y} = \frac{m}{\Delta m} \tag{3.3}$$

where Δy is the beam diameter at the exit aperture i.e. for the present mass filter it is the height of the exit aperture (which is the same as the size of the entrance aperture), and Δm is the full width at half maximum (FWHM) for the mass filter resolution curve. In the current mass filter y=72mm, Δy=6 or 12mm and so the expected resolution of our mass filter is 12 or 6 respectively. This is quite sufficient for the device fabrication experiments of interest to us.[6, 7]

Von Issendorff and Palmer assumed that a is a fixed distance, determined by the geometry of the mass filter. Under this assumption (which will be re-visited in the discussion below) the values of t_p and t_d determined from Equations 3.1 and 3.2 are dependent only on the mass to be selected and U_a. U_a can be in the range 10-1000V (upper limit determined by the high voltage switching units), and a "rule of thumb" is required to choose the optimum value of a.

In addition, the value of a used in Equations 3.1 and 3.2 can be chosen to be any value less than the geometric lateral distance between the higher edge of the entrance aperture and Plate 2. The throughput of the mass filter is therefore a complex function of m, a, and U_a, and an object of the present work is to elucidate the dependencies of the transmission on these parameters. It should be noted that the effect of changing b is mainly that it controls the angle at which the transmission saturates (see below). However, it is also the case that when a changes from 1mm to 10mm, b changes from 70mm to 52mm.

3.3. Experimental

A magnetron sputtering source developed in a collaboration with the University of Freiburg[8] was used to produce ionised clusters inside the ultra high vacuum compatible system.[9] The design is shown schematically in Figure 3.2,[10] and it is discussed in more detail in Reference [10]. Argon (Ar) gas was used to generate plasma and to aggregate Pd clusters from a Pd target fixed on the magnetron sputter head. The source was operated with a pressure in the range of 0.2-1.5Torr using a discharge power of up to 50W, and variable aggregation length (k) which is defined as the distance from the sputter target surface to the source exit nozzle (Figure 3.2).

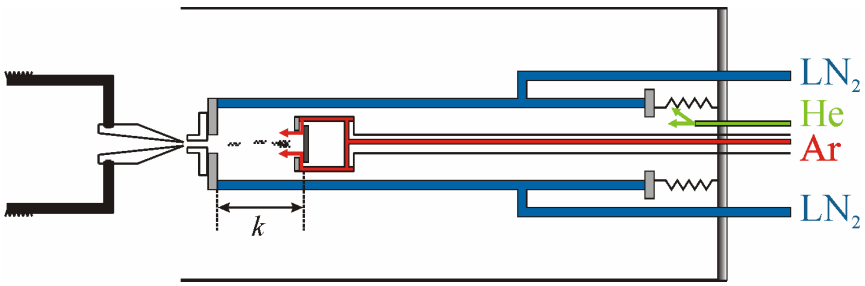

Figure 3.2 A schematic diagram of the magnetron sputtering source. After Reference [10].

In the current implementation of the mass filter the separations between the plates are: 26mm between 1 and 2, 31mm between 2 and 3, and 26mm between 3 and 4 (Figure 1(a)). Unlike von Issendorff and Palmer's mass filter, in the present case long horizontal openings in Plates 2 and 3 (290mm) were used to increase the ion transmission (discussed in detail in Section 3.4). Two high voltage switch units (DEI, model PVM-4150) were used to generate two identical pulses with a delay between them. The high voltage was supplied from two high voltage power supplies, and the switches were driven by a purpose-built signal generator controlled by a Labview program. Faraday cups were positioned in the deposition chamber (i.e. in line with the exit aperture of the filter shown in Figure 3.1(a)) and at the end of the mass filter chamber in the "straight through" position to detect, respectively, the mass selected and the directly transmitted ions (using Keithley 6514 Electrometers).

3.4. Simulations of the mass filter

This section describes the simulation procedure of this study. It also presents and discusses the study of the mass filter operation conditions using simulations. The effect on the transmission of changing a, U_a, m, and θ (which is the deflection angle shown in figure 3.3) are discussed in three subsections.

Simion (version 7) software was used to study the effect of each factor in Equations 3.1 and 3.2 on the mass filter performance. For each simulation, 700 ions (with the same or different masses) and a constant horizontal velocity were allowed to enter the entrance opening with random y, z positions (within the entrance opening). A horizontal ion velocity υ_0=210m/sec is assumed for all simulations (it will be shown in Section 3.5.1 that this is close to the measured ion velocity). The transmission is quoted as the ratio between the number of transmitted ions and those which entered the mass filter.

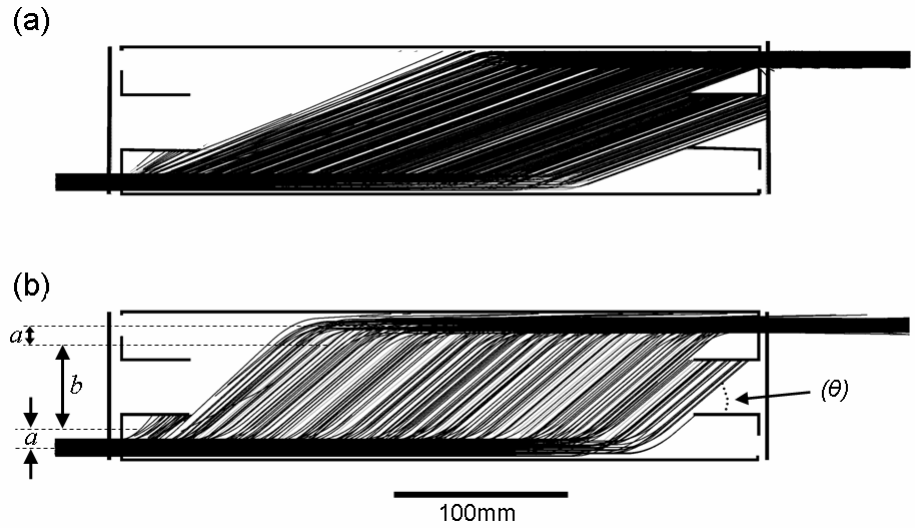

Figure 3.3 Trajectories of the 9nm ions in the simulated mass filter using U_a=1000V. (a) a=2.2mm and θ=20.2°, (b) a=12mm and θ=40.7°.

To study the effect of a on the percentage of transmitted ions from the mass filter, Pd ions with a diameter of 9nm were used in the simulations (in the following text the ion diameter will be used instead of the ion mass, assuming spherical particles with bulk material density). Figure 3.3(a) shows the simulated ion trajectories for U_a=1000V and a=2.2mm. It is immediately clear that some ions are lost because they hit Plate 3 and that the transmission can be estimated from the number of ions which reach the region between plates 3 and 4, but this calculation is only approximate as not all such ions reach the exit aperture. The percentage of the ions lost depends on the beam deflection angle (θ). Figure 3.3(b) shows that if we maintain U_a=1000V and choose a=12mm a higher percentage of the ions pass through Plate 3.

In Figure 3.3(b) the higher transmission was achieved by increasing a (and thereby increasing θ) while maintaining U_a=1000V: clearly the higher angle could also have been achieved by increasing U_a while maintaining a=2.2mm. It is not immediately obvious which is the correct procedure, and so, as described below, a series of simulations were carried out to clarify this point.

It is apparent in Figure 3.3 that the vast majority of the ions follow parallel trajectories and this is an indication that the effects of distortions of the electric fields are unimportant. This is confirmed by detailed mapping of the electric field distribution using Simion. Figure 3.4 shows a section of the electric field mapping in the vicinity of the horizontal opening in Plate 2 and the entrance aperture. A high voltage of 1000V was applied to Plate 1 while the other plates were grounded. No distortions can be observed next to the horizontal opening in Plate 2 (similar result was found for the opening in Plate 3). However, an obvious distortion can be observed next to the entrance aperture at the times of applying the high voltage pulses. The only ions affected by this distortion are those few ions which are close to the entrance aperture at that time (within ~10mm). The vast majority of the ions are far from the entrance and exit apertures and the transmission is therefore not affected. Similar distortion was observed for the exit aperture.

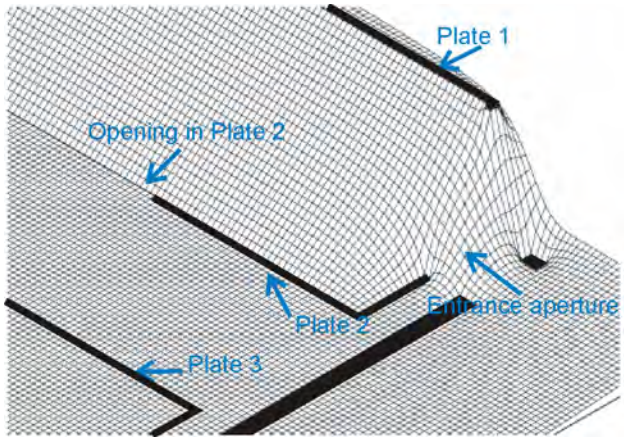

Figure 3.4 A section of the electric field mapping of the mass filter in the vicinity of the opening in Plate 2 and the entrance aperture.

Figure 3.5 shows the dependence of the percentage of transmitted ions on U_a for three values of a of 0.1, 1, and 10mm. t_p and t_d values were calculated from Equations 3.1 and 3.2 for a fixed ion mass corresponding to 9nm Pd ions. Figure 3.5 shows that for each value of a there is a minimum pulse height below which no ions are transmitted (because the ions are not deflected through a large enough angle, θ). As U_a increases above this minimum value, the ion transmission increases (for a fixed a). The figure also shows that as the a-value is decreased higher voltages are required in order to preserve a high ion transmission.

Figure 3.6 shows the simulated dependence of the percentage of transmitted ions on a for 9nm ions using U_a=1000V, and that the highest transmission is achieved by increasing a until a~10mm. For a >10mm, the transmission decreases, because there is a maximum a set by the system's geometry (a_{max}) corresponding to the lateral distance between the higher edge of the entrance aperture and the second plate (i.e. ~12mm in the present mass filter). These results show clearly that careful choice of a and U_a for a given m and υ_0 is essential if the mass filter is to be used efficiently.

3.4.1. Choice of a and U_a

Figures 3.5 and 3.6 show the dependence of the transmission on U_a and a, but do not indicate the optimal (a, U_a) pair. The correct choice of U_a and a is the one that gives the highest transmission efficiency for the mass, m, and incident velocity, υ_0, of the ions of interest. Both large a and large U_a will increase the ion deflection angle θ. This is shown in Figure 3.3, where increasing a from 2.2 to 12mm (U_a fixed at 1000V) increased θ from 20.2˚ to 40.7˚, with a corresponding increase in transmission (from ~57% to ~77%). The dependence of θ on U_a and a is given by the equation:

$$U_a = \frac{1}{2} m v_0^2 \frac{d}{ea} \tan^2 \theta \qquad (3.4)$$

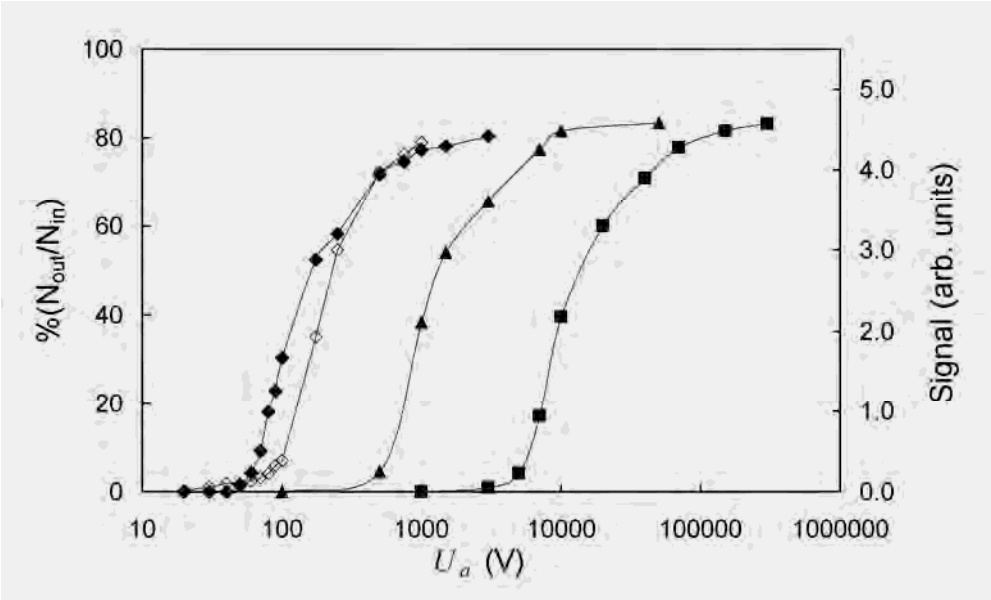

Figure 3.5 The dependence of the mass filter transmission of the 9nm ions on U_a using a=0.1 (closed squares), 1 (closed triangles), and 10mm (closed and open diamonds). The closed points are the simulation results, while the open ones are the experimental results (as discussed below). The lines in the figure serve as guides to the eye.

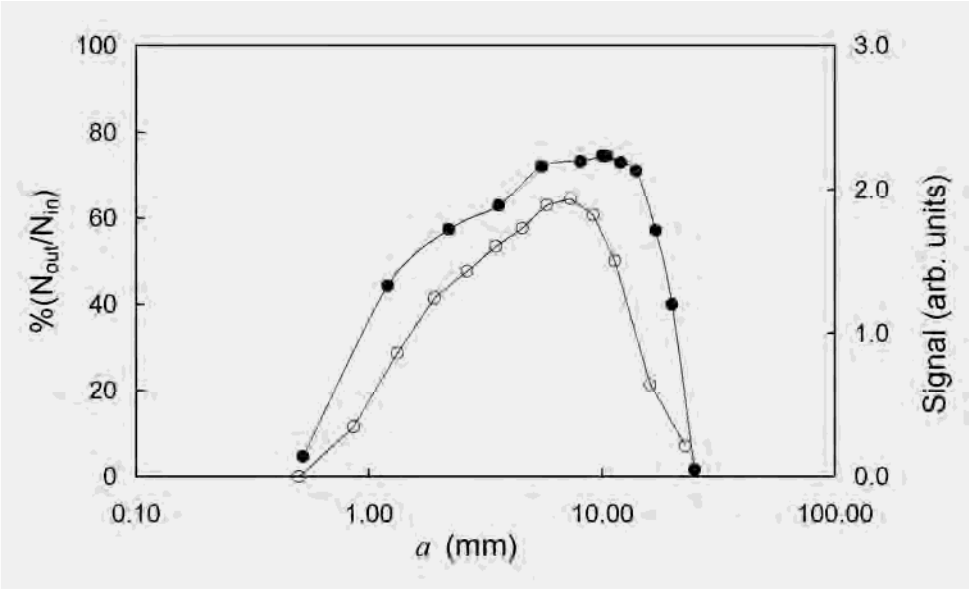

Figure 3.6 The dependence of the mass filter transmission on a. Closed circles are the simulation results while open circles are the experimental results (discussed below) for the 9nm ions. A constant U_a of 1000V was used in both the simulation and the experiment. The lines in the figure serve as guides to the eye.

In Figure 3.7, the simulation data from Figures 3.5 and 3.6 (for $a<a_{max}$) are re-plotted against the beam deflection angle and it is clear that all the data collapses into a single curve. Hence, as long as $a<a_{max}$, knowledge of θ is sufficient to allow calculation of the mass filter transmission. Figure 3.7 also shows that the mass filter transmission saturates (~80%) at high angles (θ>30˚).

The geometry of the mass filter can be used to explain the dependence of the transmission on θ. Figure 3.8 shows schematic diagrams which illustrate the transmission for four distinct cases. The ions with the right mass which lie within the gray areas, i.e. corresponding to a horizontal length of Γ, are expected to be transmitted. The ions within the dashed lines will be lost under Plate 3 (i.e. horizontal length of ζ) and under Plate 2 (i.e. horizontal lengths of ξ). All of the ions lying within the length η (~10mm) will be affected by the electric field distortion next to the entrance aperture. At θ=24º (Figure 3.8(a)), an ion at the entrance aperture should be transmitted. However, the ions next to entrance aperture will be affected by the electric field distortion and get lost. This should produce a transmission of (Γ-η)/(Γ+ζ+η). Hence, a high transmission is obtained which is less than 80% (80% is the maximum transmission in Figure 3.7). For 30º>θ>24º (Figure 3.8(b)), the number of ions which are affected by the electric field distortion decreases. ζ also decreases while ξ increases, thus, they balance each other. As a result, the transmission increases but it is still below 80%. For θ>30º (Figure 3.8(c)), all of the ions within the gray area are away from the electric field distortion region. The decrease in ζ is always balanced by the increase in ξ, which maintains a constant transmission of ~80%. However, for small angles (Figure 3.8(d)) low transmissions are obtained since the ions are lost for various reasons such as: the large number of ions lost under Plate 3, some of the ions which were supposed to be transmitted are lost because of the electric field distortion (within η), and because the left-hand-side of the opening in Plate 2 and the right-hand-side of the opening in Plate 3 (pointed by the arrows in Figure 3.8(d)) could not be filled with ions. Hence, the transmission decreases below 80% and it is necessary to decrease the waiting time (discussed in Section 3.5.5) to reduce the number of lost ions.

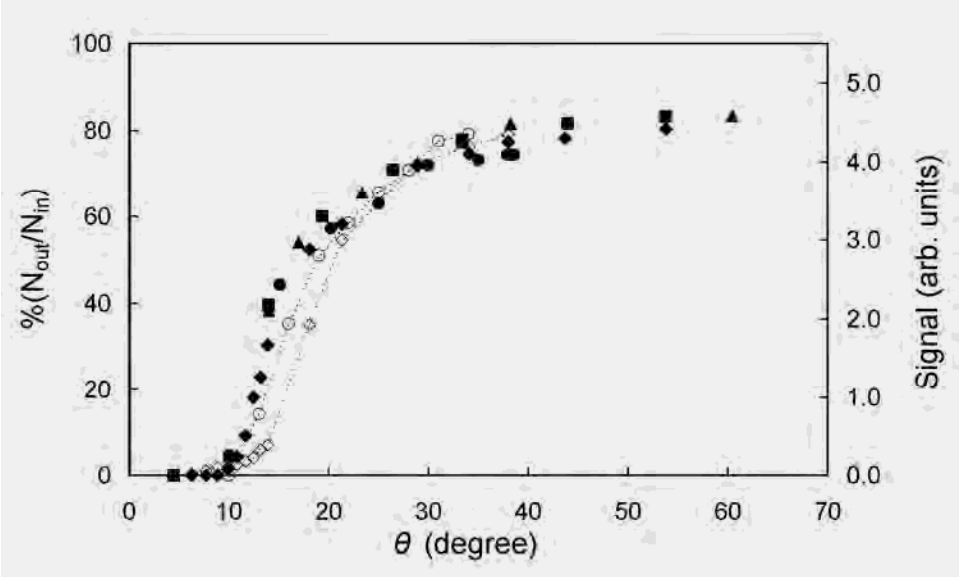

Figure 3.7 The dependence of the mass filter transmission on θ. The data presented in the figure is the data from Figures 3.5 and 3.6 with a< a_{max}. The lines in the figure serve as guides to the eye.

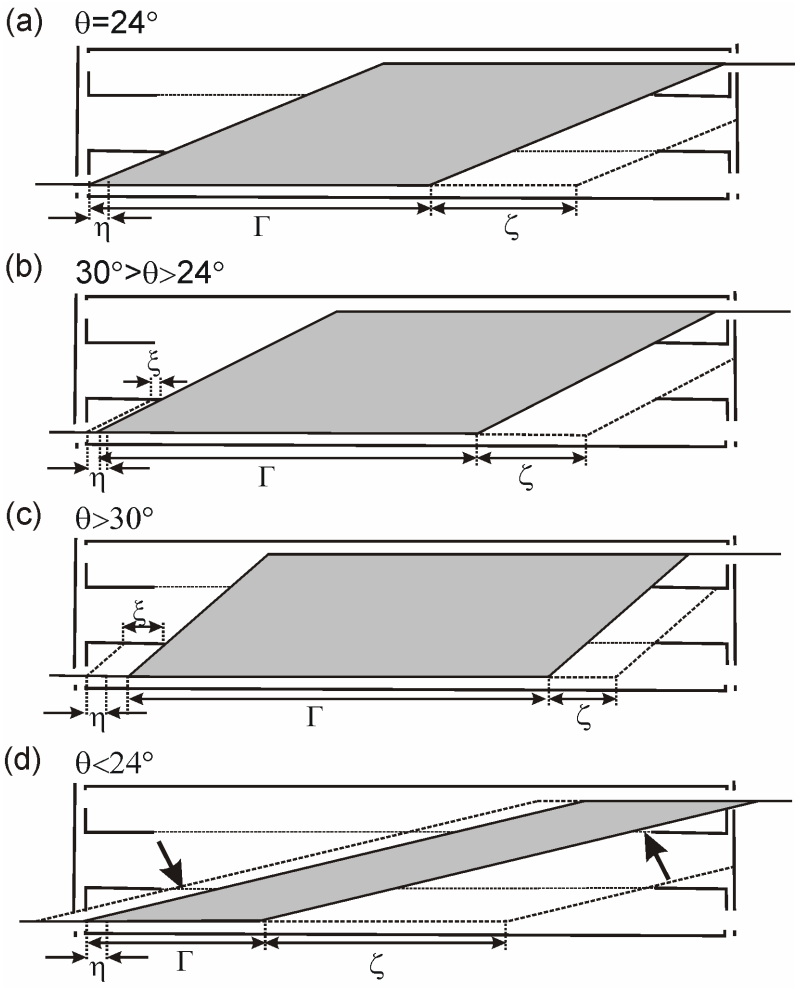

Figure 3.8 Schematic illustration of the dependence of the transmission on θ.

The data in Figure 3.7 were obtained for long (290mm) horizontal openings in Plates 2 and 3. Smaller, offset openings (as used originally by von Issendorff and Palmer – see Figure 1 in Reference [5]) were used initially. However, the offset defines a single specific angle at which maximum transmission can be achieved. In the current modified design, any ion deflected through an angle between 30˚ and 90˚ has a high probability of transmission. Also in the original design, the shorter openings increased the percentage of ions lost because they hit Plate 2 before reaching the horizontal opening. In the current mass filter, the long openings provided flexibility in selecting the beam deflection angle, and as long as θ>30˚ (this angle is determined by the distance *b* and the length of the horizontal openings), high transmission was achieved, as shown in Figure 3.7.

Since the transmission saturates for θ>30˚ in Figure 3.7, the optimal (*a* and U_a) pair is not uniquely determined by Equation (3.4). Choice of *a* and U_a then becomes a practical decision based on experimental considerations and on the ion mass, as discussed in the following section.

3.4.2. Dependence of transmission on cluster mass

Equation 3.4 can be used to optimize the mass filter throughput for a fixed ion mass (e.g. for cluster deposition experiments). However, it is generally desirable to first measure the ion mass/size distribution, and it is immediately obvious (intuitively and from Equation 3.4) that the optimal U_a and/or a will change with the ion mass. Since the applied voltage during measurements of a mass spectrum will usually be fixed for practical reasons, this means that any measured mass distribution could be significantly affected by the variation in throughput as a function of mass if a fixed a value is used for the whole mass range.

If one wishes to select heavy ions, pulses of sufficient height should be applied to ensure that $a<a_{max}$. For example, using a constant a and θ (of 12mm and 38° respectively), the heaviest ions that can be selected using 500V pulses are 9.6nm ions, while a pulse with the height of 10V will only allow ions with diameters up to 2.6nm to be selected.

The results of the previous section suggest that higher voltages and a constant value of θ (i.e. variable a) should be used when attempting to select large clusters or derive mass spectra from cluster-beams with broad mass distributions. Since the maximal transmission efficiency for any θ>30˚ is roughly constant (as shown by Figure 3.7), constant transmission can be achieved as long as a constant θ value is used (regardless of the pulse height).

3.4.3. Simulation of the effect of the ion's initial velocity

Clearly the ions' initial horizontal velocity is another factor that has an effect on θ for a particular U_a and the required m. In our experimental setup, the ion velocity is defined mainly by the inert gas (Ar) flow rate through the cluster source nozzle, and is limited to a relatively narrow range (compared with m and U_a which can all be varied over ~2-3 orders of magnitude).

Ions with a diameter of 9nm were simulated to study the effect of the horizontal velocity on the mass filter transmission. The percentage of transmitted ions was found to change from 77% to 70% when the simulated ion velocity increased from 210m/sec to 300m/sec (θ changed from 38° to 28.6° respectively), and from 77% to 83% when the simulated ion velocity decreased from 210m/sec to 100m/sec (θ changed from 38° to 58.6° respectively). These results show that the percentage of transmitted ions does not vary dramatically across the experimentally observed range of ion velocities. However, for a very high velocity (1000m/sec for example) the mass filter transmission would decrease to around zero if the mass filter settings were optimised for υ_0=210m/sec.

The above simulations show the crucial dependence of the mass filter transmission on U_a and a, underpinned by the dependence of the transmission on the beam deflection angle. The following section describes experiments performed to confirm the dependence of the mass filter transmission on U_a, a, and θ.

3.5. Comparison of experiment with simulation

Pd ions produced by the magnetron sputtering source were employed for an experimental study of the effects of different source and mass filter conditions. While the sputtering source produced positive and negative Pd ions, in this work only the negative ions were used (whose production rate was found to be typically around 10^{10} ions/sec). The following source conditions were used in all of the experiments (unless otherwise mentioned): sputtering power of 25W, aggregation length of 10cm, and an inert gas Ar flow rate of 600sccm.

This section starts by discussing the cluster velocity measurement since it is used to calculate θ. Next, the experimental results for the transmission are compared with those obtained by the simulation. The mass filter resolution is discussed in the third subsection. The optimum operation conditions were used to derive the mass distribution of the produced clusters and to study the effect on the mass distribution of changing the aggregation length in the fourth subsection. The effect on the transmission of the waiting time is discussed in the last subsection.

3.5.1. Determination of the initial velocity of the ions

The choice of θ requires knowledge of the initial kinetic energy (or the horizontal velocity) of the ions. It is therefore essential to measure the velocity distribution (using the method discussed below) prior to operating the mass filter.

The ions' kinetic energy in the axial direction was estimated by applying a retarding potential to the Faraday cup at the exit of the mass filter. Hence, those ions with energy below that of the retarding potential were repelled and not detected. The ion signal as a function of retarding voltage is shown in Figure 3.9(a) for mass-selected ions with a diameter of 9nm. Clearly there is a significant reduction in ion current at a potential around ~650V indicating the mean kinetic energy. The retarding potential was used to estimate the ion velocity, as shown in Figure 3.9(b). The velocity distribution was found by fitting the ion signal using the integral of a Lorentzian distribution centred at 214m/sec (dashed curve in Figure 3.9(b)). The FWHM of the velocity distribution is 39m/sec. Similar velocities were found for all mass-selected Pd ions with diameters in the range of 8-10nm (produced using the same source conditions).

3.5.2. Measurements of the transmission efficiency

In order to compare the simulated transmission data with the experiment in Figures 3.5 and 3.6, experiments were performed using 9nm ions and using the above source conditions. The experimental data points (open symbols) in Figure 3.5 were obtained using a fixed a of 10mm and a variable U_a in the range between 20 and 1000V. The experimental points (open diamonds) are in good agreement with the simulational results (closed diamonds).

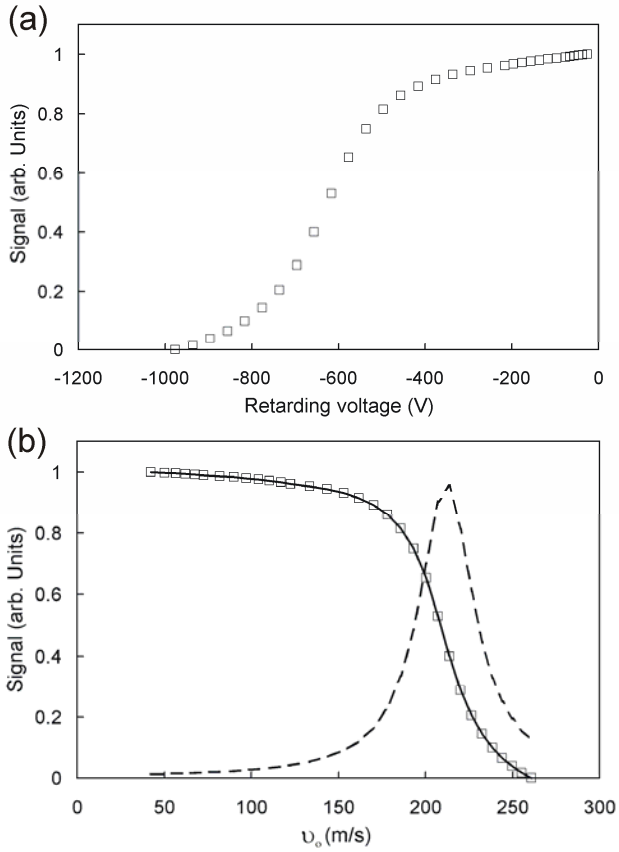

Figure 3.9 (a) The dependence of the ion signal for the 9nm ions on the retarding voltage applied on the Faraday cup. (b) The ion signal (squares) fitted using the integral of a Lorentzian (solid line), and the Lorentzian velocity distribution (dashed line).

In Figure 3.6, a fixed U_a value of 1000V and variable a in the range between 0.5 and 50mm were used. Again, the experimental data (open circles) are in good agreement with the simulations (closed circles), although the peak of the transmission in the experimental data is shifted slightly towards lower a values.

The experimental data from Figures 3.5 and 3.6 were re-plotted in Figure 3.7 (open diamonds and circles from Figures 3.5 and 3.6 respectively) and they are in reasonable agreement with the simulated data. The only minor disagreement is that the increase in the simulated transmission data is faster than that of the experimental data for θ <20°.

3.5.3. Mass filter resolution

Since it is not possible to produce clusters with a single size, it is not possible to measure the resolution of the mass filter experimentally. Therefore, simulations of the mass filter were used to study the dependence of the mass filter resolution on U_a and a. The resolution was found by using ions with a fixed diameter of 6nm and applying the pulse and delay times from Equations 3.1 and 3.2 corresponding to diameters in the range of 5.6-6.4nm. Figure 3.10 shows the dependence of the mass filter resolution on the pulse height using θ=38° for U_a=100, 500, and 1000V. The figure

shows that the resolution does not depend significantly on the pulse height. This is one of the main advantages of this mass filter. The resolution is found from the FWHM in Figure 3.10 to be ~6 ($\Delta m/m = 3\Delta D/D$, where D is the ion diameter) which is similar to the theoretical resolution from Equation 3.3. The resolution could be increased by decreasing the diameter of the ion beam (i.e. the diameter of the exit aperture), but this value is sufficient for the purpose of this work:[6, 7] we note that this resolution corresponds to a size range of ±0.17nm (one standard deviation). Simulations have been conducted with both focussed and collimated beams, demonstrating that focussing has no effect on the transmission or resolution of the mass filter.

3.5.4. Measurement of mass spectra

This section begins by noting that because the mass resolution ($\Delta m/m$) is fixed over the entire mass range, the range of masses being detected (Δm) is in fact proportional to the selected m. This means that the measured signal must be corrected by dividing by m in order to achieve the true mass distribution.

In order to measure mass spectra of the Pd ions with constant transmission, U_a and θ were fixed at 1000V and 29° respectively. The appropriate a-value was found for each ion mass using Equation 3.4. Equations 3.1 and 3.2 were then used to find the pulse and delay times corresponding to each ion mass in the range under study as shown in Figure 3.11(a). The measured size distribution is shown as the dashed line in Figure 3.11(b) for ions produced using the pulse and delay times from Figure 3.11(a). The solid line shows the corrected size distribution, i.e. after dividing the measured intensity by m. The size distribution shows a main peak at 8.9nm.

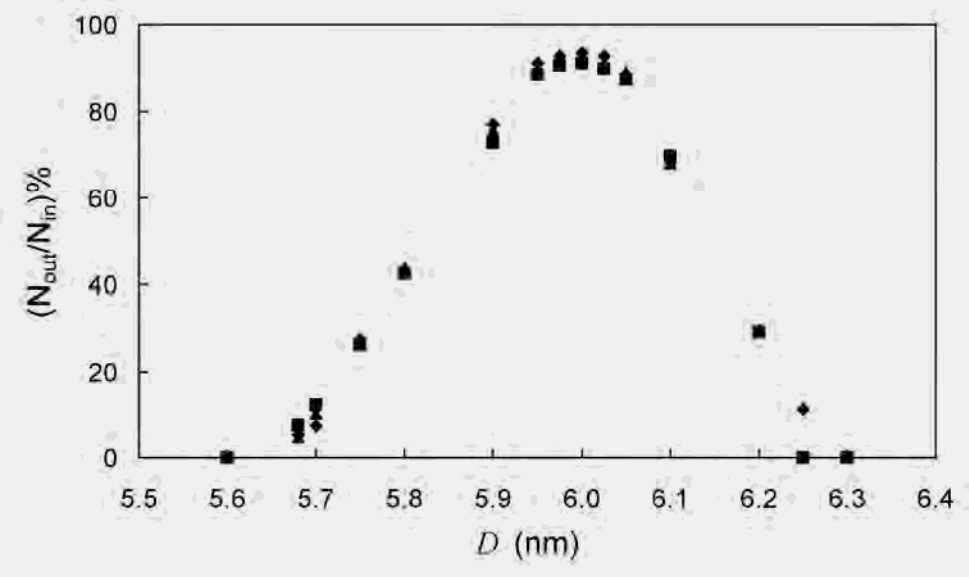

Figure 3.10 The simulated mass filter resolution for the 6nm ions using pulses with a height of 100V (squares), 500V (diamonds), and 1000V (triangles).

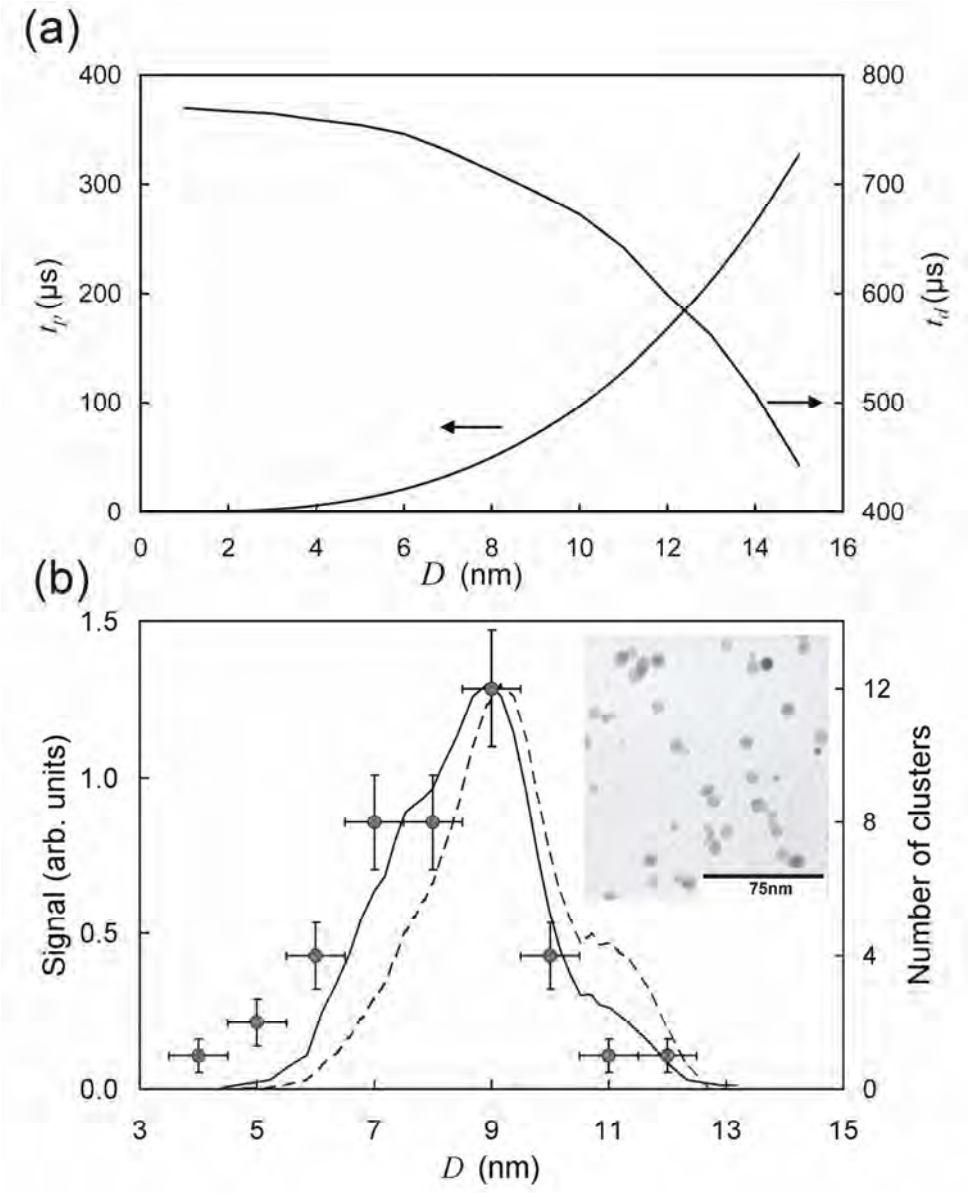

Figure 3.11 (a) The mass dependence of t_p and t_d when using θ=29°, U_a=1000V, and v_0=210m/sec for the mass range of 1-15nm. (b) The size distributions of Pd ions. The dashed line is the measured size distribution, while the solid line is the corrected one. The circles are the results found from the TEM images. The inset is a high resolution TEM image of Pd ions produced using the same source conditions as was used for the size distribution in the figure.

Transmission Electron Microscope (TEM) images of clusters which have not been mass-selected were used to confirm the size distribution of the Pd clusters. An example of these images is shown in the inset in Figure 3.11. The TEM images were used to find the size distribution using ImageJ as described in Section 2.3. The TEM results (filled circles with error bars in Figure 3.11(b)) are in good agreement with the size distribution produced using the mass filter.

As an example of the use of the mass filter to obtain mass spectra, the effect of changing the source aggregation length on the size distribution has been investigated. Figure 3.12 shows the corrected size distributions for two aggregation lengths, 10 and 13cm. For the aggregation length of 10cm the size distribution shows a main peak at

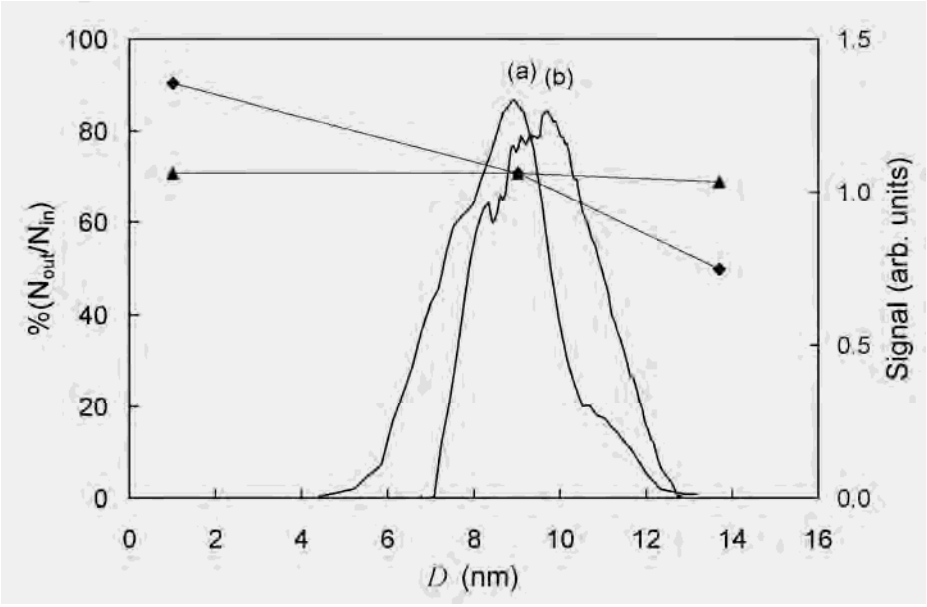

Figure 3.12 Pd ions corrected size distributions using a source aggregation length of 10cm (a) and 13cm (b). The triangles and diamonds in the figure are the simulation results of the mass filter transmission if a fixed a value of 5.2mm (diamonds), or a fixed θ of 29° for each ion mass (triangles) were used. The lines connecting the triangles and the diamonds serve as guides to the eye.

8.9nm, while the size distribution for the aggregation length of 13cm shows a main peak at 9.7nm. Increasing the aggregation length shifts the size distribution towards larger masses.[11] A similar result was reported for silver clusters produced using a similar source.[12]

The diamonds and triangles in Figure 3.12 show the simulated mass filter transmission when fixing U_a at 1000V for two distinct cases: when θ was fixed at 29° (a changes) across the mass range (triangles), or when θ changed (fixed a value of 5.2mm was used for the whole mass range) (diamonds). Clearly, allowing θ to vary could skew the measured mass spectrum. When θ is fixed for the mass range, this ensures constant transmission efficiency across the entire mass range and allows an undisturbed measurement of the mass spectrum.

3.5.5. Effect of waiting time

Using non-optimum waiting times (the time between the end and the start of two accelerating or decelerating pulses as shown in Figure 3.1(b)) will cause many ions to be lost, as discussed in Reference [5]. The mass filter efficiency can be enhanced by optimising the waiting time.

Figure 3.13 shows the experimentally measured dependence of the ion signal on the waiting time for ions with diameter of 9nm (measured using θ=40°). The curve shows a maximum in the ion signal at t_w~1300μs. The optimum waiting time is the time the ions need to travel from the mass filter entrance aperture to the far-right end of the horizontal opening in Plate 2 (Figure 3.8(c)). The decrease in the ion signal at lower waiting times is due to the mass filter not being completely filled with ions when the

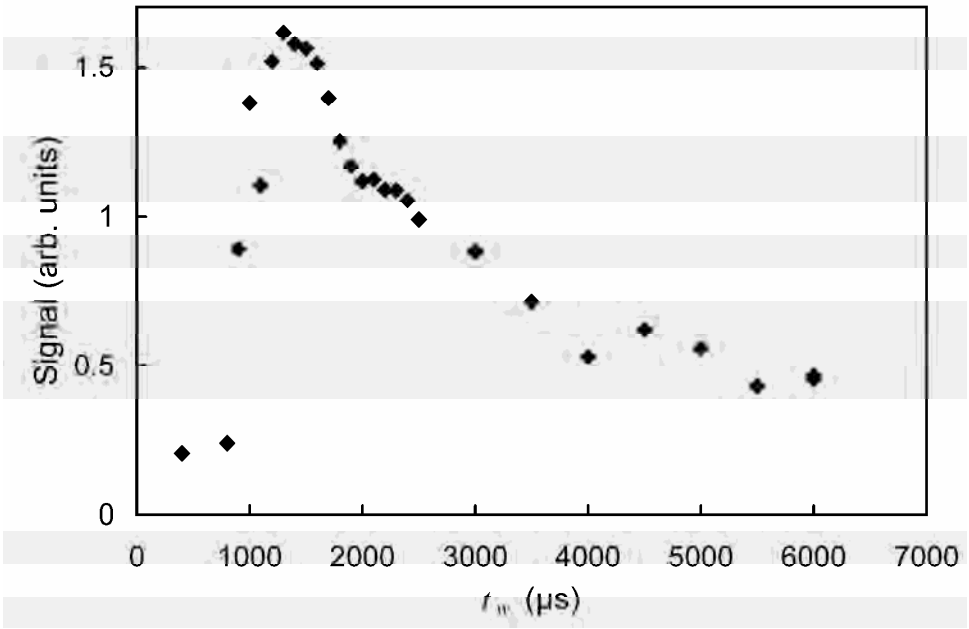

Figure 3.13 The dependence of the ion signal on the waiting time.

accelerating pulse starts, while for higher waiting times the ion signal decreases due to the loss of the ions that pass beyond the far-right end of the opening in Plate 2. Figure 3.13 shows that the ion signal drops to half of the maximum signal when the waiting time is double the optimum waiting time value, as expected. The position of the maximum in Figure 3.13 is consistent with the previous velocity measurements and the geometry of the mass filter. For υ_0=210m/sec the ions need 1270μs to reach the far-right end of the horizontal opening in Plate 2.

3.6. Conclusion

In conclusion, the transmission of the mass filter was found to be dependent on the ion beam deflection angle (θ). θ is dependent on both the accelerating voltage (U_a) and the distance the ions cover during the acceleration between Plate 1 and Plate 2 (a). Increasing U_a and/or a was found to increase the ion beam deflection angle. The transmission saturates for $\theta>\theta_m$~30° (in our embodiment of the mass filter); this angle is determined by the geometry of the mass filter. The experimentally measured and the simulated transmission data are in reasonable agreement.

The following procedure should be applied in order to optimize the ion transmission: the horizontal velocity should be measured, θ should be chosen to be greater than θ_m and the pulse height should be fixed at a value consistent with the mass range to be measured. Equation 3.4 can then be used to find the a value which corresponds to each required mass. The a values are then used to find the appropriate pulse and delay times from Equations 3.1 and 3.2, noting however that a must remain smaller than a_{max}. High U_a values (typically ~kV) are preferred when measuring mass spectra or depositing large ions so as to achieve $a < a_{max}$. It should be noted that changing a while fixing U_a was the simplest option in the current experiment because it could be achieved by changing the pulse and the delay times which were controlled by a

Labview program. In contrast U_a can only be changed by operating the power supply controls manually, and so changing U_a with a constant is not a practical option for the operation.

This chapter concludes by commenting on the practical performance of the mass filter. This mass filter provides an excellent method of measuring mass spectra for the relatively large ions which we have recently been working with.[6] [In contrast, when a standard TOF mass spectrometer was used in our laboratory, heavy and fast ions could not be measured since when the TOF is mounted perpendicular to the cluster beam (as is usual), the ions tend to collide with the walls of the drift region.] The mass filter performance (resolution, transmission) are in accordance with the original predictions of von Issendorf and Palmer,[5] but it was found in this study that the reduction in ion intensity after mass selection is very significant. Even with 90% transmission for a particular mass it must be remembered that the vast majority of the clusters produced are rejected, and that deposition times are typically increased from a few minutes to a few hours. For sources which produce a narrow range of sizes (e.g. 9±2nm for the sputtering source in Figures 3.11 and 3.12) the time-cost of the improvement in mass resolution (e.g. to 9±0.2nm) needs to be carefully considered.

References

1 R. Busani, M. Folkers, and O. Cheshnovsky, Phys. Rev. Lett. **81**, 3836 (1998).
2 M. Haruta, Catal. Today **36**, 153 (1997).
3 W. A. de Heer, Rev. Mod. Phys. **65**, 611 (1993).
4 W. Paul, H. Reinhard, and U. v. Zahn, Z. Phys. **152**, 143 (1958).
5 B. von Issendorff and R. E. Palmer, Rev. Sci. Instrum. **70**, 4497 (1999).
6 J. G. Partridge, S. A. Brown, A. D. F. Dunbar, R. Reichel, M. Kaufmann, C. Siegert, S. Scott, and R. J. Blaikie, Nanotechnology **15**, 1382 (2004).
7 J. Schmelzer, S. A. Brown, A. Wurl, and M. Hyslop, Phys. Rev. Lett. **88**, 226802 (2002).
8 H. Haberland, US patent # 5110435 (1992).
9 R. Reichel, J. G. Partridge, A. D. F. Dunbar, S. A. Brown, O. Caughley, and A. Ayesh, Journal of Nanoparticle Research **8**, 405 (2006).
10 R. Reichel, *PhD thesis, Nano scale cluster devices* (Physics and Astronomy Department, University of Canterbury, Christchurch, 2007).
11 A. Lassesson, A. I. Ayesh, and S. A. Brown, To be published.
12 S. Pratontep, S. J. Carroll, C. Xirouchaki, M. Streun, and R. E. Palmer, Rev. Sci. Instrum. **76**, 045103 (2005).

4. Results: non-contacted V-grooves

This chapter studies the morphology of Bi clusters deposited on non-contacted V-groove samples fabricated using SiO_2/Si substrates. Knowledge of the cluster wire morphology is essential to be able to fabricate cluster devices.

This chapter contains five sections. In the first section the dependence of the cluster size on the inert-gas flow rate and the source temperature is discussed. The relation between the nominal deposited thickness and plateau coverage is discussed in the second section. The third section discusses the effect of the substrate temperature on the morphology of the cluster islands. The fourth section discusses the dependence of the average wire width on V-groove width and inert-gas flow rate, and the effect of different source conditions and substrate temperatures on the cluster bouncing off the V-groove walls. The chapter is concluded by a summary of the main aspects presented in it in the last section.

4.1. Dependence of Bi cluster size on different source conditions

This section discusses the effect of various source conditions on the average cluster size. The different conditions include different inert gas flow rates (of Ar), various mixtures of Ar and He inert-gases, and cooling down the source down to ~77K instead of ~290K. The crucible temperature was fixed in each of the following experiments in the range between 780 and 820ºC.

To study the effect of the source inlet Ar flow rate on the cluster size for Bi clusters produced using an IGA source at ~290K, clusters were deposited on non-contacted V-groove samples. Source inlet Ar flow rates between 60 and 260sccm were used, and the IGA source was cooled down using water (at room temperature). Figure 4.1 shows FE-SEM images of Bi clusters on the plateaus surrounding the V-grooves for low coverage samples deposited using different source inlet Ar flow rates. The low coverage samples were used for the cluster size measurements so that isolated clusters can be distinguished. However, the images show that a few aggregates of clusters were formed despite the low coverage. These aggregates were excluded in the size measurements since they contain more than one cluster. The cluster diameter (D) will be used in the following to indicate the cluster size. Each cluster was fitted to an ellipse, and D was estimated as the average of the lengths of the major and minor ellipse axes. The images in Figure 4.1 were used to find the size distributions using ImageJ as described in Section 2.3. The size distributions are shown next to the FE-SEM images in the figures. It should be noted that each D in the histograms is an average of a period of 4nm, i.e. D is 32nm for the period of 30-34nm. The size distributions were confirmed by manual measurements from the FE-SEM images for the same samples. The size distributions were used to find the average cluster size.

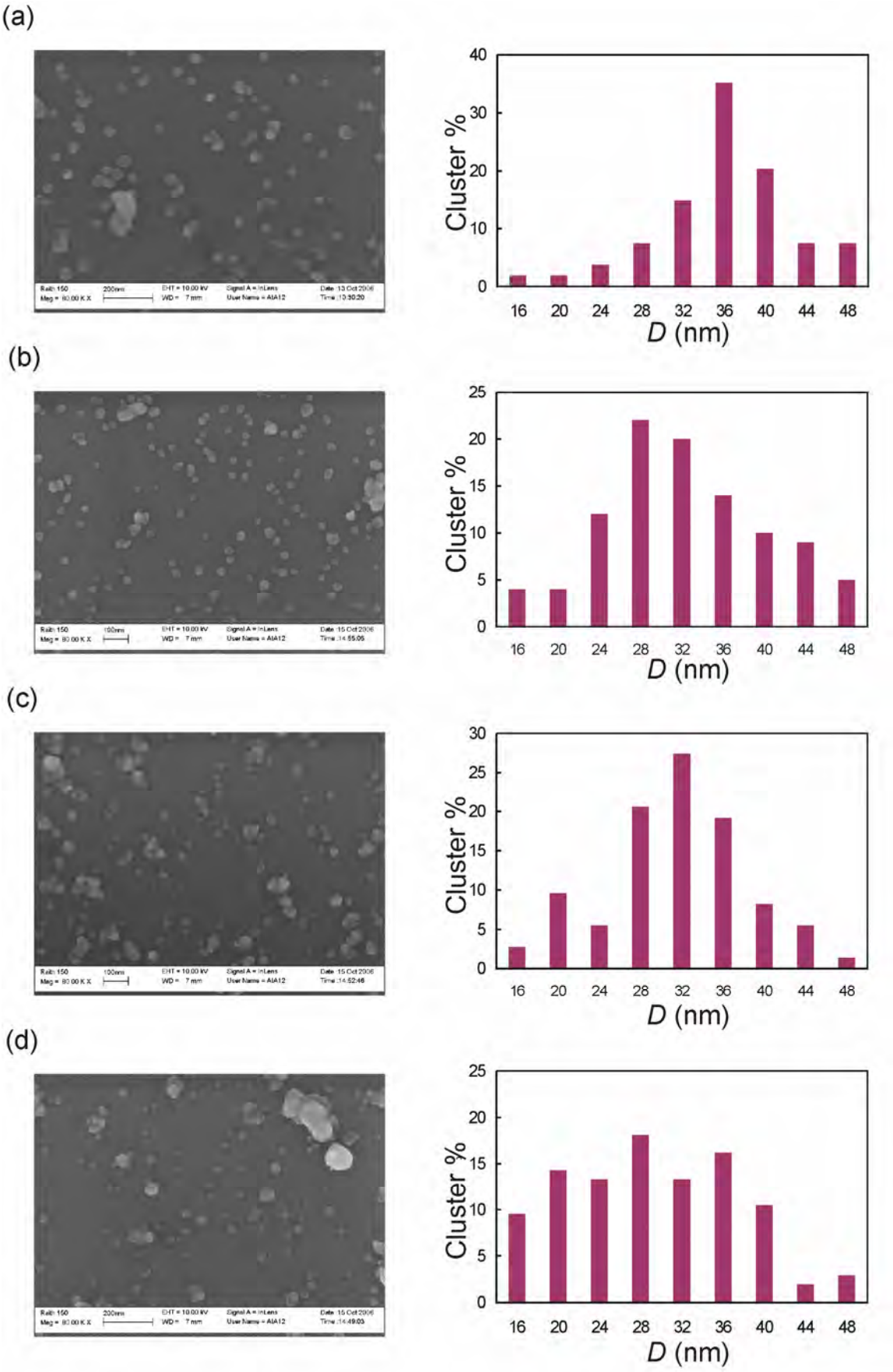

Figure 4.1 FE-SEM images of plateaus between V-grooves and the size distributions of clusters produced using source inlet Ar flow rates of (a) 80, (b) 100, (c) 150, and (d) 200sccm.

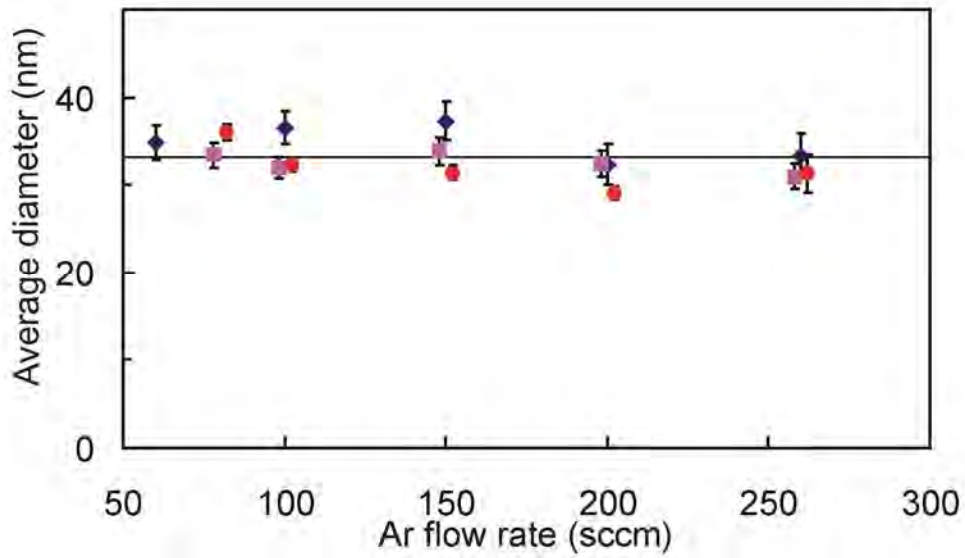

Figure 4.2 The average diameter of clusters produced using the IGA source with source inlet Ar flow rates between 60 and 260. D was measured manually (squares) and as described in Section 2.3 (circles) for the same samples. The diamonds are data points found manually for different samples.

Figure 4.2 shows the dependence of the average cluster diameter on the source inlet Ar flow rate. The uncertainty is estimated as the standard deviation divided by the square root of the number of clusters. The circles and the squares are the data points found using ImageJ and manually for the same samples, while the diamonds are data points for different samples found manually. The average cluster diameter in Figure 4.2 is seen to be approximately constant (~33 nm) across the full range of source inlet Ar flow rates. It can be seen that the three sets of results are consistent. This confirms the validity of the method described in Section 2.3 to find *D*. It also means that the source is stable since it produces the same *D* for samples produced in different depositions when using the same source conditions.

A second set of samples was used to study the effect on the cluster size of using mixtures of Ar and He inert-gases. The total inert-gas flow rate of the mixture was fixed at 180sccm. The ratio of He to Ar was changed between 0 and 60%. The FE-SEM images and the cluster size distributions of these samples are shown in Figure 4.3. The average cluster size was found from the distributions and is plotted as a function of the He/Ar ratio in Figure 4.4. Although the figure shows a decrease in the average cluster size for the 60% He/Ar ratio, this decrease is within the uncertainty. However, a decrease in the cluster size with increasing He/Ar ratio was observed for other metal clusters such as Sb.[1]

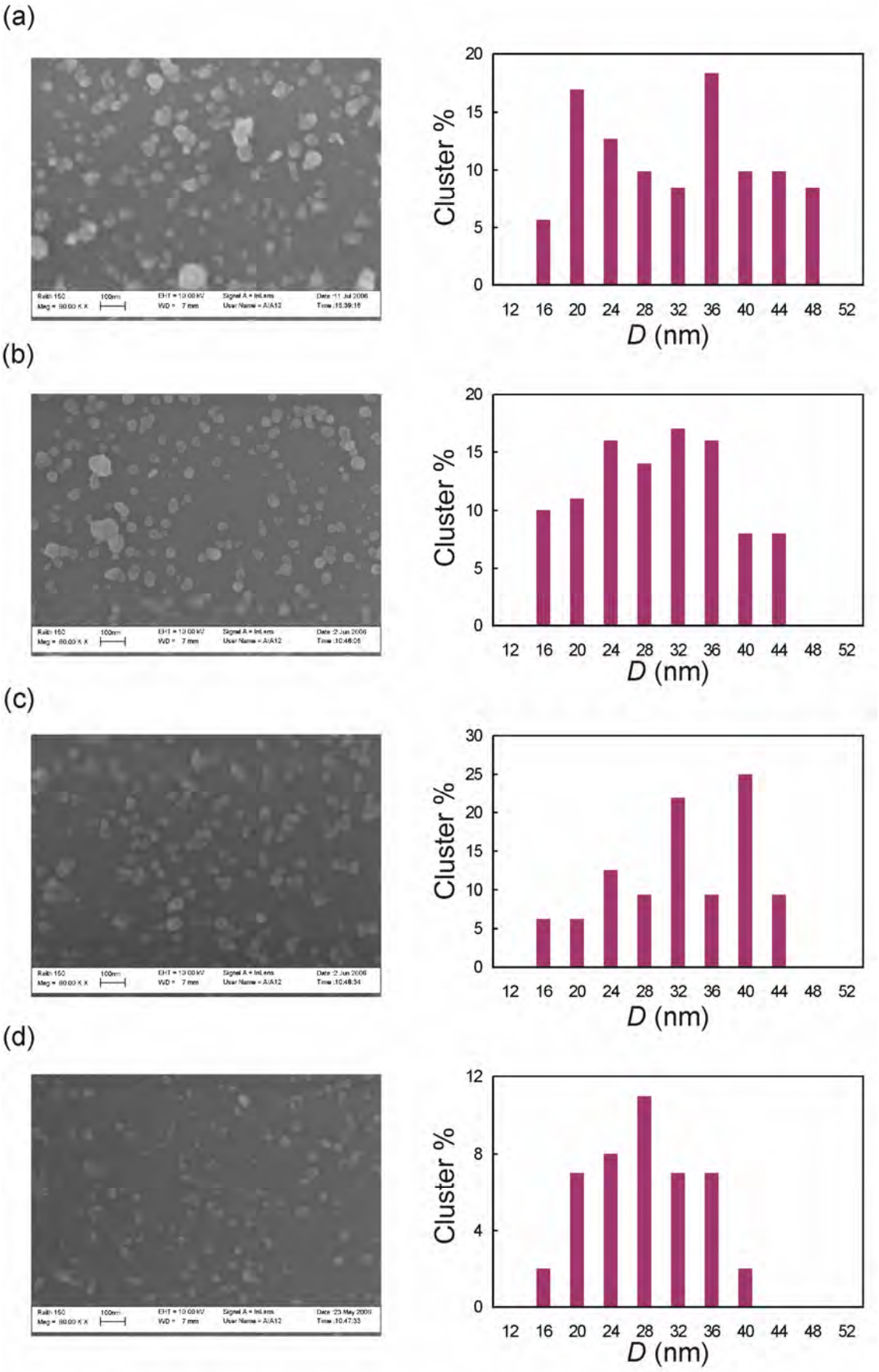

Figure 4.3 FE-SEM images and the size distributions of clusters produced using mixtures of He and Ar inert-gases with He/Ar ratios of (a) 0%, (b) 20%, (c) 40%, and (d) 60%.

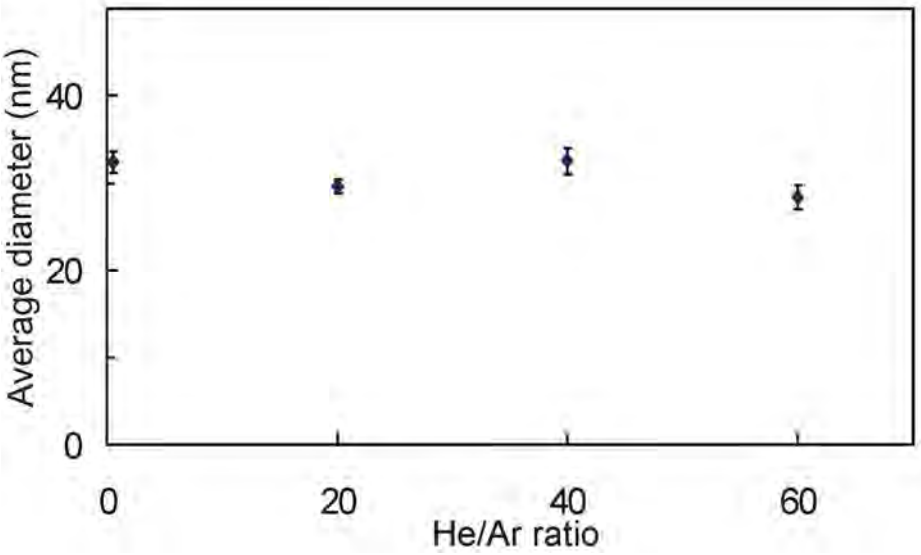

Figure 4.4 The dependence of the average cluster size on the ratio of He to Ar.

To study the effect of cooling the source down to ~77K (using LN) instead of ~290K (using water) on the cluster size, source inlet Ar flow rates between 70 and 180sccm were used to fabricate an additional set of samples. The FE-SEM images and the size distributions for different source inlet flow rates are shown in Figure 4.5. The figure shows that cooling the source down to ~77K has an obvious effect on the average cluster size (compared with the sizes in Figures 4.1-4.4). However, changing the source inlet Ar flow rate did not produce a noticeable effect on the cluster size, as can be seen in Figure 4.6. The average cluster size is 22nm.

In summary, the above results show that the average cluster size is not dependent on the change in the source inlet Ar flow rates in the ranges between 60 and 260sccm for an IGA source at ~290K and between 70 and 180sccm for an IGA source at ~77K regardless of the source cooling type. The average cluster size was also found to be independent on mixing Ar with He (percentages up to 60%) when using a total inert-gas flow rate of 180scc. However, cooling the source down to ~77K instead of ~290K decreased the average cluster size from ~33 to ~22nm (when using source inlet Ar flow rates between 70 and 180sccm).

The constant cluster diameters observed in Figures 4.2, 4.4, and 4.6 is rather remarkable – in many gas aggregation sources, changes in flow rate or adding He to the source (which necessarily cause a change in source pressure) result in a change in cluster size due to the different aggregation conditions.[2]

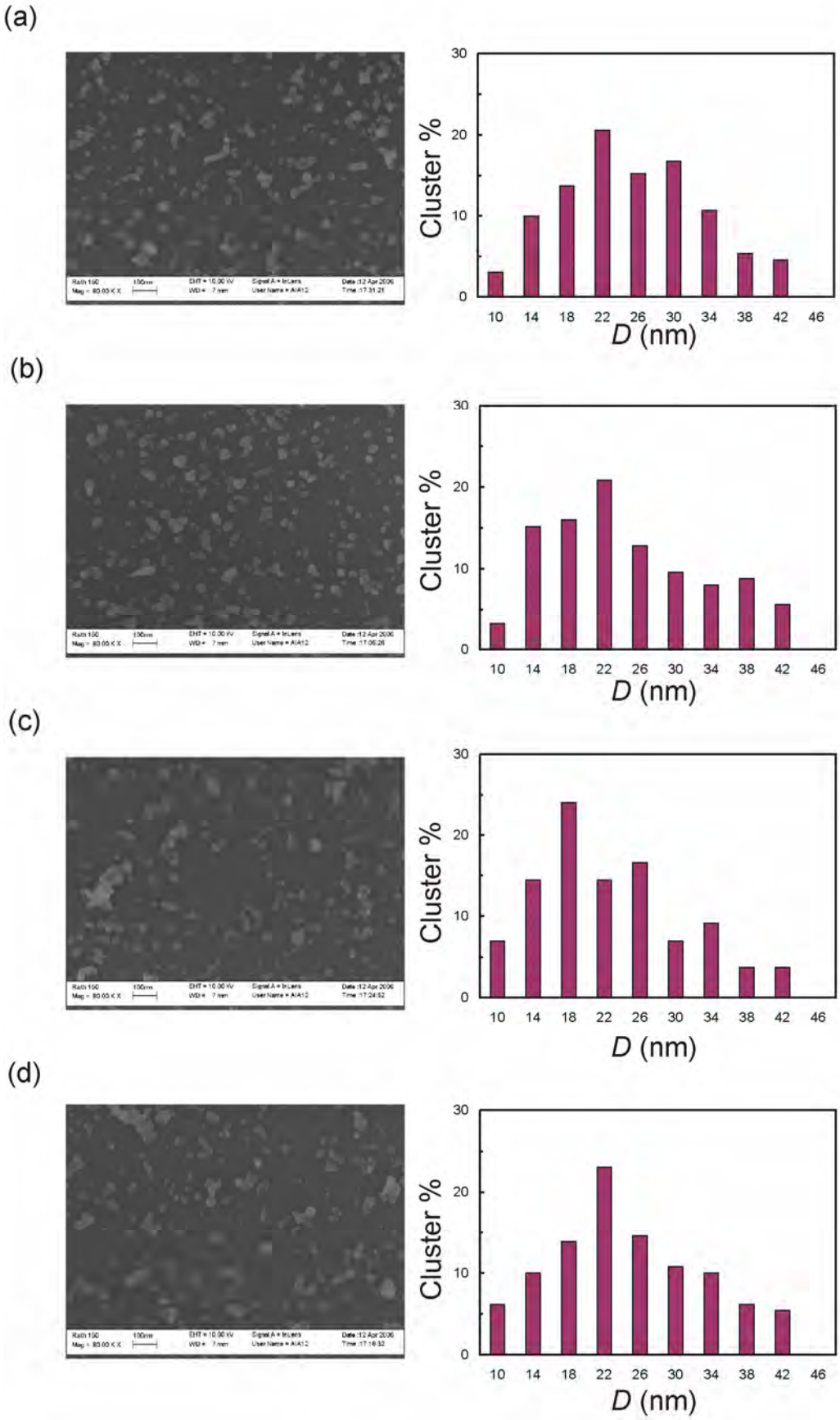

Figure 4.5 The FE-SEM images and the size distribution for samples produced using a LN cooled source, and using source inlet Ar flow rates of 70sccm (a), 100sccm (b), 140sccm (c), and 180sccm (d).

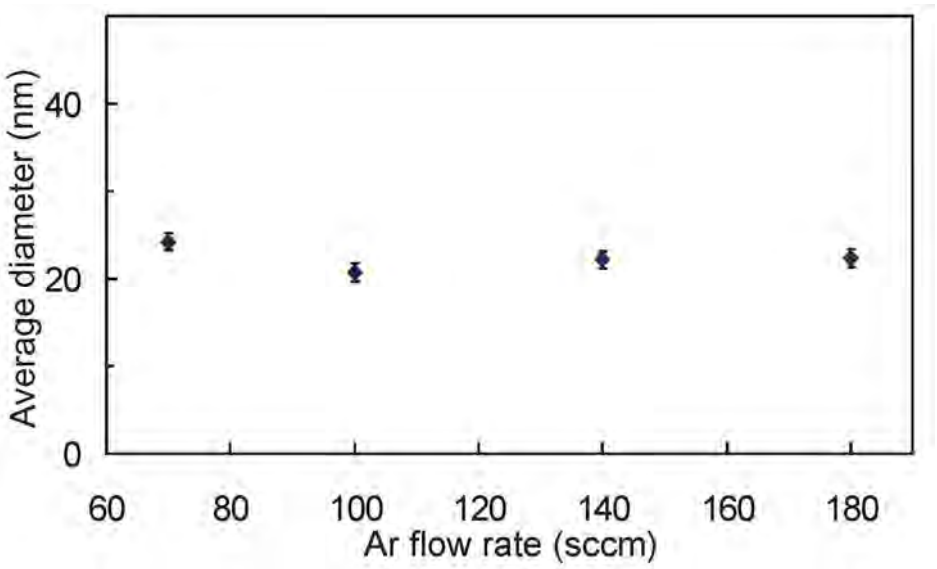

Figure 4.6 The dependence of D on the source inlet Ar flow rate for samples produced using a LN cooled source.

Previous studies reported a change in the cluster size by changing various source parameters, such as, source pressure (P_s) and temperature (T); crucible temperature (T_c); and inert gas type and flow rate.[1, 3] In the above experiments, the crucible temperature ranged between 780 and 820ºC. The change in the inert gas type and flow rate modified the source pressure. Table 4.1 shows P_s, T, average cluster size, and inert gas flow. The table indicates that the change in the average cluster size is not a result of changing the IGA source pressure in the range of 14.9-47.8Torr. However, a decrease in the source temperature decreases the average cluster size. Decreasing T provides better cooling thereby increasing the nucleation rate, as shown in Equation 2.1. As a result, the supersaturation of the vapour increases, and a larger number of critical size clusters compete for the metal vapour, leading to the formation of smaller clusters.[4]

4.2. Plateau cluster coverage versus mean thickness

Figure 4.7 shows the dependence on the nominal deposited thickness of the cluster surface coverage ($p_{surface}$) and the corrected coverage (p) on the plateau (i.e. the surface area that would have been covered had there been no stacking of clusters), for samples prepared with a source inlet Ar flow-rate of 100sccm. The cluster coverage was measured from FE-SEM images as described in Section 2.3. The corrected coverage was found using the relation:[5]

$$p = -\ln(1 - p_{surface}) \tag{4.1}$$

This relationship takes into account the probability that a new cluster might become a constituent part of the first layer or a constituent part of a higher layer. Figure 4.7 shows that, as expected, both the surface coverage and the corrected coverage increase as the total deposited thickness of clusters is increased.

Table 4.1 T, P_s, inert gases' flow rates, and average cluster size.

T (K)	Ar flow rate (sccm)	He flow rate (sccm)	P_s (Torr)	Average cluster size (nm)
290	60		14.9	33
290	80		20.6	33
290	100		24.3	33
290	150		32	33
290	180		34.9	33
290	200		38.6	33
290	260		47.8	33
290	144	36	34.8	33
290	108	72	33.3	33
290	72	108	31.4	33
77	70		12.1	22
77	100		16.1	22
77	140		20.4	22
77	180		24.7	22

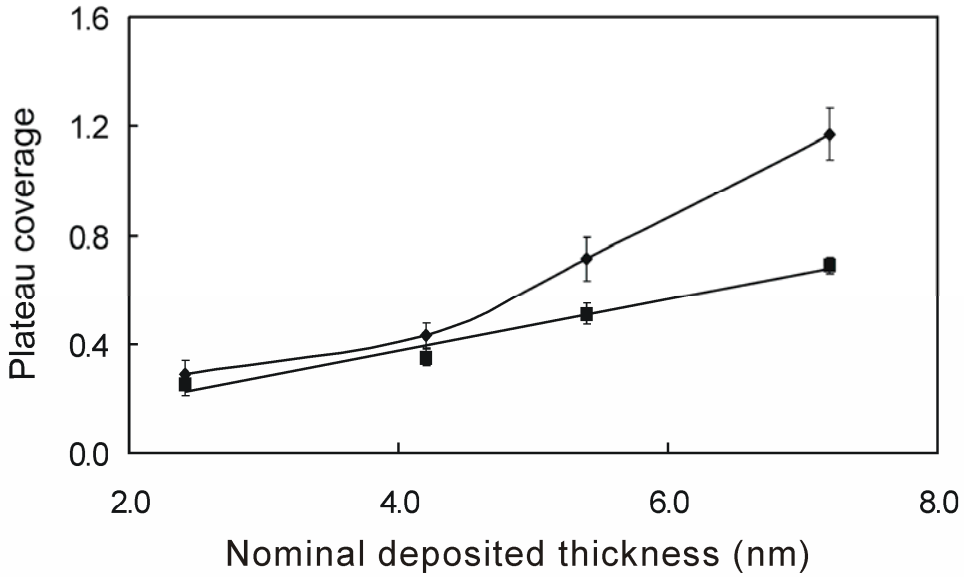

Figure 4.7 The dependence of the surface coverage (squares) and the corrected coverage (diamonds) on the V-grooves passivated plateaus on the nominal deposited thickness.

However, the apparently linear increase in the surface plateau coverage with the increase of the nominal deposited thickness of clusters is deceptive. After correction, the plateau coverage shows a higher rate of increase. It is believed that this is because incident Bi clusters bounce from clean plateaus more readily than they bounce from the surface when other clusters are attached to the plateaus, i.e. deposited clusters serve as soft-landing sites for clusters incident upon them. Bi clusters certainly bounce less easily from plateaus than Sb clusters.[6, 7] Therefore, it is believed that Bi

clusters do not bounce out of the V-grooves: when incident on a V-groove, Bi clusters always appear to be trapped, either through a soft landing site on another cluster or by the apex of the V-groove itself.

4.3. Cluster island morphology versus temperature

The focus of this section is the effect on the cluster film morphology of increasing the substrate temperature. The dependence of the cluster coverage and the cluster height on the substrate temperature are illustrated first, and then a discussion is provided.

4.3.1. Results

The samples used in this study were prepared by depositing Bi clusters on non-contacted passivated V-groove samples. The amount of the deposited material (mean thickness) was fixed at 2 and 5nm (measured using the FTM). For each mean thickness, three substrate temperatures were used: 290, 373, and 473K. Three source inlet Ar flow rates of 45, 100, and 180sccm were used for each substrate temperature. FE-SEM images with a magnification of 40000x were taken for the plateaus next to the V-grooves at the centre of the beam spot. Figures 4.8 and 4.9 show representative FE-SEM images of samples deposited using a source inlet Ar flow rate of 100sccm at the above substrate temperatures for mean thicknesses of 2 and 5nm. An increase in the cluster coverage as the mean thickness increases from 2 to 5nm can be seen in the images. The figures also show that as the substrate temperature increases, the cluster aggregates coalesce and individual clusters in the aggregates cannot be distinguished (unlike the aggregates of samples deposited at room temperature where individual clusters within the aggregates can be recognized). The images also show that increasing the substrate temperature formed more circular aggregates (from top view).

FE-SEM images of the plateaus were used to measure the cluster coverage (as described in Section 2.3) in order to study the dependence of the cluster coverage on the substrate temperature and Ar flow rate. The dependence of the surface cluster coverage ($p_{surface}$) on the substrate temperature is shown in Figure 4.10(a). The figure shows that as the temperature increases from 290 to 473K, $p_{surface}$ stays constant around 0.18 for the 2nm samples deposited using different source inlet Ar flow rates, while it decreases as the temperature increases for the 5nm samples.

The surface cluster coverage presented in Figure 4.10(a) is the ratio of the area covered by clusters to the total area. This measurement does not take into account the probability of clusters stacking. In order to consider the probability of cluster stacking, the corrected coverage was calculated as described in Section 4.2. The dependence of the corrected cluster coverage on the substrate temperature is shown in Figure 4.10(b). The symbols used in the figure are similar to those in Figure 4.10(a). The corrected coverage shows similar dependence on temperature as the surface coverage but with larger values.

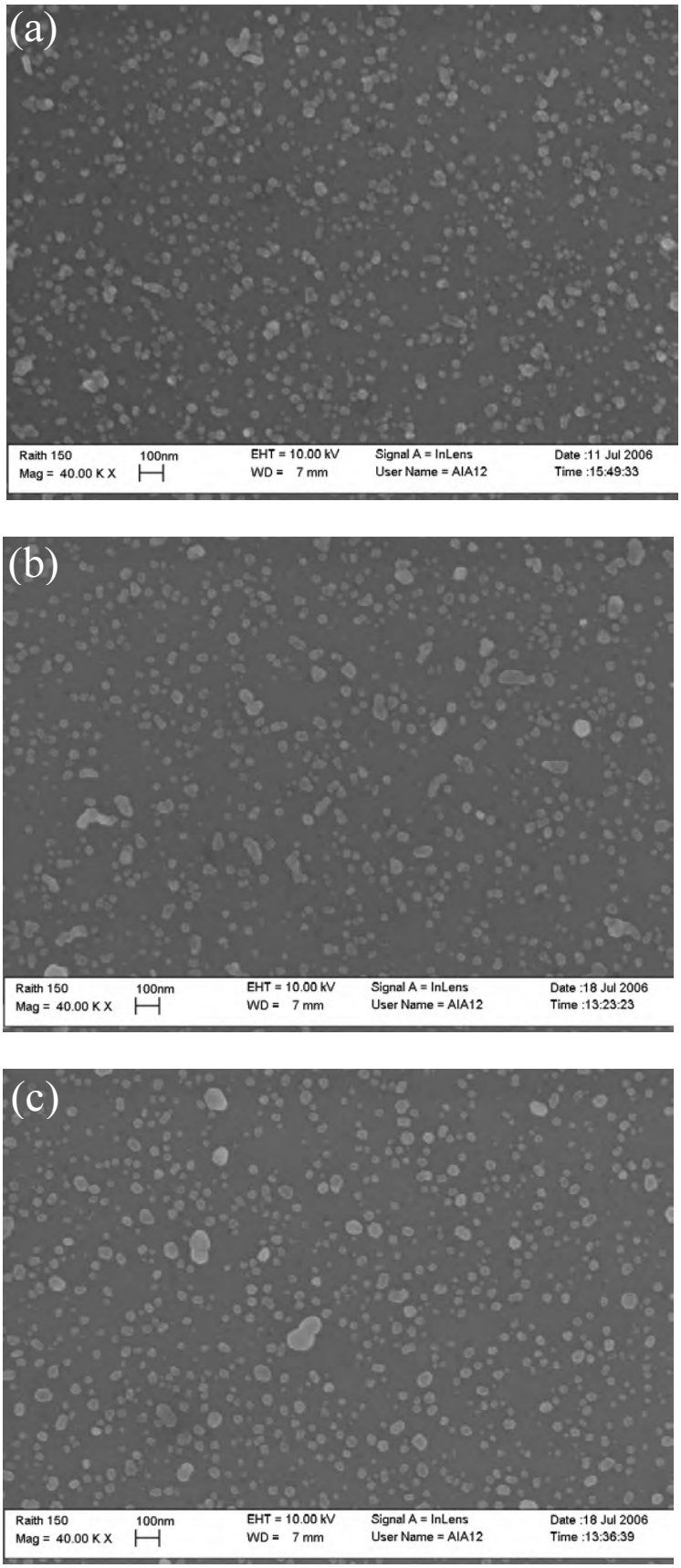

Figure 4.8 FE-SEM images of samples deposited using a source inlet Ar flow rate of 100sccm and an amount of deposited material of 2nm at substrate temperatures of 290K (a), 373K (b), and 473K (c).

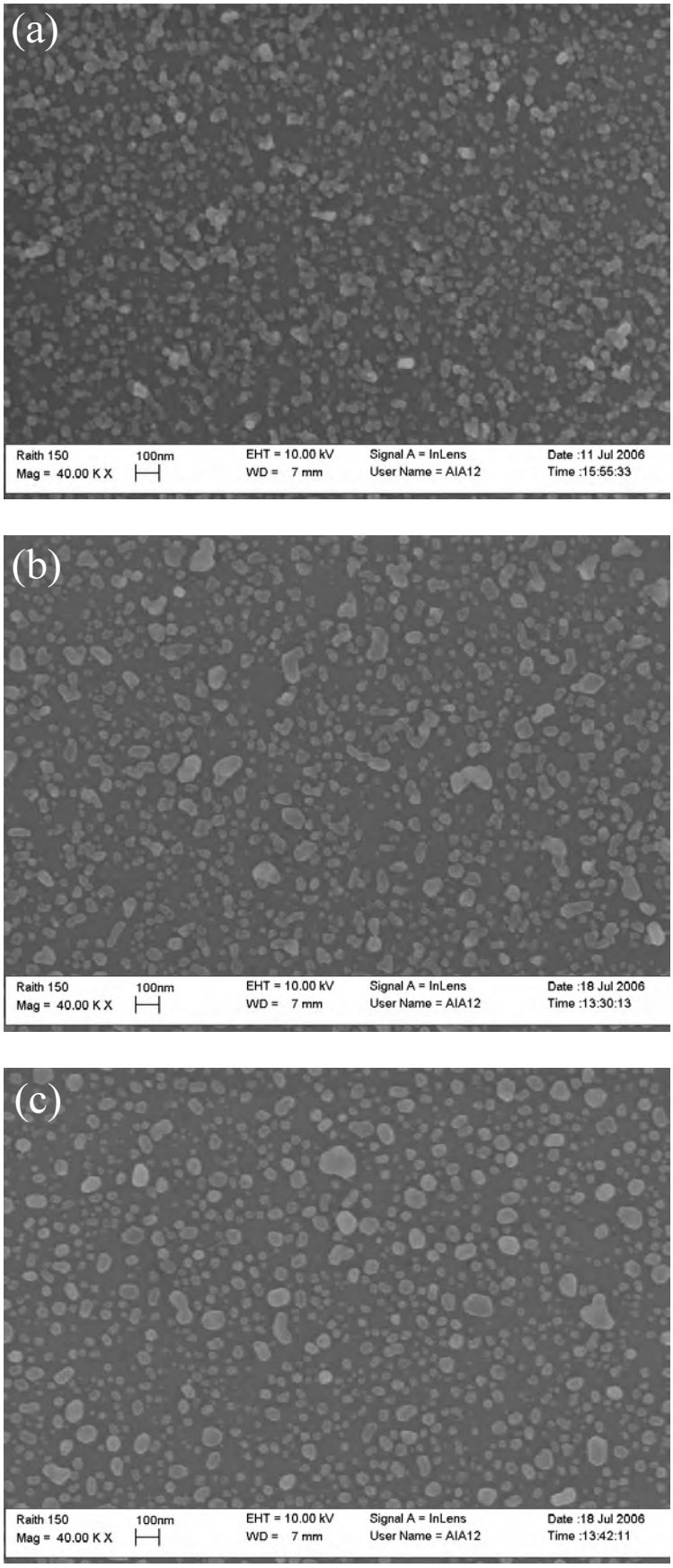

Figure 4.9 FE-SEM images of samples deposited using a source inlet Ar flow rate of 100sccm and an amount of deposited material of 5nm at substrate temperatures of 290K (a), 373K (b), and 473K (c).

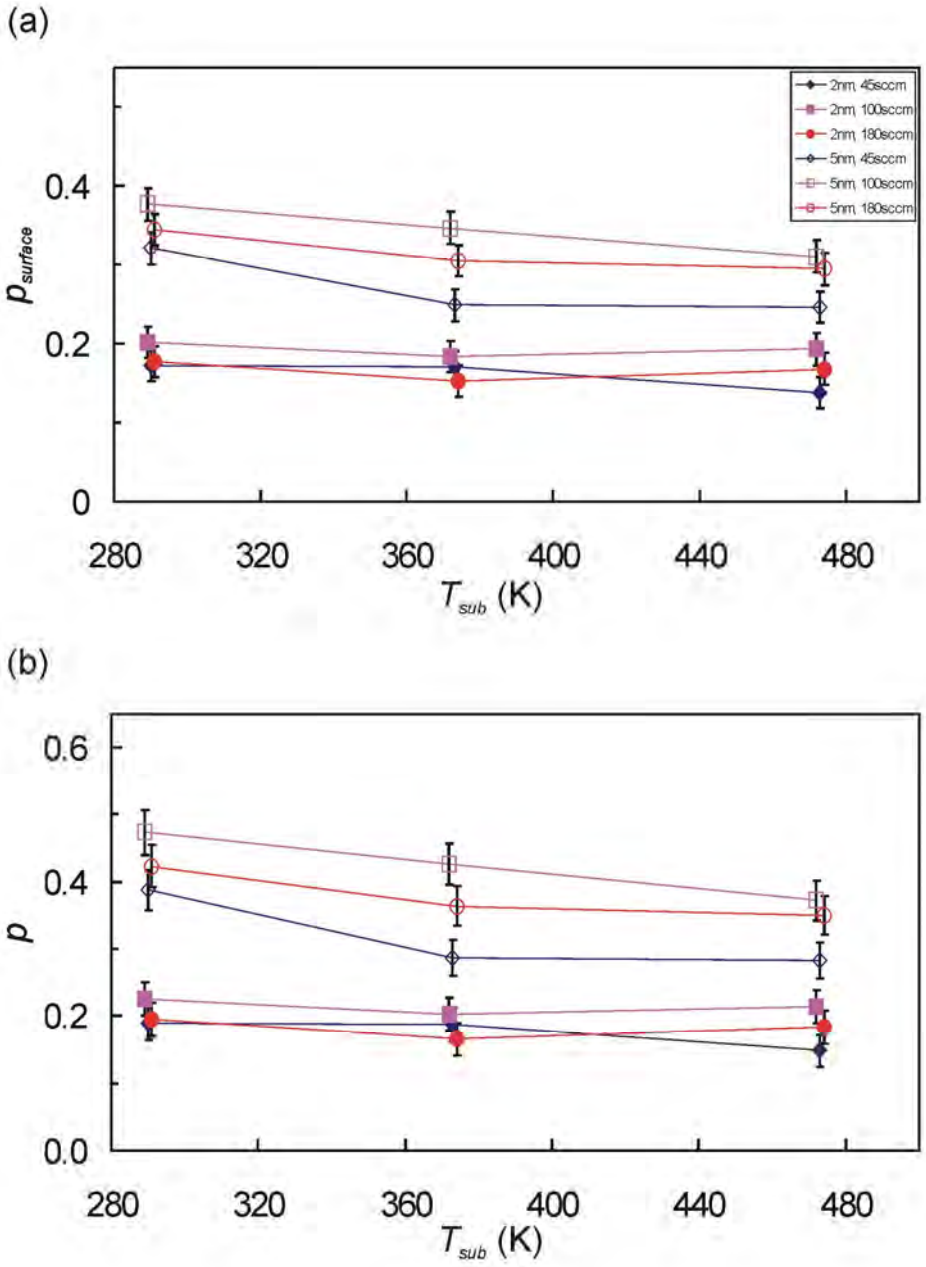

Figure 4.10 The dependence of the cluster surface coverage (a) and the corrected cluster coverage (b) on the substrate temperature. Source inlet Ar flow rates of 45, 100, and 180sccm were used. The close and open symbols are used for the amount of deposited materials of 2 and 5nm respectively. The lines in figure serve as guides to the eye.

Samples with a mean thickness of 2nm and different substrate temperatures were imaged using the AFM to investigate the effect of increasing the substrate temperature on the cluster height. Figure 4.11 shows AFM images and height profiles for samples deposited using a source inlet Ar flow rate of 180sccm at different substrate temperatures. The AFM images were used to find the cluster height as described in Section 2.3. An increase in the cluster height can be noticed as the substrate temperature increases. The dependence of the cluster height on the substrate temperature for the different source inlet Ar flow rates is shown in Figure 4.12(a). The figure shows that the cluster height increases as the substrate temperature increases. The figure also shows that the clusters at each substrate temperature have almost the same heights regardless of the source inlet Ar flow rate. The cluster heights for the different source inlet Ar flow rates were averaged at each temperature. The dependence of the average cluster height (h) on the substrate temperature is shown in Figure 4.12(b).

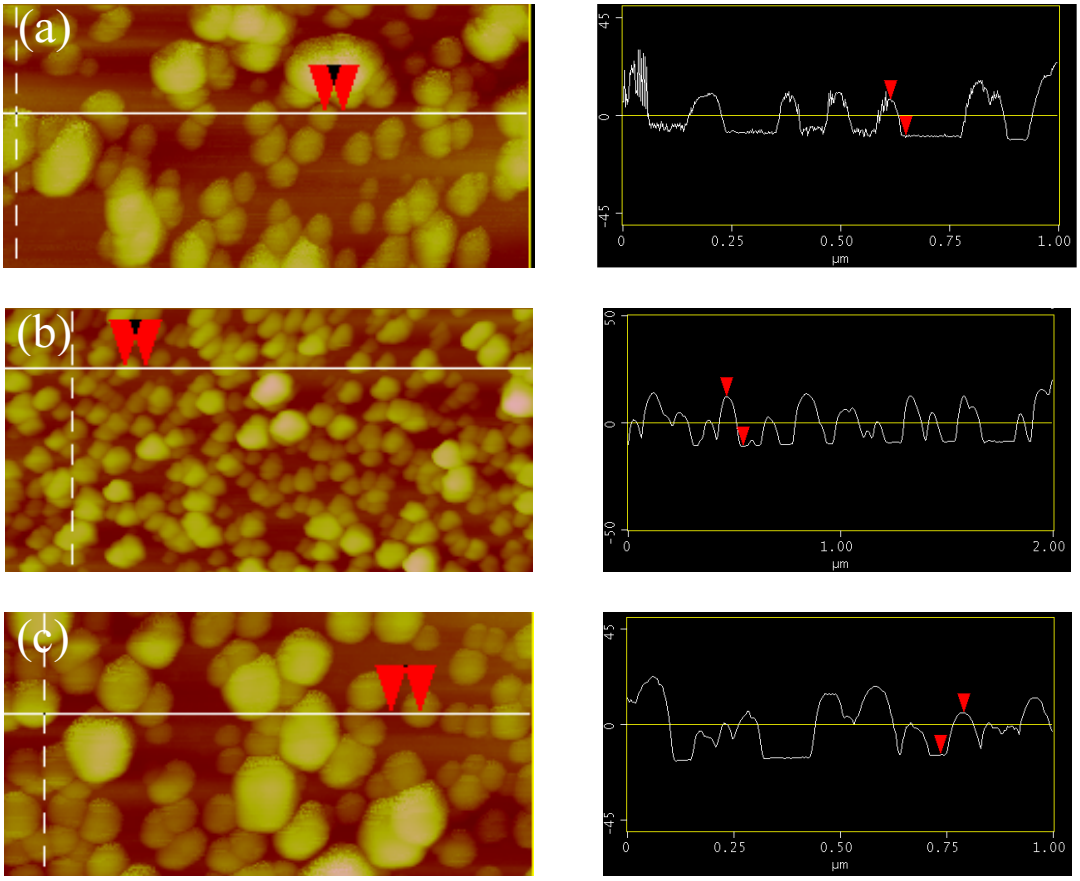

Figure 4.11 The AFM images and the height profiles for the clusters deposited using a source inlet Ar flow rate of 180sccm at 290K (a), 373K (b), and 473K (c).

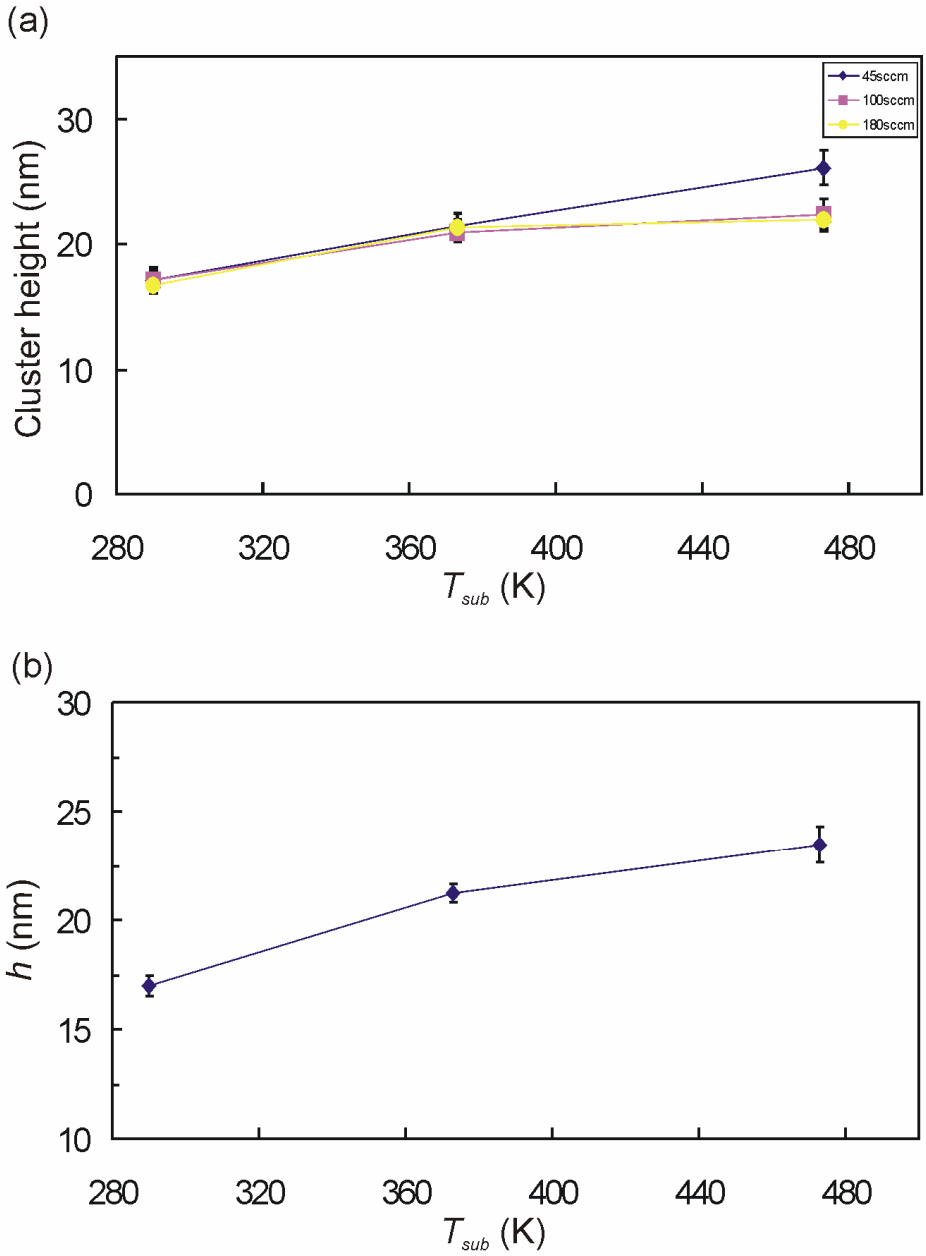

Figure 4.12 The dependence on the substrate temperature of (a) the cluster height for samples deposited using source inlet Ar flow rates of 45sccm (diamonds), 100sccm (squares), and 180sccm (circles), and (b) the average (over the source inlet Ar flow rates) cluster height. The lines in the figures serve as guides to the eye.

To confirm the increase of the cluster height as the substrate temperature increases, cross sectional FE-SEM images were taken for clusters deposited on V-groove samples at different substrate temperatures. Figure 4.13 shows cross sectional FE-SEM images of two samples fabricated using a source inlet Ar flow rate of 45sccm and substrate temperatures of ~290 and 473K. The images confirm the result that increasing the substrate temperature increases the cluster height. The ratio between the cluster height and width in the figure increases from ~53 to ~87% when the substrate temperature increases from 290 to 473K.

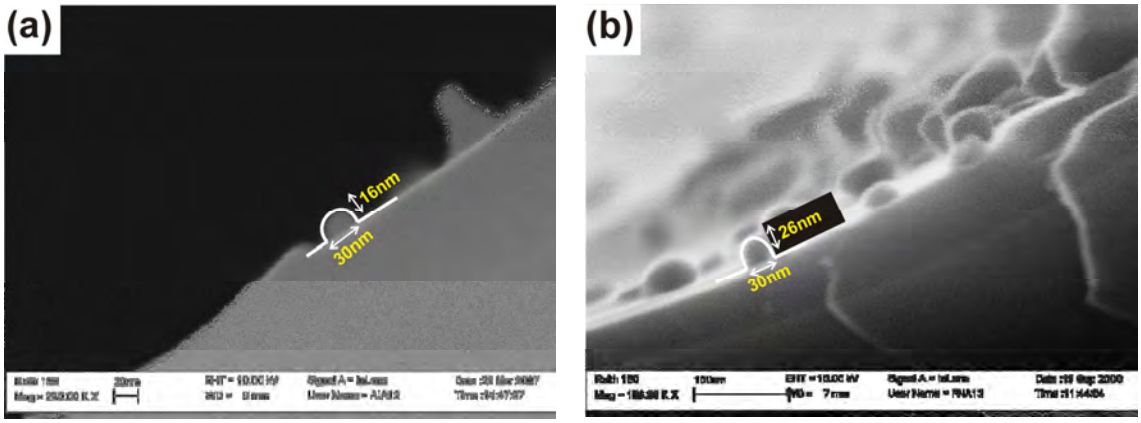

Figure 4.13 Cross sectional FE-SEM images for two V-groove samples deposited using a source inlet Ar flow rate of 45sccm at substrate temperatures of 290K (a), and 473K (b).

4.3.2. Discussion

In order to understand the decrease in the corrected cluster coverage as the substrate temperature increases, the corrected cluster coverage and the average cluster height were multiplied (*ph*) and plotted against the substrate temperature in Figure 4.14(a). The figure shows that *ph* is constant (within the uncertainty) as the substrate temperature increases. This shows that the decrease in the corrected cluster coverage in Figure 4.10(b) has been balanced by the increase in the cluster height.

The product of the average cluster height with the corrected cluster coverage should produce the mean thickness, i.e. 2 and 5nm. However, Figure 4.14(a) provides about double the thickness values measured using the FTM. Hence, *ph* was multiplied by a correction factor. This factor was used since the coverage measurements consider the clusters as boxes packed next to each other. The shape of the cluster can be approximated to a hemisphere, as can be seen in Figure 4.13. The volume correction factor is approximated, as shown in Figure 4.15, as the ratio of the volumes of a hemisphere and a box. This factor is $(2/3\pi r^3)/(4r^3) \sim 0.524$. The same factor is obtained if spherical clusters are assumed. Figure 4.14(b) shows the dependence of the corrected mean thickness ($V_c=0.524ph$) on the substrate temperature. The figure shows that the thicknesses are around 2nm for the low coverage samples and between 3.2 and 4.7nm for the higher coverage samples. Those results are close to the mean thicknesses as measured using the FTM, and the difference could be due to the different cluster stickiness to the substrate as discussed below. It should also be noted that the correction factor for hemispherical clusters is only a rough estimation. This factor will differ if the clusters have different shapes (many clusters look faceted after annealing at higher temperatures, as shown in Figures 4.8 and 4.9). This could be another factor responsible for the underestimation of the mean thicknesses in the figure. The constant value of V_c with temperature is consistent with the expectation that it is unlikely that increasing the substrate temperature causes any cluster diffusion.[8]

The increase in the cluster height as the substrate temperature increases can be understood in terms of the cluster wetting to the substrate. The energy of attachment

to a surface (E_a) associated with the cluster wetting to the surface can be described as $E_a=4\pi r^2\gamma f(\theta)$, where r is the radius of the cluster, γ is the surface tension of the cluster, and $f(\theta)$ is a function which takes into account the change in the surface energy caused by the change in the geometry of the cluster when it wets the surface.[9, 10] Increasing the substrate temperature decreases the cluster wetting to the surface and E_a; thus there is an increase in the cluster height.[11, 12]

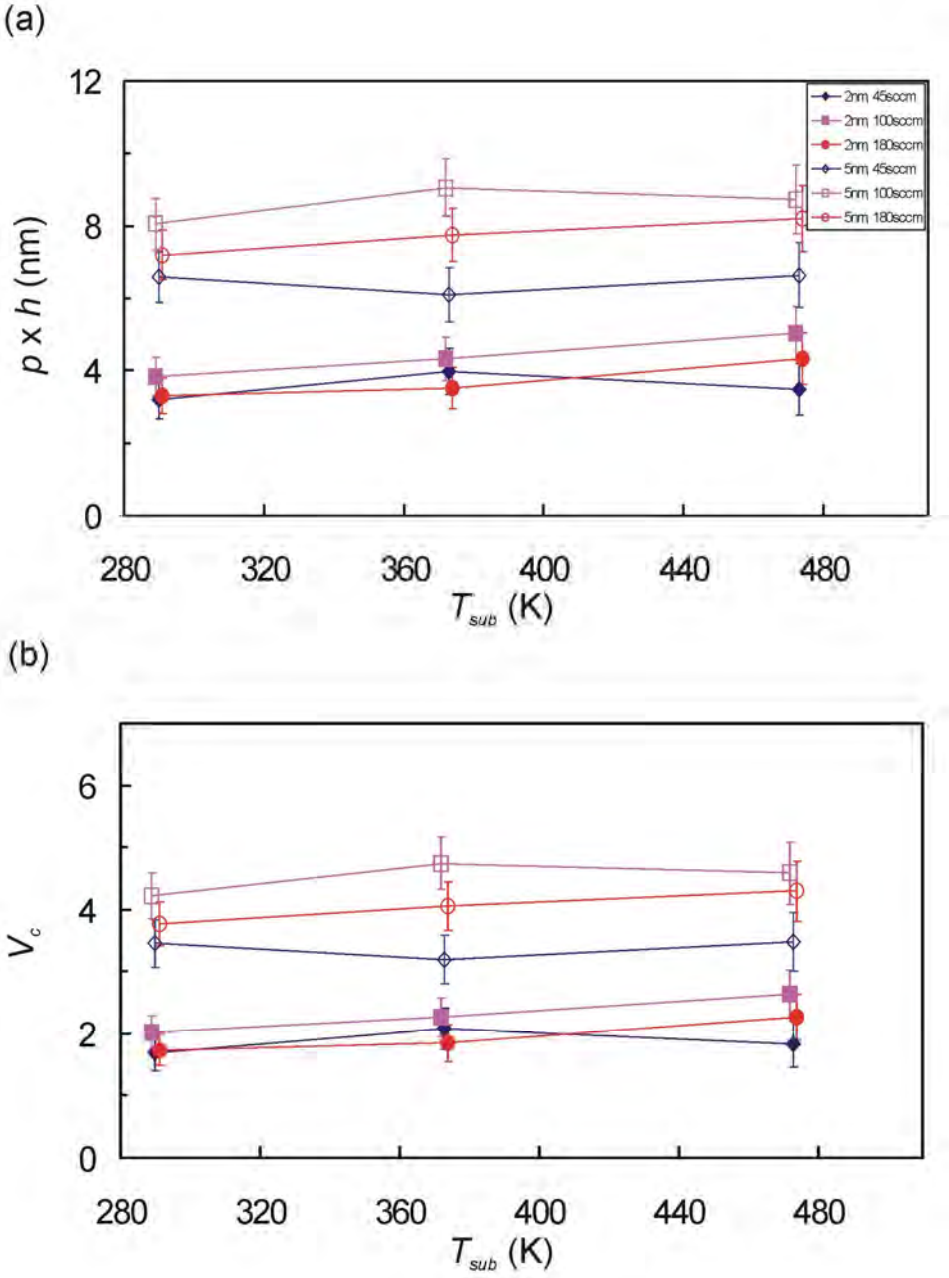

Figure 4.14 The dependence on the substrate temperature of (a) ph, and (b) V_c=0.524ph. The open and closed symbols are used for the 2 and 5nm samples, and the diamonds, squares, and circles are the data points for samples prepared using source inlet Ar flow rates of 45, 100, and 180sccm respectively.

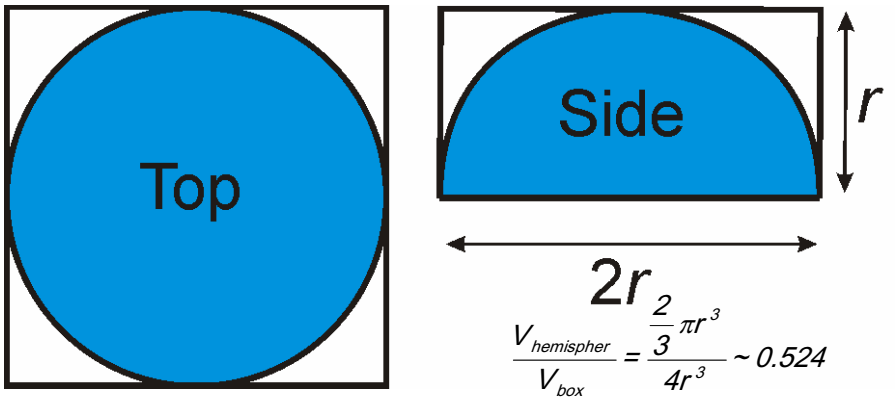

Figure 4.15 The cluster's volume correction. Top and side views of the cluster are shown.

A. Awasthi et al.[13, 14] studied the dependence of the stickiness on the cluster's initial velocity (v_o) for different adhesion coefficients (C) using molecular dynamics simulations (MD). It is interesting to compare the results of the MD with the dependence of V_c on Ar flow rate (cluster velocity). It should be noted however that comparison between the simulations and the experimental results is difficult since comparison of the cluster velocity to that of the model is tricky;[14] C for Bi clusters is unknown; and the interaction of the cluster atoms used in the simulation (Lennard-Jones potential)[13, 14] is approximation for the real one. The dependence of the stickiness on v_o for different C is shown in Figure 4.16. The velocity in the figure is rescaled for clusters with a diameter of 30nm.[14] For C=0.3 and 0.4, the figure shows that at v_o>9m/sec, the stickiness increases as v_o increases. The stickiness then decreases with v_o for v_o>25m/sec. Figure 4.17 shows the dependence of V_c on the inert gas Ar flow rate at 373K where the variation in V_c is arguably within the uncertainties. Similar variations are observed for other substrate temperatures (see Figure 4.14). The tentative conclusion is therefore that Figures 4.14 and 4.17 provide some experimental evidence for the re-entrant behaviour presented by Awasthi et. al.

4.4. Wire width versus cluster bouncing model

This section contains four subsections. An introduction to the bouncing off V-groove walls is presented first. The dependence of the wire width on the source inlet Ar flow rate and the V-groove width is discussed next. The results of the dependence of the bouncing angle on the source temperature, substrate temperature, and using mixtures of He and Ar inert gases in the source are then illustrated. The last subsection provides a discussion of the results.

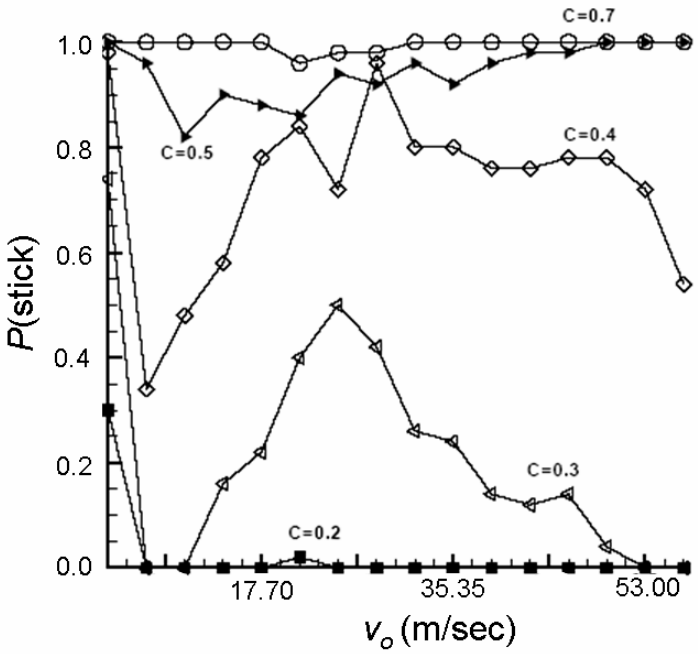

Figure 4.16 The dependence of the stickiness on the cluster's incident velocity for different C-values, after Reference [14].

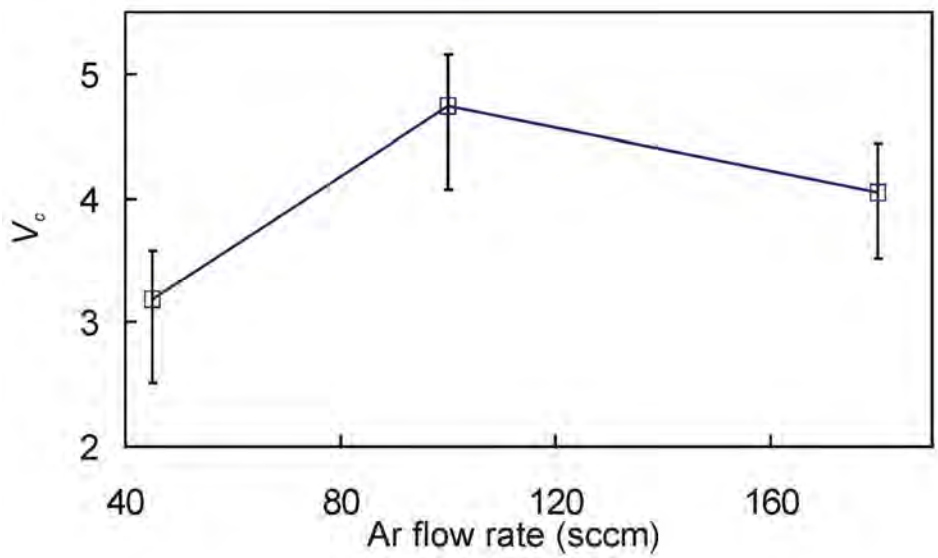

Figure 4.17 The dependence of V_c on the source inlet Ar flow rate for the 5nm samples at a substrate temperature of 373K.

4.4.1. Introduction

Studying the dependence of the wire shape and width on the source conditions can be used to determine the wire formation mechanism(s). Figure 4.18 shows FE-SEM images of two Bi cluster wires with nominal deposited thicknesses of ~2.4 and 7.2nm. Both wires were deposited using a constant source inlet Ar flow rate and a constant V-groove width (100sccm and 5μm, respectively). If the wire width measurement includes only clusters which are connected to the wire, this produces a minimum wire width, which means that the wire in Figure 4.18(a) is calculated to be narrower than the wire in Figure 4.18(b). However, if most of the clusters inside the V-groove are included in the wire width measurements, similar wire widths for both wires (the parallel lines in the figures) are produced.

Cluster wires can be formed inside V-grooves due to different mechanisms, such as either cluster sliding or bouncing off V-groove walls. Partridge et. al. studied the formation mechanisms of Bi cluster wires produced using the high vacuum (HV) cluster deposition system.[7] Partridge assumed that Bi cluster wires are formed due to cluster sliding. This assumption is revisited for the present Bi cluster wires.

Figure 4.19 shows schematic diagrams of the cross sections of wires produced by cluster sliding and single bouncing. Sliding produces wires with clusters packed next to each other, and cluster stacking is not allowed. The main feature of wires produced by the bouncing mechanism is cluster stacking. If 'sticky' clusters bounce off a V-groove wall, these clusters are expected to perform one bounce and stick to the second wall. This produces a V-shaped wire. The width of this wire is fixed (Figure 4.18) and it is determined by the bouncing angle, i.e. for a fixed bouncing angle, the maximum wire width is determined by clusters bounce off a point next to the V-groove edge

Figure 4.20(a) shows a typical FE-SEM image of Bi cluster wire in a V-groove deposited using a source inlet Ar flow rate of 100sccm, 5nm nominal deposited material, and an IGA source at ~290K. The image shows that the clusters forming the wire are stacked on top of each other. Figure 4.20(b) shows a cross sectional FE-SEM image of a different wire. The image shows that the wire has a V-shape cross section. Therefore, these wires are likely to be formed due to cluster bouncing. It should be noted that clusters which land on top of an existing cluster and stick directly, a 'soft landing', will also contribute to the wire. Their percentage contribution to the wire can be approximated by the ratio of the average wire width to the V-groove width. This ratio is around 15% for the wire in Figure 4.20(a).

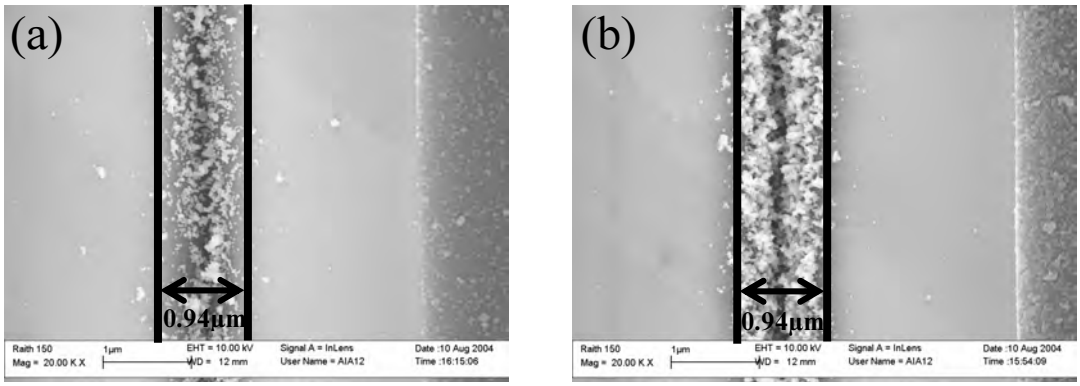

Figure 4.18 Bi cluster wires deposited on ~5µm V-grooves with nominal deposited thicknesses of ~2.4nm (a) and 7.2(b). The solid lines show the estimated wire width.

Figure 4.19 Cluster wire formation processes.

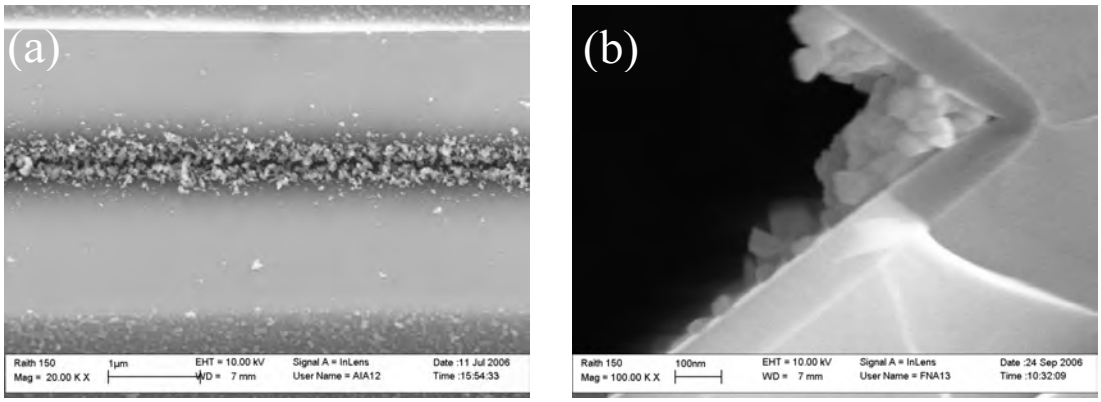

Figure 4.20 (a)FE-SEM image of Bi cluster wire formed using a source inlet Ar flow rate of 100sccm. (b) Cross sectional FE-SEM image of a different wire prepared using Ar flow rate of 45sccm.

4.4.2. Wire width versus Ar flow rate

In this study, Bi clusters were deposited on two non-contacted passivated V-groove samples with V-groove widths ~2 and ~5µm using source inlet Ar flow rates between 80 and 260sccm. Using the inert gas aggregation source, and source inlet Ar flow-rates below 45sccm, the deposition rates attainable were too low to allow clusters to be collected. A fixed deposition rate of 0.4Å/sec (measured using the FTM) and a fixed deposition time of 4min were used. The deposition was done on both samples in the same run. The two samples were fixed next to each other, where the same beam spots covered both samples. Five beam spots were deposited on the pair of samples with Ar flow rates of 80, 100, 150, 200, and 260sccm, as shown schematically in

Figure 4.21. The samples were fixed on the FE-SEM stage in the same arrangement as they were in the deposition chamber. FE-SEM images were taken at five points on each beam spot close to the sample edge. The separation between each two points was 2mm. The positions where the FE-SEM images were taken are shown by the small red points in Figure 4.21. Five wires were imaged on the first point of the 5µm sample, then another five on the opposite point on the 2µm sample, shifting 2mm to the second point, then moving to the opposite point on the 5µm sample and so on. FE-SEM images were taken also for the plateaus next to the same wires. This measurement procedure eliminated any possibility of different amounts of clusters being deposited. CorelDraw software was used to find the wire width at three points on each wire on each FE-SEM image. The average wire width for each Ar flow rate and V-groove width was found by averaging the three measurements of the five images in all of the five points (i.e. 3x5x5=75 measurements for each sample at a certain Ar flow rate and V-groove width).

Figure 4.22 shows example FE-SEM images for Bi nanocluster wires deposited with source inlet Ar flow rates of 80 and 260sccm for both samples (2 and 5µm V-grooves). The amount of the deposited material is fixed at 96nm for these samples. Clusters have assembled at the apex of the V-grooves, whilst the V-groove walls on each sample support relatively few clusters. Despite the different flow rates, wires in V-grooves with the same widths have similar widths and density of the packed clusters.

Figure 4.23 shows the dependence of the wire width on the source inlet Ar flow rate for V-grooves of widths 5µm and 2µm. The wires formed in 5µm wide V-grooves are clearly wider than those formed in 2µm wide V-grooves. In both the 5µm and 2µm wide V-grooves, the average width of the cluster assembled wires remained approximately constant (the dashed lines in the figure) over the full range of source inlet Ar flow rates. The constant wire width is a result of cluster bouncing with a fixed angle, as discussed below.

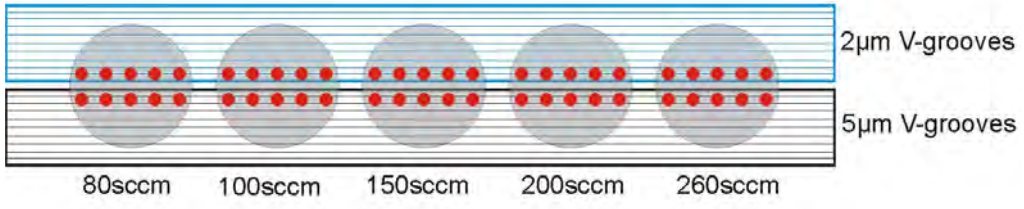

Figure 4.21 Schematic diagram of the samples' arrangement. The blue and black samples are the 5 and 2µm V-groove samples. The large circles are the beam spots, while the small circles are the positions where the FE-SEM images were taken.

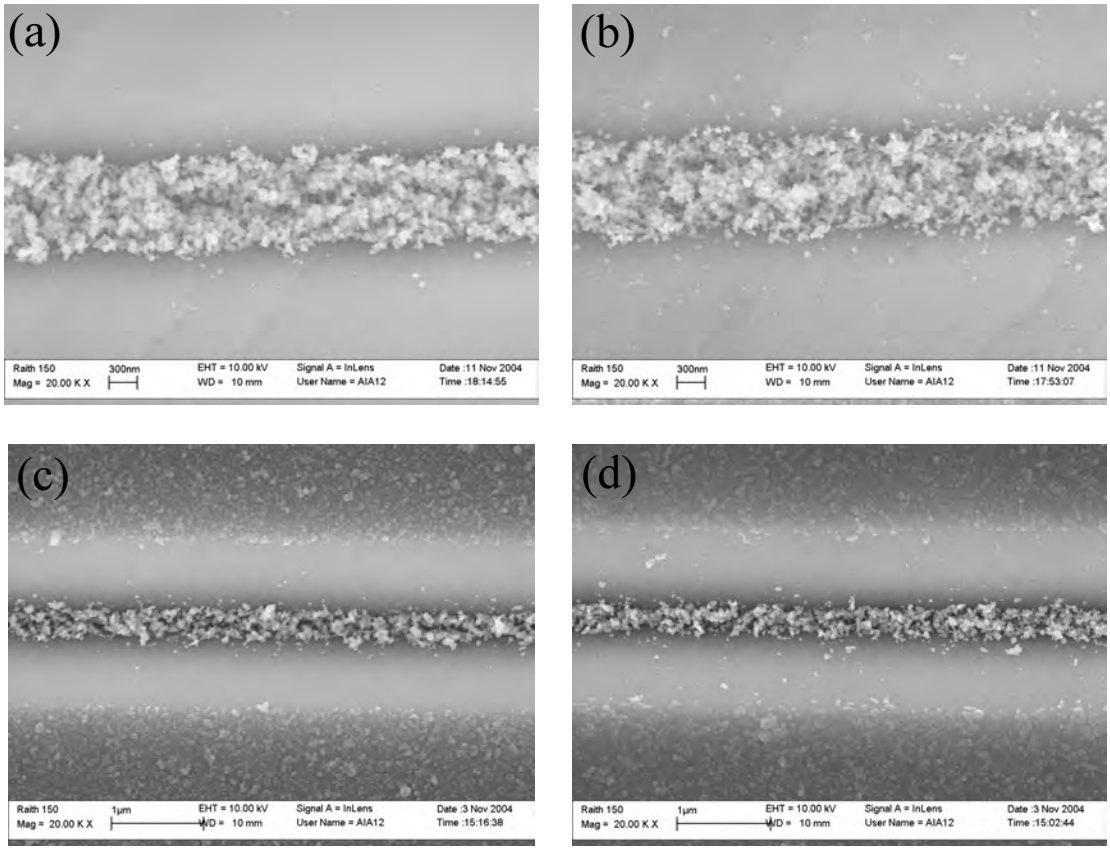

Figure 4.22 FE-SEM images of Bi nanocluster wires deposited with a mean thickness of 96nm (a) on 5μm V-groove with source inlet Ar flow rate of 80sccm. (b) 5μm V-groove with source inlet Ar flow rate of 260sccm. (c) 2μm V-groove with source inlet Ar flow rate of 80sccm. (d) 2μm V-groove with source inlet Ar flow rate of 260sccm.

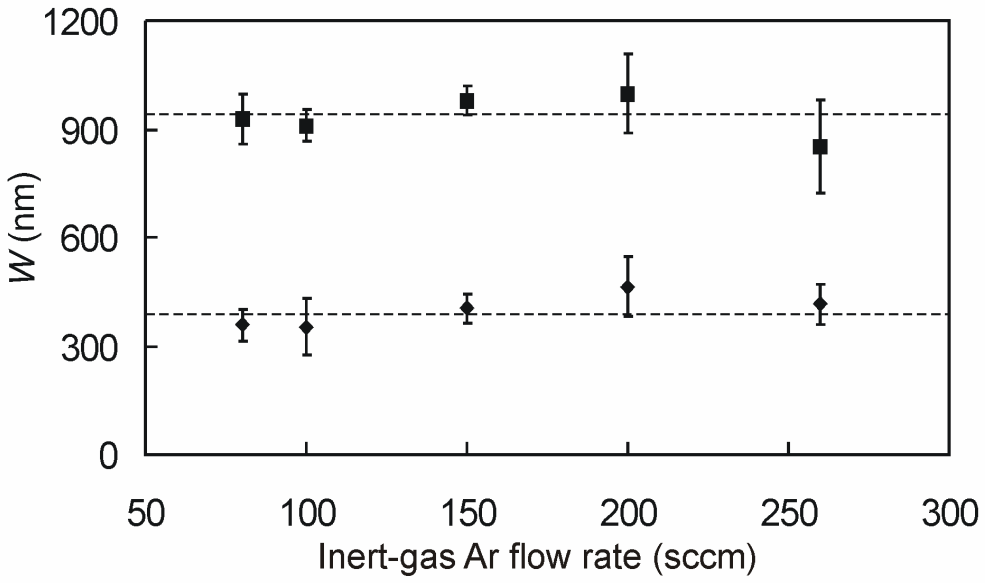

Figure 4.23 The dependence of the average wire width (W) on the source inlet Ar flow rate for wires deposited on ~2μm (diamonds) and ~5μm (squares) V-grooves.

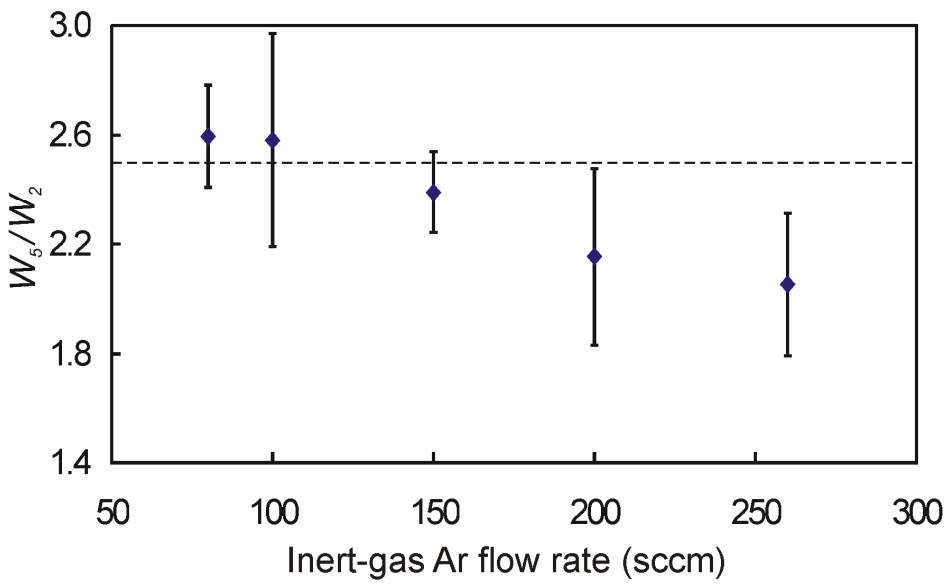

Figure 4.24 The dependence of the ratio of the widths of cluster-assembled wires fabricated in V-grooves of widths ~5μm (W_5) and ~2μm (W_2) on the source inlet Ar flow rate. The dashed line shows the ratio of the V-groove widths

Figure 4.24 shows the dependence of the ratio of the wire widths for 5μm and 2μm wide V-grooves on the source inlet Ar flow-rate. A weak trend can be seen in the ratio. The weak trend to a smaller ratio for larger flow rates is not significant. The ratio of widths strongly reflects the ratio of the V-groove widths (the dashed line in the figure). While this might at first sight seem an obvious result, it implies that the number of Bi clusters that accumulate in a V-groove is not dependent on the number of clusters already in that V-groove (since the 5μm V-grooves provide larger cluster collection area and contain more clusters than the 2μm V-grooves). This result allows an important conclusion to be drawn. Very few clusters are lost from the V-grooves, i.e. there are very few clusters that bounce out of the V-grooves.

4.4.3. Wire width versus bouncing angle

All cluster wires shown prior to this section were fabricated using an IGA source at room temperature, i.e. an IGA source which was cooled using water at room temperature. However, LN was also used to cool down the IGA source in this study. Figure 4.25 shows FE-SEM images of Bi cluster wires fabricated using sources at ~290 and ~77K. Both wires were fabricated using a source inlet Ar flow rate of 100sccm and a mean thickness of 5nm. The two V-grooves are similar in their widths. The two insets in Figure 4.25 are magnifications of sections of the wires at the same scale. The figure and the insets show that the wire width (between the two parallel lines in the insets) increases as the source temperature decreases from 290 to ~77K. This means that the cluster bouncing angle increases when cooling the source down to ~77K.

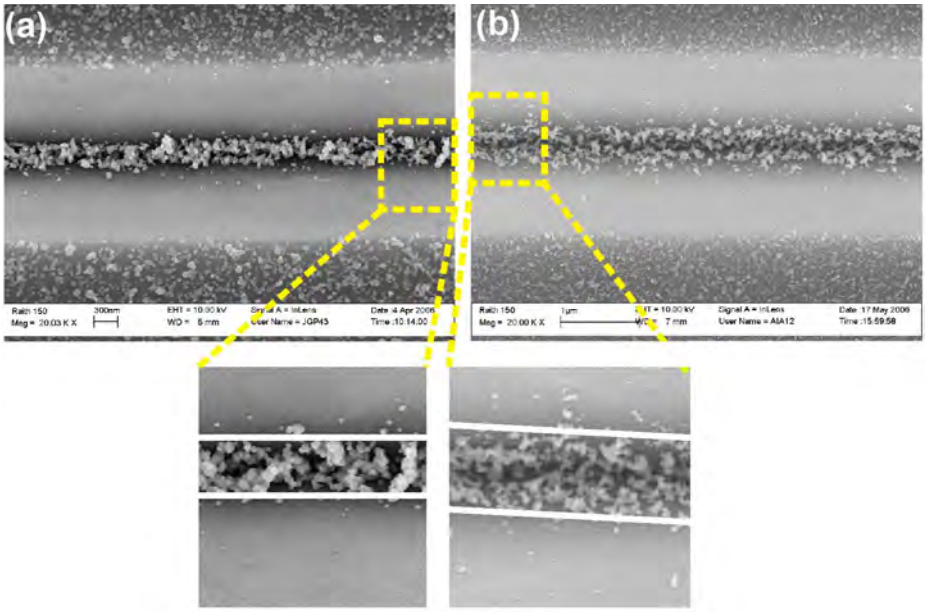

Figure 4.25 FE-SEM images of Bi cluster wires fabricated using an IGA source at ~290K (a), ~77K (b).

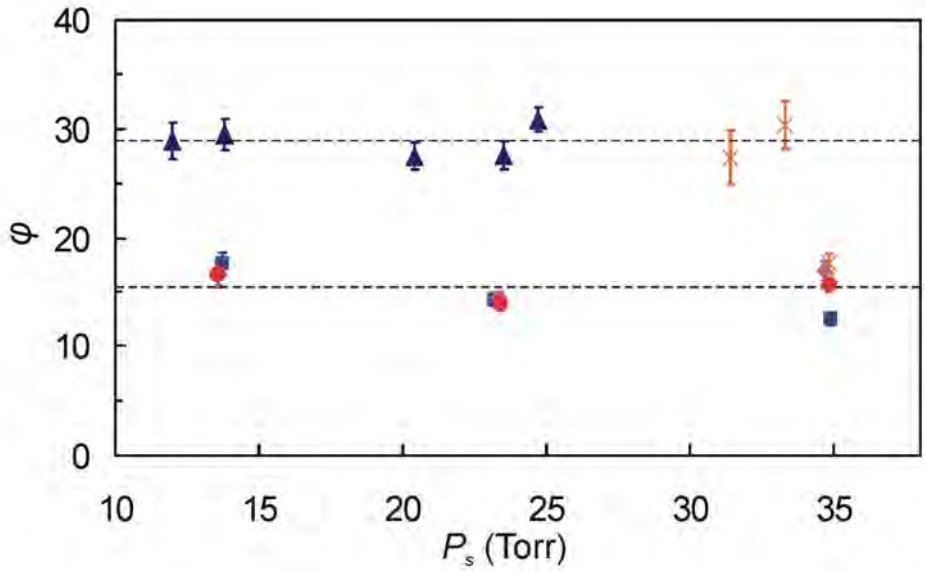

Figure 4.26 The dependence of the cluster bouncing angle on the source pressure. The triangles are data points for wires deposited using a source at ~77K on substrates at ~290K. The squares, diamonds, and circles are data points for wires deposited using a source at ~290K with substrate temperatures of 290, 373, and 473K respectively. The stars are the data points for wires deposited using a source at ~290K and mixtures of He and Ar inert-gases on substrates at ~290K.

To study the dependence of the cluster bouncing angle on the source temperature, Bi cluster wires were fabricated using source inlet Ar flow rates between 45 and 210sccm, and an IGA source at ~77 and ~290K. The cluster bouncing angles were calculated as described in Section 2.3. The dependence of the cluster bouncing angle on the source pressure is shown in Figure 4.26. The triangles and squares in the figure are data points for samples produced using sources at ~77 and ~290K respectively, along with data points for samples produced using an IGA source at ~290K at

different substrate temperatures (diamonds and circles), and mixtures of He and Ar (stars) as discussed below. The figure shows that at each source temperature, the bouncing angle is independent of the source pressure in the range between 12 and 35Torr. However, changing the source temperature from ~290 to ~77K increases the bouncing angle from ~15 to ~29º (when using Ar inert gas).

Although the samples shown in Figure 4.22 were not designed to study the bouncing angle, an estimation of the bouncing angle for those samples was made to confirm the results in Figure 4.26. These samples were deposited on V-grooves of different widths. The substrate and the source were at ~290K during the deposition. The samples were deposited using source pressures of either 20.6 or 47.8Torr. The bouncing angles are ~13.4 and ~15° for the wires in Figures 4.22(a) and 4.22(c) (deposited using a source inlet Ar flow rate of 80sccm and a source pressure of 20.6Torr), and ~14 and ~13.6° for the wires in Figures 4.22(b) and 4.22(d) (deposited using a source inlet Ar flow rate of 260sccm and a source pressure of 47.8Torr). These results are consistent with the results in Figure 4.26.

In order to study the dependence of the bouncing angle on the substrate temperature, Bi clusters were deposited on V-grooves at temperatures of 290, 373, and 473K. The IGA source temperature was ~290K for all samples. Three beam spots were deposited at each temperature using source inlet Ar flow rates of 45, 100, and 180sccm. The dependence of the cluster bouncing angle on the source pressure for the different substrate temperatures is shown in Figure 4.26. The squares, diamonds, and circles are data points for samples produced at substrate temperatures of 290, 373, and 473K respectively. The figure shows that changing the substrate temperature does not change the bouncing angle. It also shows that the bouncing angle is independent of the source pressure in the range between 13 and 35Torr (source inlet Ar flow rate between 45 and 180sccm) for the above substrate temperatures.

The effect of using mixtures of He and Ar inert gases with a total flow rate of 180sccm to fabricate cluster wires on the cluster bouncing angle was also investigated. The ratios of He to Ar flow rates (He/Ar) were 20, 40, and 60%. Although the total inert gas flow rate was fixed at 180sccm, increasing the He/Ar ratio decreased the source pressure since He has a lower atomic weight than Ar. The stars in Figure 4.26 show the dependence of the bouncing angle on the source pressure when mixtures of He and Ar are used. The bouncing angles are ~18, 30, and 27º for the 20%, 40%, and 60% He/Ar ratios respectively. The bouncing angle of the sample deposited using 20% He/Ar is similar to the bouncing angles of the other samples deposited using a source at ~290K and different Ar flow rates, while the bouncing angles of the samples deposited using 40% and 60% ratios are similar to the bouncing angles of the samples deposited using an IGA source at ~77K and different Ar flow rates.

A crude estimation of the cluster velocity has been made assuming that the cluster velocity (v_0) is similar to the inert gas velocity (v_g) when leaving the source. The inert gas flow rate when leaving the source (F_s) was assumed to follow $F_s=F_oP_oT_s/(T_oP_s)$, where P and T are pressure and temperature, and the subscripts o and s refer to the inert gas which enters and leaves the source respectively.[15, 16] It should be noted that this equation is independent of the gas type. The dependence of the cluster velocity on the source pressure, and the bouncing angle on the cluster velocity (for the data

presented in Figure 4.26) are shown in Figures 4.27(a) and 4.27(b). Figure 4.27(a) shows that cluster velocities between 37 and 58m/sec were achieved for a source pressure between 14 and 35Torr when using a source at ~290K, while cluster velocities between 17 and 25m/sec were achieved for a source pressure between 12 and 25Torr when using a source at ~77K. Figure 4.27(b) shows that constant bouncing angles were obtained for each source temperature when using Ar inert gas regardless of the cluster velocity; whereas two distinct angles were obtained when using mixtures of He and Ar (~15º for the 20% He/Ar, and ~29º for both the 40% and 60% He/Ar).

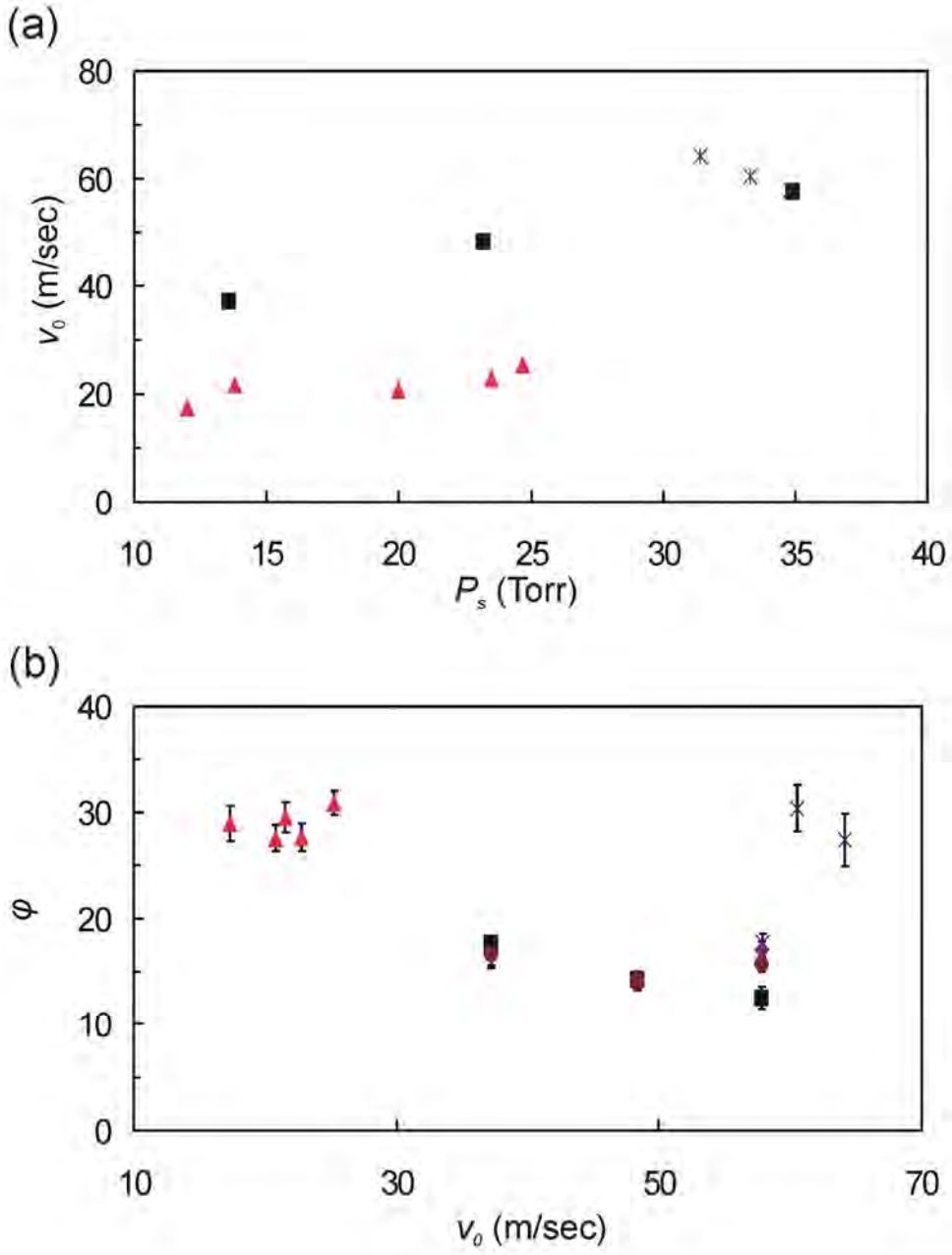

Figure 4.27 The dependence of the cluster velocity on the source pressure (a) and the cluster bouncing angle on the cluster velocity (b). The symbols used for the data points are similar to those in Figure 4.26.

In summary, the data presented in Figure 4.26 shows that the bouncing angle exhibits two distinct values: ~15 and 29º (the dashed lines in the figure). The 15º angle has been achieved for clusters produced using an IGA source at ~290K regardless of the substrate temperature (in the range of 290-473K) and the source inlet Ar flow rate (in the range of 45-180scc). It has also been achieved for clusters produced using a 20% of He/Ar when using an IGA source at ~290K. The 29º angle has been achieved for clusters produced using an IGA source at ~77K regardless of the source inlet Ar flow rate in the range of 70-210sccm, and for clusters produced using mixtures of He and Ar with 40% and 60% He/Ar ratios (using an IGA source at ~290K).

4.4.4. Discussion

The appearance of a fixed wire width for a fixed V-groove width and a source inlet Ar flow rate between 80 and 260sccm (source pressure between 20.6 and 47.8Torr) can be understood in terms of a fixed bouncing angle. Although the samples in Section 4.4.2 contained more clusters than the samples used to study the bouncing angle in Section 4.4.3, bouncing angles around 15º were also found for the samples in Section 4.4.2.

Figure 4.28 shows a schematic diagram of a cluster bouncing off a V-groove wall. The y-direction is assumed parallel to the right-hand-side wall of the V-groove. The angle between the incident cluster path and the V-groove wall is 35º. This angle is described in the following as 'incident cluster angle'. Figure 4.26 shows that the bouncing angle (φ) is expected to be smaller than the incident angle due to stickiness to the V-groove wall. The following discussion focuses on the effect of the cluster stickiness on φ.

The coefficient of restitution (e) is defined as the ratio between the cluster velocities after and before the collision (v_f / v_o). Thus, it can be used to estimate the loss in cluster kinetic energy during a collision. e exhibits a value of 1 for an elastic collision, and its value is between 0 and 1 for inelastic and plastic collisions. Bi clusters are sticky clusters and their collision with SiO_2/Si substrates is not an elastic collision. The remaining kinetic energy, after the first bounce, determines whether the cluster should undergo another bounce off the second V-groove wall or stick. If a cluster performs a second bounce, one of the following scenarios may occur. The first scenario is that the cluster bounces toward the apex of the V-groove. This scenario may occur for φ<20º, and it is likely to produce round cross sectional wires. The second scenario is that the cluster bounces out of the V-groove if φ>20º. This scenario means that the wire is likely to be formed of the clusters which perform soft landing on top of existing clusters or defects. This wire is also likely to have a round cross section, and its width is likely to increase with increasing the amount of deposited material. FE-SEM images of the Bi cluster wires show that these wires have a V-shaped cross section, and their width is constant (for constant source conditions) regardless of the amount of deposited material. In conclusion, it appears that each Bi cluster undergoes one bounce and then sticks on impact with the opposite sidewall.

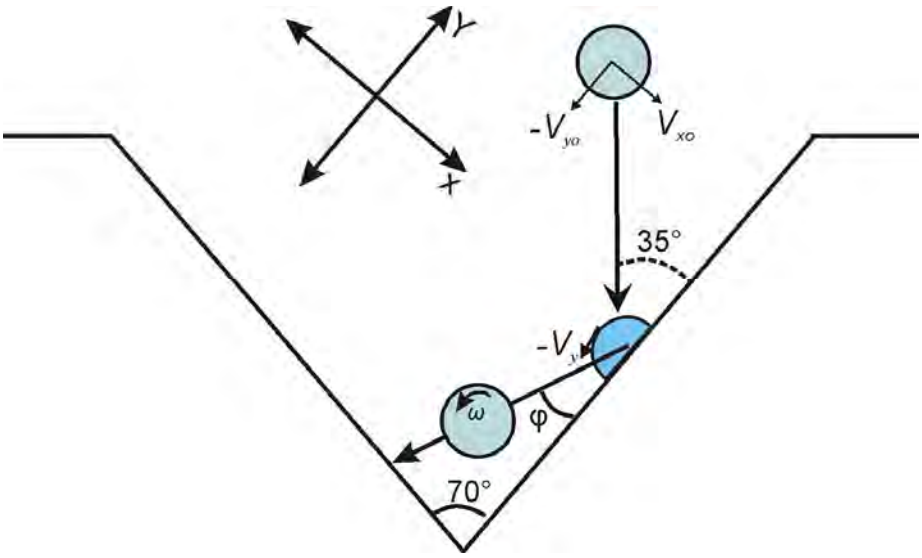

Figure 4.28 Schematic diagram of the cluster bouncing off a V-groove wall.

The two components of a cluster velocity before collision are $v_{xo}=v_o sin35$ and $v_{yo}=-v_o cos35$ (Figure 4.28). Once a cluster collides with the V-groove wall, the x–component of the velocity will produce cluster deformation, while the y–component of the velocity will push the cluster toward the V-groove apex. However, the 'attempt' of the bottom part of the cluster to slide will be inhibited by friction between the cluster and the V-groove wall, while the top part of the cluster is free to move. This creates a torque causing the cluster to spin, and would necessarily make φ smaller than the incident cluster angle for a plastic collision.

The decrease in the bouncing angle and the spinning due to the stickiness and friction between an object and a substrate was reported previously for macroscopic balls with $0<e<1$.[17] The balls were observed to deform at the collision. The amount of the deformation was dependent on e. As the ball deformation increased, φ decreased and the spinning angular velocity (ω) increased.

In the following, the appearance of two distinct bouncing angles in Figure 4.26 (i.e. 15º and 29º) is discussed. For simplicity, the labels shown in Table 4.2 are used in the following discussion to describe the source conditions.

Table 4.2 Labelling the source conditions.

Label	Inert-gas type	Source temperature
Ar-W	Ar	~290K (cooled down using water at room temperature)
Ar-LN	Ar	~77K (cooled down using LN)
Ar-He-W	Ar and He	~290K (cooled down using water at room temperature)

The clusters produced using Ar-LN are likely to be less sticky clusters since they exhibit larger φ. Those clusters have smaller average size and velocity. The former has been discussed in Section 4.1, where the average cluster size decreased from ~33 to ~22nm (Figures 4.2 and 4.6). Cooling the source to ~77K may also have other effects on the clusters such as producing more solid clusters.

The decrease in the cluster size is expected to increase the cluster stickiness to the substrate,[14] thus it is unlikely to be the reason behind increasing the bouncing angle. The decrease in the cluster velocity when using Ar-LN instead of Ar-W is not believed to be the reason behind the increase in the bouncing angle. The velocity estimation in Figure 4.27(a) shows that a decrease in the velocity of ~21m/sec occurred when the source pressure decreased from 35 to 14Torr using Ar-W source conditions. This change in the velocity did not change the cluster bouncing angle. Hence, a decrease in the velocity of ~16m/sec between the Ar-W and the Ar-LN source conditions at ~14Torr (as shown in Figure 4.27) is not expected to increase the bouncing angle. Therefore, the decrease in the cluster stickiness (for Ar-LN) may be related to more solid clusters.

Using mixtures of He and Ar inert gases in the source had a minor effect on the average cluster size as discussed in Section 4.1. Therefore, the increase in the bouncing angle for clusters produced using Ar-He-W source conditions with He/Ar of 40% and 60% is not a result of a change in the cluster size. In fact, the reason for the increase of the bouncing angle for the 40% and 60% He/Ar is not understood. However, increasing the bouncing angle may be related to the cluster velocity. The cluster velocity in Figure 4.27 for the Ar-He-W source conditions is thought to be underestimated. C. Huang et. al. found by simulation that replacing Ar inert gas by He in a source increases the gas velocity, and thus, the cluster velocity.[18] Therefore, increasing the cluster velocity may affect the cluster stickiness and bouncing angle (as discussed in Section 4.3 and References [13, 14]). Figure 4.16 shows that the stickiness decreases as the velocity increases beyond ~25m/sec for C of 0.3 and 0.4 indicating that the stickiness may be small for clusters with higher velocities. An increase in the cluster velocity when using He/Ar of 40% and 60% may decrease the cluster stickiness and increase the bouncing angle.

Other factors such as different crystal structures of clusters produced using different source conditions may affect the cluster bouncing angle. A. Wurl studied the crystallinity of Bi clusters produced using Ar and He inert gases in the HV system.[19] Wurl reported a rhombohedral structure for clusters produced using Ar inert gas and an amorphous structure for clusters produced using large ratios of He/Ar. A change in the cluster crystallinity may affect the cluster bouncing angle. However, these two factors should be studied in more detail in the future.

4.5. Summary

Bi cluster wires were fabricated using non-contacted V-groove templates in SiO_2/Si substrates. The cluster wires were found to assemble in the apex of the V-grooves, and the V-groove's walls had low cluster coverage.

The effect of changing the source conditions on the cluster size distribution was studied using clusters on the plateaus next to the V-grooves. The average cluster size was found to be ~33nm regardless of the source inlet Ar flow rate in the range between 80 and 260sccm when using an inert gas aggregation source at ~290K.

Cooling the source walls down to ~77K was found to decrease the average cluster size to ~22nm when using a source inlet Ar flow rate between 70 and 210sccm. However, using mixtures of Ar and He inert gases in the source with a fixed total flow of 180sccm, with maintaining the source temperature at ~290K, did not have a noticeable effect on the average cluster size, i.e. ~33nm.

The morphological study of cluster wires found that the cluster bouncing is the main process in the wire formation. The clusters were found to bounce with a fixed angle when using fixed source conditions. The bouncing angle (the angle between the V-groove wall and the related cluster path) was found to be less than the incident angle (the angle between the V-groove wall and the incident cluster path) due to the cluster stickiness during the impact. The bouncing angle was found to be dependent on the source conditions, where it increased when cooling the source down to ~77K (instead of ~290K) and using mixtures of He and Ar inert gases (instead of Ar only).

The study found that the wire width reflects the V-groove width, i.e. fixed wire width for a fixed V-groove width when using the same source conditions. This is due to the cluster bouncing with a fixed angle. The fixed bouncing angle sets a limit on the minimum wire width which can be formed in a V-groove using Bi clusters. To facilitate forming single cluster wide wires, the clusters are required to slide to the V-groove apex.[6, 7]

The corrected cluster coverage on the plateaus next to the V-grooves was found to increase more than linearly when increasing the nominal deposited thickness. This is because the incident clusters bounce off the clean surface more than they bounce off the existing clusters. For a fixed amount of the nominal deposited material, the corrected cluster coverage was found to decrease as the substrate temperature increased up to 473K. This was due to the increase in the cluster height as the substrate temperature increased (up to 473K). Therefore, increasing the substrate temperature increased the ratio of the cluster height to cluster diameter.

References

1 R. Reichel, J. G. Partridge, A. D. F. Dunbar, S. A. Brown, O. Caughley, and A. Ayesh, Journal of Nanoparticle Research **8**, 405 (2006).
2 A. Yokozeki and G. D. Stein, J. Appl. Phys. **49**, 2224 (1978).
3 B. Hall, M. Flueli, R. Monot, and J. Borel, Phys. Rev. B **43**, 3906 (1991).
4 H. Haberland, *Clusters of atoms and molecules* (Springer-Verlag, Heidelberg, 1994).
5 M. Schulze, S. Gourley, S. A. Brown, A. Dunbar, J. Partridge, and R. J. Blaikie, Eur. Phys. J. D **24**, 291 (2003).
6 J. G. Partridge, S. A. Brown, C. Siegert, A. D. F. Dunbar, R. Nielson, M. Kaufmann, and R. J. Blaikie, Microelectron. Eng. **73**, 583 (2004).
7 J. G. Partridge, S. Scott, A. D. F. Dunbar, M. Schulze, S. A. Brown, A. Wurl, and R. J. Blaikie, IEEE Trans. Nanotech. **61** (2004).
8 P. Jensen, Rev. Mod. Phys. **71**, 1695 (1999).
9 J. Davies and E. Rideal, *Interfacial phenomena* (Academic press, New York, 1961).
10 J. G. Partridge, S. A. Brown, A. D. F. Dunbar, R. Reichel, M. Kaufmann, C. Siegert, S. Scott, and R. J. Blaikie, Nanotechnology **15**, 1382 (2004).
11 P. Paturi, H. Huhtinen, R. Laiho, and J. Raittila, IEEE Transactions on Applied Superconductivity **11**, 3449 (2001).
12 I. Shyjumon, M. Gopinadhan, O. Ivanova, M. Quaas, H. Wulff, C. A. Helm, and R. Hippler, The European Physical Journal D - Atomic, Molecular, Optical and Plasma Physics **37**, 409 (2006).
13 A. Awasthi, S. C. Hendy, P. Zoontjens, and S. A. Brown, Phys. Rev. Lett. **97**, 186103 (2006).
14 A. Awasthi, S. C. Hendy, P. Zoontjens, S. A. Brown, and F. Natali, To be published.
15 A. Lassesson (private communication).
16 J. H. Moore, C. C. Davis, and M. A. Coplan, *Building scientific apparatus* (Addison-Wesley publishing company Inc., 1989).
17 R. Cross, Am. J. Phys. **73**, 914 (2005).
18 C. Huang, W. T. Nichols, D. T. O'Brien, M. F. Becker, D. Kovar, and J. W. Keto, J. Appl. Phys. **101**, 064902 (2007).
19 A. Wurl, *PhD thesis, Electron diffraction studies of unsupported bismuth clusters* (Physics and Astronomy Department, University of Canterbury, Christchurch, 2003).

5. Results: Contacted V-grooves

This chapter discusses the electrical measurements and the morphology of the cluster wires formed using contacted V-grooves. The first section illustrates the morphology of the wires. The *I(V)* measurements are discussed in the second section. The third section explores the effect on the source-drain current of applying a voltage to the sample's gate. The fourth section illustrates the noise in the electrical measurements. Hall effect measurements of planar samples are presented in the fifth section. Section six discusses the temperature dependence of the cluster wire resistance. The effects of annealing the cluster wires are discussed in the seventh section. The eighth section examines the effect of the wire length on the amount of material required to form an electrically conducting wire. The last section provides conclusions.

All samples used for the electrical measurements were tested for current leakage between the source and drain (SD), source and gate, and drain and gate in the voltage range between −10 and 10V (or −5 and 5V) before clusters were deposited onto them (as explained in Section 2.2). Only samples which showed resistances higher than 10GΩ between the source and drain, source and gate, and drain and gate were used for the gate measurements. An example of the leakage measurements was given in Figure 2.18 in Section 2.2. Furthermore, none of the samples showed any change in the source-drain current (I_{SD}) when applying a voltage to the gate before cluster deposition on the samples. The source-drain voltage (V_{SD}) was also constant during all gate measurements and did not depend on the gate voltage (as shown below). Therefore, there was no current leakage to the samples' gates.

Current leakage between the source and the gate, and the drain and the gate can also occur after cluster deposition if a continuous network of clusters is formed between the respective electrode pads. This is unlikely to occur because of the photoresist passivation layer on the samples' surfaces (as explained in Section 2.2). However, all samples were re-tested for current leakage by taking *I(V)* measurements between their source and gate, and drain and gate. No current leakage to the gate was observed for any of the presented samples.

5.1. Wire morphology

Figure 5.1 shows FE-SEM images of samples labelled S1-S7. These samples showed an effect of the gate voltage on I_{SD} (note that, as discussed in more detail below, the deposition chamber was not pumped down during the deposition of S5 so as to produce a deliberately oxidised wire). All the cluster wires shown in the figure are continuous. The gray areas in the images at either end of the wires are the Au (or Ag) contacts. The clusters are assembled at the apex of the V-grooves and the V-grooves' walls have low cluster coverage.

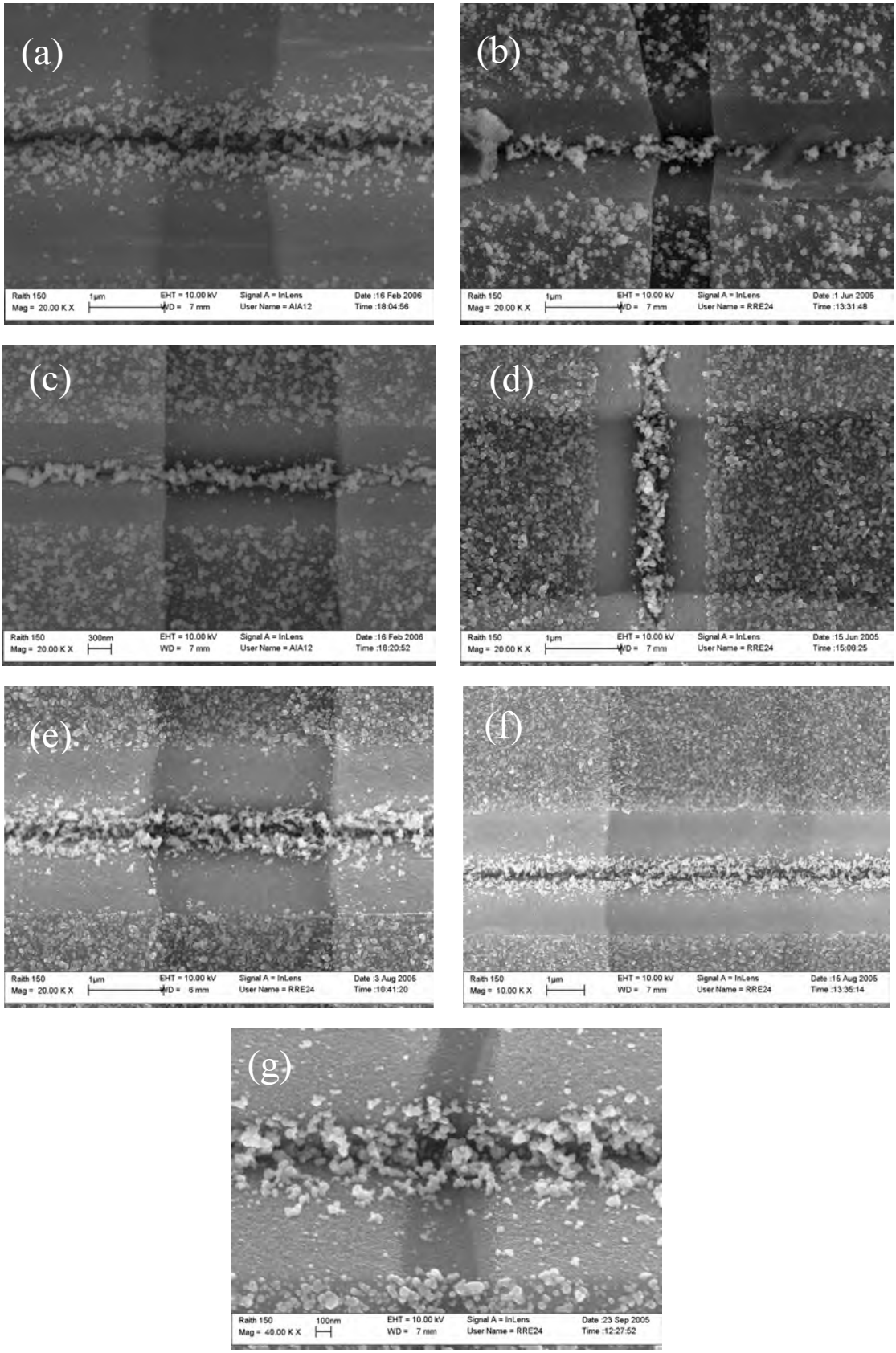

Figure 5.1 FE-SEM images of S1-S7 in (a)-(g), respectively.

Since V-grooves provide large cluster collection areas, cluster bouncing causes the formation of a continuous wire in the V-groove before the formation of a continuous network of clusters on the plateaus between the contacts. Electrical conduction occurs through a cluster film on a V-groove plateau if the cluster coverage is more than or equal to a critical cluster coverage. This critical coverage is called the percolation threshold, and its value was found to be 67.6% for Bi cluster films.[1] Hence, the cluster coverage of the plateaus of each sample was measured from FE-SEM images, as described in Section 2.3, to verify whether the electrical conduction could occur through the clusters on the plateaus. Figure 5.2 shows an FE-SEM image of the plateau of S1. The white lines in the image show the edges of the Au contacts. The image shows that the cluster coverage is less than the percolation threshold which confirms that the electrical conduction only occurs through the wires. The plateau cluster coverages for S1-S7 are shown in Table 5.1 along with the inert-gas Ar flow rates used to fabricate the samples, wire dimensions, cluster deposition rate, and mean thickness (measured using the FTM) as discussed below. The table shows that almost all samples have cluster coverages below the percolation threshold. However, the table shows that S4 has a 67% plateau coverage which means that the conduction of this sample may have occurred through the clusters on the plateaus.

Decreasing the plateau coverage below the percolation threshold requires decreasing the amount of deposited material. This can be obtained by decreasing the wire length, as can be seen in Table 5.1, and/or increasing the V-groove width. However, increasing the V-groove width increases the wire width for a given amount of deposited material, as shown in Section 4.4. A balance is required between the wire width, wire length, V-groove width, and plateau coverage when using V-grooves for device fabrication to minimize the device size.

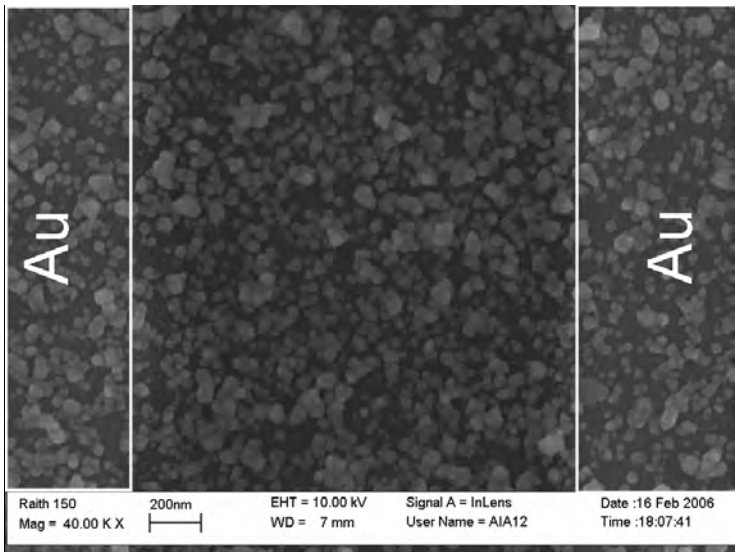

Figure 5.2 FE-SEM image of the plateau next to the V-groove of S1. The white lines show the Au contacts' edges.

Table 5.1 The wire length (L), wire width (W), V-groove width (w) (measured from FE-SEM images), inert-gas Ar flow rate, mean thickness, cluster deposition rate, and surface cluster coverage on the plateaus of S1-S7.

Sample	Ar flow rate (sccm)	*w* (μm)	Deposited material (nm)	*L* (μm)	*W* (μm)	Surface coverage (%)	Deposition rate (Å/sec)
1	160	3.67	8.7	1.30	0.80	58	0.57
2	200	1.37	12.8	0.70	0.20	43	0.62
3	160	0.95	17.7	2.23	0.24	51	0.58
4	150	1.05	15.1	2.34	0.28	67	0.62
5	200	2.20	10.0	2.34	0.43	56	0.25
6	200	3.25	13.0	16.20	0.63	59	0.25
7	200	1.68	6.2	0.33	0.33	57	0.24

Although S1-S4 were not designed to study the dependence of the mean thickness on the V-groove width and the wire length, a qualitative relation between these variables can be drawn using Table 5.1. Increasing the V-groove width decreased the mean thickness required to form a continuous wire which can be seen for S1-S4. This is due to increasing the clusters' collection area which causes the onset of conduction through the wire to occur earlier than the onset of conduction of a wire formed in a narrower V-groove. It should be noted that S5 and S7 can not be included in this comparison. This is because the deposition was stopped without an onset being observed for S5; and the substrate temperature for S7 during the deposition was ~350K which is different from the substrate temperature for the other samples, i.e. ~290K (the substrate temperature was increased in order to study the effect of increasing the substrate temperature on the onset of conduction). Although the mean thickness of S6 seems not to follow the trend, it can be explained in terms of the wire length. The wire lengths for S1-S4 are less than or equal to 2.34μm, while the length for S6 is 16.2μm. The increase in the contact separation (wire length) required more material to be deposited to form a continuous wire.

5.2. *I(V)* measurements

This section focuses on the *I(V)* measurements. The results are presented first, followed by the dependence of the conductance on the voltage across the wire (*G(V)*) and a discussion of the results. Models for explaining the steps in the conductance are also presented.

5.2.1. *I(V)* results

The *I(V)* curves of Bi cluster wires change with time. Two processes may be responsible for this change. Firstly, annealing of the wires by passing current through them, and secondly due to cluster oxidation. The two processes are discussed in Sections 5.3 and 5.7. The *I(V)* curves shown in this section were taken at times as close as possible to the times when the samples showed the gate effect.

Figure 5.3 shows the room temperature *I(V)* curves for S1-S4 and S6-S7. The measurement time after the onset of conduction is indicated on each figure (day:hours:minutes). The *I(V)* curve for S5 is not shown since it had unmeasurably

high resistance before the gate effect was observed, and it 'died' (i.e. had an open circuit resistance) before performing any *I(V)* measurement. The *I(V)* curve of S4 is linear. An almost linear *I(V)* curve can be observed for S1. The curves are non-linear for S2, S3, S6, and S7. Figure 5.3 shows that the non-linearity in the *I(V)* curves is greater for samples with higher resistances. Samples with higher resistances also tend to have more noise in the *I(V)* curves. The non-linearity is believed to be due to tunnelling conduction between the wire and the contacts.[2] A summary of the resistances (*R*) of the wires when the gate effect was seen is shown in Table 5.2 along with various other parameters discussed below. It should be noted that the cluster wire resistance is significantly higher than would be expected for a wire of similar dimensions with the bulk conductivity (see appendix A).

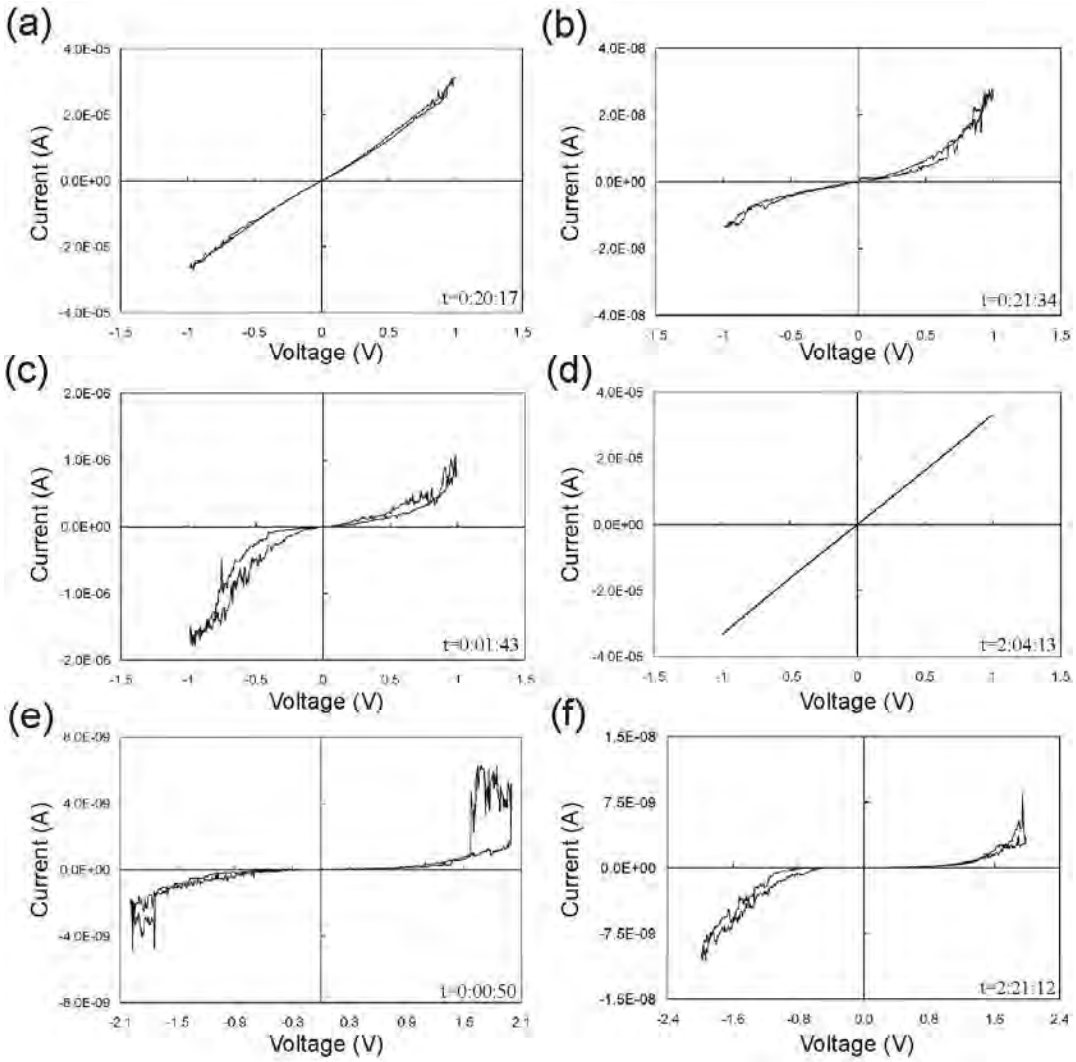

Figure 5.3 I(V) curves of S1-S4 and S6-S7 at 290K in (a)-(f) respectively. The measurement times after the onset of conduction are indicated on the figures (t=days:hours:minutes) .

Table 5.2 The electrical measurement results at 290K of S1-S7. R_{onset} is the wire's resistance directly after the onset. V_{SD} is the voltage applied across the wire when it showed the gate effect. $V_g(max)$ is the maximum applied gate voltage. I_{SD} is the SD current with $V_g=0V$. R is the wire resistance when the sample showed the gate effect with $V_g=0V$. V_t is the gate voltage value when an effect on I_{SD} started to appear/disappear. ΔI is the change in I_{SD} when the gate voltage changed from zero to $V_g(max)$ (ΔI is measured at the times shown in Figures 5.8-5.12). $(\Delta I/I_{SD})\%$ is the percentage of the increase in I_{SD} when applying $V_g(max)$ to the gate.

Sample	R_{onset} (Ω)	V_{SD} (V)	I_{SD} (A)	R (Ω)	$V_g(max)$	V_t (V)	ΔI (A)	$(\Delta I/I_{SD})\%$	Contact
1	2.1E+04	0.1	2.2E-06	4.5E+04	5	2.1/2.1	3.0E-08	1.4	Au
2	8.8E+06	0.1	1.2E-09	8.3E+07	5				Au
3	6.4E+05	0.1	2.3E-08	4.4E+06	5				Au
4	3.2E+04	0.1	2.3E-06	4.4E+04	5	1.1/1.2	2.0E-09	0.1	Au
5	>1.0E+10	5	<1.0E-10	>1.0E+10	10	2.0/1.8	6.0E-10		Au
6	7.7E+07	0.5	<1.0E-10	>1.0E+10	5	0.73/0.0	6.0E-10		Au
7	8.7E+07	0.5	1.3E-08	3.8E+07	5	0.0/1.8	6.0E-10	4.6	Ag

5.2.2. *G(V)*

To study the conduction mechanisms for the presented samples, the dependence of the conductance ($G=I_{SD}/V_{SD}$) on V_{SD} for the data in Figure 5.3 is plotted in Figure 5.4. The figure shows that *G(V)*s of S2, S3, S6, and S7 are asymmetrical, a small asymmetry appears for S1, and the characteristics are symmetrical for S4. The curves also show different slopes at different V_{SD} for each curve. Another interesting feature is the steps in the *G(V)* curves. These steps are either from low *G* to high *G* and then to low *G* again (S6 for example: a step towards high *G* occurs at ~2V and a return to low *G* at ~1.6V, and a step towards high *G* occurs at ~ −1.7V and a return to low *G* at ~ −2V), or steps toward high *G* without return (S3 for example: the step at ~ −0.4V). The *G(V)* curves of the samples are discussed below. It should be noted that infinite value of *G(V)* at V_{SD}=0 for S1 and S4 (in Figure 5.3) is due to dividing the current by a small voltage.

The dependence of the conductance on V_{SD} at 22K for S30 is shown in Figure 5.5. This sample is not presented in Figure 5.3, and it is used to investigate the conductance at a low temperature. The figure shows that the conductivity has a finite value at V_{SD} ~0V. The curve exhibits a small slope at low V_{SD}, and the slope increases as V_{SD} increases.

5.2.3. Discussion

Two types of *I(V)* curves can be distinguished in Figure 5.3: linear (S1 and S4) and non-linear (S2, S3, S6, and S7). The linear *I(V)* curve is a characteristic of the metallic behaviour of a material. The non-linear *I(V)* curve can be due to various reasons such as non-Ohmic metal-semiconductor junctions and the existence of tunnelling barriers between the wire and the contacts. The former reason is not fully consistent with the presented results since many samples had linear *I(V)*. A most likely cause for the appearance of the non-linearity in the *I(V)* curves in Figure 5.3 is the existence of tunnelling barriers in the samples.[2-5] This argument is also supported by the high resistance of the wires which exhibit non-linear *I(V)* characteristics, where the

resistance of S1 and S4 is ~$4x10^4\Omega$, while it is >$1x10^6\Omega$ for S2, S3, S6, and S7 (Table 5.2).

The tunnel barriers might be due to various sources such as a poor interface between the wire and the Au contacts, bottlenecks in the wire, and Bi-oxide layers which act as tunnelling barriers between the cluster wire and the Au contacts. The poor interface is unlikely to be the main reason behind the nonlinearity as discussed below. Bottlenecks are unlikely to produce nonlinearity in the *I(V)* curves since 4-point *I(V)* measurements taken for similar wires by R. Reichel showed linear characteristics.[2] This argument is also confirmed by the measurements presented in Section 5.7 which show linear *I(V)* characteristics for wires with bottlenecks. A Bi-oxide layer is believed to grow around Bi clusters even under a pressure as low as 10^{-7}Torr,[2, 6, 7] and it is a semiconductor.[8] Reichel found using 4-point measurements that these barriers are between the wire and contacts.[2, 7] S. Cronin et. al. found also in a different study of Bi nanowires that the nonlinear *I(V)* characteristics is due to Bi-oxide barriers between the wire and the contacts.[7]

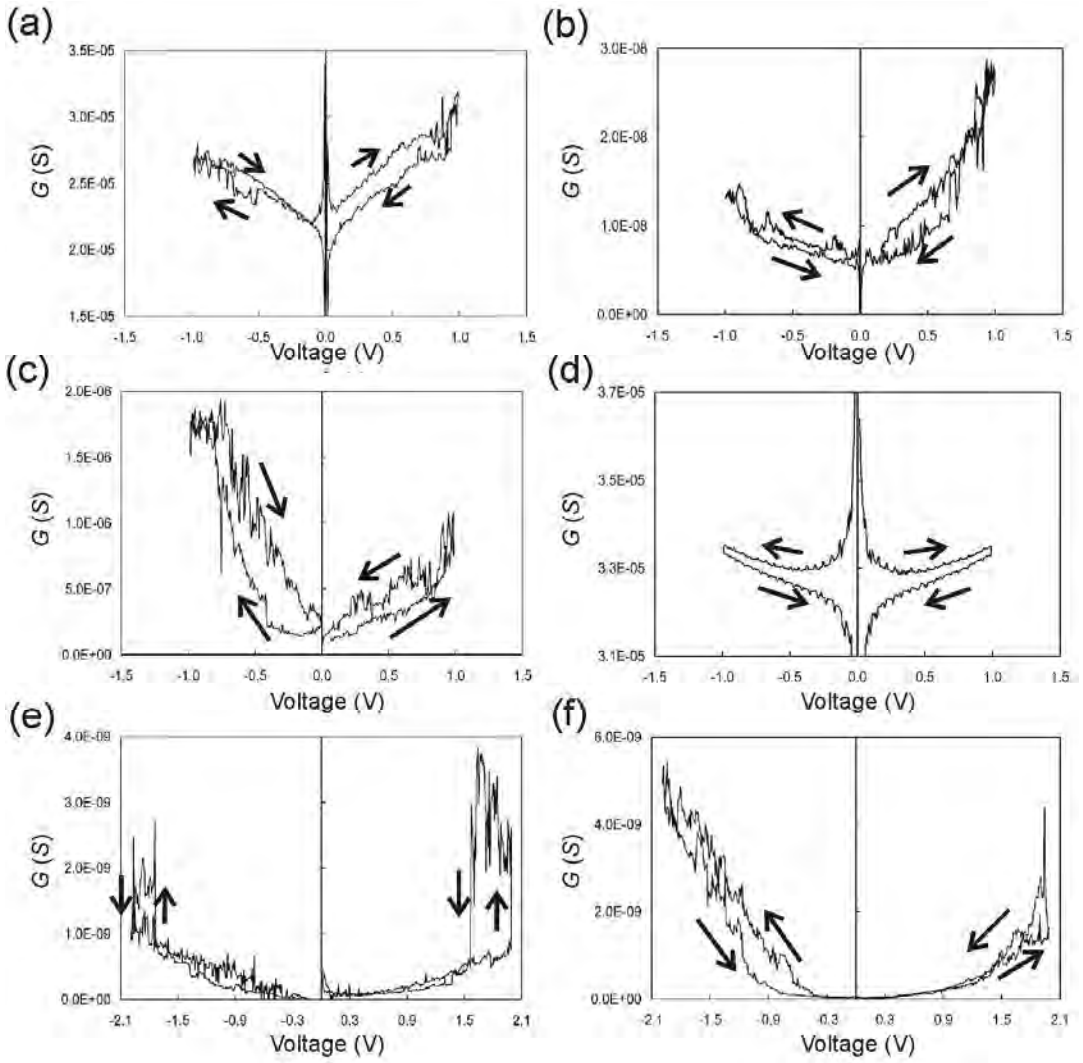

Figure 5.4 The dependence of the conductance on V_{SD} for S1-S4 and S6-S7 in (a)-(f), respectively. The arrows show the sweep direction.

The asymmetry in the *G(V)* curves means that the conduction through the wire when applying a positive V_{SD} is different from the conduction when applying a negative V_{SD}. This is presumably because barriers at each end of the wire are different in their dimensions and conductivities, which produce different tunnelling currents depending on the polarity of V_{SD}.

S6 and S7 can be modelled as two diodes with different conductance (a different barrier for each) connected together by a resistance, as shown schematically in Figure 5.6. These diodes are connected back-to-back. At low voltages, the conductance is zero for both samples. Applying a high enough positive voltage to the diode on the right-hand side (above the diode breakdown voltage) will switch it on. The current will pass through the left-hand side diode since it is in the forward bias (assuming a small diode threshold voltage). Applying a negative voltage (above the diode threshold voltage) to the right-hand side diode will allow the current to pass through. However, the left-hand side diode will not permit this current to pass through until the applied voltage is above the diode breakdown voltage. This model might also be applicable for S1-S4 if 'leaky' diodes are considered (the diodes are so leaky for S1 and S4 that they are almost short circuited). These diodes should have smaller barriers than S6 and S7 so that they are conductive at V_{SD}=0.

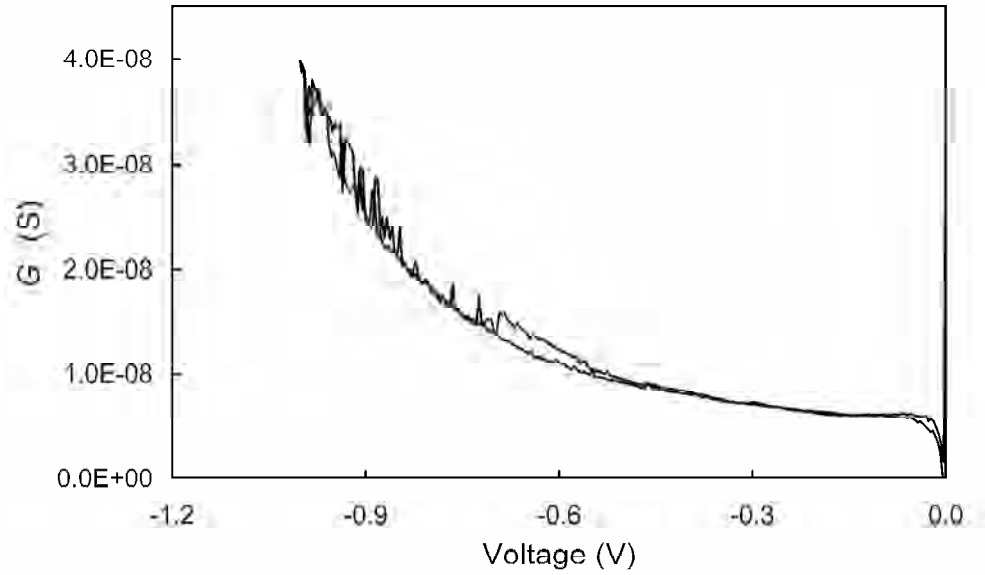

Figure 5.5 The dependence of the conductance on V_{SD} at T~22K for S30.

Figure 5.6 Schematic diagram of two back-to-back diodes connected with a resistance

5.2.4. Models for the conductance steps

The steps in the *G(V)* curves can be classified into 'permanent' and 'temporary' steps. The former are due to permanent changes in a wire. The latter is due to the addition of a temporary conduction path.[9, 10] Each cluster wire contains a single continuous network of clusters (since the cluster deposition was stopped once an onset of conduction was observed) and some discontinuous networks, as shown schematically in Figure 5.7. The continuous cluster wire can be considered as a group of (n) resistances connected in series and their total resistance R_s is given as

$$R_s = \sum_{i=1}^{n} R_i \tag{5.1}$$

where R_i is the resistance of the individual element (it can be a cluster, a bottleneck, or a Bi-oxide layer). Hence, R_s is dominated by the largest resistance in the series (for example, a Bi-oxide layer). The discontinuous networks of clusters may also affect the total wire resistance as discussed below. The steps in the *G(V)* curves are due to changes in the resistance of element(s) in the cluster network. In the following, models are presented to explain these steps.

Resistive heating model

The permanent (non-return) steps in the *G(V)* curves may occur because of morphological changes in the cluster wire driven by the electrical current, such as clusters' coalescence, electro-migration of atoms between clusters, and breaking conduction paths. Coalescence and electro-migration decrease the resistances of elements in the cluster network and this reduces the total wire resistance (Equation 5.1). Therefore, this produces steps towards the higher conductance. Steps towards the higher conductance were observed when using an electrical current to anneal Bi cluster wires in Reichel's study.[2] These steps were also observed for Bi cluster films deposited at the critical thickness (onset of conduction),[6] and when the cluster wires were annealed by heating the substrates (in Section 5.7).

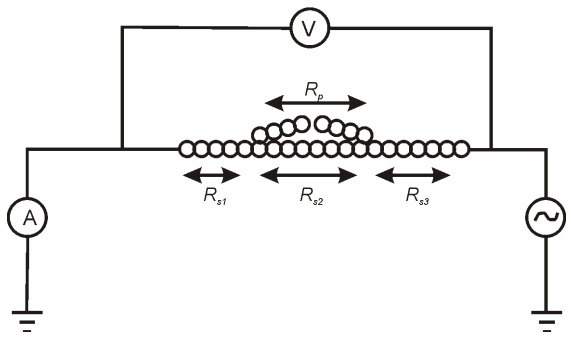

Figure 5.7 Schematic diagram of a cluster wire consisting of a continuous series of clusters and a discontinuous one.

Breaking a conduction path increases the wire resistance which produces a step towards the lower conductance. However, if no alternative parallel conduction path (to the broken one) exists, the sample will 'die', i.e. $R_s \rightarrow \infty$. Breaking a conduction path is likely to occur at the bottlenecks; for example, an electrical current of 1μA through a bottleneck of a radius of 2nm will produce a current density of ~8×10^{10} A/m^2. This high current density is likely to break the conduction path at the bottleneck.

Discontinuous network model

In this discussion, R_s will be considered as three main fragments, i.e. $R_s = R_{s1} + R_{s2} + R_{s3}$ (Figure 5.7). A discontinuous network of clusters can be considered as a large resistance (R_p) connected in parallel with the wire, i.e. $R_p \sim \infty$. Although one discontinuous network is considered here (which is the network with the smallest discontinuity gap between the wire tips), the discussion can be developed to include additional networks. The total resistance of such a wire (R_{wire}) is

$$R_{wire} = R_{s1} + R_{s3} + \frac{R_{s2} R_p}{R_{s2} + R_p} \tag{5.2}$$

As long as the parallel cluster network is discontinuous, R_p is much larger than R_{s2} and $R_{wire} \sim R_s$.

Applying V_{SD} across the wire will produce a similar voltage across the tips of the discontinuous wire, which are initially separated. This produces a very large electric field between the tips with the smallest gap. For example, a voltage of 1V across tips with a gap of ~1nm will produce an electric field of $E = 10^9$ V/m. Such an electric field is likely to make a connection between the tips by displacing a metastable Bi cluster.[9, 10] The new connection will decrease R_p and thus R_{wire} which produces a step in the *G(V)* curve towards high conductance (low resistance). The possibility of poor conduction through the established connection (for example, because of Bi-oxide shells on the tips) should be considered. This means that the conduction through the new network might occur through a tunnelling barrier. If this barrier is larger than those originally existing in the continuous wire, R_p is expected to be larger than R_{s2}. This causes a small modification to the resistance due to the new connection (a small step in the conduction). Such small steps can be seen in the conduction curves of S1, S2, S3, and S7. Alternatively, larger steps can be observed for S6 indicating that the barrier within the newly established connection might be comparable to those existing originally within the continuous wire. If another discontinuous network of clusters with a small gap separation and a metastable cluster exists, the above scenario might occur again and produce another step.

Once the contact has been established between the tips, an electrical current will flow through the parallel part of the wire, and the voltage across the tips will drop dramatically. Hence, two scenarios may occur: the two tips might fuse due to the resistive heating of the electrical current or the metastable cluster may return to its original position since the large electric field which caused its movement has dropped. The former scenario produces a permanent increase in the conduction. The latter produces temporary steps which are observed in the *G(V)* curves as 'return' steps.[9]

5.3. Gate effect

The gate effect measurements are discussed in four subsections. The results are presented first. Next, two models for explaining the gate effects are presented. The time evolution of the gate effect is then illustrated. The last subsection contains a discussion of the results.

5.3.1. The gate effect results

The gate effect measurements were performed for all samples at temperatures of ~290, ~80, and 4.2K. S1-S5 and S7 showed the gate effect only at ~290K. S6 showed a gate effect at ~290 and at 80K. A constant V_{SD} ranging between 100mV and 5V was applied across each wire. The gate voltage was swept between −5 and 5V (or between −10 and 10V for S5). The circuit used for the gate measurements is shown in Figure 1.6(a).

Figures 5.8–5.12 show the gate measurement results at ~290K for S1 and S4-S7, respectively. Only *I(V)* measurements at constant gate voltages of −5, 0, and 5V are available for S2 and S3 (Figure 5.13) since the gate effect disappeared after performing the *I(V)* measurements. The measurement time is indicated on each of the figures. Figures 5.8–5.12 show the dependence of I_{SD} (black line) on the change in the gate voltage (red line) with time (the (a) figure), and the dependence of both I_{SD} (black line) and V_{SD} (red line) on the gate voltage (the (b) figure). Although there is a great deal of variability between samples, there is a consistent effect at positive bias, i.e. I_{SD} increases for a gate voltage (V_g) which is greater than some threshold voltage (V_t). I_{SD} stays constant at its maximum value for $V_g > V_t$, and then, as the gate voltage decreases, it returns to its original value (or close to it). No change in I_{SD} was noticed for any of the samples when a negative voltage was applied to the gate. The figures show that the increase in I_{SD} due to the gate voltage compared with noise is small for S4 and S7, relatively large for S1, and it is the largest for S5 and S6. The figures also show the appearance of noise with relatively well-defined amplitudes when applying negative voltage to the gates of S5 and S6, while the noise had random amplitudes for the other samples. V_{SD} is constant in all of the figures and is independent of the gate voltage. This shows that the change in I_{SD} is not due to a change in V_{SD} or leakage to the gate. The gate measurement results are summarised in Table 5.2. The table shows the resistance of the wire at t=0 (R_{onset}), V_{SD} during the gate measurement, the maximum value of the gate voltage ($V_{g(max)}$), I_{SD} measured using V_g=0 when the gate effect was observed, R is the wire resistance with V_g=0, the values of the gate voltage when the gate effect appeared/disappeared (V_t), the change in I_{SD} due to applying $V_{g(max)}$ (ΔI), the percentage change in I_{SD} due to applying the gate voltage ($(\Delta I/I_{SD})\%$), and the contact type. It should be noted that R, R_{onset}, and I_{SD} were measured using the V_{SD} shown in the table. The values of V_t and ΔI are not available for S2 and S3 in the table since the only available measurements for these samples are the *I(V)* measurements. $(\Delta I/I_{SD})\%$ are not available for S5 and S6 since their I_{SD} were very small without applying voltages to their gates. The figures and the table show that different wires have different resistances, require different gate voltages to show an effect on I_{SD}, and have different types of noise (discussed in Section 5.4).

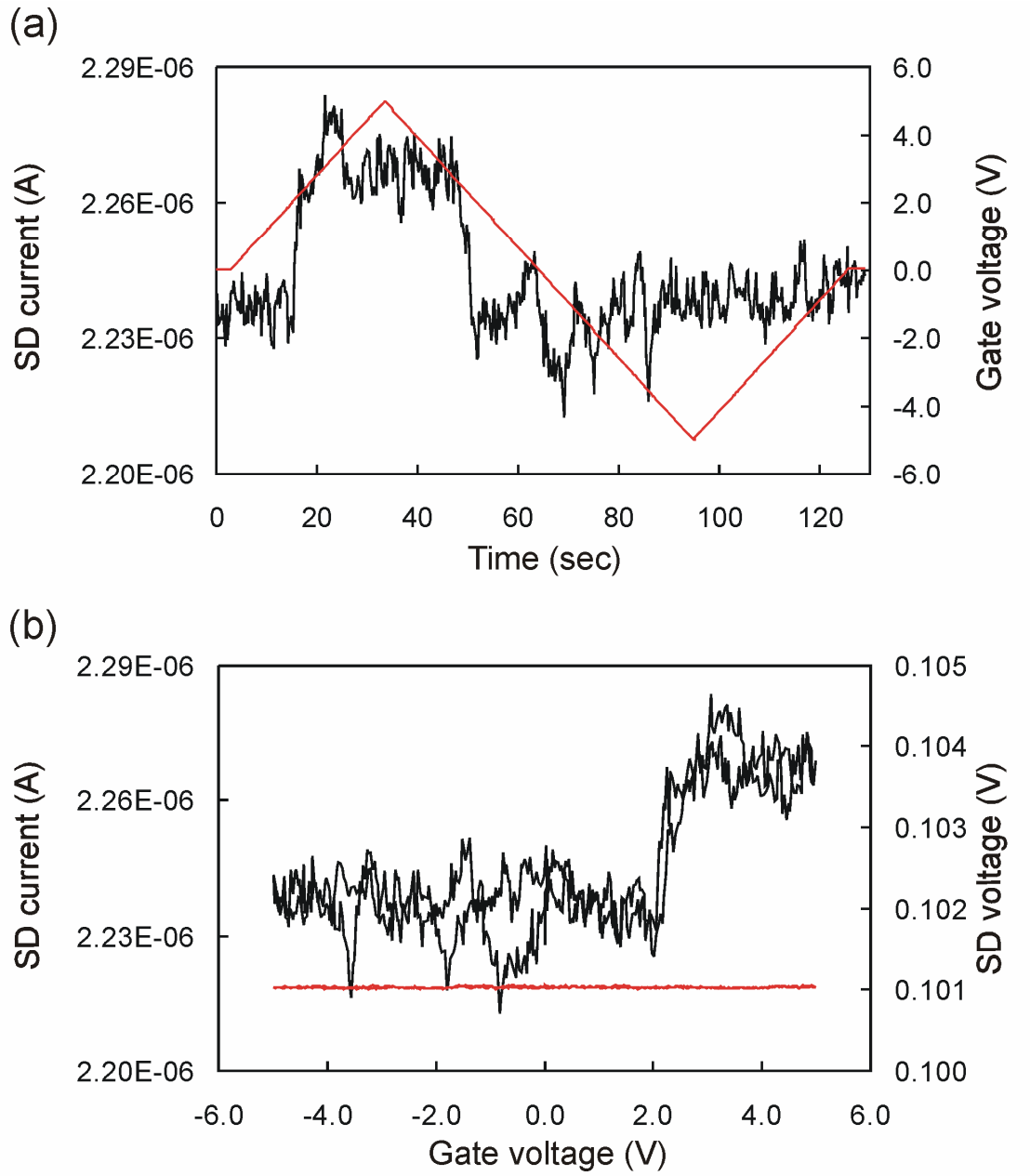

Figure 5.8 Gate measurement results for S1 at t=0:20:30. (a) The change in I_{SD} (black line) with time when changing the voltage to the gate (red line). (b) The dependence of I_{SD} (black lines) and V_{SD} (red line) on the gate voltage.

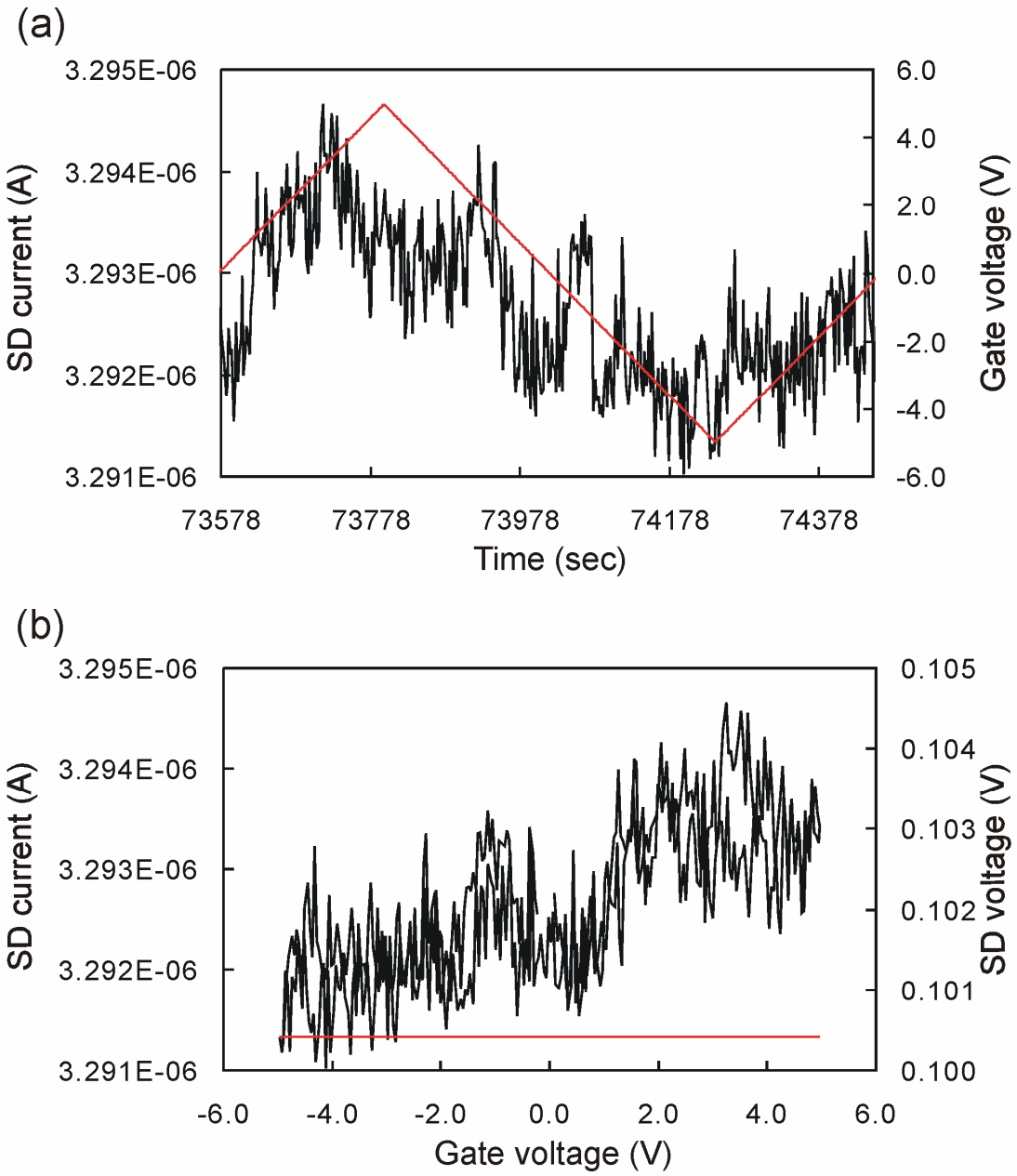

Figure 5.9 Gate measurement results for S4 at t=2:00:00. (a) The change in I_{SD} (black line) with time when changing the voltage to the gate (red line). (b) The dependence of I_{SD} (black lines) and V_{SD} (red line) on the gate voltage.

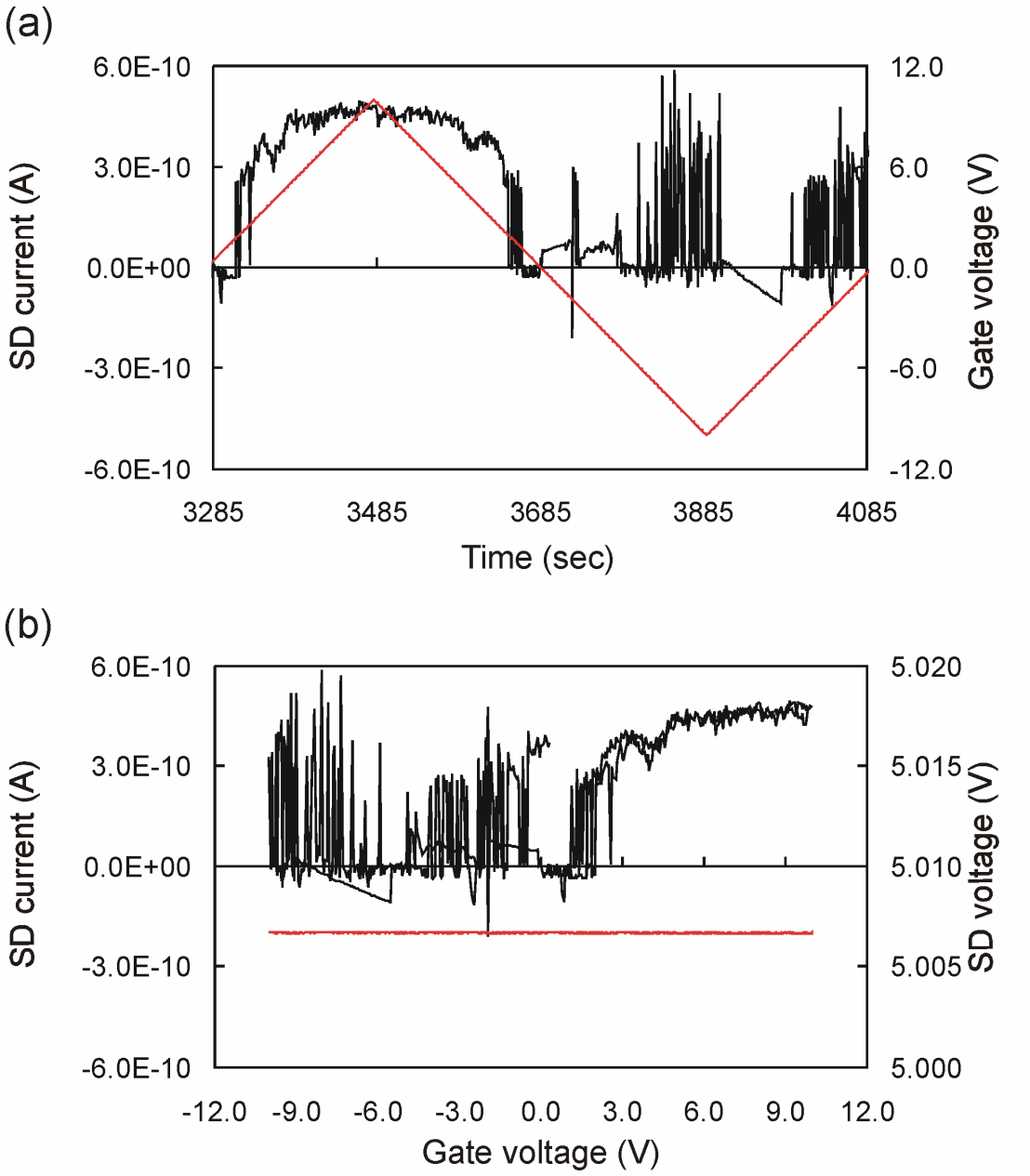

Figure 5.10 Gate measurement results for S5 at t=0:00:00. (a) The change in I_{SD} (black line) with time when changing the voltage to the gate (red line). (b) The dependence of I_{SD} (black lines) and V_{SD} (red line) on the gate voltage.

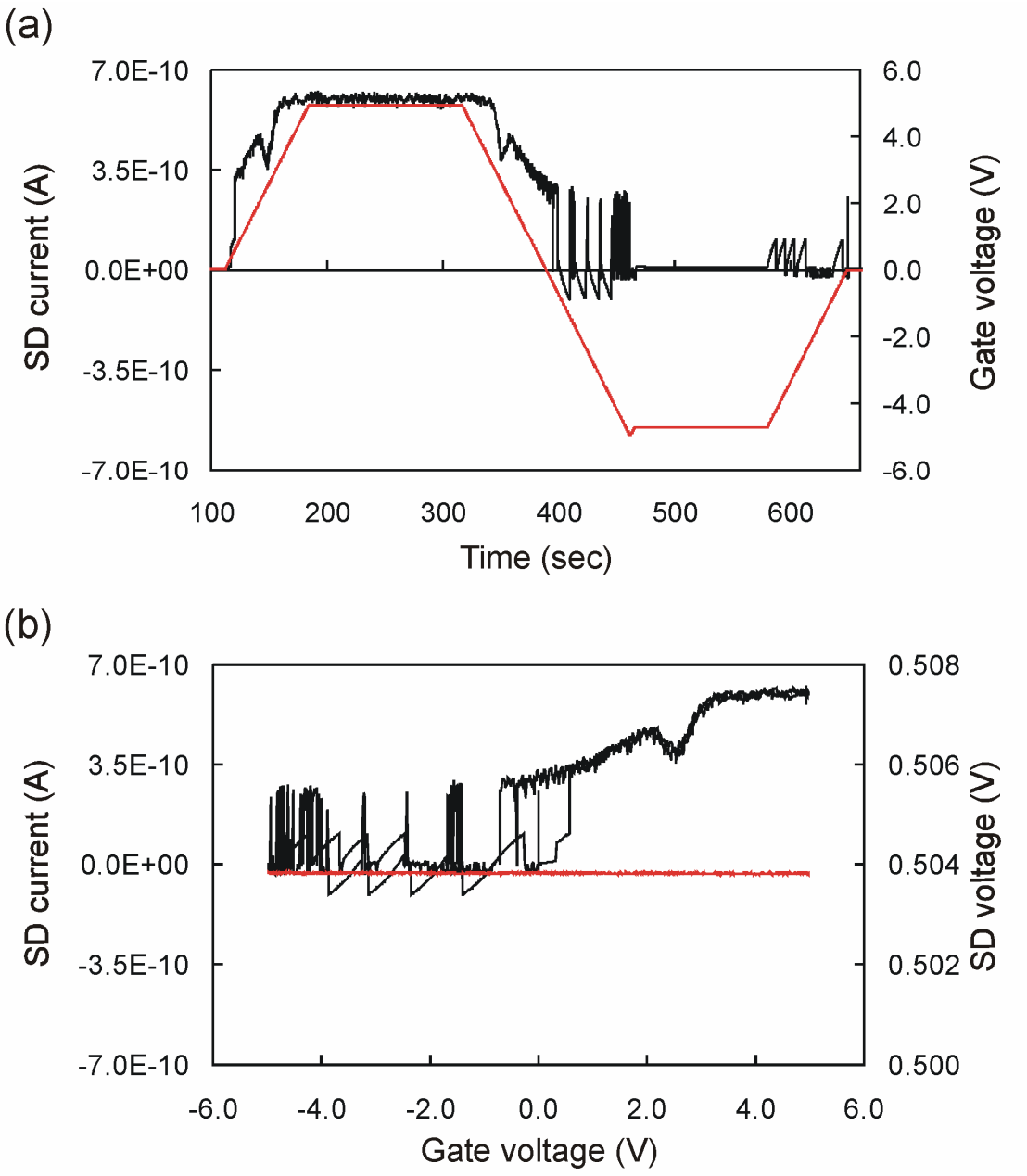

Figure 5.11 Gate measurement results for S6 at t=2:03:10. (a) The change in I_{SD} (black line) with time when changing the voltage to the gate (red line). (b) The dependence of I_{SD} (black lines) and V_{SD} (red line) on the gate voltage.

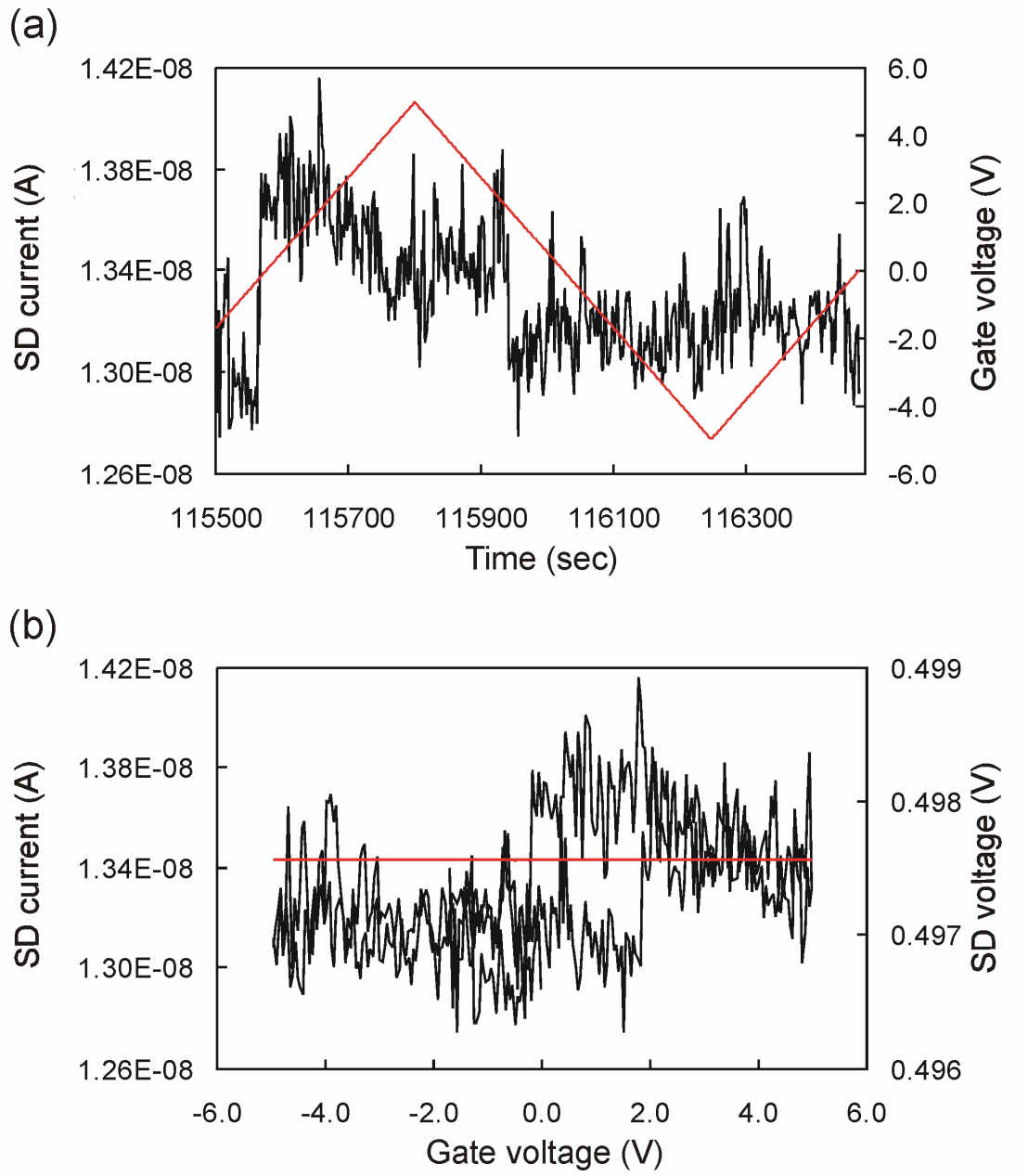

Figure 5.12 Gate measurement results for S7 at t=1:19:56. (a) The change in I_{SD} (black line) with time when changing the voltage to the gate (red line). (b) The dependence of I_{SD} (black lines) and V_{SD} (red line) on the gate voltage.

Figure 5.13 shows the *I(V)* curves for S2 and S3 when applying –5, 0, and 5V to their gates. S2 shows an increase in I_{SD} when a positive voltage is applied to the gate, and a decrease in I_{SD} for the negative gate voltage. S3 shows a decrease in I_{SD} for the negative V_{SD} when a negative voltage is applied to the gate. It is not obvious in the *I(V)* curves of S3 whether I_{SD} changes when a positive voltage is applied to the gate because of the large noise in the curve.

If we consider Figures 5.8–5.13, almost all samples (except S3) showed an increase in I_{SD} when a positive voltage was applied to the gate. The resistances of the samples were very different when they showed the gate effect. S1 and S4 had initial resistances between 10 and 50kΩ, while S2, S3, and S7 had resistances between 4 and 800MΩ, and S5 and S6 had unmeasurably high resistances, i.e. >10GΩ before

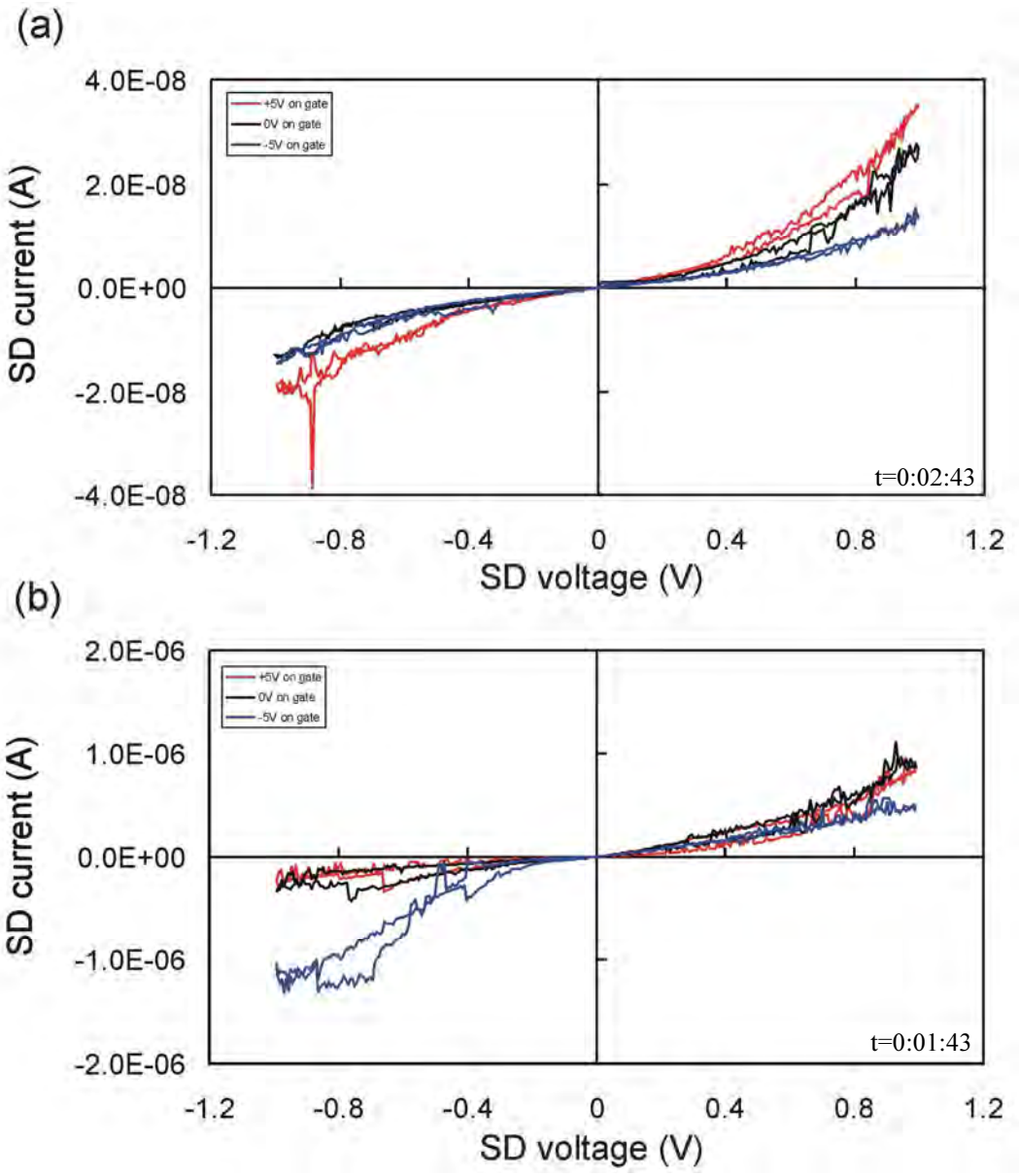

Figure 5.13 I(V) curves of (a)S2 and (b) S3 when applying –5, 0, and 5V to the gate.

applying gate voltages. S5 and S6 showed the best signal to noise ratio. It should be noted that the clusters forming S5 are oxidized clusters (clusters were oxidized inside the deposition chamber where it was left without pumping throughout cluster deposition).

Although we are not claiming that our cluster wires show semiconducting characteristics, we will compare their gate effect with the four types of the typical MOSFET discussed in Section 1.3. The increase in I_{SD} at positive V_g for S1-S2 and S4-S7 match the expected characteristics of the n-channel MOSFET. Since S5 and S6 had very low I_{SD} at V_g=0 and I_{SD} increased at positive V_g, these samples match the n-channel MOSFET in the enhancement mode. S1, S2, S4 and S7 had finite high resistances (>$10^4\Omega$) and I_{SD} of these samples increased only at positive V_g. Hence, these samples may also match the n-channel MOSFET in the enhancement mode. S3 showed only a decrease in I_{SD} when negative V_{SD} and V_g were used. Therefore, it could match an n-channel MOSFET in the depletion mode (according to the circuit described in Figure 1.6(a)).

Au has an extremely small screening length (<1nm),[11] while bulk Bi has a larger screening length (~40nm).[12, 13] The electric field produced by the gate voltage should be able to penetrate the one cluster height wire (~33nm). This means that the Au electrodes of the samples are not expected to contribute to the gate effect due to their small screening length, and the observed gate effect should be due to the Bi cluster wires.

5.3.2. Electric field effect models

The gate effect of S1-S7 is discussed within two models. The first considers the wire to be a semiconductor,[14, 15] the gate effect can therefore be explained in terms of the MOSFET characteristics described in Section 1.3. This model can be applied if the semimetal-semiconductor transformation is achieved for the cluster wires or if regions of semiconducting Bi-oxide within the device were responsible for the gate effect. The second model assumes that the wire retains semimetallic characteristics, so that the results may be explained in terms of a metal-semimetal junction. After presenting the models, they are compared with the results.

An estimation of the number of carriers accumulated or depleted as a voltage is applied to the gate is illustrated below since it is valid for both models. The number of electrons accumulated in a Bi cluster wire when applying 5V to the gate can be estimated using the Si-SiO_2-Bi capacitor structure shown in Figure 5.14 as

$$N = \frac{Q}{eV_{Bi}} = \frac{cV_g(\max)}{eAh_{Bi}} = \frac{\varepsilon_0\varepsilon_{SiO2}\frac{A}{d_{SiO2}}V_g(\max)}{eAh_{Bi}} = \frac{\varepsilon_0\varepsilon_{SiO2}}{ed_{SiO2}h_{Bi}}V_g(\max) \cong 3\times10^{17}\,cm^{-3} \quad (5.3)$$

where N is the density of accumulated electrons, Q is the charge accumulated on the capacitor plate, V_{Bi} is the volume of the wire, c is the capacitance of the SiO_2 layers, A is the wire surface area, h_{Bi} is the wire thickness, d_{SiO2} is the thickness of the SiO_2 layer (~100nm), and $\varepsilon_0\varepsilon_{SiO2}$ is the permittivity of the SiO_2 layer ($3.9\varepsilon_0$). In the above estimation, the volume of the wire is approximated as a rectangle of one cluster high

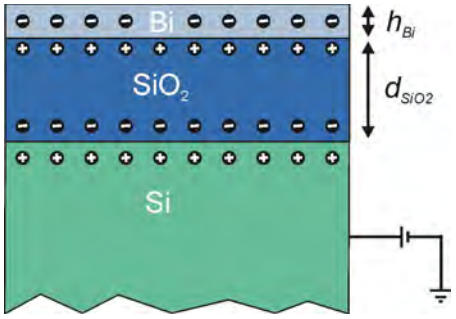

Figure 5.14 Schematic diagram of the Si-SiO_2-Bi capacitor when applying a positive voltage to the gate.

(33nm). The number of carriers in a Bi nanocluster wire at room temperature without applying any voltage to the gate is ~$3x10^{18}cm^{-3}$ (assuming the bulk carrier concentration).[16, 17] Thus, the number of accumulated electrons is ~1/10 of the total number of electrons in the wire. Those electrons are extra electrons should cause an increase in conduction. The same number of electrons (N) will be depleted if a voltage of –5V is applied to the gate.

Metal-semiconductor junction model

The discussion below focuses on an n-type semiconductor since all samples showed characteristics similar to the n-type MOSFET. Analogous to the traditional metal-semiconductor junction, the conduction and valence bands' edges of Bi are bent when a junction is formed between Bi and Au because of the difference in their work functions. This occurs by bending both bands' edges at the Au-Bi junction until the Bi Fermi level aligns with the Au Fermi level as shown schematically in Figure 5.15(a). The conduction band bending will create a barrier for electrons in the conduction band of Bi. This is the case for the two Au-Bi junctions (the two ends of the wire).

Applying a voltage between the source and drain, V_{SD}, creates the potential difference required for electrons to flow from the source to the drain. Applying a positive voltage to the gate bends the conduction band in Bi towards lower energy as shown in Figure 5.15(b) (i.e. shifting Fermi level towards higher energy). This enables more electrons to tunnel from the Au electrode to the Bi conduction band. Applying a negative voltage to the gate bends the conduction band toward higher energy as shown in Figure 5.15(c) (i.e. shifting the Fermi level towards lower energy). This increases the barrier height and decreases the number of electrons which are able to tunnel from an Au electrode to the Bi conduction band. This leads to lower conduction. It should be noted that the holes' participation to the conduction process is expected to be negligible compared with the electrons' participation for an n-type semiconductor.[16-19]

It is known that a Schottky barrier can occur when a metal is directly contacted to a semiconductor. Gold (Au) contacts were used for the first six samples, while silver (Ag) was used for S7. The work functions are 5.1, 4.3, and 4.22eV for Au, Ag, and bulk Bi,[20] respectively. The expected barrier created by the conduction band bending is due to the difference in the work function between the contact and the wire. This

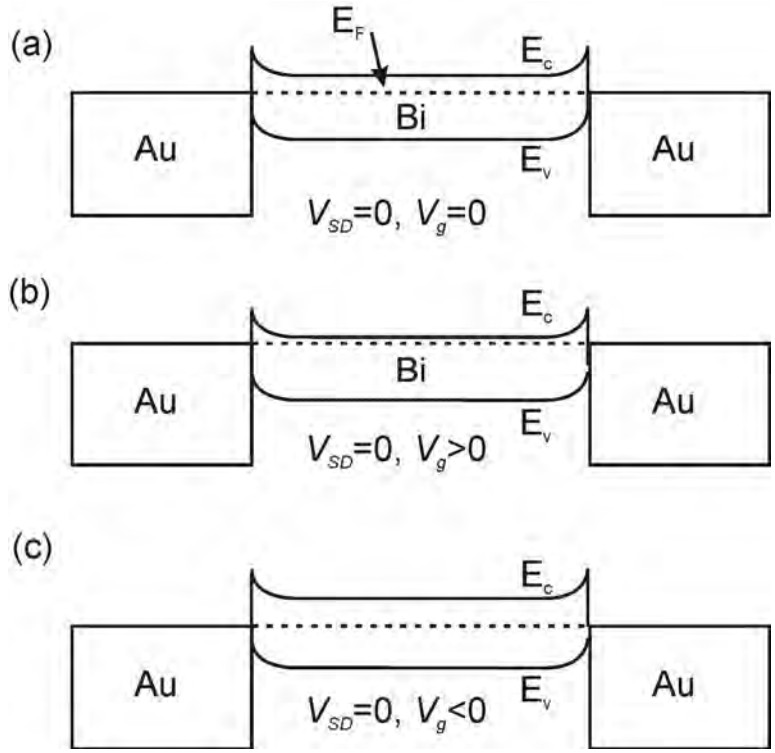

Figure 5.15 Schematic diagrams for Au-Bi-Au junction for different V_g. E_F is Fermi energy, E_v is the valence band energy, and E_c is the conduction band energy.

difference is ~0.88eV for the Au-Bi junction and ~0.08eV for the Ag-Bi junction. It should be noted that since the measurements were performed at room temperature, the difference will be reduced by k_BT~0.025eV. The *I(V)* characteristics of the Au-Bi (or Ag-Bi) junction should be non-linear. The non-linearity should be higher for the Au-Bi junction than that of the Ag-Bi junction since the Au-Bi junction barrier is higher than that of Ag-Bi.

Metal-semimetal junction model

If we consider the second model, bulk Bi is a semimetal with a band overlap between the L-point of the conduction band and the T-point of the valence band of 38meV.[21] The Fermi energy measured from the valence band edge is 15meV.[22] The band overlap is assumed to be constant throughout the discussion whether or not a voltage is applied to the gate. When Bi is brought into contact with Au, the Fermi levels of Bi and Au will line up. A barrier of the height of $e\Phi_B$ ~0.84eV from the edge of the Bi conduction band to the Au Fermi level will be introduced ($e\Phi_B=W_{Au}-W_{Bi}$-15meV- k_BT, where W is the work function of each material). Schematic diagrams of one Au-Bi junction and the number of electrons and holes are shown in Figure 5.16 (the other junction will look similar). No barrier will exist for the Bi valence band, i.e. holes (Figure 5.16(b)). At equilibrium, no current will flow through the junction. When a bias voltage is applied to Au electrodes (V_{SD}), electrons will flow from the negative electrode to the wire by tunnelling through the barrier and holes will flow in the opposite direction. Applying 5V to the gate will accumulate $3x10^{17}cm^{-3}$ electrons in the wire and push the conduction and the valence bands in Bi towards lower energy, as shown in Figure 5.16(c). The accumulated electrons will be distributed between the

conduction and valence bands. This will increase the number of electrons in the conduction band and decrease the number of holes in the valence band. It will also decrease the barrier height for electrons. As the number of holes decreases, fewer holes will contribute to the conduction. However, electrons in Bi are 10 times more mobile than holes.[16-19] Thus, electrons are believed to play the major role in electrical conductivity in Bi. As a result, the conductance will increase where the number of accumulated electros which participate in the conduction is less than 10% of the original number of electrons.

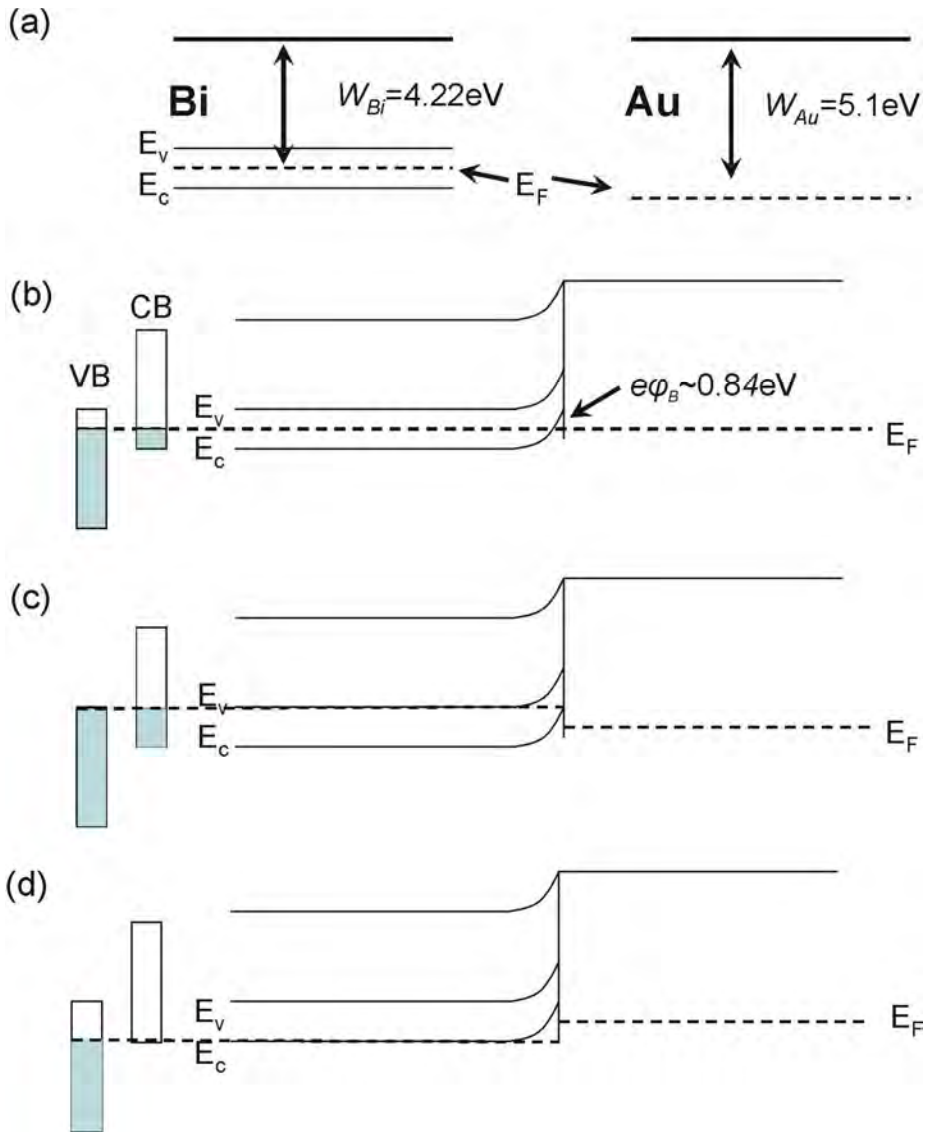

Figure 5.16 Schematic drawing of the band diagram of Bi-Au junction, and the number of electrons in the conduction and valence bands (the highlighted areas). W_{Bi} and W_{Au} are the work functions of Bi and Au respectively, E_F is Fermi energy, E_v is the valence band energy, E_c is the conduction band energy, and CB and VB refer to the conduction and valence bands respectively. (a) Bi and Au are separate. (b) The band diagram of Bi-Au junction at thermal equilibrium. (c) The band diagram of the Bi-Au junction when applying a positive voltage to the gate. (d) The band diagram of Bi-Au junction when applying a negative voltage to the gate.

Applying −5V to the gate will produce the opposite effect, where $3x10^{17}cm^{-3}$ electrons in the conduction and valence bands will be depleted, and the conduction and valence bands will be shifted towards higher energy. This will produce a decrease in the number of electrons in Bi conduction band, an increase the number of holes in Bi valence band, as well as increase the barrier height for electrons in Bi conduction band, as shown in Figure 5.16(d). The lower mobility of holes (compared to electrons) in Bi also adds to the three effects. It is not obvious whether the conduction will increase or decrease, and these effects are modelled below.

In the following, an attempt to simulate the effect on the conductivity of applying a voltage to the sample's gate is presented. This model incorporates the effects of applying a voltage to the gate on the number of electrons and holes and the barrier height. If the barrier between Bi and Au is disregarded first, the conductivity (σ) in the semimetallic Bi is given as the sum of the conductivities of electrons (σ_e) and holes (σ_h) (since both participate in conduction). The conductivity of a particular carrier is given as ($en\mu$), where e is the electron charge, n is the carrier concentration (n_e or n_h), and μ is the carrier mobility (μ_e or μ_h). μ_h will be assumed to be $0.1\mu_e$ in the following.[16-19] Figure 5.17(a) shows the dependence of $e\mu n$ on the gate voltage. The bulk values of n_e, n_h, and μ_e for Bi at room temperature were used to produce the figure.[16, 17] The figure shows that applying a positive voltage to the gate increases $e\mu_e n_e$ (the diamonds) and decreases $e\mu_h n_h$ (the squares). The increase of $e\mu_e n_e$ is faster than the decrease of $e\mu_h n_h$. If the barrier does not exist, the conductivity will be the sum of the two curves (the circles in the figure). The sum shows that I_{SD} should increase when applying a positive voltage to the gate and decrease when applying a negative voltage. However, this is not the case for the presented samples. Hence, the effect of the barrier needs to be considered.

Since a barrier exists for electrons, its contribution will be multiplied by the electron conductivity. The probability of electron tunnelling is dependent on the barrier height ($e\Phi_B$), the sample temperature, and the gate voltage (V_g) (since the barrier height can be changed by changing V_g). Hence, the probability of electron tunnelling can be given as $exp(-e(\Phi_B - V_g)) / k_BT)$. The total conductivity can be given as

$$\sigma = \sigma_e + \sigma_h \cong e(e^{\frac{-e(\Phi_B - V_g)}{k_B T}} n_e \mu_e + n_h \mu_h) \cong e\mu_e (e^{\frac{-e(\Phi_B - V_g)}{k_B T}} n_e + 0.1 n_h) \qquad (5.4)$$

where $e\Phi_B \sim 0.84$eV for Au-Bi junction, and $n_e + n_h$=constant.

Equation 5.4 was used to plot the dependence of the conductivity on the applied gate voltage in Figure 5.17(b) using the bulk values of n_e, n_h, and μ_e[16, 17] for Bi at room temperature. The figure shows that the conductivity is almost constant at $V_g < \Phi_B$. A sharp increase in the conductivity can be seen when the gate voltage is greater than Φ_B. The conductivity then increases gradually as the gate voltage increases.

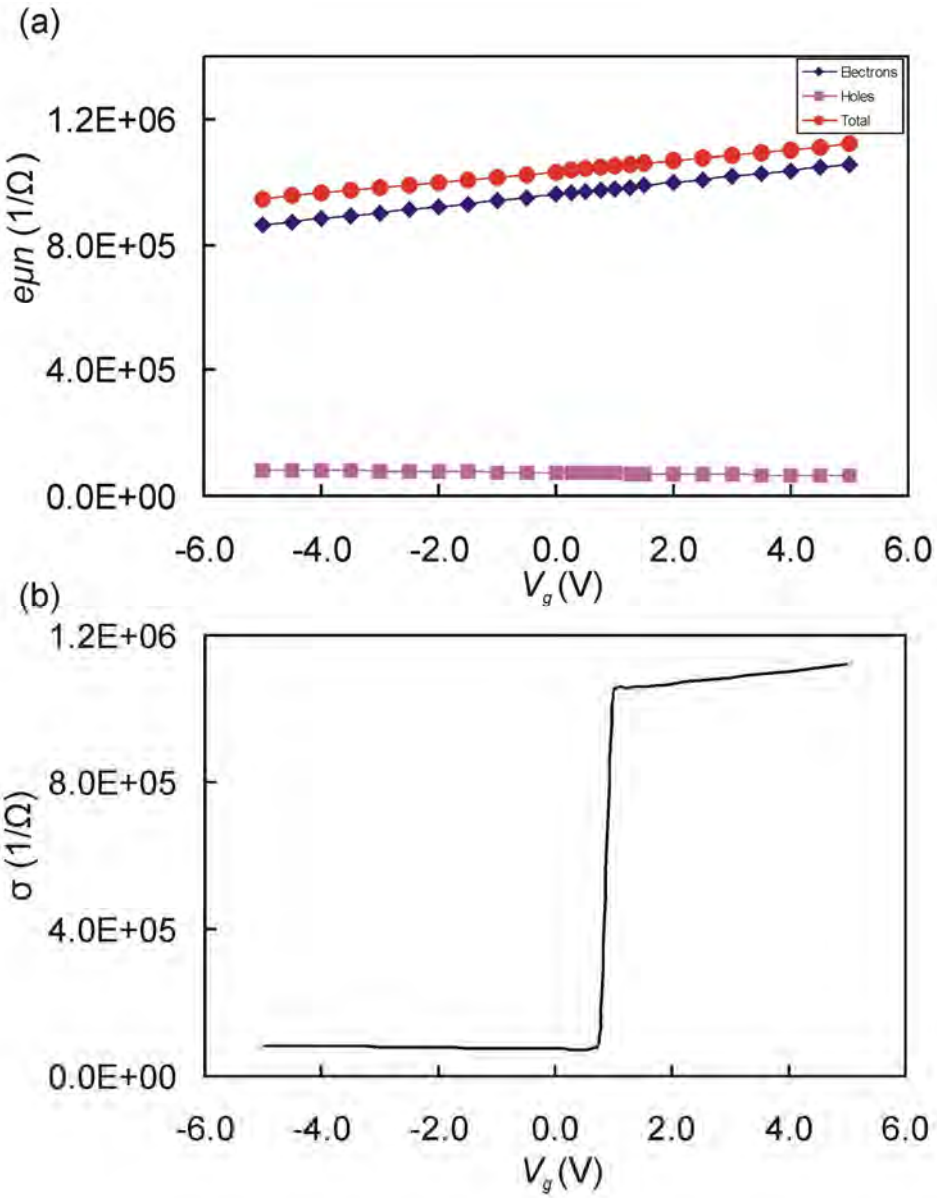

Figure 5.17 (a) The dependence of enμ on the gate voltage. The diamonds and the squares are used for electrons and holes respectively, while the circles are their sum. (b) The dependence of the conductivity on the gate voltage.

Comparing the models with the results

The gate effects of S1-S7 (Figures 5.8 -5.13) are qualitatively consistent with both of the models in Figures 5.15 and 5.16. Both models explain the appearance of the gate effect at positive voltages, and the lack of gate effect at negative voltages. The models also explain the increase in I_{SD} after a particular positive voltage.

Previous studies reported a semimetal-semiconductor transformation for single crystal Bi nanowires with diameters less than 65nm.[14] Although the Bi cluster size is ~33nm, the measurements do not provide enough evidence to show that Bi cluster wires exhibit semiconductor properties. Hence, it can not conclusively be argued that a

semimetal-semiconductor transformation occurred for the above samples. In addition, the cluster wire can not be dealt with as a simple single crystal wire aligned between two contacts.

The minimum gate voltages (V_t) required to modify I_{SD} for S1, S4, S5, S6, and S7 are between 2.1 and 0.73V when using Au contacts, and ~0V when using Ag contacts (Table 5.2). According to the two models, the gate effect should appear at $V_g \geq \Phi_B$ (~0.84 and 0.04V for Au and Ag contacts respectively). V_t values of S1, S4, and S5 are consistent with the models. However, S6 showed the gate effect at V_t values to be lower than Φ_B (~0.73V). The minor difference could be due to many reasons such as an increase in the sample temperature by the resistive heating of the wire. The difference between V_t and Φ_B for S7 is very small and it is within the measurement uncertainty. In summary, V_t values are consistent with both models. The appearance of the gate effect at a lower V_t for the sample with Ag contacts (i.e. S7) than those with Au contacts is also consistent with both models where Φ_B is smaller for Bi-Ag junction than Bi-Au junction.

5.3.3. The time evolution of the gate effect

The resistances of the samples were observed to either increase or decrease within a few minutes after the onset of conduction. These changes are dependent on many factors such as forming or losing current paths and enhancing an existing current path by cluster coalescence. The gate measurements were performed for the samples after their resistances stabilized in order to make sure that any change in I_{SD} is due to a change in the gate voltage and not to wire instability. However, none of the seven samples showed the gate effect directly after the onset of conduction. The gate effect observed for these samples was also not permanent. Table 5.3 shows the time that elapsed after the onset of conduction before the gate effect appeared (T_w), and how long this effect lasted (T_D).

Table 5.3 T_w and T_D for S1-S7.

Sample	T_w (min)	T_D (min)
1	1230	15
2	150	17
3	230	14
4	2880	1070
5	500	360
6	2730	81
7	4050	150

The gate effects for S1-S3 lasted between 10 and 17min. This limited the number of measurements performed for each sample while the gate effect existed. S4 showed a gate effect for a relatively long time. However, the signal to noise ratio was too small and the gate effect did not appear in all of the gate voltage ramping cycles when a continuous gate effect measurement was taken.

S5 and S6 had very low I_{SD} ($<10^{-11}$A) before showing the gate effect. The gate effect appeared/disappeared in both samples without any special treatment. The exact reasons behind the appearance/disappearance of the gate effect are not known. However, annealing the wires with an electrical current is known[17] to increase the mobility of the carriers in Bi. Oxidation of Bi clusters produces semiconducting Bi-oxide layers. Oxidation of the Bi wires and high resistive heating of the wires might be responsible for their 'death'. These effects play major roles in the time evolution of the samples' gate effect and are discussed in detail in the next subsection.

S5 showed a gate effect for 360min. The clusters forming this wire were oxidized during deposition. The sample had an open circuit resistance when no voltage was applied to the gate. The maximum I_{SD} (using $V_{g(max)}$=10V and V_{SD}=5V) increased from ~0.40nA, when the gate effect first appeared, to ~0.67nA over 166min (Figure 5.18(a)). The dashed lines in Figure 5.18(a) show the growth of the gate effect with time. I_{SD} stayed almost constant (~0.65nA) when the sample was cooled down to 82K (Figure 5.18(b)) 158min after performing the measurement in Figure 5.18(a).

Unlike S5, S6 showed a decrease in I_{SD} with time. The dashed line in Figure 5.19 shows the time evolution of the gate effect for S6. I_{SD} (using $V_{g(max)}$=5V and V_{SD}=0.5V) decreased from ~0.66nA to ~0.46nA in 45min. The gate effect disappeared 81min after the gate effect appeared for the first time and then only noise was measured.

S7 showed a small gate effect for 150min. The gate effect was not observed for many gate ramping cycles. I_{SD} dropped suddenly from ~1.3×10^{-8}A to ~1×10^{-10}A (using V_g=0 and V_{SD}=0.5V) after the measurement in Figure 5.12. S7 'died' ~20min after the sudden decrease in I_{SD} and the capacitance effect became more dominant than the gate effect. In these runs I_{SD} alternated between 1×10^{-10} and -1×10^{-10}A as the gate voltage ramping direction changed from increasing to decreasing (charging and discharging a capacitor respectively).

5.3.4. Discussion

Most of the previous studies performed on undoped bulk and thin film Bi showed that they exhibit n-type conduction.[18, 23] However, a few studies reported p-type conduction of Bi thin films.[24] The p-type conductivity is normally attributed to the presence of localized surface acceptor states[25] added to the sample through heat treatment.[18] These states appear mainly in the process of the sample preparation.[18] The n-type conductivity in Bi is an indication of diminishing contributions of various defect states.[18] The gate effect results for the samples showed that these wires hold the same type of conduction as undoped bulk and thin film Bi (n-type conduction).

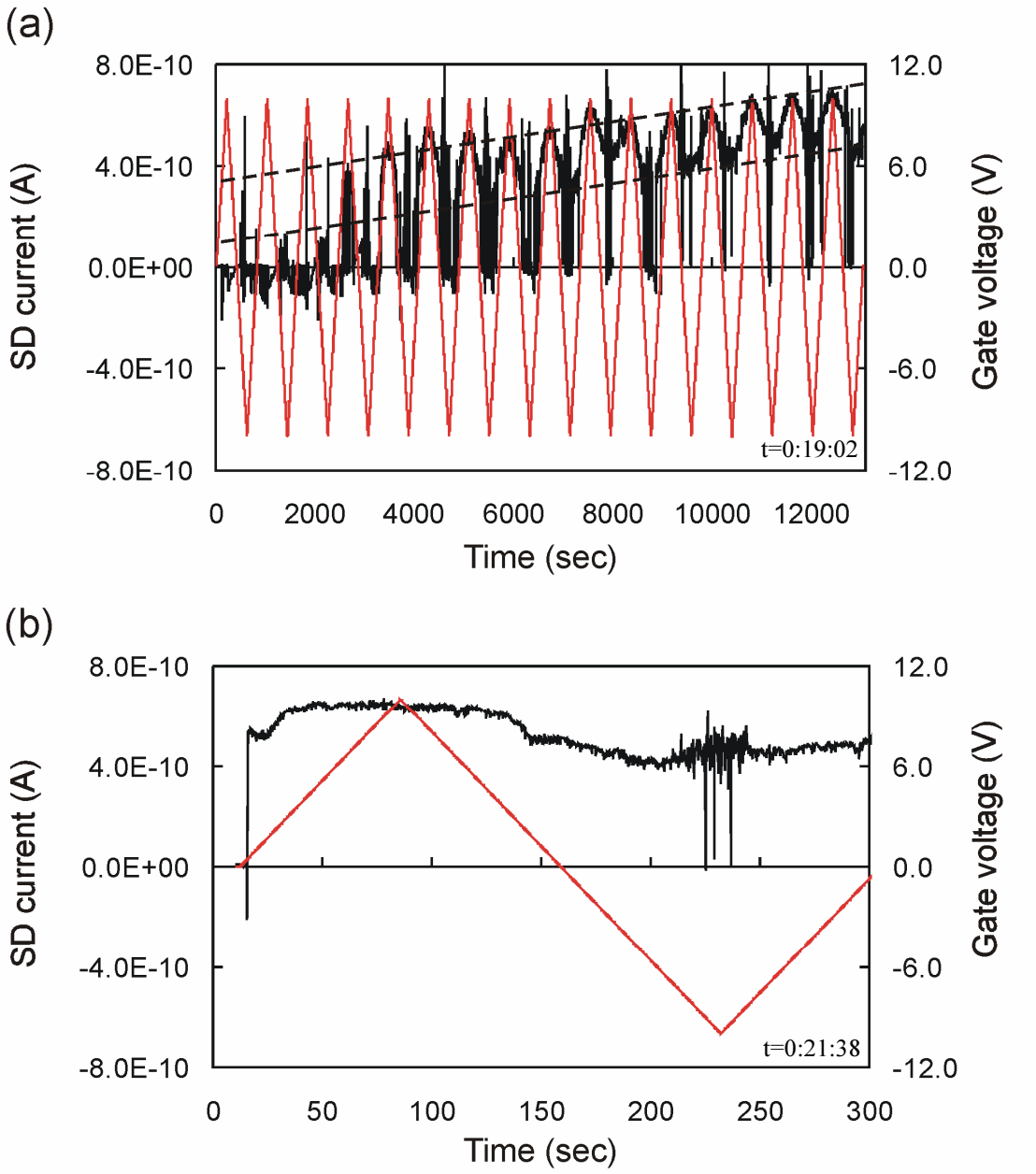

Figure 5.18 The time evolution of the gate effect of S5. The black line is I_{SD}, while the red line is V_g. (a) The room temperature measurement. The dashed lines show the increase in I_{SD} with time. (b) The 82K measurement.

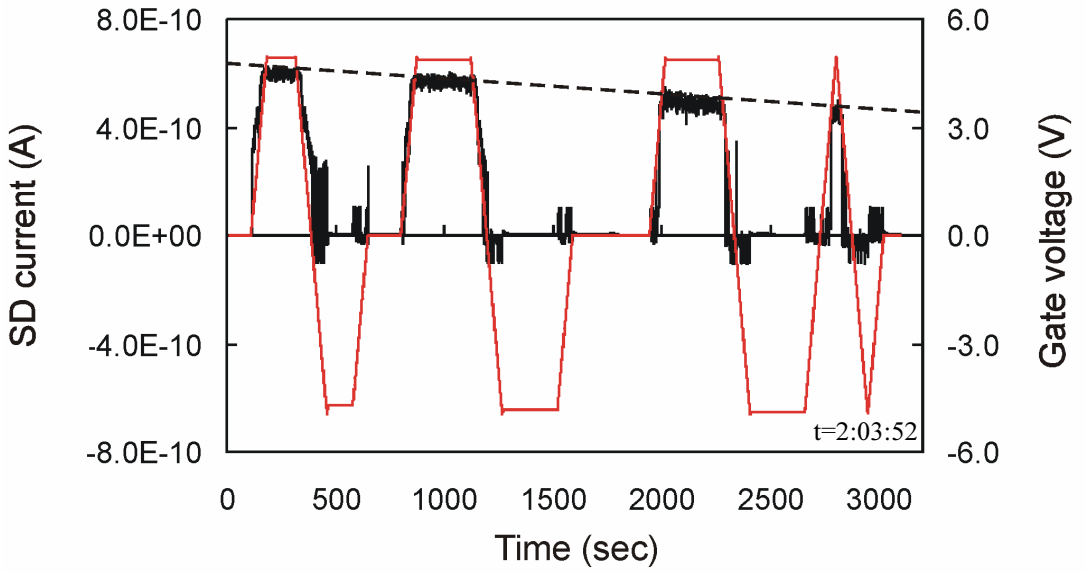

Figure 5.19 The time evolution of the gate effect for S6. The black line is I_{SD}, while the red line is V_g. The dashed line shows the decrease of the gate effect with time.

The gate effect appeared for all samples and disappeared after some time without special treatment. Three factors, at least, can be used to explain the appearance/disappearance of the gate effect: formation of Bi-oxide layers, bottleneck connections breaking, and wire annealing by the resistive heating of the electrical current. The following discussion illustrates the effects that each of these factors could have on the gate effect.

Bi-oxide has been observed to grow during cluster deposition at low pressure (10^{-6} Torr) in the HV cluster deposition system.[6] The oxidation rate was a function of deposition rate,[6] and it was due mainly to the presence of water film on the substrates.[6] Although the pressure of the UHV compatible deposition chamber is one order of magnitude lower than that of the HV system, Bi-oxide is expected to grow because of the water residual on the samples. A monolayer of water grows under a pressure of 10^{-7}Torr in ~26sec.[26]

Bi-oxide, which may be formed around Bi clusters, is believed to be the β phase of Bi_2O_3.[27] β-Bi_2O_3 is expected to form amorphous shells around the clusters.[27] This oxide is a semiconductor with band gaps of 2.58 and 3.9eV for 3-6nm wires and bulk Bi_2O_3 respectively.[8] Bi-oxide layers between Bi clusters (for S5) or between Bi cluster wires and Au contacts form tunnelling barriers.[2] The dimensions of these barriers are dependent on the deposition conditions, such as the deposition chamber pressure and cluster deposition rate, and they may increase with time[6] (see Figure 5.20). Increasing the barrier dimensions decreases the probability of carrier tunnelling and, consequently, decreases I_{SD}. An example of decreasing I_{SD} due to oxidation is shown in Figure 5.20. The figure shows a decrease in I_{SD} of S8 (no gate effect was observed for S8) when this sample was exposed to air. The decrease in I_{SD} is expected to be due to the growth of Bi-oxide barriers.[6] It should be noted that a constant V_{SD} of 100mV was used during the measurement in Figure 5.20.

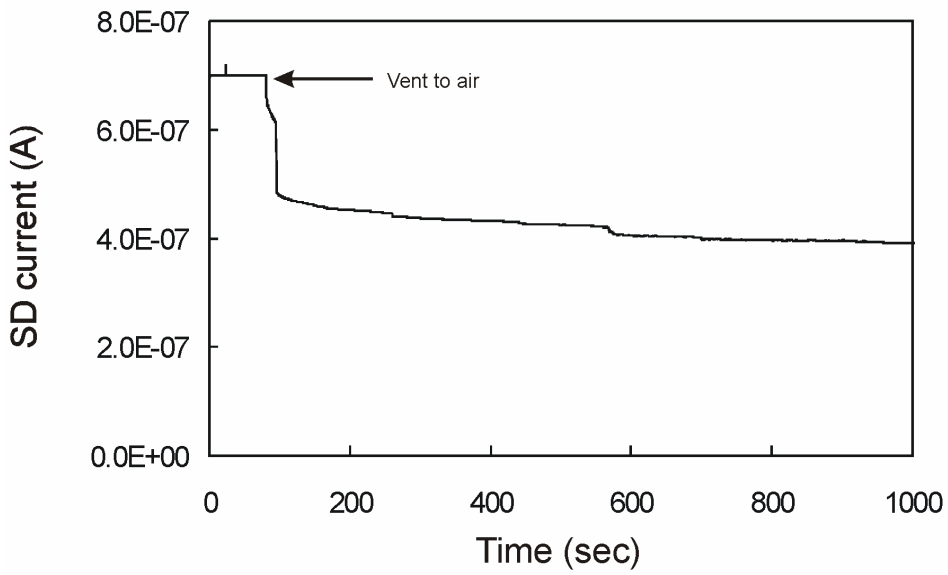

Figure 5.20 The change of I_{SD} with time when the deposition chamber was vented to air for S8. The deposition chamber was vented at 81sec.

The observed reduction in the amount of deposited material to form an electrically conducting wire of S7 (Table 5.1) is likely due to increasing the substrate temperature. The substrate temperature of S7 during the deposition was 350K (instead of 290K as for S1-S6). The higher substrate temperature may have reduced the amount of water on the substrate and thus reduced the oxidation. It should be noted that the wire length, V-groove width, and cluster deposition rate of S7 are not expected to be the reasons for reducing the amount of material for this sample. The short wire length of S7 (which reduces the amount of material) is balanced by the narrow V-groove width (which increases the amount of material). The deposition rate of S7 was the lowest deposition rate for any of the seven samples which typically increases the amount of required material (Table 5.1).[6]

Annealing a cluster wire by passing an electrical current through it increases clusters coalescence[28] (Section 4.3), and it may enhance its conductivity.[2] Annealing is also known to enhance the crystal quality[16] and the carrier's mobility of Bi thin films.[17] The increase in the I_{SD} in Figure 5.18(a) after ~3000sec (the lower dashed line) may be related to the annealing effect. However, annealing may also create discontinuities within a wire by melting parts of it and beading the molten clusters if the electrical power through the wire is $\geq 10^{-6}$W.[2] This process is likely to occur at bottlenecks in a wire as discussed in Section 5.7.

Although oxidation and annealing affect the electrical conduction of a cluster wire, the ratio of their effects cannot be found in our experiments. However, to minimize the oxidation effect, new heating tapes were fixed around the UHV compatible system. The system will be baked in the future before cluster deposition to reduce water residues in the system and thus cluster oxidation. This will also enhance the vacuum in the deposition chamber.[26] Increasing the substrate temperature during cluster deposition will also decrease the amount of water on the substrate and cluster oxidation. However, increasing the substrate temperature will anneal the cluster wire

and change its morphology and conductivity. These effects are discussed in Section 5.7. It should be noted that increasing the substrate temperature up to 473K did not affect the cluster bouncing angle (Section 4.4) which means that it is not expected to change the wire formation mechanism.

Coating Bi wires with a protective layer should be considered in the future to reduce cluster oxidation. Using a protective layer will also provide a chance to characterise the samples outside the UHV compatible system and it may increase the lifetime of the gate effect. EuS is an example of the materials that can be used as protective layers for Bi cluster wires[18] and it can be evaporated on the wires using the electron-beam evaporation method.[29]

In conclusion, the gate effect was observed for samples which have linear and non-linear *I(V)* curves. Oxidation and current driven changes in the wire are believed to have large effects on the gate effect of cluster wires.

5.4. Noise

This section discusses the noise in the electrical measurements in three subsections. The subsections include a brief introduction to the noise, the results, and a discussion of the results.

5.4.1. Introduction

When the noise in electrical measurements switches suddenly at random times between two well-defined resistance states, this noise is called random telegraph noise (RTN). The mean times the system spends in the lower and the higher resistance states (τ_1 and τ_2, respectively) can be used to find the frequencies of the RTN. The statistical properties of those times are found by the probabilities of finding the system in each resistance state and the probability of transition between the two states. If the spectral density of the noise increases as its frequency decreases, this noise is called the (*1/f*) noise.[30]

In a study of percolating nanocomposite films, Raquet et. al. reported the presence of the two types of noise described above in their samples.[31] The resistance fluctuations were explained in terms of slow charge carrier exchanges between the clusters' network path and an isolated cluster in the vicinity of the conducting pathway.[31] This caused the conductance to switch on and off according to local random electrical field fluctuations.[31]

5.4.2. Results

This section illustrates the noise results for samples regardless of whether they showed a gate effect or not. Two types of noise were observed for Bi cluster wires: random amplitude noise and noise with particular amplitudes. The former might be due to various phenomena such as background noise or a superposition of transitions between various resistance levels. The latter is due to transitions between well-defined resistance states, and it is the focus of this section. It should be noted that the

sampling rate in all of the presented results is 5points/sec, which means that any noise with duration below 0.2sec is not resolved.

The noise observed for S1 and S32 is presented here as examples of the RTN observed during the resistance-time measurements. The resistance-time curve for S1 at ~290K (measured using a constant V_{SD} of 0.1V) is shown in Figure 5.21. The figure shows large steps in the resistance and some 'spikes' with various heights. The noise was either above or below the resistance base level. However, RTN can be observed between 5200 and 8200sec. An enlargement of this section of the curve is shown in Figure 5.21. The resistance is switched between ~3.69x10^4 and ~3.86x10$^3\Omega$, i.e. about 4.6% of the base resistance. The frequency of the noise is variable as well. The mean times τ_1 and τ_2 are estimated to be 70 and 59sec.

S32 was measured using a V_{SD} of 50mV at 290K. It was also measured at 4.2K to reduce the thermal noise. The noise observed in the room temperature measurement was random noise and it did not show any well-defined amplitudes. The 4.2K measurement showed RTN of resistance as shown in Figure 5.22. The figure shows a low background noise and a RTN below the base resistance which is ~6% of the base resistance. The mean times τ_1 and τ_2 are estimated to ~2 and 10sec, respectively.

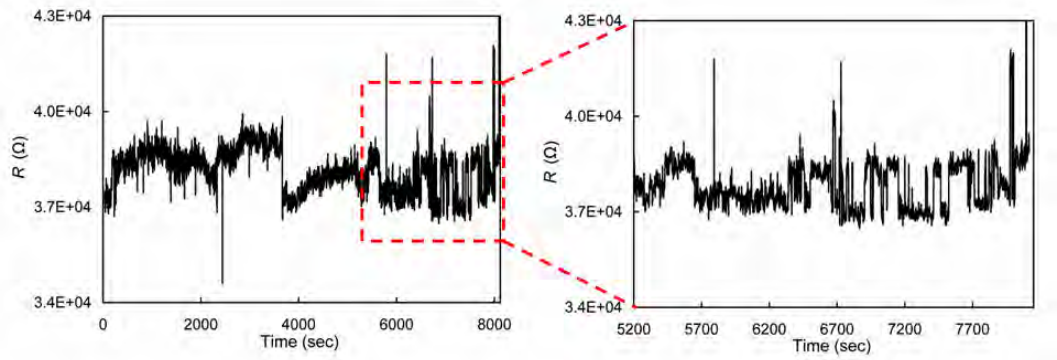

Figure 5.21 The change of the resistance with time at ~290K for S1 using V_{SD}=0.1V and V_g=0V, and an enlargement of a section of the results.

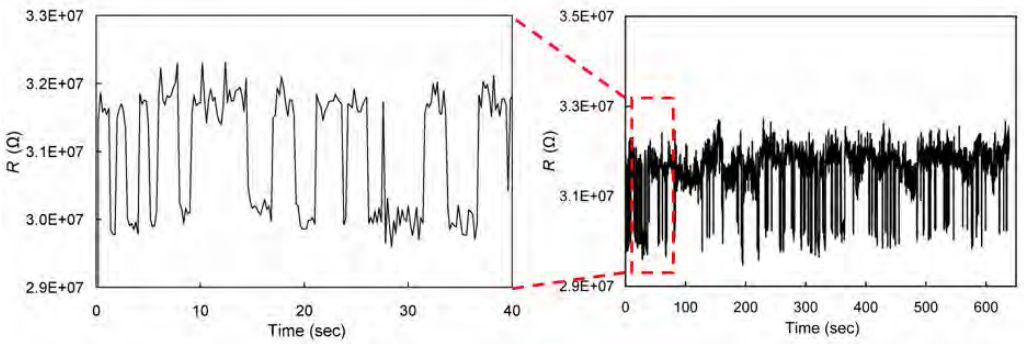

Figure 5.22 The change of the resistance with time at ~4.2K for S32 using V_{SD}=0.05V and V_g=0V, and an enlargement of the section between 0 and 50sec.

5.4.3. Discussion

Resistance fluctuations of cluster systems are greater than expected for homogeneous conductors. The fluctuations are affected by non-uniform distribution of the electric field across the elements of a cluster wire.[32] A possible mechanism that may produce resistance fluctuations through Bi cluster wires is described below.[30, 31, 33, 34] As the carriers are moving through a current path, a modulation and a release of the Coulomb potential occur due to the random variation of the Coulomb charges of nearby traps. Those charges move to the traps by the slow charge exchange. The potential barrier is altered by the Coulomb field of the charged traps within a small distance in random times. Therefore, the modulation of the potential barrier will modulate carrier transmission which switches the conductance across the barrier on and off depending on the local fluctuations of the electric field. Hence, resistance fluctuations should be observed as a result of all modulation events.

The probability of carrier tunnelling, which causes the system to fluctuate between two levels of the resistance, can be found using the probabilities of finding the system in the first and the second states (w_1 and w_2 respectively) and the probability that the carriers are transmitted between states, i.e. 1→2 or 2→1. The transition between states might include different numbers of carriers. Assuming that the energies of states (1) and (2) are *E(1)* and *E(2)* (where *E(2)* > *E(1)*), the system will have an energy difference of E_t=*E(2)-E(1)*. Hence, the system will exhibit probabilities of $w_1 = w_2$=½ if[33]

$$E_t = E_F + k_B T \tag{5.5}$$

where E_F is the Fermi energy. The above system is expected to spend similar times in states 1 and 2. Using Equation 5.5, three other scenarios are also possible. (i) If $E_t - E_F > k_B T$, the system is expected to spend more time in state 2 than in state 1 (Figure 5.22 for example). (ii) If $E_t - E_F < k_B T$, the system is expected to spend more time in state 1 than in state 2 (Figure 5.21 for example). (iii) If $E_t - E_F >> k_B T$ or $E_t - E_F << k_B T$, one of the states is rarely occupied and the fluctuations are not likely to appear.

5.5. Hall effect

This section discusses Hall effect measurements of Bi cluster films. An overview of Hall effect principle is presented in the first subsection. Sample fabrication and the measurement apparatus are described in the second subsection. The results and discussions are provided in the third and fourth subsections.

5.5.1. Introduction

If a conductor (or a semiconductor) is placed in a magnetic field (B) and an electric current (I) flows through the conductor perpendicular to the magnetic field direction, the magnetic field will introduce a transverse force on the moving carriers. This will push the carriers on both sides of the conductor, depending on their charge types,

creating a transverse electric field, as shown schematically in Figure 5.23. The voltage produced by the transverse electric field is called Hall voltage (V_h), and it is given as

$$V_h = R_h I \tag{5.6}$$

where R_h is Hall coefficient and its value is dependent on the material thickness (d), B, and the carrier concentration (n). R_h can be given as[35]

$$R_h = \frac{B}{edn} \tag{5.7}$$

A full discussion of Hall effect theory can be found in solid state text books.[35] Equations 5.6 and 5.7 show that carrier concentration can be provided directly by measuring Hall voltage.

5.5.2. Experimental technique

Hall effect measurements were taken for Bi cluster films. These films were deposited on planar SiO_2/Si substrates. The clusters were produced using the IGA source described in Section 2.1. In the following, Hall effect sample fabrication and the measurement apparatus are described.

Sample fabrication

SiO_2/Si substrates were used to prepare Hall effect samples using the standard optical lithography and lift-off technique. These samples are different from the V-groove samples, described in Section 2.2, since they are planar samples, larger than the V-groove samples, and have a different contact pattern. Figure 5.24(a) shows the mask pattern used to fabricate the contacts of Hall effect samples. The white and black areas are the transparent and non-transparent areas respectively. Any photoresist under the transparent areas was exposed and developed. The contacts were created by atomic deposition of ~5 and 20nm of Titanium (Ti) and Au. Ti was used (instead of NiCr) as a sticking material between SiO_2 and Au since it is a non-magnetic material. The contact numbers are as in Figure 5.24(a). Contacts A and B were not used in Hall effect experiments. It should be noted that the bi-layer method was used to create contacts with smooth slopes as described in Section 2.2.

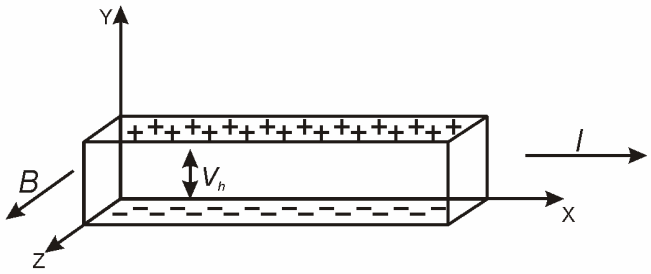

Figure 5.23 Geometry of Hall effect.

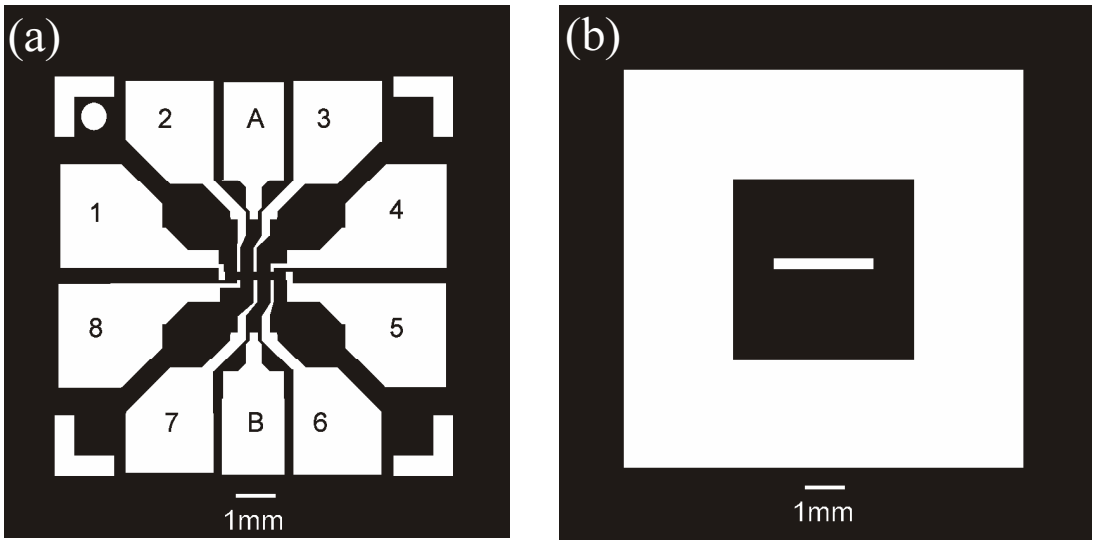

Figure 5.24 The patterns used to produce Hall effect samples. The contact and window patterns are shown in (a) and (b) respectively.

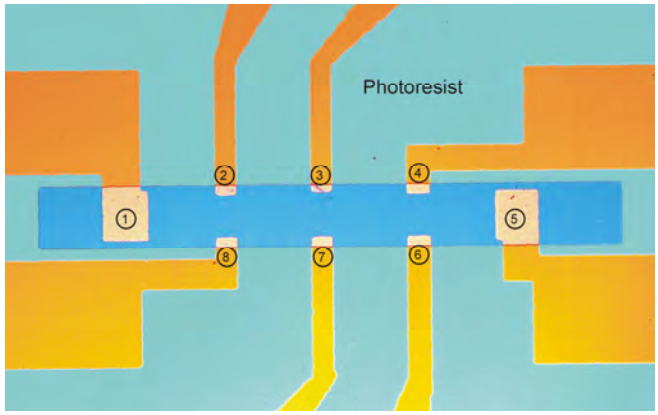

Figure 5.25 A Hall effect sample. The brown, green, and blue areas are Au contacts, photoresist, and SiO_2, respectively. The contacts are numbered as in Figure 5.24(a).

To limit cluster deposition within the area between the contacts, a photoresist layer was spun and exposed using a mask with rectangular opening as shown in Figure 5.24(b). This created a photoresist passivation layer and a window in the photoresist as shown in Figure 5.25. The passivation layer ensures that electrical conductivity occurs only through clusters within the window.

Measurement setup

Two permanent magnets with a diameter of 5cm each were fixed inside a holder (made of iron) with a spacing of 2.5cm between them, as shown in Figure 5.26. The magnets produced a magnetic field of 0.3T between them in the centre (measured using a Group3 Teslameter model DTM-141-DS). The magnetic field is relatively homogeneous in the centre between the magnets (away from the magnets' edges)

within the dimensions of the sample (1.05x1.05cm), while a decrease in the magnetic field was measured close to the magnets' edges. The holder was then fixed on a linear translator on the bottom of the deposition chamber. This arrangement allowed the magnets to be moved vertically inside the deposition chamber so that they could be positioned around the sample.

Each sample was fixed on the cryostat finger in order to deposit Bi clusters on it. The spring loaded sample holder (shown in Figure 2.8) was used to make the electrical contact to the contact pads (in Figure 5.24(a)). A voltage of ~100mV was applied between Contacts 1 and 5, and an onset of conduction was measured once a continuous network of clusters was formed. Cluster deposition was then stopped by closing the gate valve between the deposition chamber and the main chamber. To perform a Hall effect measurement, the magnet holder was moved so that the sample was in the centre between the two magnets. The sample surface was perpendicular to the magnetic field.

Figure 5.27 shows a diagram of the circuit used to perform Hall effect measurements. The contact numbers in the figure match up with the contact numbers of Figure 5.24(a). A constant electrical current was passed between Contacts 1 and 5, and Hall voltage was measured between Contacts 3 and 7. A constant current source was obtained by connecting a high resistance ($R_L >> R_s$, where R_L and R_s are the large resistance and the sample resistance respectively) with the sample in series and applying a constant voltage across both (the sample and the resistance) as shown in Figure 5.27. Since the total resistance was constant ($\sim R_L$), the current passing through the circuit was also constant.

The voltage between Contacts 3 and 7 was measured before, during, and after the sample was placed in the magnetic field. This measurement procedure was used to ensure that the voltage across these contacts was zero without the magnetic field. The sample's temperature was controlled during the measurement as described in Section 2.3.

Figure 5.26 The two magnets fixed inside the holder. The holder is attached to a linear translator.

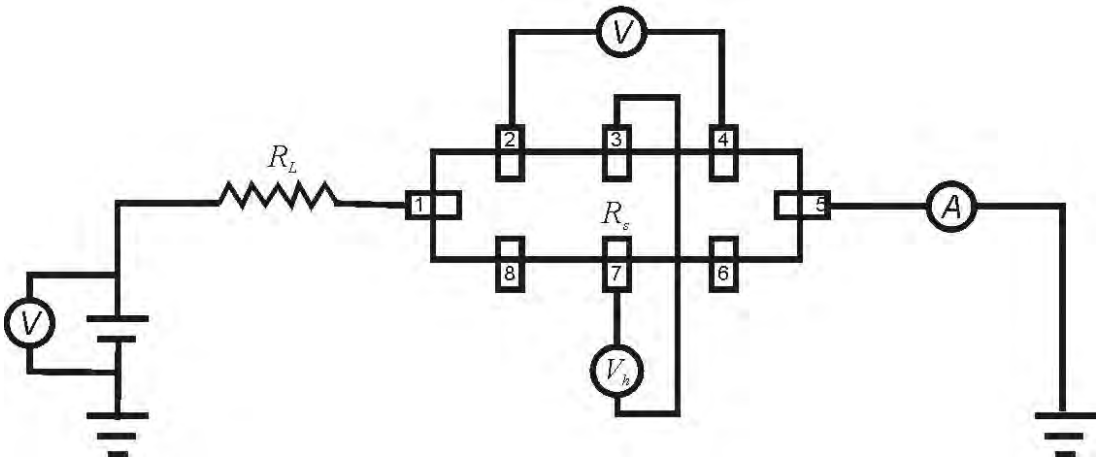

Figure 5.27 The Hall effect measurement circuit. The contacts are labelled as in Figure 5.24(a).

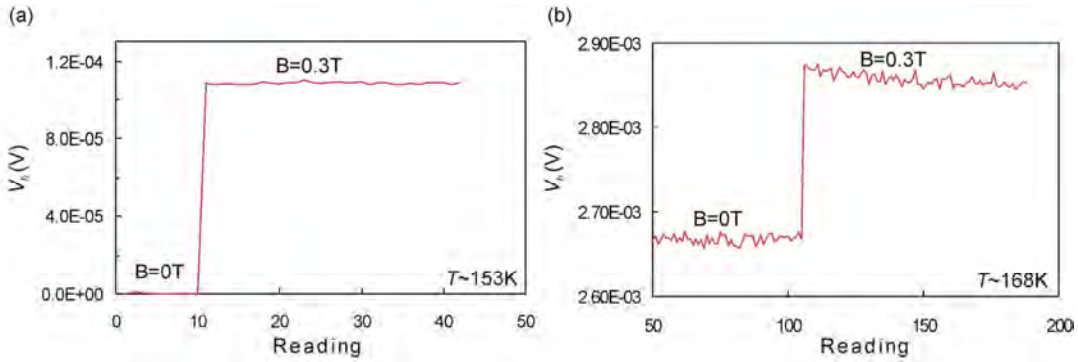

Figure 5.28 V_h using a 0.3T magnetic field for (a) S31 (no offset), and (b) S36 (offset voltage).

5.5.3. Hall effect results

The results presented in this subsection include the dependence of the Hall voltage, Hall coefficient, and carrier concentration on temperature.

Figure 5.28(a) shows an example of a V_h measurement for S31. The V_h values are ~0 in the absence of the magnetic field and ~1.1x10^{-4}V with the magnetic field. In comparison, Figure 5.28(b) shows an example of a V_h measurement for S36. The figure shows an offset of ~2.67x10^{-3}V in the absence of the magnetic field. The offset voltage is discussed in the next subsection. Hall effect measurements were performed for 10 samples. The samples showed potential differences across Contacts 3 and 7 when they were exposed to the magnetic field, and V_h increased as their temperatures decreased. However, offset voltages before the samples were placed in the magnetic field were measured for all samples except for S31. Although carrier concentrations obtained for the samples with offset voltages at room temperature were between 3.1x10^{24} and 4.0x10^{24}m^{-3}, which is consistent with the literature values,[16, 17] the focus here is on the results of the sample without offset voltage (S31).

Figure 5.29 shows the temperature dependence of Hall voltage and Hall coefficient for S31 in the temperature range of 153-290K. The sample 'died' after taking these measurements. The deposition conditions of S31 are: inert-gas Ar flow rate of 100sccm, cluster film thickness of 94.5nm (measured using the FTM), and a resistance of ~136kΩ. The arrows in Figure 5.29(a) indicate the zero value of V_h without any magnetic field, i.e. B=0T at these points. Figures 5.29(a) and 5.29(b) show that as the temperature decreases, the Hall voltage and the coefficient increase.

Equation 5.7 and R_h values, in Figure 5.29(b), were used to calculate n. Figure 5.30 shows the dependence of n on temperature between 153 and 290K. The figure shows that as the temperature decreases from 290 to 153K, n decreases by a factor of ~100. Most of the decrease in n occurs between 250 and 290K, while a smaller decrease can be observed between 153 and 170K.

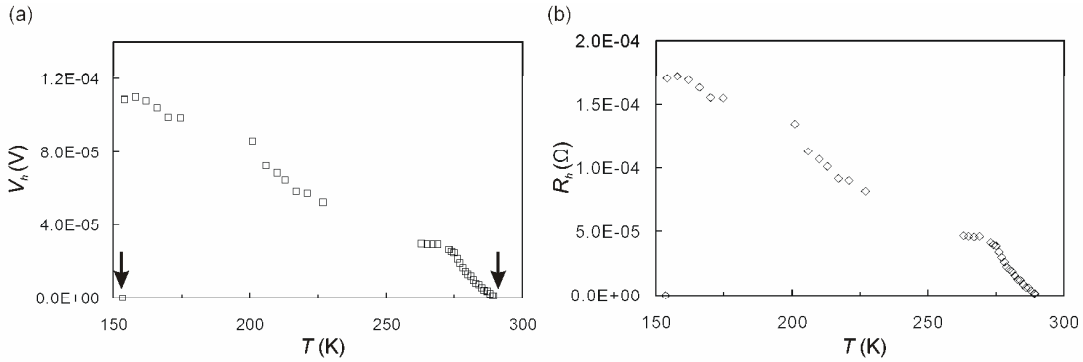

Figure 5.29 The dependence on temperature of (a) Hall voltage and (b) Hall coefficient of S31 taken at B=0.3T. The arrows in the figure indicate the points with B=0T.

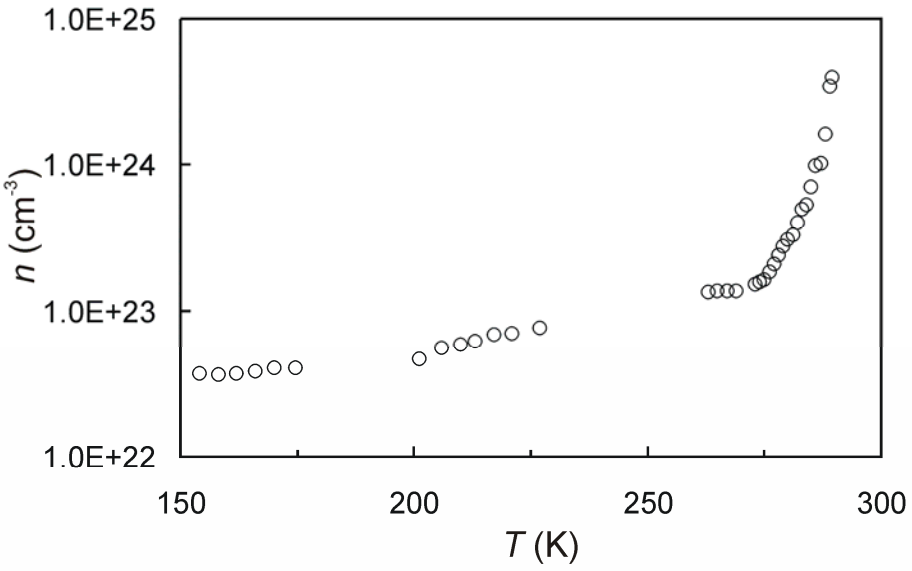

Figure 5.30 The temperature dependence of n for S31.

5.5.4. Discussion

Various research groups have previously studied the temperature dependence of the carrier concentration of bulk Bi,[36, 37] Bi thin films,[16, 17, 19] and Bi single crystal nanowire.[14] The carrier concentration was found to depend on factors, such as, the sample temperature,[16] sample preparation method,[16, 17, 19] sample crystallinity,[36, 37] and sample dimensions.[14, 16] Nevertheless, all reported values of *n* for different samples were found to be of the order of ~$10^{24}$$m^{-3}$ at room temperature, and they decreased as the sample temperature decreased. Although the temperature dependence of *n* of Bi cluster films had not been reported in previous studies (to the best of our knowledge), the measured *n* at room temperature and its general dependence on temperature are in agreement with the previous reports as shown in Table 5.4.

To compare *n* of S31 with those of the bulk and nanowire Bi, the normalized carrier concentrations to the room temperature concentrations are plotted in Figure 5.31. The figure is produced using *n* in Figure 5.30, the bulk *n* taken from References [37, 38], and *n* of 65nm Bi single crystal wires taken from Reference [14]. The figure shows that *n* increases with temperature for all Bi structures. The figure also shows that as the temperature decreases from 290 to 153K, the carrier concentrations of bulk, nanowire, and cluster wire decrease to around 40, 10, and 1%, respectively, of their room temperature values. The sharp decrease of the carrier concentration with temperature for the cluster sample compared with that of the bulk is not surprising because such a decrease has been observed for single crystal nanowire.[14] However, the low values of the carrier concentration for the cluster sample compared to the single crystal nanowire at low temperatures can be understood by studying many effects, such as the smaller size of the cluster (~33nm) than the single crystal nanowire (~65nm); the confinement in three dimensions for the cluster; and the random crystal orientations of clusters within the sample. In fact, it is believed that as the temperature increases the rapid increase of *n* for nanocluster Bi samples (compared with that of bulk Bi) outweighs the decrease in the carrier mobility.[14] This is the main reason behind the negative TCR discussed in Section 5.6.

Table 5.4 Reported values of n at room temperature.

Bi structure	***n*** **(m^{-3})**	**Reference**
Bulk	$2.45x10^{24}$	37
Thin film	~$4x10^{24}$	17
Thin film	$2.5x10^{24}$ - $4x10^{24}$	16
Thin film	~$1x10^{24}$	19
Cluster film	~$4x10^{24}$	This study

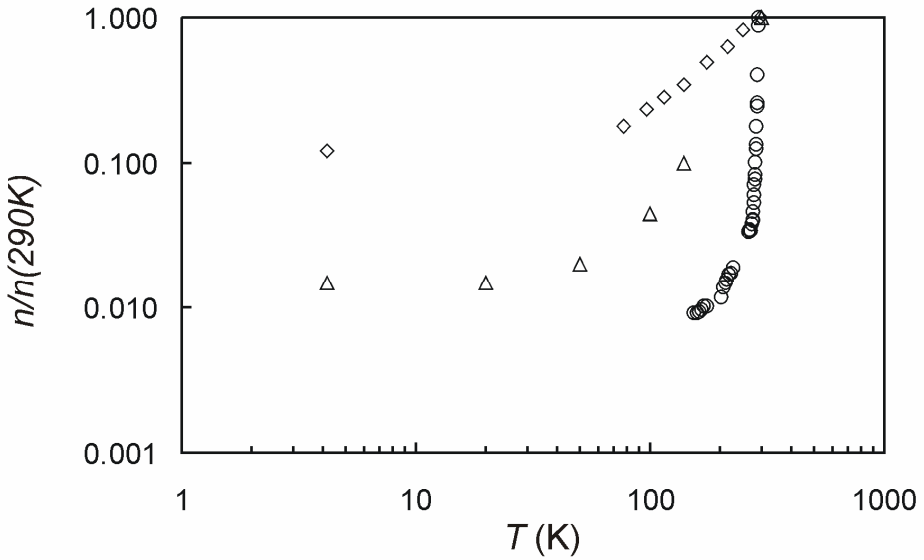

Figure 5.31 The temperature dependence of the normalized carrier concentration for bulk Bi[37, 38] (diamonds), 65nm single crystal nanowires[14] (triangles), and S31 (circles).

A cluster film with cluster coverage at the percolation threshold provides a continuous network of clusters that allows an electrical current to flow through it. All the samples with cluster coverages around the percolation threshold (onset of conduction) had an offset in V_h in the absence of a magnetic field. The offset was not observed for the sample with cluster coverage above the percolation threshold (S31). Since the current was passed between Contacts 1 and 5 (the far contacts) during Hall measurements, no current was supposed to flow to the transverse contacts before the magnetic field was applied. The appearance of the offset can be understood in terms of equipotential surfaces as illustrated schematically in Figure 5.32. No offset voltage should be observed if the cluster network between Contacts 3 and 7 is parallel to the equipotential surfaces, as shown in Figure 5.32(a). However, this is not the case for cluster films deposited at the percolation threshold. The continuous cluster network between Contacts 3 and 7 might not be parallel to the equipotential surfaces as illustrated in Figure 5.32(b). Hence, an offset in V_h which is equal to the difference between the two equipotential surfaces in the figure will appear. Depositing more clusters after the onset of conduction creates extra cluster conduction paths and increases the probability that one of them is parallel to the equipotential surfaces. Thus, no offset in V_h was observed for S31.

Finally, it is worth comparing n of Bi with those of other elements in group (V) of the periodic table, such as, antimony and arsenic.[37] n of bulk Bi decreases by an order of magnitude when the temperature decreases from 290 to 4.2K, while it is almost constant for these elements in the same temperature range.[39, 40] Since n for Bi clusters decreases two order of magnitudes lower than that of the bulk when the temperature decreases from 290 to 4.2K, n is expected to decrease for antimony and arsenic clusters with temperature rather than staying constant.

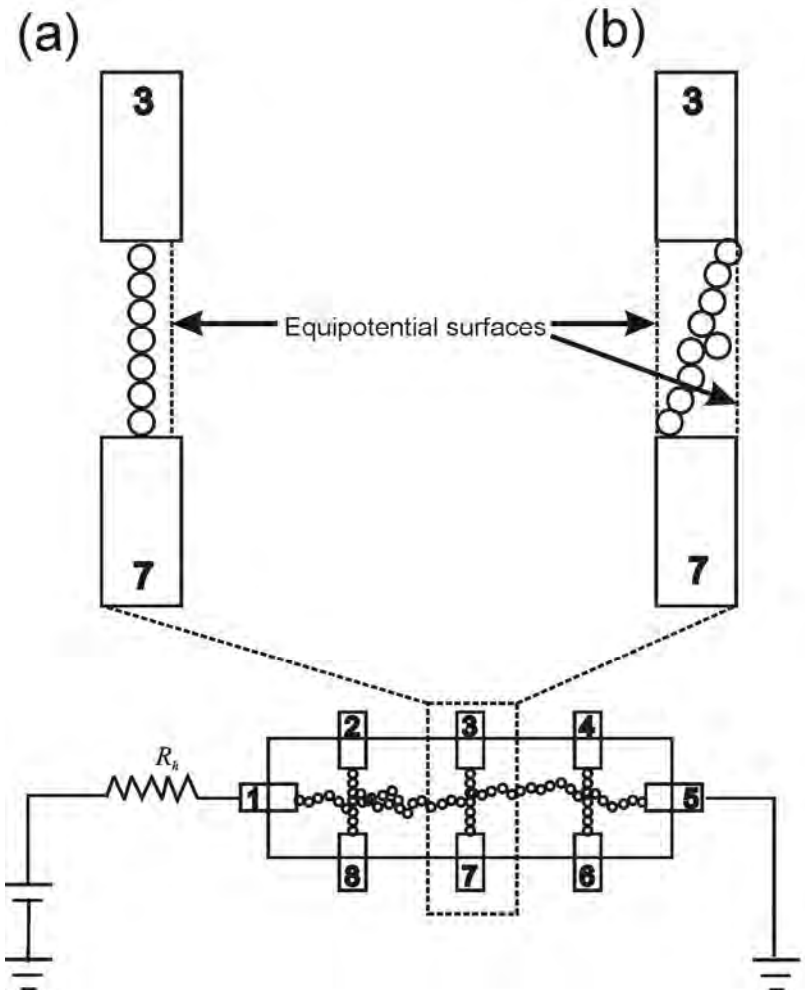

Figure 5.32 Schematic diagrams show continuous networks of clusters aligned between Contacts 3 and 7 within a sample. (a) The network is parallel to the equipotential surface. (b) The network is aligned between two equipotential surfaces.

5.6. Temperature dependence of the resistance

This section discusses the temperature dependence of the resistance of Bi cluster wires. The results are presented in the first subsection. The next two subsections include data fitting and discussions.

5.6.1. *R(T)* results

The results presented in this section are for S9-S11. These samples were not used for the gate effect study. Although their dimensions and deposition conditions will not be discussed in this section, they are given in Table 5.5 since these samples were not presented before.

Figure 5.33(a) shows *R(T)* curves for S9-S11 in the temperature range of 4.2-290K. *R(T)* measurements were performed using a fixed voltage of 100mV as described in Section 2.3. Figure 5.33(b) shows *I(V)* curves for S11 at 4.2, 85, and 290K in the voltage range between −100 and 100mV. The figures show that the resistances of the

three samples decrease as their temperatures increase. This is described as a negative temperature coefficient of the resistance (negative TCR). Figure 5.33(a) shows that the temperature dependence on the resistance at low temperatures (below 50K) is small. It should be noted that the *R(T)* measurements in Figure 5.33(a) were taken while heating the samples from 4.2 to 290K. However, a similar temperature dependence of the resistance was observed while cooling the samples down in the same temperature range. The negative TCR was also observed for all measured Bi cluster wires regardless of the differences between wires, i.e. the dimensions, deposition conditions, and resistances. Therefore, the negative TCR is a property of Bi cluster wires.

Attempts to fit the temperature dependence of the resistance to various models were made. The fitting helps to understand the carrier transport in the cluster wires. The resistance of a typical disordered metal increases as $\sim T$ in the temperature range of 4.2-290K.[41] Bulk Bi is different from other metal (as discussed in Section 1.3) because its resistance increases as $\sim T^2$ in the same temperature range.[36, 37] Neither of the above dependences on temperature can be fitted to the *R(T)* curves of S9-S11. Hence, different dependences of the resistance on temperature with negative TCR are considered to fit the results such as those of semiconductors and granular metallic regions separated by non-conducting barriers.[3] The temperature dependence of the resistance did not follow Arrhenius dependence (Figure 5.33(a)), i.e. it is not an activated dependence. However, the *R(T)* curves were found to fit to Sheng's model (Equation 1.3)[42] at temperature below 77K. This model describes the electrical conduction between metallic regions separated by non-conducting materials. Nevertheless, the fit to Sheng's model will not be discussed here since they could not be verified.

Table 5.5 The deposition conditions, and the wire and V-groove dimensions of S9-S11.

Sample	Ar flow rate (sccm)	Nominal deposited material (nm)	*W* (μm)	*L* (μm)	*w* (μm)
9	130	12.3	0.42	100	2.1
10	160	13.2	0.72	4.6	2.5
11	200	10.6	0.71	3.5	2.8

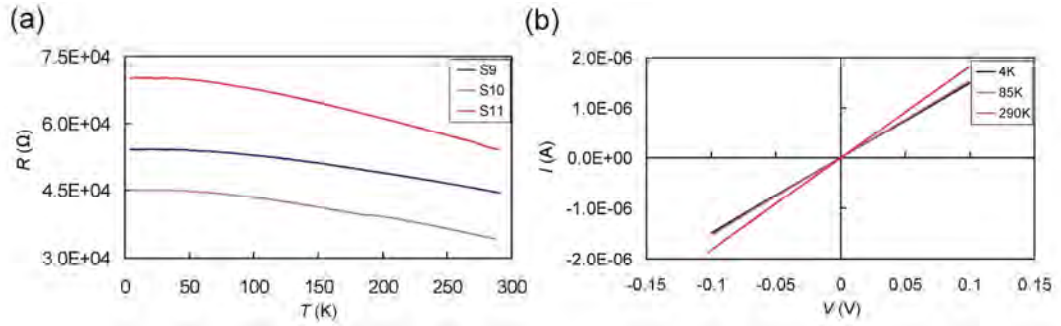

Figure 5.33 (a) The temperature dependence of the resistance of S9, S10, and S11. (b) I(V) curves of S11 at 4.2, 85, and 290K.

5.6.2. Discussion

Whereas positive TCR was reported previously for bulk Bi,[14, 37] Bi cluster wires had negative TCR. The positive TCR is consistent with the fact that bulk Bi is a semimetal. In the following, the negative TCR for Bi cluster wires is discussed and it is argued that it is due to the increase in the carrier concentration as the temperature increases.

The carrier concentration measurements presented in Section 5.5 show that the carrier concentration decreases from $3.5 \times 10^{24} m^{-3}$ to $3.7 \times 10^{22} m^{-3}$ as the temperature decreases from 290 to 150K. The measurements also show that the decrease of the carrier concentration as the temperature decreases is two orders of magnitude more than that of bulk Bi.[37]

The carrier mobility of Bi single crystal nanowires was found to increase as the temperature decreases and it saturates at temperatures below 70K (Figure 1.3).[14] This is different from the carrier mobility of bulk Bi where it increases continuously as the temperature decreases and its value is one order of magnitude larger than that of the nanowires at 4.2K.[14, 36, 37] For Bi cluster wires, it is likely that the mobility dependence on temperature is reduced at temperatures below 70K (compared with bulk) because the dominant scattering mechanism is the boundary scattering, while phonon scattering which gives rise to the mobility is minimal.[14, 43]

The negative TCR can be explained in terms of the carrier concentration of Bi cluster wires and using

$$\sigma(T) = e\mu(T)n(T) \tag{5.10}$$

where e is the electron charge, and $\sigma(T)$, $\mu(T)$, and $n(T)$ are the temperature dependent conductivity, carrier mobility, and carrier concentration respectively. As the temperature decreases from 290K to 4.2K, the decrease in carrier concentration outweighs any increase in carrier mobility.[14] This behaviour is different from that of bulk Bi[36, 37] where increasing the carrier mobility outweighs the decrease of the carrier concentration. The temperature dependence of the resistance for Bi cluster wires is consistent with the reported results for single crystal Bi nanowires with diameters below 65nm.[14]

5.7. Annealing the wires or depositing on hot substrates

The cluster wires presented in this section were prepared either by depositing Bi clusters on hot V-groove sample or by depositing the clusters on V-groove samples and then anneal them. The terms ‘hot substrate’ and ‘annealing’ will be used in the following to describe the two types of samples, and the term ‘heat treatment’ will be used to describe both. The effects of the heat treatment on the cluster wire morphology and electrical properties are discussed in this section. The results are presented in three subsections. The last subsection provides discussions.

5.7.1. Wire morphology

Figure 5.34 shows the FE-SEM images of S12-S16 used in this study. S12-S14 were deposited and then annealed up to a temperature of 373K (for S12 and S13) and 413K (for S14). S15-S16 were deposited on hot substrates at 373K and the heater was switched off after cluster deposition. All samples showed onsets of conductions. The gray areas in the images are Au/NiCr contacts. The figure shows that the wires are formed of large aggregates of coalesced clusters which are different from the wires presented in Section 5.1. The dimensions of the wires and V-grooves of S12-S16 are shown in Table 5.6 along with the deposition conditions as discussed below.

Figure 5.34 also shows that S12 is discontinuous. The discontinuity occurred due to the annealing. S14 has the narrowest wire and it is a solid wire. This wire has some bottlenecks (pointed by the arrows in Figure 5.34(c)) where the wire becomes very narrow. Most of the clusters forming S15 are molten which form a solid wire. S12 and S13 'died' when their temperature became ~373K, while S14 was 'functional' until venting the deposition chamber. The difference between S12-S13 and S14 is that cluster deposition was stopped directly after the onset of conduction for S12-S13, while extra clusters of (nominal thickness ~12Å) were deposited after the onset of conduction for S14. Additional annealing occurred for S15 when the electrical current through this sample increased suddenly because of a sudden decrease in the sample resistance. This sudden change produced a power across the wire of ~$2X10^{-5}$W (using V_{SD}=0.1V and I_{SD}=0.2mA). This power is the highest power applied across any Bi cluster wire in this study, and it is believed to be the reason behind melting S15. S16 was 'functional' until venting the deposition chamber.

The wire widths of S12-S16 were used to estimate the cluster bouncing angle (φ) as explained in Section 2.3. φ was between 14.6 and 17.2 for all samples. This range is consistent with the bouncing angles found in Section 4.4.

5.7.2. The dependence on temperature of the resistance

Figure 5.35 shows *I(V)* curves taken during annealing at temperatures between 290 and 373K for S12. The curves are linear in the voltage range between −0.1 and 0.1V. *I(V)* curves of resistances above ~100kΩ show some noise. All the other samples also showed linear *I(V)* curves in the above voltage range. The measurement temperatures are labelled on the figure. The sample resistance increases from ~44kΩ at 290K to ~204kΩ at 337K. The resistance then decreases with increasing temperature (to ~373K) to ~68kΩ before the sample 'dies'.

S13 had an onset resistance of ~11.6kΩ at room temperature. The resistance decreased with annealing to ~7.4kΩ at 373K. The resistance increased suddenly at 373K to ~10.3kΩ and the sample then 'died'. The resistance of S14 was changing in steps (increasing and decreasing). S15 had an initial resistance of ~4.7kΩ after the onset of conduction at 373K. The resistance dropped suddenly to ~490Ω at 363K and the sample then 'died'. S16 had resistances of ~20.6kΩ and ~22.0kΩ at 373K (after the onset of conduction) and 290K respectively. No sudden changes in the resistance of this sample were observed. In summary, the change of resistance in steps is a

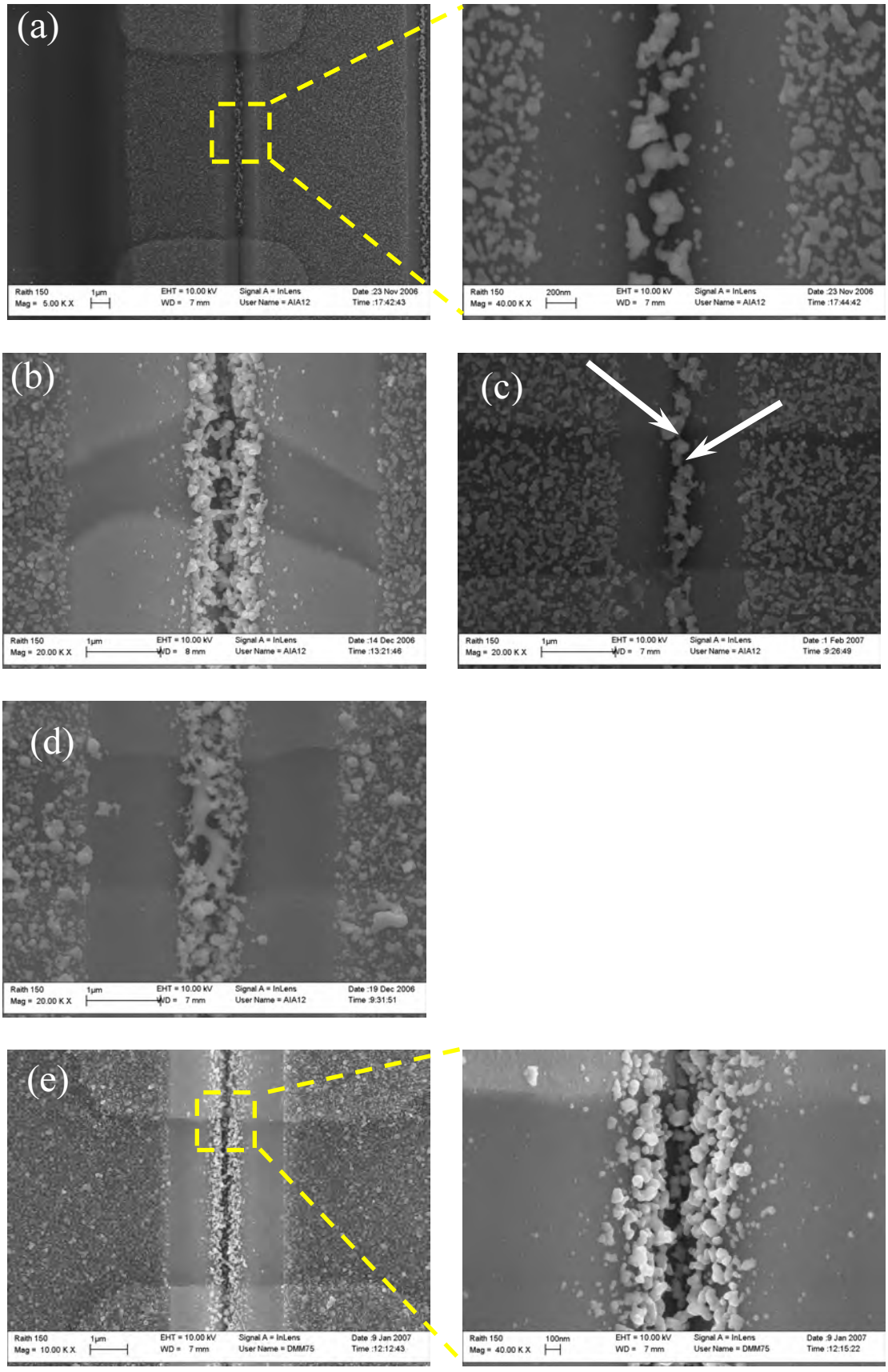

Figure 5.34 FE-SEM image of S12-S16, (a)-(e) respectively. The arrows in (c) point to the bottlenecks.

Table 5.6 The wire widths and length (W and L), V-groove width (w), inert-gas Ar flow rate, mean thickness (Θ), and substrate and annealing temperatures (T_{sub} and T_{ann}) for S12-S16.

Sample	Ar flow rate (sccm)	w (µm)	W (µm)	L (µm)	Θ (nm)	T_{sub} (K)	T_{ann} (K)
12	150	1.76	0.41	9.98	14.6	290	373
13	150	4.23	0.87	1.48	8.8	290	373
14	50	1.69	0.23	1.79	7.8	290	413
15	150	3.43	0.65	1.89	23.2	373	
16	150	3.12	0.78	4.48	12.4	373	

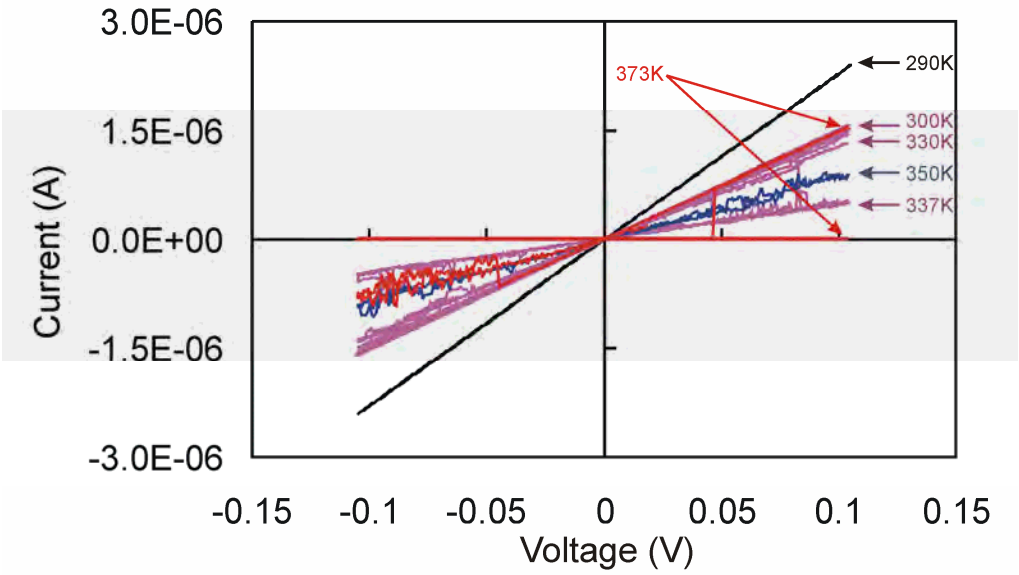

Figure 5.35 I(V) curves for S12 during annealing. The annealing temperatures are colour coded and quoted next to each I(V) curves.

common feature among the annealed samples, while the smooth increase of resistance as temperature decreases is a feature of samples deposited on hot substrates. The temperature dependences of the resistances for S14 and S16 are given as examples for those two categories in Figure 5.36. It should be noted that the measurement was taken while heating S14, whereas it was taken while cooling S16.

5.7.3. Gate effect results

This section focuses mainly on the gate effect results of S14 and S16. This is because S12, S13, and S15 'died' before any gate measurements were taken for them. However, one gate measurement run for S13 was taken while the sample temperature was increasing and it will be used for a qualitative argument.

Figures 5.37-5.39 show gate measurements for S13, S14, and S16. The measurements were taken at ~326K, ~300K, and ~290K for S13, S14, and S16 respectively. Contant V_{SD} of 50mV was used for S13 and S14 and V_{SD} of 150mV was used for S16. Each figure shows an increase in I_{SD} as a positive voltage is applied to the gate. S13 shows

an increase in I_{SD} at negative voltages. This increase is due to the increase of the sample temperature during the measurements.

The gate effects of S14 and S16 are similar to that of S4 discussed in Section 5.3. $\Delta I/I_{SD}$ is about 0.03% and 0.05% for S14 and S16. No obvious change in I_{SD} can be seen when applying a negative voltage to the gates. The gate effect appeared for both samples once their temperatures cooled down to room temperature and it was reproducible.

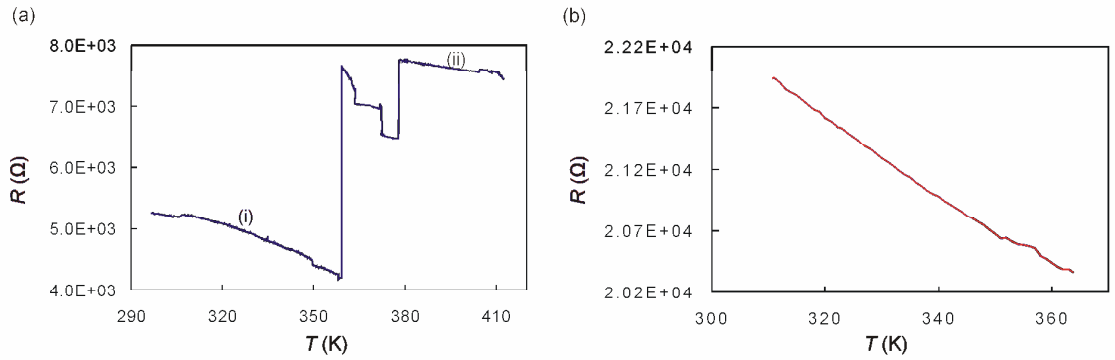

Figure 5.36 R(T) for S14 (a) and S16 (b). (i) and (ii) label the fragments of the curve with negative TCR.

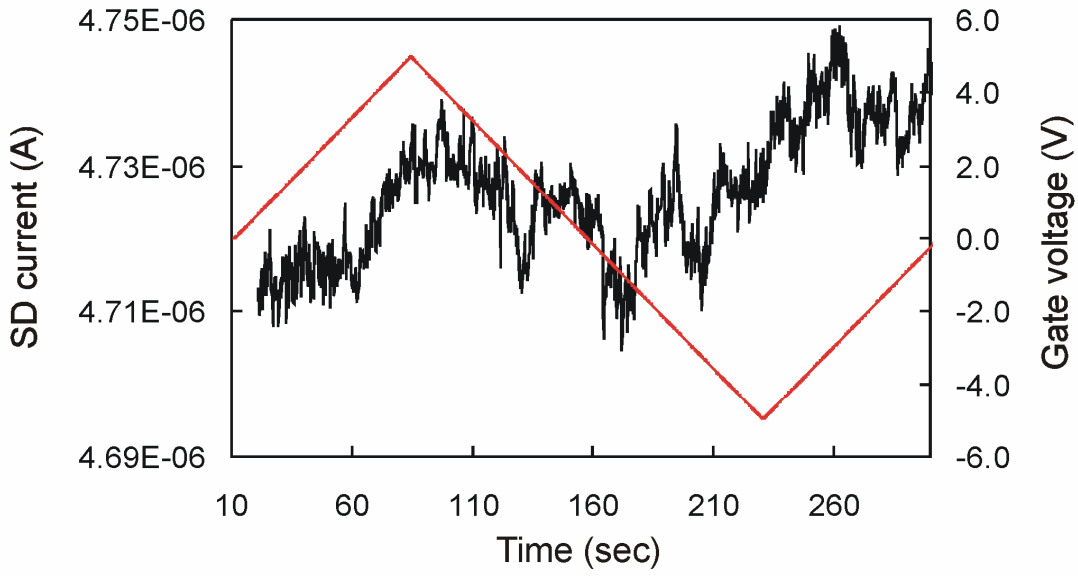

Figure 5.37 The changes in I_{SD} (black line) with time when changing the gate voltage (red line) for S13.

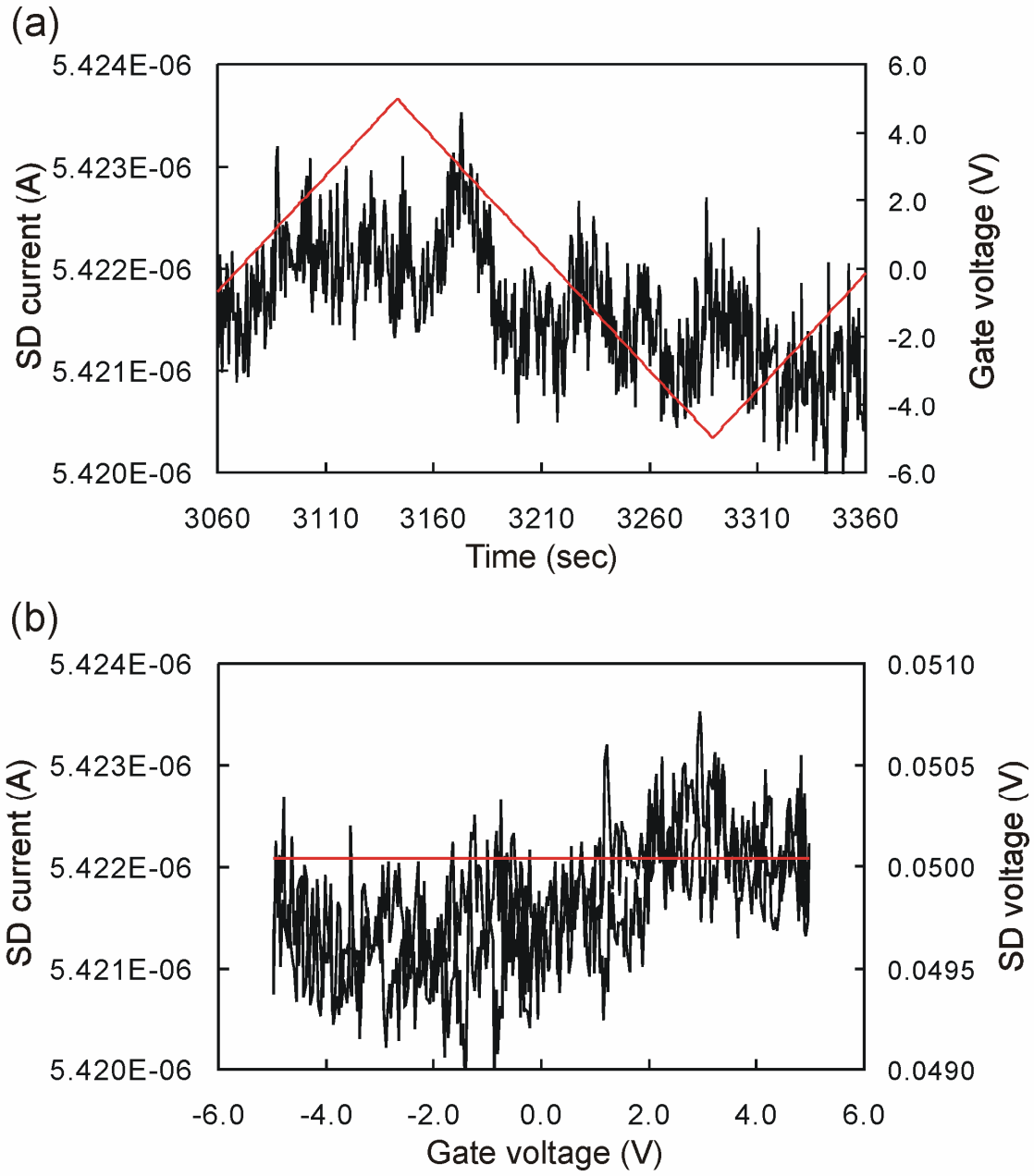

Figure 5.38 The change in I_{SD} (black line) with time when changing the gate voltage (red line) (a), and the dependence of I_{SD} (black line) and V_{SD} (red line) on the gate voltage (b) for S14.

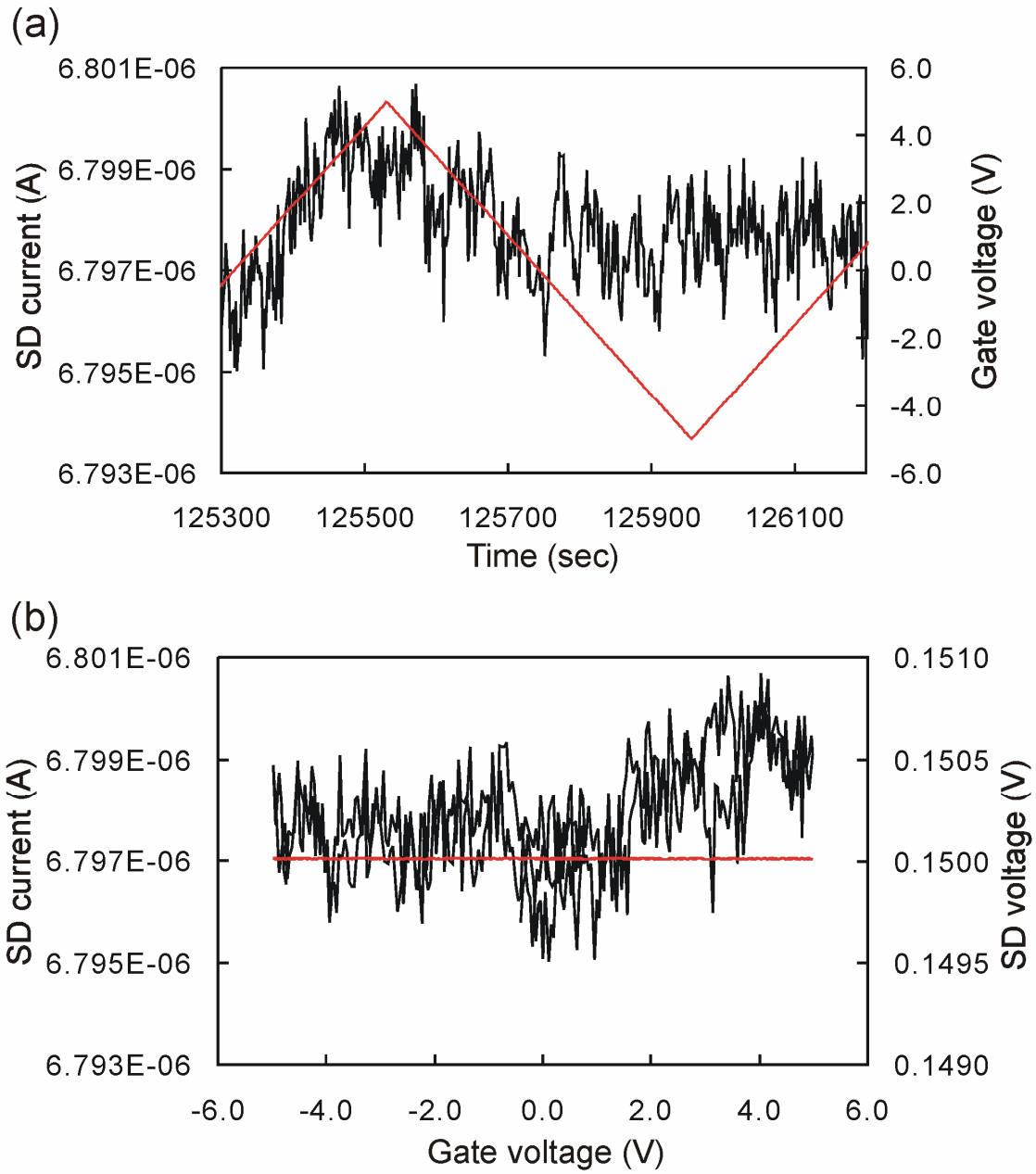

Figure 5.39 The change in I_{SD} (black line) with time when changing the gate voltage (red line) (a), and the dependence of I_{SD} (black line) and V_{SD} (red line) on the gate voltage (b) for S16.

5.7.4. Discussion

The heat treatment of Bi cluster wires changed the morphology of the wires. Most of the wires were formed of large aggregates of clusters. The change in the morphology can be assigned mainly to and the clusters' coalescence when annealing the samples [28] (except for S15). The beading of the cluster aggregates of S12 into separate islands in Figure 5.34(a) provides an example for this effect. It should be noted that beading the clusters of S12 is unlikely to be mainly due to the resistive heating of the electrical current because of the low electrical power passed through this sample (maximum of ~2.4x10^{-7}W using V_{SD}=0.1V and I_{SD}=2.4x10^{-6}A), and since all the clusters including those which are not within the current path are beaded.

Stopping cluster deposition once an onset of conduction is observed means that there is at least one point through the wire where the electrical conduction occurs through a single conduction path. Annealing such a wire includes the risk of forming a discontinuity at that point in the wire when the clusters start beading, as for S12. This risk can be overcome using two methods: forming a narrow and dense wire or forming a wire with regular width and homogeneous round cross section. The latter was achieved previously using Sb clusters (which are less sticky than Bi clusters).[44] However, this is not possible for Bi clusters because of their greater stickiness (see Section 4.4). Hence, S14 was used to test the former method (i.e. using a narrow and dense wire) using the narrowest V-groove in this study (w~1.69μm), and by depositing extra clusters of 12Å after the onset of conduction was observed. Decreasing the V-groove width decreases the wire width (Section 4.4). It should be noted that since depositing extra clusters may form a continuous network of clusters on the V-groove plateaus, a source-inlet Ar flow rate of 50sccm was used to fabricate this sample. Some clusters were found to bounce off the plateaus when using this flow rate which decreases the plateau coverage (Section 4.3), while all the clusters deposited within the V-groove are likely to be trapped inside it. The plateau coverage of S14 was measured as explained in Section 2.3 and it was ~50% which is less than the percolation threshold. This sample was successfully annealed up to 413K while maintaining a continuous wire.

The steps in *R(T)* toward low resistance during annealing the wires (Figure 5.36(a)) are a result of clusters' coalescence. However, further increase of the sample temperature produced steps toward high resistance where conduction paths might get lost (Section 5.2). The two bottlenecks pointed out by the arrows in Figure 5.34(c) support the idea that further annealing of S14 is likely to cause discontinuities at those bottlenecks. A cluster wire with many current conduction paths can be speculated as a group of resistances connected on parallel. Losing a current path (resistance) increases the total parallel resistance. It should be noted that the negative slope of the *R(T)* curve (fragments (i) and (ii) in Figure 5.36(a)) is due to the negative TCR discussed in Section 5.6.

Unlike S1-S7 (Section 5.3), the gate effect was observed for the heat treated samples directly once their temperatures stabilized. The gate effect of those samples was sustainable during their lifetime, and it was similar to that of S4.

The heat treatment enhanced the conduction of a cluster wire by enhancing the carrier transport between clusters (as explained above). The heat treatment might also have other effects on the cluster wires such as decreasing the oxidation rate of the clusters by decreasing the amount of water on the sample,[6] reducing an existing Bi-oxide layer between a wire and contacts (Reichel observed a change of the *I(V)* curves from non-linear to linear when he annealed Bi cluster wires),[2] and enhancing the clusters' crystallinity.[16]

Although S14 had two bottlenecks, its *I(V)* curves were linear. This means that the non-linearity observed for the samples in Section 5.2 is unlikely to be because of bottlenecks. This is also confirmed by the linear 4-point *I(V)* measurements taken by Reichel for similar wires where he observed linear *I(V)* characteristics.[2]

In conclusion, the wires produced by depositing Bi clusters on hot substrates have longer lifetimes than those annealed after deposition. This is because, unlike the wires annealed after deposition, the clusters are not expected to undergo further melting once their temperature and resistance are stabilized. Depositing Bi clusters on hot substrates has another advantage where heating the substrate evaporates any water residues on it[6] which reduces the initial cluster wire oxidation. A small gate effect was observed for all of the heat treated samples. This effect was sustainable for the samples' lifetimes.

5.8. Mean thickness versus wire length

This section discusses the dependence on the wire length of the mean thickness required to form an electrically conducting wire. Results are presented first. This is followed by a discussion of the results.

Although sample fabrication is described in Section 2.2, the special features of the samples used in this study are described here. Each sample contains two V-grooves with a fixed width (w) of 3.75±0.40μm. The difference between the widths of each pair of V-grooves within a sample was less than 5%. The length of the first wire was fixed at 1.75±0.40μm, while the length of the second wire varied between 1.75±0.40μm and 47.00±0.40μm. The first wire was used as a reference for the mean thickness since the cluster coverage was not homogeneous within the cluster beam spot. Nevertheless, the cluster coverage was homogeneous within the wire dimensions and the separation between the two V-grooves (<100μm).

Bi clusters used in this study were produced using an inert-gas Ar flow rate of 180sccm. A constant voltage of 100mV was applied between the samples' electrodes for the onset of conduction measurements. For all samples, the onset of conduction was observed first for the shorter wire. Cluster deposition was continued until an onset of conduction was observed for the longer wire. The onset times and deposition rate (measured using the FTM) were used to calculate the mean thicknesses of the deposited clusters.

FE-SEM images with a magnification of 20000x were used to measure wire widths. The widths of the reference and longer wires were the average of 10 and 20

measurements, respectively, of each wire width. The uncertainty in the wire width is considered as one standard deviation.

FE-SEM images with a magnification of 40000x of the plateaus next to the V-grooves were used to calculate the cluster coverage as described in Section 2.2. It should be noted that this coverage corresponds to the mean thickness required to provide an onset of conduction for the longer wire since cluster deposition was stopped after the onset of conduction was observed for the longer wire.

5.8.1. Results

The dependence of the mean thickness required to provide an onset of conduction (Θ) on the wire length (L) was studied using thirteen samples (S17-S29). The dimensions of the longer wires of these samples are shown in Table 5.7 along with the onset times (t_1 and t_2), the cluster deposition rate, Θ (calculated form the onset times and deposition rates), and the corrected cluster coverage (p) on the plateaus calculated from the FE-SEM images (see Equation 4.1). In the following, the subscripts '1' and '2' refer to the reference and longer wires, respectively. The table shows some variation in Θ_1 although the lengths of the reference wires were similar. This is likely to be due to the inhomogeneity of cluster coverage within the cluster beam spot. However, the changes of Θ_2 and p are consistent with that of Θ_1, which verify the need of reference wires in this study.

Figure 5.40 shows FE-SEM image of the reference wire of S17. The image shows that the wire exhibits a V-shape rather than a compact wire. The average width (W_1) of this wire is 0.81±0.16μm. The image also shows that the clusters forming the wire are stacked on top of each other. The above were common features among S17-S29 although they were different in their lengths.

Table 5.7 t_1, t_2, deposition rates, L, W, Θ, and p for S17-S29. The subscripts 1 and 2 refer to the reference and the longer wires.

Sample	t_1 (sec)	t_2 (sec)	Deposition rate (Å/sec)	L_2 (μm)	W_2 (μm)	Θ_1 (Å)	Θ_2 (Å)	p
17	200.8	205.6	0.43	1.80	0.81	86.34	88.41	0.67
18	199.2	216.1	0.43	4.78	0.86	85.66	92.92	0.73
19	182.8	230.2	0.43	23.60	0.98	78.60	99.12	0.89
20	212.3	226.2	0.46	1.71	0.74	96.60	102.92	0.65
21	279.8	320.4	0.45	4.60	1.06	124.51	142.58	0.69
22	244.5	302.3	0.47	23.51	0.82	113.69	140.57	1.05
23	175.0	183.0	0.42	1.63	1.08	73.50	76.86	0.78
24	180.0	216.0	0.44	10.49	0.77	79.20	95.04	0.84
25	202.0	220.0	0.45	23.53	0.86	90.90	99.00	0.82
26	188.0	249.0	0.41	23.58	0.90	77.08	102.09	0.97
27	98.0	107.0	0.41	1.47	0.45	40.18	43.87	0.40
28	153.0	172.0	0.41	9.97	0.63	62.73	70.52	0.92
29	140.0	182.0	0.41	47.30	0.50	57.40	74.62	0.99

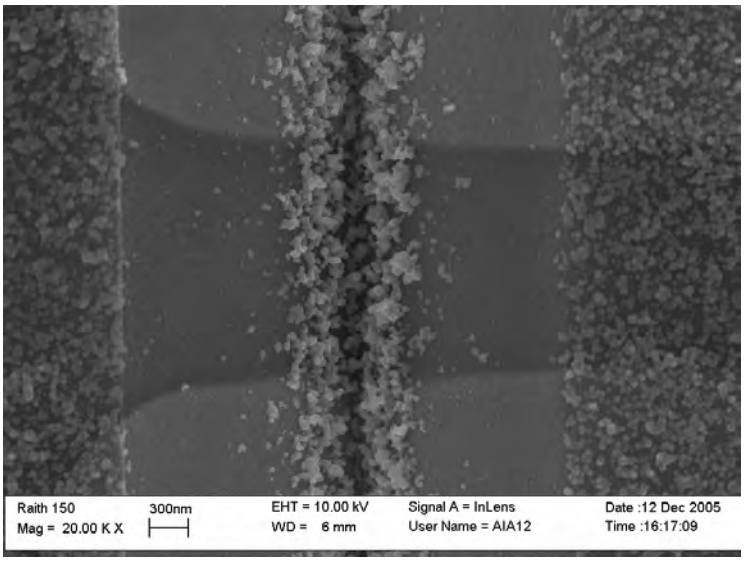

Figure 5.40 FE-SEM image of the reference wire of S17.

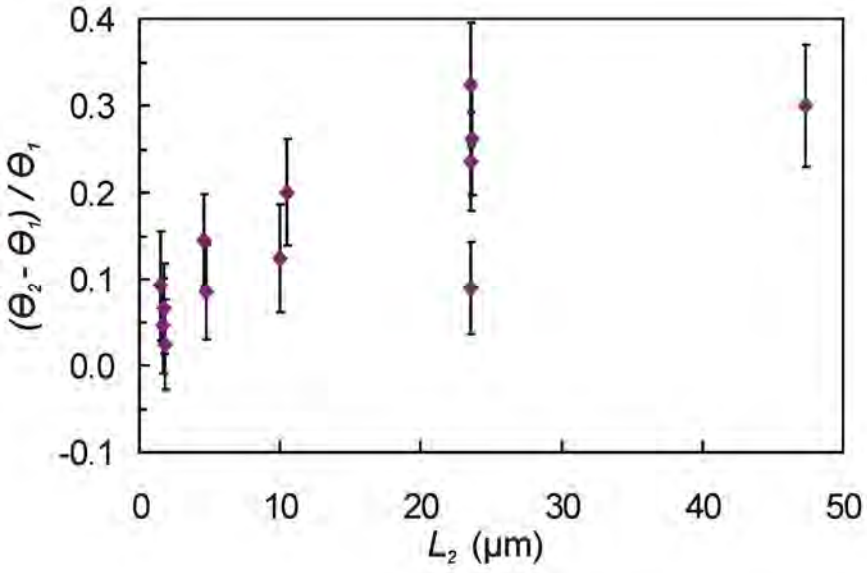

Figure 5.41 The dependence of $((\Theta_2 - \Theta_1) / \Theta_1)$ on L_2.

Figure 5.41 shows the dependence of the relative thickness of the clusters required to provide an electrically conducting wire ($(\Theta_2 - \Theta_1) / \Theta_1$) on the wire length ($L_2$). The figure shows that as L_2 increases from ~1.75 to ~47.30, ($(\Theta_2 - \Theta_1) / \Theta_1$) increases from ~0.05 to ~0.30. Most of the increase in ($(\Theta_2 - \Theta_1) / \Theta_1$) occurs at small L_2, and it appears to saturate at L_2>20μm.

Since the cluster wires consist of clusters stacked on top of each other, p was used to estimate the number of cluster layers required to form the longer wire (n_2). If we assume that the number of clusters per unit area which landed and stuck on the plateaus is similar to the number of those that landed and were trapped inside the V-groove,

$$n_2 = 0.5238 \times p \times \frac{w_2}{W_2} \tag{5.8}$$

The factor (0.5238) in Equation 5.8 is the packing factor used in Section 4.3 (since the clusters are assumed to be spheres or hemispheres rather than cubes). The dependence of n_2 on L_2 is shown in Figure 5.42. The solid line is a linear fit for the data. The figure shows that the number of the cluster layers increases as the wire length increases. The figure also shows that a ~1.57 cluster layer is required to provide an onset of conduction for a wire with $L_2 = L_1$.

5.8.2. Discussion

It was shown in Section 4.4 that using V-grooves with a fixed width provides wires with a fixed average width. This is also illustrated in Table 5.7, where only small variations in W_2 can be observed, i.e. the average value of W_2 is 0.80μm and the standard deviation is 0.19.

The average value of W_2 (Table 5.7) can be used to estimate the cluster bouncing angle as explained in Section 2.3. The average W_2 corresponds to a bouncing angle of ~12.2º. This angle is consistent with the angle estimations in Figure 4.24 for the same source conditions (i.e. 12.5º for a water cooled source with Ar flow at P_s~35Torr in Figure 4.24).

Increasing the wire length increases the amount of material required to form a continuous network of clusters.[45] A model that describes wire formation by combining cluster bouncing with percolation theory could be envisaged, in which case the percolation is thought of as a L_2xW_2 two dimensional system with $L_2 > W_2$ (similar to that in Reference [46] but there $W_2 > L_2$). However, such a model is beyond this study and will not be discussed here.

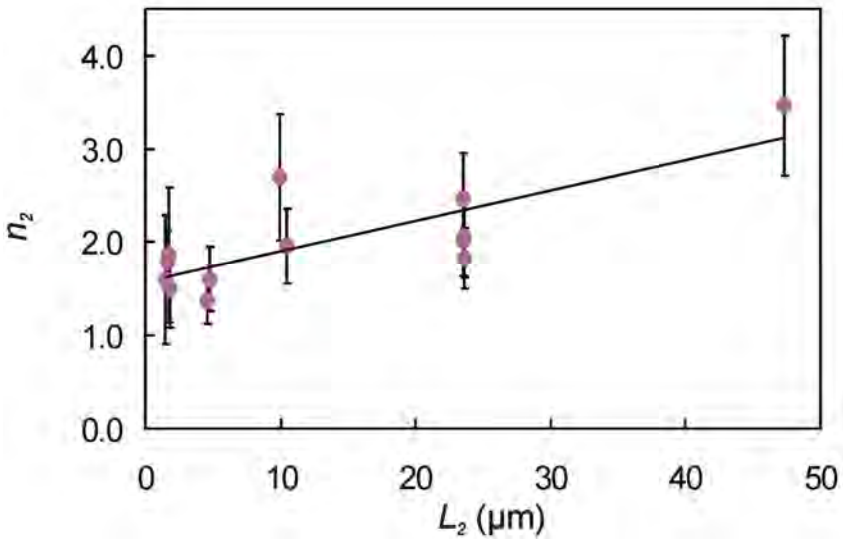

Figure 5.42 The dependence of the number of cluster layers forming the longer wire on its length. The line on the figure is a linear fit.

5.9. Summary

Contacted V-grooves were used successfully to fabricate cluster wires which can be used for device applications. The large cluster collection area provided by the V-groove causes formation of a continuous wire inside the groove before a continuous network of clusters was formed on the plateaus. Various electrical measurements for the contacted wires were taken in order to characterise them.

Two types of *I(V)* characteristics were observed for cluster wires: linear and non-linear. The linear characteristics were observed for samples with low resistances (~kΩ), whereas the non-linear characteristics were observed for samples with high resistances (~MΩ). The non-linearity was assigned to the existence of tunnelling barriers between the wire and the contacts of each sample. These barriers are likely to be Bi-oxide layers, which are likely to be semiconducting.

The *I(V)* curves were found to contain steps toward high conductance. These steps returned to the low conductance (temporary steps) or stayed at the new conductance (permanent steps). The steps were explained in terms of two models. The first model assigns the permanent steps to resistive heating which causes fusion of clusters and breaking conduction paths. The second model assigns the steps to the movement of two close tips of a discontinuous network of clusters due to the large electric field across the tips. If the tips met, the electric field could drop and the tips could revert to their original position causing a temporary step. The tips could also fuse together once they met due to the resistive heating of the electrical current passing through them, which would cause permanent steps.

The gate effect measurements showed that the source-drain current can be modified by applying a voltage to the sample gate. Samples with large resistances showed large gate effects. Small and sustainable gate effects were observed for the heat treated samples which have low resistance (~kΩ).

Annealing was found to enhance the conductivity through the wire by coalescing clusters, and it could possibly enhance the crystallinity of the wire. Annealing was also found to cause wire discontinuities by creating bottlenecks and then beading the clusters. The deposition of clusters on hot substrates was found to produce heat treated wires which were electrically stable.

Hall effect measurements were performed for Bi cluster films using a constant magnetic field of 0.3T. The Hall constant was used to calculate the carrier concentration (n). n decreased as the sample temperature decreased from 290 to 153K. Although the room temperature value of n for the cluster films was similar to the reported values of bulk and thin films of Bi, n of the cluster film was two orders of magnitude lower than those of the bulk and thin films as the temperature decreased to 153K. The large decrease in n of the cluster film with temperature (compared to that of the bulk Bi) was a main reason behind the negative temperature coefficient of resistance (TCR) observed for the cluster wires, i.e. it was a result of the dominance of n which outweighed any decrease in the carrier mobility as the temperature increased from 4.2 to 290K.

The electrical measurements of the cluster wires were found to contain noise with well-defined amplitudes (i.e. RTN). This noise could be understood as a result of modulation of potential barriers in the wire caused by the random variation of Coulomb charges of nearby traps.

An increase in wire length (defined by the contact separation) was found to increase the mean thickness required to cause an onset of conduction for short wires. For long wires, the required mean thickness appears to saturate. The quantitative measurements presented in this chapter were in agreement with our finding in Chapter 4 that cluster bouncing (rather than sliding) was the main process for forming Bi cluster wires in the V-groove. The measurements illustrated the cluster stacking which occurred as a result of the cluster bouncing, and an estimation of the number of cluster layers forming a wire was provided.

References

1 A. D. F. Dunbar, J. G. Partridge, M. Schulze, and S. A. Brown, Eur. Phys. J. D **39**, 415 (2006).

2 R. Reichel, *PhD thesis, Nano scale cluster devices* (Physics and Astronomy Department, University of Canterbury, Christchurch, 2007).

3 A. Kaiser, Rep. Prog. Phys. **64**, 1 (2001).

4 A. B. Kaiser and Y. W. Park, Synth. Met. **152**, 181 (2005).

5 B. Ozturk, C. Blackledge, and B. Flanders, Appl. Phys. Lett. **88**, 073108 (2006).

6 M. Schulze, S. Gourley, S. A. Brown, A. Dunbar, J. Partridge, and R. J. Blaikie, Eur. Phys. J. D **24**, 291 (2003).

7 S. B. Cronin, Y. M. Lin, M. R. Black, O. Rabin, and M. S. Dresselhaus, Proceedings of the 21st international conference on thermoelectrics 243 (2002).

8 B. Yang, M. Mo, H. Hu, C. Li, X. Yang, Q. Li, and Y. Qian, European Journal of Inorganic Chemistry **9**, 1785 (2004).

9 D. Corbett, M. Warner, S. Gourley, and S. Brown, Unpublished (2006).

10 S. Gourley, *MSc thesis, Electronic properties of cluster deposited bismuth nanowires* (Physics and Astronomy Department, University of Canterbury, Christchurch, 2002).

11 K. S. Novoselov, A. K. Geim, S. V. Morozov, D. Jiang, Y. Zhang, S. V. Dubonos, I. V. Grigorieva, and A. A. Firsov, Science **306**, 666 (2004).

12 A. Boukai, K. Xu, and J. R. Heath, Adv. Mater. **18**, 864 (2006).

13 V. T. Petrashov, A. N. Antonov, and B. Nilsson, J. Phys.: Condens. Matter **48**, 9705 (1991).

14 Z. Zhang, X. Sun, M. S. Dresselhaus, J. Y. Ying, and J. Heremans, Phys. Rev. B **61**, 4850 (2000).

15 Y. T. Tian, G. M. Meng, G. Z. Wang, F. Phillipp, S. H. Sun, and L. D. Zhang, Nanotechnology **17**, 1041 (2006).

16 D. Partin, J. Heremans, D. Morelli, C. Thrush, C. Okl, and T. Perry, Phys. Rev. B **38**, 3818 (1988).

17 S. Cho, Y. Kim, A. J. Freeman, G. K. L. Wong, J. B. Ketterson, L. J. Olafsen, I. Vurgaftman, J. R. Meyer, and C. A. Hoffman, Appl. Phys. Lett. **79**, 3651 (2001).

18 E. I. Rogacheva, S. N. Grigorov, O. N. Nashchekina, S. Lyubchenko, and M. S. Dresselhaus, Appl. Phys. Lett. **82**, 2628 (2003).

19 S. Kochowski and A. Opilski, Thin Solid Films **28**, L35 (1975).

20 H. Jupnik, Phys. Rev. **60**, 884 (1941).

21 R. T. Isaacson and G. A. Williams, Phys. Rev. **185**, 682–688 (1969).

22 R. J. Dinger and A. W. Lawson, Phys. Rev. B **7**, 5215 (1973).

23 G. A. Ivanov and Y. T. Levitskii, Fiz. Met. Metalloved **24**, 253 (1967).

24 J. Buxo, M. Saleh, G. Sarrabayrouse, G. Dorville, J. Berty, and M. Brieu, Revue de Physique Appliquee **15**, 961 (1980).

25 S. Agergaard, C. Sondergaard, H. Li, M. Nielsen, S. Hoffmann, Z. Li, and P. Hofmann, New journal of physics **3**, 15.1 (2001).

26 J. H. Moore, C. C. Davis, and M. A. Coplan, *Building scientific apparatus* (Addison-Wesley publishing company Inc., 1989).

27 K. J. Stevens, K. S.Cheong, D. M. Knowles, N. J. Laycock, A. Ayesh, J. Partridge, S. A. Brown, and S. C. Hendy, Curr. Appl. Phys. **6**, 453 (2006).
28 S. Hendy, S. A. Brown, and M. Hyslop, Phys. Rev. B **68**, 241403 (2003).
29 E. I. Rogacheva, T. V. Tavrina, O. N. Nashchekina, S. N. Grigorov, K. A. Nasedkin, M. S. Dresselhaus, and S. B. Cronin, Appl. Phys. Lett. **80**, 2690 (2002).
30 K. S. Ralls and R. A. Buhrman, Phys Rev Lett **60**, 2434 (1988).
31 B. Raquet, M. Goiran, N. Nègre, J. Léotin, B. Aronzon, V. Rylkov, and E. Meilikhov3, Phys. Rev. B **62**, 17144 (2000).
32 R. Rammal, C. Tannous, P. Breton, and A. M. S. Tremblay, Phys. Rev. Lett. **54**, 1718 (1985).
33 S. Kogan, *Electronic noise and fluctuations in solids* (Cambridge university press, Cambridge, 1996).
34 S. Brouer, G. Weiss, and H. B. Weber, Europhys. Lett. **54**, 654 (2001).
35 J. R. Hook and H. E. Hall, *Solid state physics* (John Wiley and sons, 1991).
36 R. Hartman, Phys. Rev. **181**, 1071 (1969).
37 J. P. Michenaud and J. P. Issi, J. Phys. C: Solid State Phys. **5**, 3061 (1972).
38 R. N. Bhargava, Phys. Rev. **156**, 785 (1967).
39 O. Öktu and G. A. Saunders, Proc. Phys. Soc. **91** 156 (1967).
40 A. P. Jeavons and G. A. Saunders, Proc. R. Soc. A **310**, 512 (1969).
41 R. van Vucht, H. van Kempen, and P. Wyder, Rep. Prog. Phys. **48** 853 (1985).
42 P. Sheng, Phys. Rev. B **21**, 2180 (1980).
43 J. Fischer, I. Sosnowska, and M. Szymanski, J. Phys. C **11**, 1043 (1978).
44 J. G. Partridge, S. Scott, A. D. F. Dunbar, M. Schulze, S. A. Brown, A. Wurl, and R. J. Blaikie, IEEE Trans. Nanotech. **61** (2004).
45 R. Monetti and E. Albano, Z. Phys. B **82**, 129 (1991).
46 J. Schmelzer, S. A. Brown, A. Wurl, and M. Hyslop, Phys. Rev. Lett. **88**, 226802 (2002).

6. Conclusions and outlook

The focus of this project was to produce self-assembled nanocluster devices using V-grooves in SiO_2/Si substrates as a template. Devices were fabricated using bismuth clusters produced using an inert gas aggregation source. The device fabrication required detailed studies of the morphology and the electrical properties of the cluster wires. This project also included a study of the operation conditions of a high transmission mass filter since it may be used to fabricate cluster devices in the future. The mass filter was built according to von Issendorff and Palmer's design, and it was commissioned in this project. An experimental and simulational study of the optimum operation conditions of the mass filter was performed during this project.

6.1. The self-assembly in a template

Bi cluster wires were fabricated using V-grooves as a template. The clusters were assembled in the apex of the V-grooves, and the wires exhibited a V-shaped cross section. The clusters were also found to be stacked on top of each other. The detailed study of the cluster wires' morphology showed that the cluster wires were formed mainly because of the clusters bouncing off the V-groove walls. Clusters with a particular size and velocity were found to bounce with a fixed angle which is less than the incident angle. These clusters performed a single bounce because of their stickiness. The fixed bouncing angle determined the wire width. The wire width was changed by changing the cluster bouncing angle when changing the source conditions. Because of the fixed bouncing angle, the wire width was also changed by changing the V-groove width. However, the bouncing angle was found to be insensitive to the increase in the substrate temperature up to 473K.

The morphological study showed that a careful choice of the V-groove width and the contact separation, which defines the wire width, is required when fabricating the device. Decreasing the V-groove width was found to increase the amount of the deposited material required to form a continuous wire since it decreases the cluster collection area. Reducing the wire length had the opposite effect. The V-groove width and the wire length were selected for the device so that the wire was formed prior to forming a continuous network of clusters on the plateaus next to the V-groove.

6.2. Bi cluster device

Devices were fabricated using Bi clusters deposited on V-grooves with pre-formed electrical contacts. The devices exhibited either linear or non-linear *I(V)* characteristics. The non-linear *I(V)* indicates the existence of tunnelling barriers within the device. These barriers were likely to be Bi-oxide layers between the wire and the contacts. The non-linearity in the *I(V)* curves and the sample resistance reflected the barriers' dimensions and the amount of tunnelling through the device.

All of the measured devices showed a negative temperature coefficient of the resistance. This was due to the increase in the carrier concentration which outweighed

any decrease in the carrier mobility as the temperature increased up to room temperature. The *R(T)* curves did not follow an Arrhenius dependence which indicates the non-activated behaviour.

Applying a voltage to the device gate was found to modify the electrical conduction of the device. This gate effect appeared mainly because of the accumulation of electrons in the wire. The gate effect was observed for devices with linear *I(V)* characteristics and low resistance, and for devices with non-linear *I(V)* characteristics and high resistances. The latter gate effect was larger than the former. It should be noted that the observed gate effects were transient effects.

The annealing of the cluster wire was found to either enhance the conduction through the wire or to bead the wire around the bottlenecks causing discontinuities and an increase in the sample resistance. These two effects were observed as steps in the *R(T)* curves during annealing. Annealing wires which contained more clusters than those required to cause the onset of conduction coalesced the clusters, formed solid wires, and enhanced the conduction through the wires. However, all of the annealed wires showed linear *I(V)* characteristics and small gate effects. This gate effect was not transient.

The device study showed that using V-grooves as a template has a potential in the device fabrication. However, more work needs to be done in order to reduce the dimensions of the device while maintaining a low cluster coverage on the plateaus. A low cluster coverage should be obtained if the plateaus are coated by a material such photoresist. This work also suggests that depositing clusters on a hot substrate should be considered in the future device fabrication to reduce the cluster oxidation. Finally it will be interesting in the future to use the novel techniques developed in this project to fabricate cluster devices with different cluster materials, especially semiconductors which are expected to a large and sustainable gate effect to be observed.

6.3. The mass filter

The operation conditions of the von Issendorff and Palmer mass filter were studied by simulation and experimentally using ionized Pd clusters. The study showed that the transmission can be defined as a function of one variable (i.e. the beam deflection angle) instead of using many variables such as the high voltage pulse height, the ion velocity, the ion mass, and the lateral distance the ions cover during the acceleration. The transmission was found to saturate at ~80% for beam deflection angles beyond a certain angle, which is defined by the mass filter geometry. The waiting time between each pair of high voltage pulses applied to the mass filter and the next pair was also found to have a significant effect on the transmission. The maximum transmission was obtained when using the optimum waiting time which allowed the mass filter to be totally filled with ions.

The optimum operation conditions of the mass filter were employed to derive mass distributions of Pd clusters. The study showed that changing the source conditions by increasing the aggregation length increases the size of the produced clusters.

6.4. Outlook

Many opportunities exist to extend the current study of device fabrication using the V-grooves as a template and to fabricate devices with better performance. Different cluster materials can be used for the device fabrication including semiconducting clusters where it is likely that a larger gate effect will be observed. Obviously, a detailed morphological study of the cluster wires is required for each new cluster material.

Thinning the SiO_2 layer will enhance the penetration of the gate electric field to the cluster wire. Further research on the effect of the thinning on the gate effect and the leakage current can be performed.

Reducing the Bi cluster wire width to a single cluster wide wire reduces the device dimensions, and it is likely to facilitate observing the semimetal-semiconductor transition. Such a wire can be formed if the clusters are sliding on the V-groove walls rather than bouncing. This is an opportunity for future studies. Changing the cluster size and velocity, and coating the V-groove walls with non-sticking material such as the photoresist may help the clusters to slide.

In conclusion, this study presented a novel method for fabricating self-assembled cluster devices using V-grooves as a template. This method can be used to fabricate cluster devices using clusters made of different materials or with different preparation conditions.

List of figures

List of tables

List of abbreviations

AFM	atomic force microscope
Ar-He-W	Ar and He inert gases are used in a cluster source which cooled down using water at room temperature
Ar-LN	Ar inert gas is used in a cluster source which cooled down using liquid nitrogen
Ar-W	Ar inert gas is used in a cluster source which cooled down using water at room temperature
FE-SEM	field emission scanning electron microscope
FTM	film thickness quart crystal monitor
HV	high vacuum
IGA	inert gas aggregation source
LN	liquid nitrogen
MOSFET	metal oxide semiconductor field effect transistor
MR	magneto resistance
TCR	temperature coefficient of the resistance
UHV	ultra high vacuum

List of symbols

a	lateral distance the ions cover during the acceleration
C	adhesion coefficients
c	the capacitance
D	cluster diameter
eU_p	the energy the ions gain from the high voltage pulse
F_s	fraction of the surface atoms
G	the conductance
h	average cluster height
$\hbar$	Planck constant
I_{SD}	source-drain current
k_B	Boltzmann constant
L	wire length
m	the cluster mass
MFR	the mass filter resolution
N	number of atoms in a cluster
n	the carrier's concentration
n^*	the number of the critically-sized droplets
P	pressure
p	cluster corrected coverage
p_c	cluster percolation threshold
P_s	source pressure
$p_{surface}$	cluster surface coverage
$q\Phi_B$	the tunnelling barrier height
$q\Phi_m$	metal work function
$q\chi$	electron affinity of the semiconductor
R	resistances
T	temperature
t_d	the delay between the end and the start of two high voltage pulses
t_p	the high voltage pulse widths
t_w	the high voltage pulses repetition rate
U_a	high voltage pulse height
V_g	gate voltage
V_{SD}	source-drain voltage
V_t	the gate voltage value when the gate effect to appears/disappears
W	wire width
w	V-groove width
γ	the surface tension
ΔF^*	maximum free energy
ΔI	the change in I_{SD} when the maximum gate voltage is applied
ε_0	the permittivity of vacuum
θ	ion beam deflection angle
μ	the carrier's mobility
σ	the conductivity
υ	cluster velocity

φ	cluster bouncing angle
Θ	the amount of the deposited material required to provide an onset of conduction

Appendix A: properties of bulk Bi

Property	Parameter	Value	Remarks	Reference
Rhombohedral Lattice constants	a α	4.7458Å 57.23Å	T=298K	[1]
Band overlap	E_0	-0.038eV	T=0K	[2]
Direct band gab	E_{gL}	0.015eV	T=0K	[2]
Electron concentration	n_e	2.73×10^{17} cm^{-3}	T=4.2K	[3]
Dielectric constant	ε	~100	T=300K	[4]
Thermal conductivity	κ	7.92 W/(mK)	T=300K	[5]
Fermi wavelength	λ_F	40nm	T=300K	[6]
Electron mobility	μ_e	$1(m^2/Vs)$	T=300K	[7]
Hole mobility	μ_h	$0.2(m^2/Vs)$	T=300K	[7]

1 D. Schiferl and C. S. Barrett, J. Appl. Crystallogr. **2**, 30 (1969).
2 R. T. Isaacson and G. A. Williams, Phys. Rev. **185**, 682–688 (1969).
3 R. J. Dinger and A. W. Lawson, Phys. Rev. B **7**, 5215 (1973).
4 E. Gerlach, P. Grosse, M. Rautenberg, and W. Senske, Phys. Status Solidi (b) **75**, 553 (1976).
5 D. R. Lide, *CRC Handbook of Chemistry and Physics* (CRC Press, Boston, 1998).
6 G. E. Smith, G. A. Baraff, and J. M. Rowell, Phys Rev **135**, A1118 (1964).
7 D. Partin, J. Heremans, D. Morelli, C. Thrush, C. Okl, and T. Perry, Phys. Rev. B **38**, 3818 (1988).

Appendix B: selection of references used in this work and published by the University of Canterbury Cluster group

1. A. I. Ayesh, A. Lassesson, S. A. Brown, A. D. F. Dunbar, M. Kaufmann, J. G. Partridge, R. Reichel, and J. Van Lith, 'Experimental and simulational study of the operation conditions for a high transmission mass filter', Rev. Sci. Inst. 78, 053906 (2007).
2. J. G. Partridge, R. Reichel, A. I. Ayesh, D. M. A. Mackenzie, and S. A. Brown, 'Production and assembly of atomic clusters', Phys. Stat. Soli. A - Appl. and Mate. Scie. 203, 1217, (2006).
3. R. Reichel, J. G. Partridge, F. Natali, T. Matthewson, and S. A. Brown, A. Lassesson, D. M. A. Mackenzie, A. I. Ayesh, and K. C. Tee, A. Awasthi, and S. C. Hendy, 'From the adhesion of atomic clusters to the fabrication of nanodevices', Appl. Phys. Lett. 89, 213105 (2006).
4. R. Reichel, J. G. Partridge, A. D. F. Dunbar, S. A. Brown, O. Caughley, and A. I. Ayesh, 'Construction and application of a UHV compatible cluster deposition system', Jou. Nanop. Res. 8, 405 (2006).
5. K. J. Stevens, K. S. Cheong, D. M. Knowles, N.J. Laycock, A. I. Ayesh, J. Partridge, S.A. Brown, and S.C. Hendy, 'Electron microscopy of bismuth building blocks for self-assembled nanowires', Curr. Appl. Phys. 6 , 453, (2006).
6. A. I. Ayesh, J. G. Partridge, R. Reichel, A. D. F. Dunbar, and S. A. Brown, 'Assembly of Bi clusters into Nanowires using etched V-grooves as templates', Proceedings of the 2004 Conference on Optoelectronic and Microelectronic Materials and Devices, IEEE Press, p324 (2005).
7. J. G. Partridge, S. Scott, A. D. F. Dunbar, M. Schulze, S. A. Brown, A. Wurl, and R. J. Blaikie, IEEE Trans. Nanotech. 61 (2004).
8. J. G. Partridge, S. A. Brown, C. Siegert, A. D. F. Dunbar, R. Nielson, M. Kaufmann, and R. J. Blaikie, Microelectron. Eng. 73, 583 (2004).
9. J. Schmelzer, S. A. Brown, A. Wurl, and M. Hyslop, Phys. Rev. Lett. 88, 226802 (2002).
10. M. Schulze, S. Gourley, S. A. Brown, A. Dunbar, J. Partridge, and R. J. Blaikie, Eur. Phys. J. D 24, 291 (2003).

Acknowledgements

I would like to thank my supervisor Assoc. Prof. Simon Brown for his constant encouragement, patience, and guidance throughout this thesis.

I would also like to thank Dr. Jim Partridge for the technical guidance throughout the device fabrication and the stimulating discussions.

This thesis has benefited greatly from the input of Dr. Shaun Hendy and Dr. Aruna Awasthi at Industrial Research Ltd. They performed molecular dynamic simulations of the cluster bouncing, which were used extensively in this thesis.

Vital information and support from the Post Doc(s) and my fellow students in the cluster group: Dr. René Reichel, Dr. Martin Kaufmann, KC Tee, Dr. Euan Boyd, Dr. Franck Natali, David Mackenzie, David MacCarthy, Dr. Alan Dunber, Dr. Shelley Scott, Gaelle Parguez, and Kiri Nichol.

I would like also to thank the staff of NCD Ltd for the support and the motivating discussions: Dr. Andreas Lassesson, Dr. Joris van Lith, Monica Schulze, and Shannon Kopp.

The enthusiasm and the expertise of the staff in the University of Canterbury were greatly beneficial to this thesis. In particular, I would like to mention the Physics and Astronomy Department technicians, Owen Caughley, Stephen Hemmingsen, and Graeme Kershaw who, amongst other tasks, machined the source crucibles and the sample holders. The efforts of Ross Ritchie and Geoff Graham in building the pulse generator for the mass filter were highly appreciated. I would like also to express my thanks to Bob Flygenring for his steady supply of cryogenic fluids. The assistance in the sample processing of Helen Devereux and Gary Turner in the Electrical Engineering Department is also appreciated, and likewise the assistance of the staff members of the Learning Skills Centre.

Finally, I would like to express my sincere thanks to my family members: my parents, my wife, Ishraq, and my sons, Hashem, Malek, and Omar. They have encouraged and inspired me throughout the years of my thesis.